ABSTRACT

Title of Dissertation: Trapped Ions: From Error Correction to Simulation of Quantum Field Theories

Hong Nhung Nguyen
Doctor of Philosophy, 2024

Dissertation Directed by: Assistant Professor Norbert Linke
Department of Physics

Trapped ions stand out as a leading platform for quantum computing due to their long coherence times, high-fidelity quantum gates, and the ability to precisely control individual qubits, enabling scalable and precise quantum computations. This dissertation reports advances in quantum computing with trapped ions, focusing on robust and high-fidelity entanglement generation, logical qubit encoding, and applications in quantum simulations of high-energy physics.

In particular, we report the implementation of a novel pulse optimization scheme for achieving high-fidelity entangling gates in our setup. The scheme enables a balanced trade-off between robustness to experimental drift, laser power, and gate duration, without the need for expensive optimization. We also demonstrate the implementation of the Shor code with different code distances on our trapped-ion quantum computer, highlighting the fault-tolerant preparation of a logical qubit with high fidelity and showcasing the potential for reliable quantum computing.

Finally, we detail an experimental quantum simulation of the Schwinger model, a quantum electrodynamics theory in 1+1 dimensions, using two, four, and six qubits, demonstrating non-perturbative effects such as pair creation over extended periods of time. We study the gate requirement for two formulations of the model using a quantum simulation algorithm, considering the trade-offs between Hamiltonian term ordering, the number of time steps, and experimental errors. We employ a symmetry-protection protocol with random unitaries and a symmetry based post-selection technique to minimize errors. This work emphasizes the importance of the integrated approach between theory, algorithms, and experiments for efficient simulation of complex physical systems like lattice gauge theories.

TRAPPED IONS:
FROM ERROR CORRECTION
TO SIMULATION OF QUANTUM FIELD THEORIES

by

Hong Nhung Nguyen

Dissertation submitted to the Faculty of the Graduate School of the
University of Maryland, College Park in partial fulfillment
of the requirements for the degree of
Doctor of Philosophy
2024

Advisory Committee:
Professor Alicia Kollár, Chair
Professor Norbert Linke, Advisor and Co-Chair
Professor Zohreh Davoudi
Professor Ian Spielman
Professor Xiaodi Wu

Table of Contents

List of Tables

List of Figures

List of Abbreviations

AOM	Acousto-Optic Modulator
AWG	Arbitrary Waveform Generator
COM	Center-of-mass
CPU	Central Processing Unit
DAC	Digital to Analog Conveter
DAQ	Data Acquisition
DDS	Direct Digital Synthesizer
DOE	Diffractive-Optic Element
EOM	Electro-Optic Modulator
FPGA	Field Programmable Gate Array
FTXX	Fourier-series based entangling gates
GPIB	General Purpose Interface Bus
GUI	Graphical User Interface
LAN	Local Area Network
MAX	Measurement and Automation Explorer
NHEP	Nuclear and High-Energy Physics
NI	National Instruments
PBS	Polarized Beam Splitter
PMT	Photo-Multiplier Tube
RF	Radio Frequency
RWA	Rotating Wave Approximation
SFP	Software Front Panel
SK1	1st order Solovay-Kitaev composite pulse
SPAM	State Preparation And Measurement
TTL	Transistor-Transistor Logic
UHV	Ultra-High Vacuum
VDT	Very Dumb Terminal
VISA	Virtual Instrument Software Architecture
VVA	Voltage Variable Attenuator
XOP	External Operation

Chapter 1: Introduction

Quantum computing represents a revolutionary approach to information processing that exploits the phenomena of quantum mechanics, such as superposition and entanglement, to perform certain calculations at speeds unattainable by classical computers. The inception of quantum computing dates back to the early 1980s when Richard Feynman proposed the idea of a quantum computer to simulate and understand complex quantum systems [5], a task challenging for traditional computers. Since then, the field has burgeoned, with significant theoretical and technological advancements. The potential of quantum computing is vast and varied, promising to solve certain types of problems, like factoring large numbers [6], solving large optimization problems [7–14], and simulating molecular structures for drug discovery [15–18], considerably faster than the best supercomputers today. This potential extends to revolutionizing fields like cryptography, materials science, and complex system modeling.

The fundamental unit of quantum computing is the qubit, which, unlike a classical bit, can exist in a superposition of states 0 and 1. A useful way to visualize the difference between a qubit and a classical bit is by using the Bloch sphere, a three-dimensional space, with the north and south poles corresponding to the 0 and 1 states, respectively. Any point on the surface of the sphere represents a possible state of the qubit, while only the

poles are the equivalent of the classical bit. This allows a quantum computer to hold and process a vast amount of information with far fewer qubits than classical bits. The ability to encode information not just in binary states, but across a continuum of probabilities and phases (the lattitudes and longitudes of the Bloch sphere), is the core of quantum computing's potential power. To achieve the speed up in calculation, the qubits are often prepared in a superposition of many states, each state represents a possible outcome of the problem. Then these superposed states are manipulated, through a series of carefully designed quantum gates, to interfere constructively or destructively with each other so that only the states that encode the right answer to the problem remain [19].

Quantum computers can be constructed using various physical systems, each with its own set of advantages and challenges. Leading platforms include superconducting circuits, which leverage Josephson junctions to create qubits; trapped ions, where qubits are formed from the electronic states of ions held in place by electromagnetic fields; and semiconductor qubits, which use the spin states of individual electrons confined in quantum dots. Rydberg atoms, another promising platform, utilize highly excited states of neutral atoms, Rydberg states, whose amplified electric dipole moments let them interact with each other over relatively large distances. These atoms are trapped in an reconfigurable array of optical tweezers, allowing them to be rearranged for parallel gate operations and low cross-talk measurement.

Trapped-ion Quantum Computers—Among these platforms, trapped ion quantum computing stands out for several reasons. Historically, it was one of the first methods to be proposed and demonstrated. Trapped ions are excellent candidates for qubits due to their

long coherence times and strong confining potential, allowing for more quantum operations to be performed before the system decoheres. Additionally, ions are identical by nature, providing uniform qubits, and can be manipulated with high precision using lasers. Trapped ions offer high-fidelity quantum gates, a crucial requirement for quantum error correction—a procedure that enables quantum computers to detect and correct errors. The ability to entangle any ions in the chain, no matter how far apart they are, with extreme accuracy makes trapped ions a compelling choice for constructing quantum computers.

Over the past few years, trapped ion quantum computing has seen significant progress. Quantum gates on a chain of two ions have been substantially improved, both in terms of fidelity (99.94% for 2-qubit, 99.993% for single qubit [20–22]) and speed (1.6 μs [23]). The first instances of quantum algorithms were performed on a longer chain of (five) ions, achieving fidelity of 98% for two-qubit gates and 99% for single-qubit gates [3, 24, 25]. The second generation of these experiments have demonstrated the same level of gate fidelity even when scaling up to chains of 15 to 25 ions [26–28].

Instead of having a long chain of ions, another approach called quantum charge-coupled device (QCCD) [29, 30] employs multiple trapping zones, each with only two computational ions at a time. In QCCD, entangling gates are only performed on a pair of ions when they are in the same trapping zone. The short chain reduces the complexity of the sub-system and allows extremely high fidelity entangling operation. To retain connectivity between the qubits, the ion pairs are split, shuttled, and merged into different pairs between implementations of quantum gates. While shuttling operations are time-consuming and increase the complexity of the system (trap, scheduling, etc.), QCCD-based quantum computers have proved feasible [31, 32] and demonstrated remarkable gate fidelity (99.8%

for 2-qubit, 99.997% for single qubit) in a system of 32 qubits [33, 34].

Efforts are currently being made to scale up trapped-ion quantum computers to support hundreds of qubits and beyond. A promising strategy involves connecting multiple traps through photonic links [35,36]. In this method, ions are induced to emit photons that are entangled with the ions' states. These photons, when emitted from ions in separate traps and measured in an entangled state, facilitate the entanglement of the ions themselves [37]. An experimental demonstration has successfully established a photonic link, achieving entanglement between ions in traps separated by a few meters. The experiment showed relatively high fidelity (94%) and a sub-Hz entanglement generation rate [38]. Current efforts are focused on enhancing both the efficiency and fidelity of these ion-photon entanglement operations.

Besides increasing the system size and improving the gate fidelity, additional capabilities have also been added to trapped-ion quantum computers. Many of the devices mentioned earlier (both long chains and QCCD) are now capable of performing mid-circuit measurement with low cross-talk [31,32,34,39–42]. Some of them can also support parallel two-qubit operations [31–34,43,44]. These enhancements broaden the computational capabilities of trapped-ion systems and pave the way for more complex and efficient quantum computing operations, including the implementation of quantum error correction.

Quantum Error Correction—Quantum states are highly sensitive to environmental disturbances, leading to errors that can disrupt quantum computations and undermine their potential advantages. This necessitates sophisticated error correction mechanisms to ensure the stability and accuracy of quantum information. Quantum error correction (QEC)

protects quantum information by encoding the state of a single qubit across multiple physical qubits, employing redundancy and entanglement to detect and correct errors without directly measuring the quantum state itself. Errors are identified and rectified by observing the collective properties of entangled qubits.

The process of encoding of a logical qubit involves multiple physical qubits and physical gates, each subject to its own set of imperfections. To ensure the benefits of logical encoding, the physical gates must be of high fidelity and be carefully designed to suppress the propagation of errors. Numerous experiments with trapped ions have successfully showcased the fault-tolerant encoding of logical qubits, along with error detection achieved through projective measurement [26, 45, 46]. Subsequent experiments have introduced non-destructive measurement using ancillary qubits [32, 39]. This technique permits the real-time identification and correction of errors [32], marking a significant step towards fault-tolerant quantum computing. Remarkably, in some experiments, the fidelity of logical state preparation [26, 47] have surpassed that of the physical state.

Once information has been encoded in logical qubits, quantum computers must also be able to apply logical quantum gates. A universal set of logical operations typically includes single- and two-qubit Clifford gates (CNOT, Hadamard, X, Y, Z gates), together with a non-Clifford gate such as the T gate [48]. Implementing a logical T gate requires the fault-tolerant preparation of a so-called magic state. In recent years, trapped-ion experiments have made significant advancements in realizing this logical gate set, including single-qubit Clifford gates [26] and two-qubit Clifford gates [39,47], alongside non fault-tolerant [26] and fault-tolerant magic state preparation [39]. Notably, in an experiment reported in Ref. [47], the logical two-qubit gate fidelity after real-time error correction is higher than that of the

physical gate.

Early Applications—While the development of quantum error-corrected devices is ongoing, the potential of quantum computing is already being demonstrated on small-scale quantum devices. Important among these demonstrations are foundational quantum algorithms, such as Shor's algorithm [1, 6, 25] for the efficient factoring of large numbers, and Grover's algorithm [7, 49] for searching unsorted databases, both offering substantial speed advantages over their classical counterparts under error-free conditions on sufficiently large qubit systems. Additionally, there are emerging algorithms such as the Quantum Approximate Optimization Algorithm (QAOA) [12, 50–53], aimed at solving optimization problems, and Variational Quantum Eigensolvers (VQE) [54–56], designed for approximating the ground states of complex Hamiltonians. The advantage of these algorithms over classical methods are still being explored, rendering them prime candidates for experimental validation and further research.

One of the most exciting applications of quantum computers is quantum simulation, echoing the Richard Feynman's original idea of using quantum systems to simulate quantum systems. Several highly entangled quantum states of interest to quantum information and quantum many-body physics have been realized with trapped ions [34,57–60]. By mapping physical particles to qubits and decomposing their evolution into a series of quantum gates, quantum computers enable the simulation of complex dynamics across various fields, including condensed matter physics [61–66], nuclear and high-energy physics [67, 68], and quantum chemistry [69–74]. This approach enhances our understanding of fundamental physical phenomena and opens new avenues for scientific discovery by modeling interac-

tions at the quantum level.

Outline of the Dissertation—The research towards this dissertation yielded several contributions to the evolving field of quantum computing over the course of my doctoral study, all of which are published in 20 research papers listed below. Here, we highlight selected works on the development of a new method for generating robust entanglement in a long chain of ions, encoding a logical qubit using the Shor code with nine ions, and applying the most recent advances in quantum algorithms to simulation of high-energy physics (HEP). The dissertation is structured as follows.

Chapter 2 lays the theoretical framework necessary for understanding the dynamics of trapped ions and explains their role in constructing the quantum computing toolbox.

Chapter 3 describes the experimental hardware that allows us to trap and cool ions, control their states with high fidelity to create a fully connected trapped ion quantum computer.

Chapter 4 describes the structure of the experimental software stack that converts the abstract notion of a quantum gate into a series of laser pulses that controls the states of the ions. We also highlight several upgrades that enhances the capability of the experiment.

Chapter 5 focuses on the implementation of a novel pulse optimization scheme for achieving high-fidelity entangling gates in our setup. The scheme enables a balanced trade-off between robustness to experimental drift, laser power, and gate duration, without the need for expensive optimization. This chapter is based on the following publication:

- *Efficient, stabilized two-qubit gates on a trapped-ion quantum computer*, R Blümel, N Grzesiak, **NH Nguyen**, AM Green, M Li, A Maksymov, NM Linke, Y Nam, Phys.

Rev. Lett. 126, 220503 (2021).

Chapter 6 reports experimental implementations of the Shor code with different code distances on our trapped-ion quantum computer. Specifically, we prepared m-qubit GHZ states and sampled the measurement results to construct the logical states of the distance m Shor code that can tolerate up to m physical errors ($m = 3, 5, 7$). The synthetic logical fidelity shows how deeper encoding can compensate for additional gate errors in state preparation for larger logical states. The optimal code size depends on the physical error rate and, in our system, we find that choosing $m = 5$ results in the best performance. We also present a fault-tolerant preparation of logical states $|\pm\rangle_L$ of the Shor code distance 3 with 9 qubits, with 98.8(1)% and 98.5(1)% fidelity, respectively. This chapter is based on the following publication:

- *Demonstration of Shor encoding on a trapped-ion quantum computer*, **NH Nguyen**, M Li, AM Green, CH Alderete, Y Zhu, D Zhu, KR Brown, and NM Linke, Phys. Rev. Appl. 16, 024057 (2021).

Chapter 7 shows an experimental quantum simulation of a quantum electrodynamics theory in 1+1 dimensions, the Schwinger model. We simulate the real-time dynamics of the model with two, four, and six qubits, and demonstrate non-perturbative effects such as pair creation for times much longer than previously accessible. We study the gate requirement of two formulations of the model using a quantum simulation algorithm, as well as the trade-off between errors from the ordering of the Hamiltonian terms, the number of time steps, and experimental imperfections. To mitigate experimental errors, we implement a symmetry-protection protocol for suppressing coherent errors and a symmetry-inspired post-selection.

Our work demonstrates the integrated theoretical, algorithmic, and experimental approach that is essential for efficient simulation of lattice gauge theories and other complex physical systems. This chapter is based on the following publication:

- *Digital Quantum Simulation of the Schwinger Model and Symmetry Protection with Trapped Ions*, **NH Nguyen**, MC Tran, Y Zhu, AM Green, CH Alderete, Z Davoudi, NM Linke, PRX Quantum 3, 020324 (2022).

While a universal gate set is sufficient to implement an arbitrary unitary evolution, simulating infinite-level particles, such as bosons, with finite-level qubits can be inefficient. Chapter 8 presents a blueprint for encoding bosonic degrees of freedom with the motion of trapped ions. Coupling these motional degrees of freedom to the qubits' states enables efficient simulations of models that consists of both finite- and infinite-level particles. We report the progress of an experimental implementation of such spin-phonon gates on our quantum computer towards simulating the dynamics of a system of fermions interacting with scalar bosons via Yukawa interactions.

Other work not reported in this dissertation include:

- *Pairwise-parallel entangling gates on orthogonal modes in a trapped-ion chain*, Y Zhu, AM Green, **NH Nguyen**, CH Alderete, E Mossman, NM Linke, Adv. Quantum Technol. 2300056 (2023).

- *Bespoke Pulse Design for Robust Rapid Two-Qubit Gates with Trapped Ions*, SS Vedaie, EJ Páez, **NH Nguyen**, NM Linke, BC Sanders, Phys. Rev. Res. 5, 023098 (2023).

- *Realizing two-qubit gates through mode engineering on a trapped-ion quantum computer*, M Li, **NH Nguyen**, AM Green, J Amini, NM Linke, Y Nam, arXiv:2208.01584.

- *Para-particle oscillator simulations on a trapped ion quantum computer*, CH Alderete, AM Green, **NH Nguyen**, Y Zhu, NM Linke, BM Rodriguez-Lara, arXiv:2207.02430.

- *Experimental measurement of out-of-time-ordered correlators at finite temperature*, AM Green, A Elben, CH Alderete, LKh Joshi, **NH Nguyen**, TV Zache, Y Zhu, B Sundar, NM Linke, Phys. Rev. Lett. 128, 140601 (2022).

- *Multi-round QAOA and advanced mixers on a trapped-ion quantum computer*, Y Zhu, Z Zhang, B Sundar, AM Green, CH Alderete, **NH Nguyen**, KRA Hazzard, NM Linke, Quantum Sci. Technol. 8 015007 (2023).

- *Quantum computational advantage attested by nonlocal games with the cyclic cluster state*, AK Daniel, Y Zhu, CH Alderete, V Buchemmavari, AM Green, **NH Nguyen**, TG Thurtell, A Zhao, NM Linke, A Miyake, Phys. Rev. Research 4, 033068 (2022).

- *Experimental realization of para-particle oscillators*, CH Alderete, AM Green, **NH Nguyen**, Y Zhu, BM Rodriguez-Lara, NM Linke, arXiv:2108.05471.

- *Cross-Platform Comparison of Arbitrary Quantum Computations*, D Zhu, ZP Cian, C Noel, A Risinger, D Biswas, L Egan, Y Zhu, AM Green, CH Alderete, **NH Nguyen**, Q Wang, A Maksymov, Y Nam, M Cetina, NM Linke, M Hafezi, C Monroe, Nat. Commun. 13, 6620 (2022).

- *Probing many-body localization on a noisy quantum computer*, D Zhu, S Johri, **NH**

Nguyen, CH Alderete, KA Landsman, NM Linke, C Monroe, AY Matsuura, Phys. Rev. A 103, 032606 (2021).

- *Architecting Noisy Intermediate-Scale Quantum Computers: A Real-System Study*, P Murali, NM Linke, M Martonosi, AJ Abhari, **NH Nguyen**, CH Alderete, IEEE Micro, 40 (3), 73 (2020).

- *Quantum walks and Dirac cellular automata on a programmable trapped-ion quantum computer*, CH Alderete, S Singh, **NH Nguyen**, D Zhu, R Balu, C Monroe, CM Chandrashekar, NM Linke, Nat. Commun. 11, 3720 (2020).

- *Generation of thermofield double states and critical ground states with a quantum computer*, D Zhu, S Johri, NM Linke, KA Landsman, CH Alderete, **NH Nguyen**, AY Matsuura, TH Hsieh, C Monroe, Proc. Natl. Acad. Sci. USA 117 (41), 25402 (2020).

- *Dynamical mean field theory algorithm and experiment on quantum computers*, I Rungger, N Fitzpatrick, H Chen, CH Alderete, H Apel, A Cowtan, A Patterson, D Munoz Ramo, Y Zhu, **NH Nguyen**, E Grant, S Chretien, L Wossnig, NM Linke, R Duncan, arXiv:1910.04735.

- *Training of Quantum Circuits on a Hybrid Quantum Computer*, D Zhu, NM Linke, M Benedetti, KA Landsman, **NH Nguyen**, CH Alderete, A Perdomo-Ortiz, N Korda, A Garfoot, C Brecque, L Egan, O Perdomo, C Monroe, Sci. Adv. 5, 10 (2019).

- *Noise reduction using past causal cones in variational quantum algorithms*, O Shehab, IH Kim, NH Nguyen, KA Landsman, CH Alderete, D Zhu, C Monroe, NM Linke,

arXiv:1906.00476.

Chapter 2: Quantum Computing with Trapped Ions

In this chapter we describe the general theoretical background underpinning the trapped-ion quantum computing architecture. We will consider abstract ions confined in a three dimensional harmonic potential and leave the specific details of the experimental realization of the ions, techniques to trap, cool them, to manipulate and detect their states to Chapter 3.

2.1 Ions as Qubits

Ions are charged atoms that interact strongly via the Coulomb interaction when held in a common electromagnetic potential. Their internal degrees of freedom (dof) are electronic states (sometimes coupled with the nuclear spin) and external dofs are the center-of-mass motion in different directions in space. The qubit or spin is encoded in two states from many electronic levels of an ion. The ions are usually confined by a potential with different strengths in different directions to form an one- or two-dimensional crystal. The ions' motion are coupled via the Coulomb interaction (Section 2.2). These coupled motion are used to mediate interactions between qubits that belong to ions in the same crystal,

while photons whose polarizations are correlated with the qubit states are used to mediate interaction between qubits from different crystals. In this thesis, we will focus on the former case, specifically laser-mediated interactions between ions in a linear chain (1D crystal).

Lasers can be used to initialize and read out the states of the ions (see Section 3.4). While both lasers and microwave fields can be used to perform single-qubit and multi-qubit gates on ions [3,26,75], the individual ion addressing is more straight-forward with lasers. In this thesis, we will focus on the laser-based single- and two-qubit gates, specifically the two-qubit XX-type interaction (Chapter 5). Any other multi-qubit gates can be decomposed into a series of arbitrary single-qubit gates and XX-type two-qubit gates. We define $|0\rangle = \begin{pmatrix} 1 \\ 0 \end{pmatrix}$, $|1\rangle = \begin{pmatrix} 0 \\ 1 \end{pmatrix}$, and the Pauli matrices

$$\hat{\sigma}^z = \begin{pmatrix} 1 & 0 \\ 0 & -1 \end{pmatrix}, \ \hat{\sigma}^x = \begin{pmatrix} 0 & 1 \\ 1 & 0 \end{pmatrix}, \ \hat{\sigma}^y = \begin{pmatrix} 0 & -i \\ i & 0 \end{pmatrix}. \tag{2.1}$$

Related useful matrices are $\hat{\sigma}^+ = (\hat{\sigma}^x + i\hat{\sigma}^y)/2$ and $\hat{\sigma}^- = (\hat{\sigma}^x - i\hat{\sigma}^y)/2$.

The native gates are single-qubit Z rotations

$$R_z(\theta) = \mathrm{e}^{-i\theta/2\ \hat{\sigma}^z} = \begin{pmatrix} \mathrm{e}^{-i\frac{\theta}{2}} & 0 \\ 0 & \mathrm{e}^{i\frac{\theta}{2}} \end{pmatrix}, \tag{2.2}$$

single-qubit rotations around an axis ϕ in the XY plane of the Bloch sphere

$$R(\theta, \phi) = \mathrm{e}^{-i\theta/2\ \hat{\sigma}^\phi} = \begin{pmatrix} \cos\frac{\theta}{2} & -i\mathrm{e}^{-i\phi}\sin\frac{\theta}{2} \\ -i\mathrm{e}^{i\phi}\sin\frac{\theta}{2} & \cos\frac{\theta}{2} \end{pmatrix}, \tag{2.3}$$

with $\hat{\sigma}^{\phi} = \hat{\sigma}^{+}\mathrm{e}^{-i\phi} + \hat{\sigma}^{-}\mathrm{e}^{i\phi} = \hat{\sigma}^{x}\cos\phi + \hat{\sigma}^{y}\sin\phi$, and two-qubit gate

$$XX(\chi) = \mathrm{e}^{-i\chi\hat{\sigma}^{x}\hat{\sigma}^{x}} = \begin{pmatrix} \cos\chi & 0 & 0 & -i\sin\chi \\ 0 & \cos\chi & -i\sin\chi & 0 \\ 0 & -i\sin\chi & \cos\chi & 0 \\ -i\sin\chi & 0 & 0 & \cos\chi \end{pmatrix}, \tag{2.4}$$

where ϕ specifies the axis of rotation for the single-qubit gates, θ and χ are the rotation angles of the single- and two-qubit gates, respectively. The above matrices are written using the nice property of a string of Pauli matrices $\hat{\mathrm{P}} = \hat{\sigma}_1^{\alpha_1}\hat{\sigma}_2^{\alpha_2}...\hat{\sigma}_{\mathrm{n}}^{\alpha_{\mathrm{n}}}$, where $\alpha_k = x, y, z$, that $\hat{\mathrm{P}}^2 = \mathrm{I}$, where I is the $2^n \times 2^n$ identity matrix. Hence

$$\mathrm{e}^{i\theta\ \hat{\mathrm{P}}} = \cos\theta\ \mathrm{I} + \mathrm{i}\sin\theta\ \hat{\mathrm{P}}. \tag{2.5}$$

The above native gates form a universal gate set. Any unitary operators can be decomposed into these gates. The easiest to see are the Pauli-gates, Pauli-X is $R_x(\pi) = R(\pi, 0)$, Pauli-Y is $R_y(\pi) = R(\pi, \pi/2)$, Pauli-Z is $R_z(\pi)$, S-gate is $R_z(\pi/2)$, T-gate is $R_z(\pi/4)$, all up to a global phase. Below are the decomposition of other common gates (H, CNOT, CZ, Toffoli or CCNOT) in quantum computing using our native gate set.

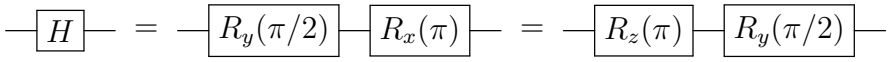

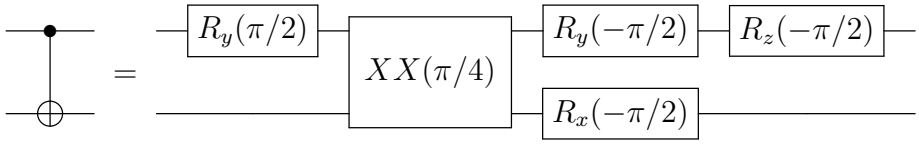

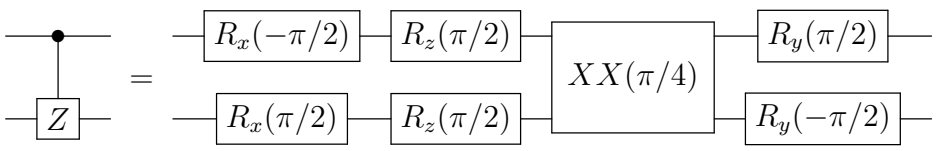

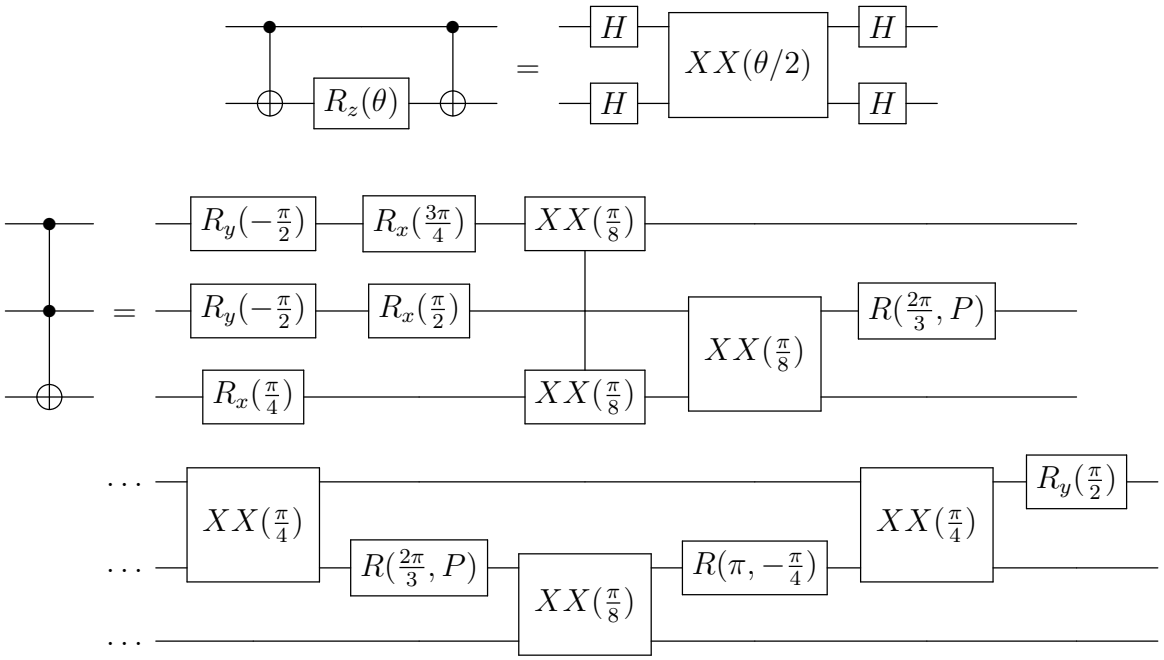

where $P = -\arcsin\left(\sqrt{\frac{2}{3}}\right)$. A more thorough discussion of how to optimally decompose common unitaries to our native gate set and complete characterization of these gates can be found in Chapter 5 of Ref. [4]. For general ideas about how to construct arbitrary unitary operations, refer to Chapter 4.3 of Ref. [19] (especially the exercises).

2.2 Ion Motion

The collective motion of the ions are an important resource for quantum information processing with trapped ions. While the ion motion are not explicitly present in a quantum gate, they mediate the generation of entanglement between the ions through the spin-motion interaction. The quantized collective motion or phonons are also interesting by themselves. They are the intrinsic bosonic degrees of freedom in trapped ions, which will be a extremely useful and powerful tool for quantum computing and simulation when arbitrary phonon-phonon interactions can be engineered in a controllable and tunable fashion.

2.2.1 Equilibrium Position

Consider a chain of N ions of mass m, charge Q confined in a three-dimensional potential in vacuum. The potential is generated by DC and RF electrodes, commonly known as the Paul trap [76, 77]. We will describe the trap in details in Section 3.2. For now, we assume it is a purely quadratic potential characterized by the confinement strength ω_x, ω_y, ω_z.

$$\phi = \sum_{i=1}^{N} \frac{1}{2} m \Big(\omega_x^2 x_i^2(t) + \omega_y^2 y_i^2(t) + \omega_z^2 z_i^2(t) \Big), \tag{2.6}$$

where i denotes the ion index. The ion motion can be decomposed into three orthogonal axes: one axial (z, along the chain), and two radial (x, y), i.e.,

$$\vec{r_i}(t) = x_i(t)\vec{e_x} + y_i(t)\vec{e_y} + z_i(t)\vec{e_z}. \tag{2.7}$$

The ions' positions at equilibrium are determined by the Coulomb interaction between the ions and the confining potential ϕ. The total potential energy is [78]

$$V = \sum_{i=1}^{N} \frac{1}{2} m \Big(\omega_x^2 x_i^2(t) + \omega_y^2 y_i^2(t) + \omega_z^2 z_i^2(t) \Big) + \sum_{\substack{i,j=1 \\ i \neq j}}^{N} \frac{Q^2}{8\pi\epsilon_0 \left| \vec{r_i}(t) - \vec{r_j}(t) \right|}. \tag{2.8}$$

Since the ions lie along the chain at equilibrium, $\vec{r_i}^{(0)} = z_i^{(0)}\vec{e_z}$, we only need to minimize the potential with respect to the axial direction to determine their equilibrium positions [79]

$$\left. \frac{\partial V}{\partial z_i} \right|_{\vec{r_i} = \vec{r_i}^{(0)}} = \left. \frac{dV_z}{dz_i} \right|_{z_i = z_i^{(0)}} = 0, \tag{2.9}$$

with

$$V_z = \sum_{i=1}^{N} \frac{1}{2} m \omega_z^2 z_i(t)^2 + \sum_{\substack{i,j=1 \\ i \neq j}}^{N} \frac{Q^2}{8\pi\epsilon_0 \left| z_i(t) - z_j(t) \right|}. \tag{2.10}$$

Eq. (2.9) can be solved analytically for $N = 2, 3$ and numerically for longer chain [79]. The key features of the solutions are:

i) The ion spacing is smallest at the center of the chain and largest towards the ends, as expected of a quadratic potential.

ii) When scaled by the length scale

$$l = \sqrt[3]{\frac{Q^2}{4\pi\epsilon_0 m\omega_z^2}}, \tag{2.11}$$

the dimensionless equilibrium positions $u_i = z_i^{(0)}/l$ now only depends on the number of ions in the trap, not the confining potential ω_z or mass of the ions m [79]. This property allows ω_z to be deduced from the ion spacing. It is particular relevant in our experiment, where the (Raman) beams driving the motion have negligible overlap with z direction, hence do not excite the z motion.

2.2.2 Normal Mode Picture

Small perturbation (by optical or magnetic fields or collisions with the background gas) causes the ions to oscillate around its equilibrium position $\vec{r}_i^{(0)}$. The ions' positions can be rewritten as $\vec{r}_i(t) = \vec{r}_i^{(0)} + \vec{\delta r}_i(t)$. The ions are coupled through Coulomb interaction. Their motion can be described as a superposition of the eigen-modes (normal modes) with eigen-frequencies ω_m. These normal modes of the COM of the ions are purely classical. When the ions are sufficiently cooled down (their kinetic energy is on the order of a few tens of $\hbar\omega_m$), these energy levels are best described by the quantum harmonic oscillators.

The ion motion is described by the Lagrangian $L = T - V$, where T is the kinetic energy and V is the potential energy given by Eq. (2.8). Since ions' displacements are small,

we can expand the Lagrangian about the equilibrium positions and ignore terms higher than second order in $\vec{\delta r}_i(t)$ (which cause coupling between the orthogonal modes) [78]

$$L \approx \frac{m}{2}\sum_{i=1}^{N}\dot{\vec{\delta r}}_i^{\,2} - \frac{1}{2}\sum_{i,j=1}^{N}\left(\delta x_i \delta x_j \frac{\partial^2 V}{\partial x_i \partial x_j} + \delta y_i \delta y_j \frac{\partial^2 V}{\partial y_i \partial y_i} + \delta z_i \delta z_j \frac{\partial^2 V}{\partial z_i \partial z_j}\right)\Bigg|_{\delta r_i, \delta r_j = 0} \tag{2.12}$$

We can separate the above Lagrangian into three equations for each direction. Since the two radial directions are similar to each other, with only a difference in confinement strength $\omega_{x,y}$, we will focus on one of them, say x.

$$L_z \approx \frac{m}{2}\left[\sum_{i=1}^{N}\left(\frac{d}{dt}\delta z_i\right)^2 - \omega_z^2 \sum_{i,j=1}^{N} A_{ij}\delta z_i \delta z_j\right], \tag{2.13}$$

$$L_x \approx \frac{m}{2}\left[\sum_{i=1}^{N}\left(\frac{d}{dt}\delta x_i\right)^2 - \omega_z^2 \sum_{i,j=1}^{N} B_{ij}\delta x_i \delta x_j\right], \tag{2.14}$$

where [78]

$$A_{ij} = \frac{1}{m\omega_z^2}\frac{\partial^2 V}{\partial z_i \partial z_j} = \begin{cases} 1 + 2\sum_{k=1, k\neq j}^{N} \frac{1}{|u_j - u_i|^3} & \text{if } i = j \\ -\frac{2}{|u_j - u_i|^3} & \text{if } i \neq j, \end{cases} \tag{2.15}$$

$$B_{ij} = \frac{1}{m\omega_z^2}\frac{\partial^2 V}{\partial x_i \partial x_j} = \begin{cases} \left(\frac{\omega_x}{\omega_z}\right)^2 - \sum_{k=1, k\neq j}^{N} \frac{1}{|u_j - u_i|^3} & \text{if } i = j \\ \frac{1}{|u_j - u_i|^3} & \text{if } i \neq j, \end{cases} \tag{2.16}$$

and $u_i = z_i^{(0)}/l$ are the dimensionless equilibrium positions of the ions.

Diagonalizing the A and B matrices

$$A\vec{d}_p = \alpha_p \vec{d}_p \quad (p = 1, 2, \ldots, N) \tag{2.17}$$

$$B\vec{b}_p = \beta_p \vec{b}_p \tag{2.18}$$

give us the mode frequencies based on the eigenvalues α_p, β_p

$$\omega_{z,p} = \sqrt{\alpha_p}\,\omega_z \tag{2.19}$$

$$\omega_{x,p} = \sqrt{\beta_p}\,\omega_z, \tag{2.20}$$

and normal mode vectors $\vec{d}_p$, $\vec{b}_p$ (eigenvectors) for the axial and radial modes, respectively. The participation matrix $\mathbf{d}$, $\mathbf{b}$ for each direction is the matrix whose columns are the normal mode vectors. The columns and rows of these matrices are orthonormal, i.e., $\sum_{m=1}^{N} \mathbf{b}_{m,p}\mathbf{b}_{m,q} = \vec{b}_p \cdot \vec{b}_q = \delta_{pq}$ and $\sum_{p=1}^{N} \mathbf{b}_{m,p}\mathbf{b}_{n,p} = \delta_{mn}$.

The ion motion in each direction can be written in the normal mode basis $Q_{z,p}(t)$, $Q_{x,p}(t)$ as $\delta z_i(t) = \sum_{p=1}^{N} d_{i,p}Q_{z,p}(t)$, $\delta x_i(t) = \sum_{p=1}^{N} b_{i,p}Q_{x,p}(t)$. The same can be done for the Lagrangians in Eqs. (2.13) and (2.14). These oscillators can be quantized ($Q \to \hat{Q} = \xi(\hat{a} + \hat{a}^\dagger)$, $m\dot{Q} \to \hat{P} = i(\hbar/2\xi)(\hat{a} - \hat{a}^\dagger)$, $\xi = \sqrt{\hbar/2m\omega}$).

$$L_z = \frac{m}{2}\sum_{p=1}^{N}\left[\dot{Q}_{z,p}^2 - \omega_{z,p}^2 Q_{z,p}^2\right] \to \hat{H}_{0,z} = \sum_{p=1}^{N}\hbar\omega_{z,p}\hat{a}_{z,p}^\dagger\hat{a}_{z,p} \tag{2.21}$$

$$L_x = \frac{m}{2}\sum_{p=1}^{N}\left[\dot{Q}_{x,p}^2 - \omega_{x,p}^2 Q_{x,p}^2\right] \to \hat{H}_{0,x} = \sum_{p=1}^{N}\hbar\omega_{x,p}\hat{a}_{x,p}^\dagger\hat{a}_{x,p} \tag{2.22}$$

While diagonalizing these matrices are done numerically for $N > 2$, we can make a few observations from the simple cases with $N = 1, 2$ that can be solved analytically [79,80].

i) The in-phase or COM motion of the chain have the same frequency as those of one ion given the same potential. The frequencies $\omega_{x,1}$, $\omega_{y,1}$, $\omega_{z,1}$ of the COM modes depend only on the confining potential $\omega_{x,y,z}$, specifically

$$\omega_{z,1} = \omega_z \quad \text{or } \alpha_1 = 1, \tag{2.23}$$

$$\omega_{x,1} = \omega_x \quad \text{or } \beta_1 = 1, \tag{2.24}$$

$$\omega_{y,1} = \omega_y. \tag{2.25}$$

ii) For the axial direction, the COM mode has the lowest frequency. For non-COM axial modes, there are always some ions that move out-of-phase with each other and reduce their distances momentarily, thereby increasing the strength of the Coulomb interactions. The axial mode with the next lowest frequency is the breathing mode where the two halves of the chain move out-of-phase with each other. If the number of ions N is odd, the middle ion does not move or participate in the breathing mode. The frequency of the breathing mode is [79]

$$\omega_{z,2} = \sqrt{3}\,\omega_z \quad \text{or } \alpha_2 = 3. \tag{2.26}$$

iii) For each radial direction, the COM mode have the highest frequencies compared to the other normal modes. For non-COM radial modes, when the ions do not move in-phase with each other radially, their distances increase, thereby reducing the strength of the Coulomb potential. Assume that the trap is radially symmetric (which is not the case in the experiment intentionally), then the two radial directions are degenerate, i.e., x- and y- modes have the same frequencies $\omega_{x,p} = \omega_{y,p}$. The radial frequencies are related to the axial frequencies by [80]

$$2(\omega_x^2 - \omega_{x,p}^2) = \omega_{z,p}^2 - \omega_z^2. \tag{2.27}$$

In the case of the radial mode with the next highest frequency, the so-called tilt mode, using Eqs. (2.26) and (2.27), the relationship is simplified as

$$\omega_x^2 - \omega_{x,2}^2 = \omega_z^2. \tag{2.28}$$

These equations are useful in case where measurement of the axial frequencies is difficult if the laser beam has no projection on z. Eq. (2.29) means that the radial frequencies are a

lot more closely spaced than the axial frequencies for a linear chain since $\omega_z/\omega_x \sim 0.1$ (in our experiment, $\omega_z/2\pi \sim 300$ kHz while $\omega_x/2\pi \sim 3$ MHz).

$$\omega_{x,p+1} - \omega_{x,p} = \frac{1}{2}\frac{\omega_{z,p+1} + \omega_{z,p}}{\omega_{x,p+1} + \omega_{x,p}}(\omega_{z,p+1} - \omega_{z,p}). \tag{2.29}$$

2.3 Laser-Ion Interaction

In this section, we discuss briefly the laser-ion interaction, which serves as the basis for performing the native set of gates mentioned in Chapter 2 with lasers. The internal dof of the ion is limited to two levels, but this can be extended to more levels as we shall see in Section 3.5.2. Throughout this section, we shall set $\hbar = 1$.

Combining the internal and external dof of the ions (Eqs. (2.21) and (2.22)), the Hamiltonian for the ions in the lab frame is

$$\hat{H}_0 = -\frac{\omega_0}{2}\sum_{i=1}^{N}\hat{\sigma}_i^z + \sum_{p=1}^{3N}\omega_p \hat{a}_p^\dagger \hat{a}_p, \tag{2.30}$$

where $p = 1, \ldots, N$ denotes the x-radial modes, $p = N+1, \ldots, 2N$ denotes the y-radial modes, $p = 2N+1, \ldots, 3N$ denotes axial modes. Consider a laser beam addressing an ion $i = 1, \ldots, N$, whose position is described by $\vec{r}_i(t)$, through the interaction with the laser's electric field $\vec{E}_i(\vec{r}_i) = \vec{E}_{i,0}\cos(\vec{k}\cdot\vec{r}_i - \omega_{L,i}t + \phi_i)$. The interaction is described by

$$\hat{H}_i = -\hat{\vec{v}}\cdot\vec{E}_i(\vec{r}_i) = \Omega_i(\hat{\sigma}_i^+ + \hat{\sigma}_i^-)\cos(\vec{k}\cdot\vec{r}_i - \omega_{L,i}t + \phi_i), \tag{2.31}$$

where $\Omega_i = -\langle 1|\,\hat{\vec{v}}\cdot\vec{E}_{i,0}\,|0\rangle = -\langle 0|\,\hat{\vec{v}}\cdot\vec{E}_{i,0}\,|1\rangle$. The electric moment $\vec{v}$ can be of a dipole, quadrupole, etc. The transition can be mediated by one photon, two photons or more. If it is a two-photon transition (as the case of our experiment) then $\vec{k}$ is the difference between the two k-vectors and $\omega_{L,i}$ is the difference between the two frequencies. The

ion' position can be expanded around its equilibrium position as $\vec{r}_i(t) = \vec{r}_i^{(0)} + \vec{\delta r}_i(t)$. As discussed previously, the ion's displacement from its equilibrium $\vec{\delta r}_i(t)$ can be rewritten in terms of the normal modes $\vec{\delta r}_i(t) = \sum_{p=1}^{3N} \vec{e}_p b_{i,p} Q_p(t)$ and be quantized $\vec{\delta r}_i(t) \to \hat{\vec{\delta r}}_i(t) = \sum_{p=1}^{3N} \vec{e}_p b_{i,p} \xi_p (\hat{a}_p^\dagger + \hat{a}_p)$.

Let μ_i be the detuning of the laser from the qubit transition, i.e., $\mu_i = \omega_{L,i} - \omega_0$. Assuming that $\omega_{L,i} \approx \omega_0 \gg \mu_i$ In the interaction picture, the Hamiltonian after the RWA (ignoring the rapidly oscillating terms proportional to $\mathrm{e}^{\pm i(\omega_{L,i}+\omega_0)t}$) becomes

$$\hat{H'}_i = \mathrm{e}^{i\hat{H}_0 t} \hat{H}_i \mathrm{e}^{-i\hat{H}_0 t} \approx \frac{\Omega_i}{2} \left(\hat{\sigma}_i^+ \ \mathrm{e}^{-i(\vec{k}\cdot\vec{r'}_i + \mu_i t + \phi_i)} + \hat{\sigma}_i^- \ \mathrm{e}^{i(\vec{k}\cdot\vec{r'}_i + \mu_i t + \phi_i)} \right), \tag{2.32}$$

where (see Appendix A of Ref. [81])

$$\vec{r'}_i = \mathrm{e}^{i\hat{H}_0 t} \vec{r}_i \mathrm{e}^{-i\hat{H}_0 t} = \mathrm{e}^{i\hat{H}_0 t} (\vec{r}_i^{(0)} + \hat{\vec{\delta r}}_i(t)) \mathrm{e}^{-i\hat{H}_0 t} \tag{2.33}$$

$$= \vec{r}_i^{(0)} + \sum_{p=1}^{3N} \vec{e}_p b_{i,p} \xi_p \left(\hat{a}_p^\dagger \mathrm{e}^{i\omega_p t} + \hat{a}_p \mathrm{e}^{-i\omega_p t} \right). \tag{2.34}$$

Here, $b_{i,p}$ are the participation matrices and ξ_p as defined in Section 2.2.2, $\vec{e}_p = \vec{e}_x$ for $p = 1, \ldots, N$, $\vec{e}_p = \vec{e}_y$ for $p = N+1, \ldots, 2N$, $\vec{e}_p = \vec{e}_z$ for $p = 2N+1, \ldots, 3N$.

$$\hat{H'}_i \approx \frac{\Omega_i}{2} \hat{\sigma}_i^+ \mathrm{e}^{-i(\vec{k}\cdot\vec{r}_i^{(0)} + \mu_i t + \phi_i)} \prod_{p=1}^{3N} \mathrm{e}^{-i\eta_{ip}(\hat{a}_p^\dagger \mathrm{e}^{i\omega_p t} + \hat{a}_p \mathrm{e}^{-i\omega_p t})} + \mathrm{h.c.}, \tag{2.35}$$

where $\eta_{ip} = \vec{k} \cdot \vec{e}_p \ b_{i,p} \xi_p$ is the Lamb-Dicke parameter for ion i and mode p. The Lamb-Dicke parameter describes the phase modulation of the laser as a result of the ion motion. It is simply the ratio of the zero-point spread of the harmonic motion ξ_p over the laser's wavelength λ. For typical experiments with $\xi_p \sim 10$ nm and $\lambda \sim 600$ nm, $\eta \sim 0.1$.

Eq. (2.35) describes coupling between states $|0, n_p\rangle$ and $|1, n_p'\rangle$, where n_p, n_p' are the motional quantum numbers. Whether Eq. (2.35) can be simplified further depends on

the magnitude η_{ip} and the laser detuning μ_i. If the laser is aligned along one of the principal axes, say x , then we can ignore the normal modes in the other directions. So we only need to sum over $p = 1, \ldots, N$. If the laser is tuned close to one of the motional transitions $\mu_i = m_p\omega_p$ with an integer m_p, then we can ignore the coupling to all but $|0, n_p\rangle \leftrightarrow |1, n_p + m_p\rangle$ (provided that Ω_i is small enough). With $m_p \neq 0$, this transition is an m-th order sideband transition, called a blue sideband if $m_p > 0$, and a red sideband if $m_p < 0$. If $m_p = 0$, it is a carrier transition, where the qubit state changes but the motion does not. The coupling strength between the state $|0, n_p\rangle$ and $|1, n_p + m_p\rangle$ is

$$\langle 1, n_p + m_p| \hat{H'}_i |0, n_p\rangle = \frac{\Omega_i}{2} \langle n_p + m_p| \, \mathrm{e}^{-i\eta_{ip}(\hat{a}_p^\dagger \mathrm{e}^{i\omega_p t} + \hat{a}_p \mathrm{e}^{-i\omega_p t})} |n_p\rangle \equiv \frac{1}{2}\Omega_{n_p+m_p,n_p}, \tag{2.36}$$

where the matrix element [29, 82, 83] for $|0, n\rangle \to |1, n + m\rangle$

$$\mathcal{M}_{n+m,n} \equiv \langle n + m| \, \mathrm{e}^{-i\eta(\hat{a}^\dagger \mathrm{e}^{i\omega t} + \hat{a}\mathrm{e}^{-i\omega t})} |n\rangle = \mathrm{e}^{-\eta^2/2}\eta^{|m|} L_n^{|m|}(\eta^2) \left(\frac{n!}{(n+m)!}\right)^{\mathrm{sign(m)}/2} \tag{2.37}$$

with the Laguerre polynomial

$$L_n^\alpha(x) = \sum_{k=0}^{n} (-1)^k \binom{n+\alpha}{n-k} \frac{x^k}{k!}. \tag{2.38}$$

Eq. (2.36) has many important implications.

First, the strength of the carrier transition, $\mu_i = 0$, depends on the motion of the ions even though the motional state does not change. The carrier Rabi frequency is the product of the Rabi frequencies of all transitions where $m_p = 0$, i.e.,

$$\Omega_{c,i} = \Omega_i \prod_{p=1}^{N} \mathcal{M}_{n_p,n_p}^{i,p} = \Omega_i \prod_{p=1}^{N} \mathrm{e}^{-\eta_{ip}^2/2} L_{n_p}^0(\eta_{ip}^2) \equiv \Omega_i D_i^0. \tag{2.39}$$

Here $\prod_{p=1}^{N} \mathcal{M}_{n_p,n_p}^{i,p} \equiv D_i^0$ is the Debye-Waller factor indicating a reduction in the carrier coupling strength due to phase modulation of the laser by the ion motion [29]. Note that

the carrier Rabi frequency depends on the motional quantum number, since for $\eta_{ip} \ll 1$, $\mathcal{M}^{i,p}_{n_p,n_p} = \mathrm{e}^{-\eta_{ip}^2/2} L^0_{n_p}(\eta_{ip}^2) \approx 1 - \eta_{ip}^2(n_p + 1/2)$ and

$$D_i^0 \approx 1 - \sum_{p=1}^{N} \eta_{ip}^2 \left(n_p + \frac{1}{2} \right). \tag{2.40}$$

The Hamiltonian for the carrier transition is then

$$\hat{H}_i^{\mathrm{c}} = \frac{\Omega_i}{2} D_i^0 \left[\hat{\sigma}_i^+ \mathrm{e}^{-i(\vec{k}\cdot\vec{r}_i^{(0)} + \phi_i)} \right] + \mathrm{h.c.}, \tag{2.41}$$

The first-order blue sideband, $m_p = 1$, from $|0, n_p\rangle \rightarrow |1, n_p + 1\rangle$ has the same coupling strength as the reverse first-order red sideband $m_p = -1$, from $|0, n_p\rangle \leftarrow |1, n_p + 1\rangle$

$$\mathcal{M}^{i,p}_{n_p+1,n_p} = \mathrm{e}^{-\eta_{ip}^2/2} \eta_{ip} L_n^1(\eta_{ip}^2) \frac{1}{\sqrt{n_p + 1}} = \mathcal{M}^{i,p}_{n_p,n_p+1}. \tag{2.42}$$

A nice property that will come in handy for measuring the temperature $\bar{n}$ (through a method known as sideband thermometry [84]) is

$$\frac{\Omega_{n+1,n}}{\Omega_{n-1,n}} = \frac{\mathcal{M}_{n+1,n}}{\mathcal{M}_{n-1,n}} = \sqrt{\frac{n}{n+1}}. \tag{2.43}$$

The Hamiltonian for driving a blue sideband with $\mu_i = \omega_p + \delta_p$ with $\delta_p \ll \omega_p$ is

$$\hat{H}_i^{\mathrm{b}} = \frac{\Omega_i}{2} D_{ip}^{\mathrm{spec}} \mathcal{M}^{i,p}_{n_p+1,n_p} \left[\hat{\sigma}_i^+ \mathrm{e}^{-i(\omega_p+\delta_p)t} \mathrm{e}^{-i(\vec{k}\cdot\vec{r}_i^{(0)} + \phi_i^{\mathrm{B}})} \right] + \mathrm{h.c.}, \tag{2.44}$$

where $D_{ip}^{\mathrm{spec}} \equiv \prod_{k=1,k\neq p}^{N} \mathcal{M}^{i,k}_{n_k,n_k}$ is the Debye-Waller factor due to the other x modes (or modes coupled by $\vec{k}$ but is not p).

Similarly if we drive a red sideband by tuning $\mu_i = -\omega_p - \delta_p$,

$$\hat{H}_i^{\mathrm{r}} = \frac{\Omega_i}{2} D_{ip}^{\mathrm{spec}} \mathcal{M}^{i,p}_{n_p-1,n_p} \left[\hat{\sigma}_i^+ \mathrm{e}^{i(\omega_p+\delta_p)t} \mathrm{e}^{-i(\vec{k}\cdot\vec{r}_i^{(0)} + \phi_i^{\mathrm{R}})} \right] + \mathrm{h.c.}. \tag{2.45}$$

2.3.1 Lamb-Dicke limit

In the Lamb-Dicke limit, $2\eta^2(n+\frac{1}{2}) \ll 1$ [29, 83], $\mathcal{M}^{i,p}_{n_p,n_p} \approx 1$. Therefore all the Debye-Waller factors due to spectator modes become identity, i.e., $D^0_i \approx 1$, $D^{\text{spec}}_{ip} \approx 1$. This means the laser's phase modulation caused by the spatial variation of the ions due to their motion is very small. The carrier transition now no longer depends on the motional quanta, i.e.,

$$\hat{H}^{\text{c}}_i \approx \sum_{i=1}^{N} \frac{\Omega_i}{2} \left[\hat{\sigma}^+_i \text{e}^{-i(\vec{k}\cdot\vec{r}^{(0)}_i+\phi_i)}\right] + \text{h.c.}, \tag{2.46}$$

In the Lamb-Dicke limit, we can approximate

$$\text{e}^{i\eta_{ip}(\hat{a}^\dagger_p \text{e}^{i\omega_p t}+\hat{a}_p \text{e}^{-i\omega_p t})} \approx 1 - i\eta_{ip}(\hat{a}^\dagger_p \text{e}^{i\omega_p t} + \hat{a}_p \text{e}^{-i\omega_p t}). \tag{2.47}$$

Therefore the first-order sidebands are

$$\hat{H}^{\text{b}}_i = -i\eta_{ip}\frac{\Omega_i}{2}(\hat{a}^\dagger_p \text{e}^{i\omega_p t} + \hat{a}_p \text{e}^{-i\omega_p t}) \left[\hat{\sigma}^+_i \text{e}^{-i(\omega_p+\delta_p)t} \text{e}^{-i(\vec{k}\cdot\vec{r}^{(0)}_i+\phi^{\text{B}}_i)}\right] + \text{h.c.}, \tag{2.48}$$

$$\hat{H}^{\text{r}}_i = -i\eta_{ip}\frac{\Omega_i}{2}(\hat{a}^\dagger_p \text{e}^{i\omega_p t} + \hat{a}_p \text{e}^{-i\omega_p t}) \left[\hat{\sigma}^+_i \text{e}^{i(\omega_p+\delta_p)t} \text{e}^{-i(\vec{k}\cdot\vec{r}^{(0)}_i+\phi^{\text{R}}_i)}\right] + \text{h.c.}. \tag{2.49}$$

Ignoring the terms with $\text{e}^{\pm 2i\omega_p t}$ (a second RWA), we have

$$\hat{H}^{\text{b}}_i \approx -i\eta_{ip}\frac{\Omega_i}{2}(\hat{a}^\dagger_p \text{e}^{-i\delta_p t})\hat{\sigma}^+_i \text{e}^{-i(\vec{k}\cdot\vec{r}^{(0)}_i+\phi^{\text{B}}_i)} + \text{h.c.}, \tag{2.50}$$

$$\hat{H}^{\text{r}}_i \approx -i\eta_{ip}\frac{\Omega_i}{2}(\hat{a}_p \text{e}^{i\delta_p t})\hat{\sigma}^+_i \text{e}^{-i(\vec{k}\cdot\vec{r}^{(0)}_i+\phi^{\text{R}}_i)} + \text{h.c.}. \tag{2.51}$$

Chapter 3: Experimental Hardware

In this chapter, I will briefly discuss the level structure of $^{171}Yb^{+}$ ions, how we trap them, cool them and manipulate their internal and motional states to do interesting science. Many of the details about our experiment can also be found in previous graduate students' theses [1, 4, 85]. I will refer to these theses where relevant and highlight the modifications that we made.

An overview of our experimental hardware is shown in Fig. 3.1. At the heart of the experiment are the $^{171}Yb^{+}$ ions confined a linear chain in vacuum. Lasers are used to cool, initialize, detect and change the states of the ions. However, only the laser beams for coherent operations are shown this figure. The beams for cooling, initialization and detection are not shown. The coherent operation is realized by a two-photon process, called a Raman transition, performed by two counter-propagating beams, one of which is split into ten beams by a diffractive optic element. Each of the ten beams addresses one ion, and through the use of a multi-channel AOM, providing a complete and individual control of the ions. The fluorescence from the ions are imaged on the a multi-channel PMT by a specially designed objective to ensure high-fidelity state detection. The direction of the ion chain is z, the direction of the Raman beams is x, y is perpendicular to the optical table.

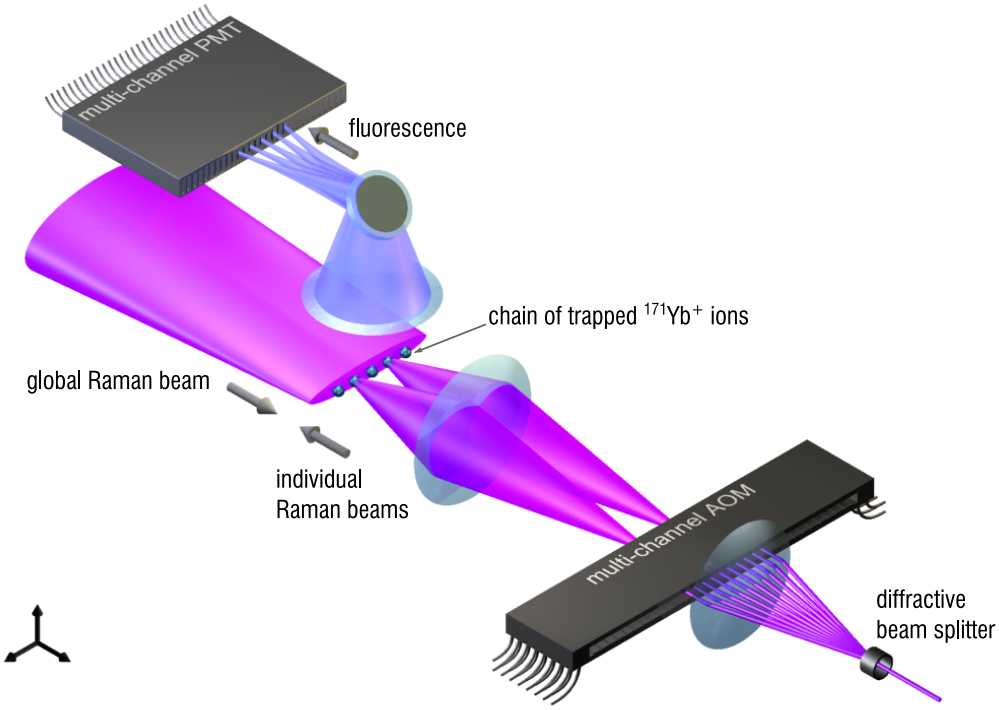

Figure 3.1: Schematic of the setup showing the counter-propagating Raman beams, the 32-channel AOM and 32-channel PMT. Image adapted from Ref. [1].

3.1 $^{171}Yb^{+}$ Electronic Structure

$^{171}Yb^{+}$ is the ion of choice in our experiment for the following reasons. First, it is a stable and relatively abundant isotope of Ytterbium (Yb) that has many "clock" transitions. These transitions have long coherence time and insensitive to external fields, perfect for storing quantum information. Since $^{171}Yb^{+}$ is also used for optical clocks, these transitions are well understood and measured to a very high accuracy. Second, many of these transitions are accessible by commercially available laser diodes, hence these ions can easily be laser-cooled to their motional ground states, initialized with high fidelity via optical pumping, straight-forwardly detected via state-dependent fluorescence and individually addressed for computation. Third, it has nuclear spin 1/2 so there are fewer hyperfine states

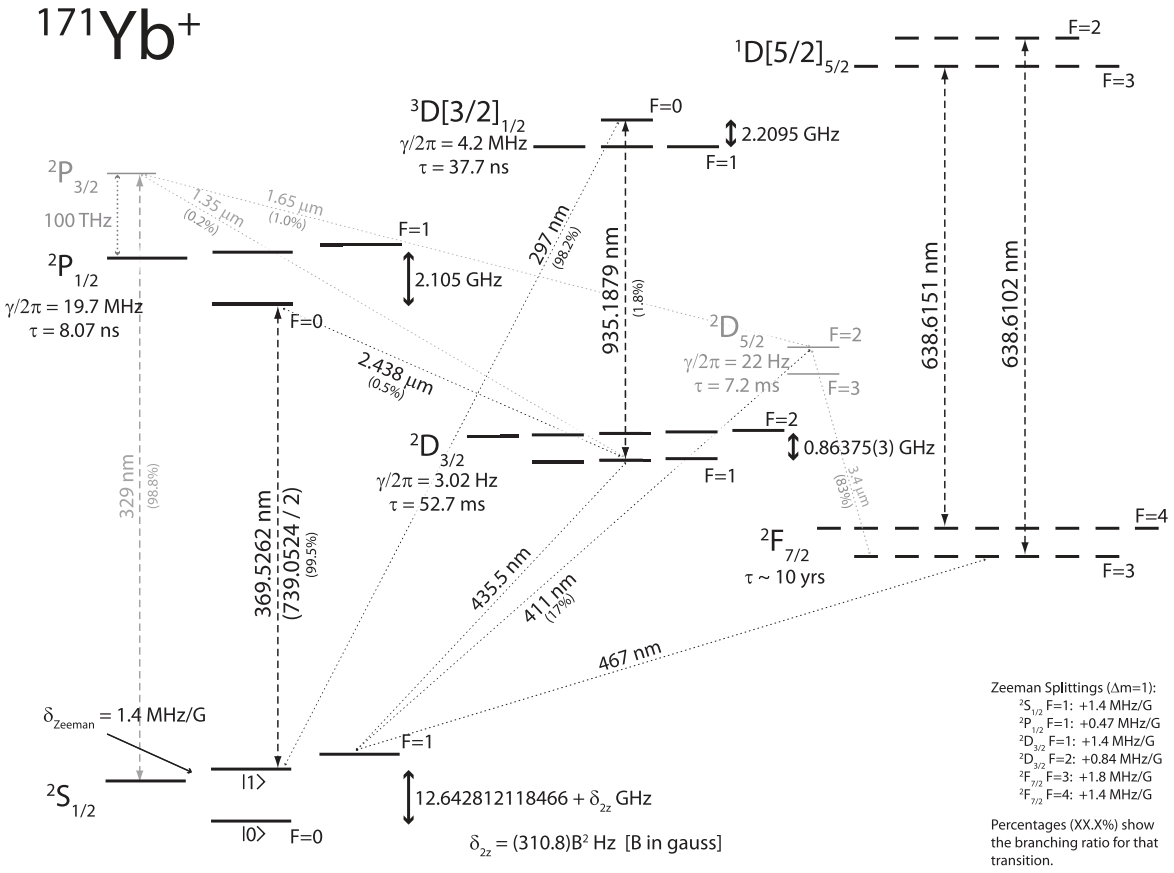

Figure 3.2: The internal levels of $^{171}Yb^{+}$ (images adapted from Ref. [2])

than that of an isotope with a higher nuclear spin, which simplifies state initialization and detection. Fourth, it has many excited states (Fig. 3.2), which can be used for shelving to increase detection fidelity, reduce cross-talk during the mid-circuit measurements or sympathetic cooling during long circuits.

However, there are also disadvantages when using $^{171}Yb^{+}$. One of them is the near UV frequency of the Raman transition used for coherent operations. To reduce spontaneous scattering, the Raman laser is chosen to be far detuned from the P excited states, which requires high laser power to drive the transition sufficiently fast. A high-power laser at near UV can damage the optics a lot faster than a laser with the same power at a lower frequency,

which can be an obstacle to scaling up the system. Also $^{171}Yb^+$ is heavier compared to other ions, which means more laser power is required to drive sideband transitions necessary for sufficiently fast entangling gates. For this reason, many groups are exploring Ba^+ as an alternative to Yb^+ as the relevant transitions in Ba^+ are in the visible range.

The relevant energy levels of $^{171}Yb^+$ for our experiment are shown in Fig. 3.2. Although Yb (Xe $4f^{14}6s^2$) is an element in the lanthanide series, it shares a feature with the alkaline earth elements: a closed outer s shell ($L = 0$). Therefore, an Yb^+ ion has a hydrogen-like structure with one outer electron and a closed shell, i.e., a Yb^+ ion has the ground state $^2S_{1/2}$ and frequently accessed low-lying excited states $^2P_{1/2}$, $^2P_{3/2}$, $^2D_{3/2}$, $^2D_{5/2}$. However, since it has the accessible f shell as the next outermost, it has the excited state $^2F_{7/2}$ and several "bracket" states, where L and S are no longer good quantum numbers.

We choose a well-established qubit, which is encoded in the hyperfine ground states $|^2S_{1/2}, F = 0, m_F = 0\rangle$ and $|^2S_{1/2}, F = 1, m_F = 0\rangle$ of $^{171}Yb^+$ [86–88] (see Fig. 3.2). The qubit splitting ω_{HF} is about 12.6428 GHz. These states are magnetic-field insensitive to first order. The second order dependence is weak

$$\omega_{\mathrm{HF}}/2\pi = (12642812118.4 + 310.8B^2)\ \mathrm{Hz}, \tag{3.1}$$

where B is the magnetic field in Gauss. In our experiment we apply a 5 Gauss magnetic field to separate the Zeeman states of $|^2S_{1/2}, F = 1\rangle$ to avoid coherent population trapping. Thus the Zeeman splitting at this field is about 7 MHz. The magnetic field is applied in the x direction, which is perpendicular to the chain axis and parallel to the optical table (see Fig. 3.1 and Fig. 3.3).

3.2 Blade Trap - Single Ion Dynamics

In general, a confining potential in all three dimensions cannot be created with just a static electric field. To trap charged particles, it is common to use either an oscillating electric field (Paul trap) or a static magnetic field (Penning trap) . In our experiment, we use a blade trap, a type of linear Paul trap. It is similar to the quadrupole Paul trap [76] with two differences. First, the axial confining potential is a lot weaker than the radial pseudo-potential, hence the ions form a linear chain instead of a 3D cloud. Second, the electrodes are not hyperbolically shaped but are sharp blades. In this section we briefly review the theory of ion trapping and how it applies to our experiment.

3.2.1 Ion Trapping In Theory

For the trap to have a perfect quadrupole potential, the electrodes must be hyperbolically shaped. However these electrodes provide limited optical access. Since the ions are cooled to very low temperature, they are confined to a very small region in the center of trap ($\sim$ 10 nm compared to the electrode distance of $\sim 100\mu$m). Therefore other electrode geometries which can approximate a quadrupole potential in the center region of the trap suffice.

We trap a linear chain of ions by applying the RF potential in the radial plane (x-y) and applying a much weaker DC potential in the axial direction (z). If the confining DC potential is also quadrupole in nature then the potential becomes [1]

$$\phi(r_i,t) = V\cos(\Omega_{RF}t)\sum_{i=x,y,z}\alpha_i\Big(\frac{r_i}{\tilde{R}}\Big)^2 + U\sum_{i=x,y,z}\alpha_i'\Big(\frac{r_i}{\tilde{R}'}\Big)^2 + V_0\cos(\Omega_{RF}t) + U_0, \qquad (3.2)$$

where $i = x, y, z$ (not the ion index), $\vec{r} = \sum_i r_i\hat{e}_i$ is the distance from the center of the

trap, $\tilde{R}$, $\tilde{R}'$ depend on the distance from the electrodes to the center of the trap, α_i and α_i' are the strength of the RF and DC potential respectively. $\sum_i \alpha_i = 0 = \sum_i \alpha_i'$ so that $\Delta\phi = 0$. If the RF electrodes are perfectly parallel to the trap axis (ideal blade trap), there is negligible RF potential in the axial direction hence $\alpha_z \approx 0$ and $\alpha_x = -\alpha_y$ [77]. The confining DC axial potential $\alpha_z' > 0$ creates a small deconfining potential in radial directions $\alpha_x' + \alpha_y' < 0$.

The equation of motion for a single ion with charge Q and mass m has the form of the Matthieu equation

$$\frac{d^2u_i}{d\xi^2} + (a_i - 2q_i\cos(2\xi))u_i = 0, \tag{3.3}$$

where $u_i = \frac{4}{\Omega_{RF}^2} r_i$, $\xi = \frac{\Omega_{RF}}{2} t$ and

$$a_i = -\frac{8\alpha_i' QU}{m\tilde{R}'^2\Omega_{RF}^2}, \tag{3.4}$$

$$q_i = \frac{4\alpha_i QV}{m\tilde{R}^2\Omega_{RF}^2}. \tag{3.5}$$

The general solutions for each direction are of the form [89]

$$u_i(\xi) = A\sum_{n\in\mathbb{Z}} C_{2n}\cos((2n+\beta_i)\xi) + B\sum_{n\in\mathbb{Z}} C_{2n}\sin((2n+\beta_i)\xi) \tag{3.6}$$

where

$$\beta_i = \sqrt{a_i + \frac{q_i^2}{2}}. \tag{3.7}$$

Whether the ion is confined within the trap is determined by the a_i and q_i. If a_i and q_i are such that β_i is imaginary then there is no stable trajectory for that dimension.

In the limit of $a_i \ll q_i \ll 1$ (meaning the DC offset is much smaller than the RF amplitude and the RF frequency is high enough) the solution can be approximated by a

slow motion periodic with frequency ω_i known as secular motion and a fast periodic motion at the same driving frequency Ω_{RF} known as micromotion [83]

$$r_i(t) \approx r_i^0 \cos(\omega_i t + \phi_i)(1 + \frac{q_i}{2}\cos(\Omega_{RF} t)) \tag{3.8}$$

$$\omega_i \approx \beta_i \frac{\Omega_{RF}}{2} \tag{3.9}$$

Therefore, the ponderomotive potential given in Eq. (3.2) can be approximated by the pseudo-potential

$$\phi = \frac{m}{2} \sum_{i=x,y,z} \omega_i^2 r_i^2 = \frac{1}{2} m \Big(\omega_x^2 \; x^2 + \omega_y^2 \; y^2 + \omega_z^2 \; z^2 \Big) \tag{3.10}$$

In our experiment, the electrodes are on four sharp blades with RF electrodes on the blades at two diagonally opposite corners and DC electrodes on other two (Fig. 3.3b). The tip-to-tip electrode distances are $R_x = 325$ μm and $R_y = 450$ μm, making the trap slightly rectangular. The distance from the blades to the trap axis is $R \sim 250\mu$m. The blades are segmented. The segments on the RF blades are electrically connected and have the same voltage. The segments on the DC blades are designed to have higher voltages for the end-cap segments (DC10, DC5, DC1, DC6) than for the mid-cap segments (DC3, DC8) to create a confining potential along the trap axis. However, due to the rough edges of segments DC1, DC2, DC6 of the blades leading to axial micromotion, we are only using six out of ten segments. The DC blades are RF grounded by a large capacitance ($\sim$ 1nF) so there is no oscillating voltages at RF on the DC blades. We apply an RF voltage at $\Omega_{RF} = 2\pi \times 23.8167$ MHz with an amplitude of ≈ 444 V, which is calculated from Eq. (3.9) and the measured secular frequency ω_x from $2\pi \times 3.045$ MHz to $2\pi \times 3.065$ MHz, assuming $\alpha_x = 1/2$. More details on the blade trap assembly can be found in Section 2.5.3 of Ref. [1].

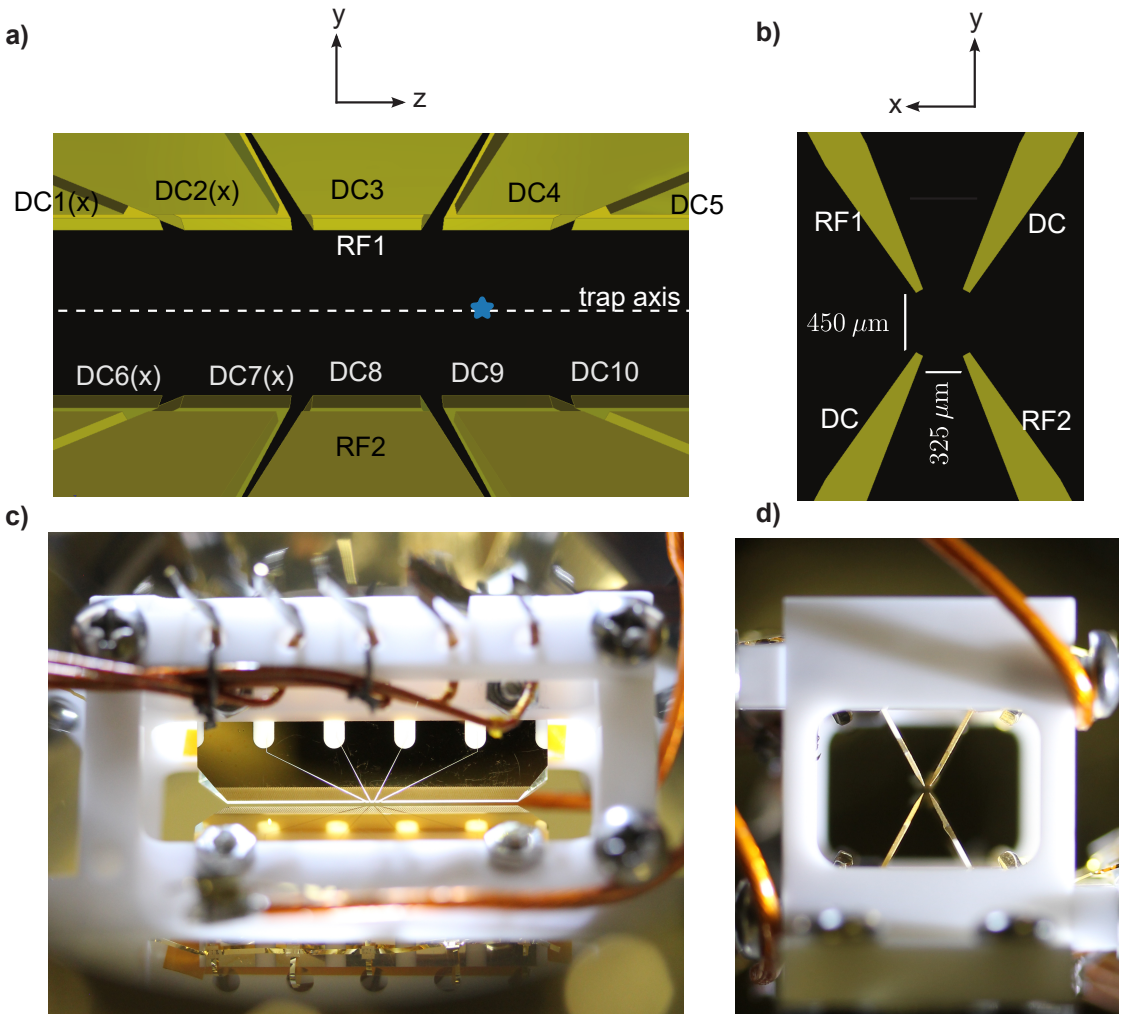

Figure 3.3: The blade trap. Drawings of the segmented blades a) looking from x with the front blades denoted in black and the back blades in white, b) looking along z (along the ion chain). The segments marked with (x) are grounded and not used. The star marks the axial micromotion null position, where the ions are during experiment. Photographs of the trap currently in the vacuum chamber c) looking from x, d) looking along z. Images adapted from Ref. [1]. Photo credit: Shantanu Debnath.

The depth of the trapping potential is given by the geometry of the electrodes R_i, the secular frequency and the mass of the ion [83]

$$D_i = \frac{m}{2}\omega_i^2 R_i^2. \tag{3.11}$$

For our experiment, $D \approx 10^5$ K or $D \approx 10^{30}$ GHz, which is much higher than room temperature or the oven temperature. The depth of the Paul trap is many orders of magnitude higher than that of an optical dipole trap.

3.2.2 Ion Trapping In Practice

Imperfections such as static stray fields can make the real trap deviate from Eq. (3.2). The stray fields can come from the uneven surface finish of the gold coating on the blades, the protruded sharp features along the edges of the blades and built-up charges on the insulating or poorly conducting surfaces near the trap such as the Macor trap holder, the kapton coated cables and the stainless steel screws used to secure the blades to the holder. This adds a dipole term $\phi_b(r_i, t) = \sum_i E_i r_i$ to $\phi(r_i, t)$, which shifts the quadrupole null from the center of the trap to a different position r_i^e, which can be corrected by adding compensating DC voltages. The trajectory of a single ion under the stray field is approximated by [90]

$$r_i(t) \approx (r_i^e + r_i^0 \cos(\omega_i t + \phi_i))(1 + \frac{q_i}{2}\cos(\Omega_{RF} t)), \tag{3.12}$$

where $r_i^e = \frac{eE_i}{m\omega_i^2}$.

Another imperfection is the phase difference φ_{ac} between the two RF blades adding

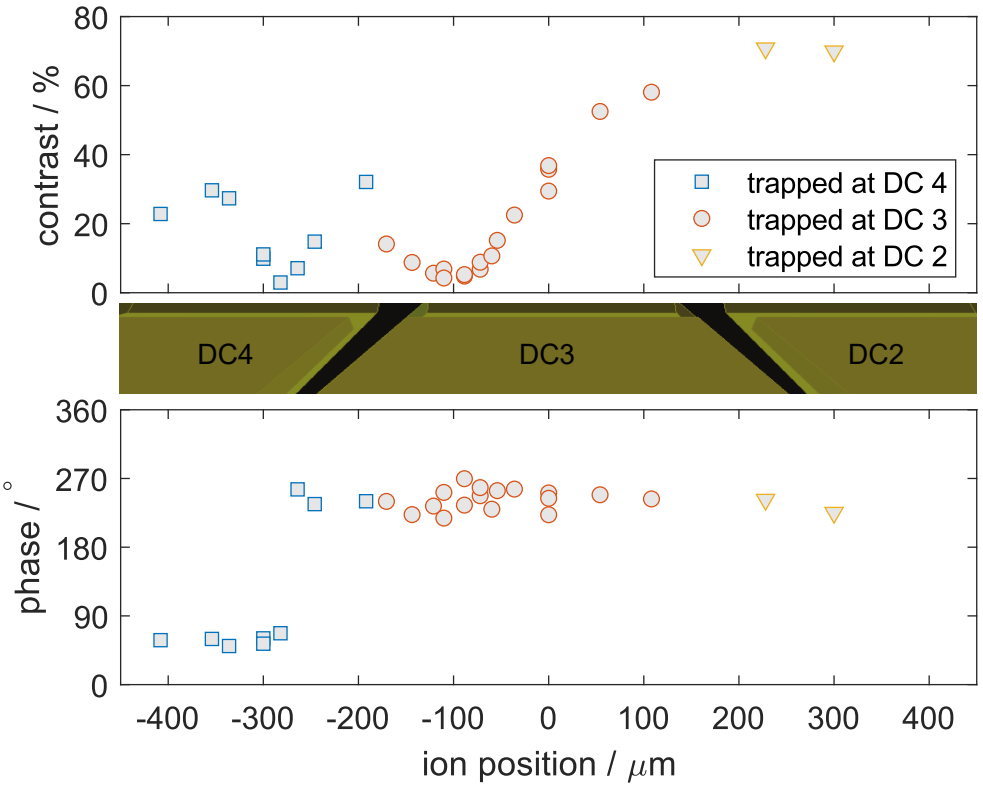

Figure 3.4: Axial micromotion at different DC segments. Image credit: Norbert Linke.

an additional oscillating term to Eq. (3.12) [90]

$$r_i(t) \approx (r_i^e + r_i^0 \cos(\omega_i t + \phi_i))(1 + \frac{q_i}{2}\cos(\Omega_{RF} t)) - \frac{1}{2} q_i R \kappa \varphi_{ac} \sin(\Omega_{RF} t). \tag{3.13}$$

In our set up, this is minimized by RF shorting (via a large capacitor) the two RF electrodes [91].

The imperfections that cause the most problems for us are the defects on the trap blades, which cause significant axial micromotion. The axial micromotion null is also shifted off to one end of the trap (see Fig. 3.4). To minimize the effect of the uneven electric field caused by the defects, we only use six electrodes near one end of the trap (DC3, DC4, DC5 and DC8, DC9, DC10) and ground the others (DC1, DC2, DC6, DC7).

The blades are also not perfectly parallel even though best efforts were spent to align

them under the microscope [1]. This causes the position dependent confinement along the axial direction, i.e., $\alpha_{x,y}(z)$.

3.3 Blade Trap - Linear Chain of Ions

In the previous section we talk about the dynamics of a single ion in the trap in order to understand how the pseudo-potential is physically created. Using the pseudo-potential approximation, the dynamics of a linear chain of ions follows as described in Section 2.2. In this section, we will discuss the regimes where ions form a linear chain.

3.3.1 Coulomb Crystal

When the ions are trapped by the potential in Eq. (3.2) they form a cloud of ions, not an ionic crystal unless sufficiently cooled down. The phase transition from the gaseous or disordered phase to the crystal or ordered phase of the ions of charges Q is characterized by the coupling parameter g, which is approximately the ratio of Coulomb energy E_C to kinetic energy E_K [92]

$$g \equiv \frac{Q^2}{4\pi\epsilon_0 a k_B T} \sim \frac{E_C}{E_K}, \tag{3.14}$$

where $a = (3/4\pi n)^{1/3}$ is the Wigner-Seitz radius corresponding to the ion number density n. For Coulomb crystallization to happen,

$$g \geq 175. \tag{3.15}$$

The highest reachable ion number density in a Paul or Penning trap is $n \sim 10^{15}$ m^{-3} or $a \sim 10$ μm, which leads to the temperature limit for the Coulomb crystallization to be

$$T \leq T_{CC} \sim 10\text{mK} \tag{3.16}$$

This temperature can be easily reached with Doppler cooling with most cooling transition. For $^{171}\text{Yb}^{+}$, the $^2S_{1/2}$ to $^2P_{1/2}$ transition has the Doppler temperature of ~ 1 mK.

3.3.2 Equilibrium Configuration

The Coulomb crystal is a linear chain if the radial confinement is very strong compared to the axial confinement, specifically the radial COM frequencies have to be larger than the highest axial mode $\omega_{x,y} > \omega_{z,N}/\sqrt{2}$ [78, 93]. This condition is satisfied in the voltage configurations we used for experiments (except when loading ions). Otherwise, the ions will form a 2D crystal or a zig-zag configuration.

As seen in Section 2.2.1, if the axial confinement is purely quadratic like in Eq. (3.2), then the ions are not equally spaced. The spacing is smallest at the center of the chain. Since the individual addressing beams for coherent operations are equally spaced, this significantly impacts beam alignment and the fidelity of the coherent operations. To make a linear chain of ions with equal spacing, we need a quartic term r_i^4 in the potential (Figure 2.2 in Ref. [2]). This requires at least five segments on each DC blades (ten in total), which we no longer have due to defects as discussed in Section 3.2.2. We use extra ions at the ends of the chain (which are not used as qubits) to partly reduce the spacing's difference between the ions in the middle. Thus we trap 3 ions for 3 qubits, 7 ions for 5 qubits, 9 ions for 7 qubits, and 13 ions for 9 qubits.

3.3.3 Principal Axes for Radial Motion

Applying the RF voltages on the RF blades only generates a radial symmetric pseudo-potential [77]. Therefore with RF voltages alone, there is no distinction between x and y, the two principal axes of radial motion, i.e., $\omega_x = \omega_y$. This configuration is not good for Doppler cooling with one near-detuned beam since the principal axis perpendicular to the beam will not be cooled. For efficient Doppler cooling, we either need two near-detuned beams or the ability to rotate the principal axes to lift the degeneracy between ω_x and ω_y. The ability to rotate the principle axes also allows a "twisted" ion chain (where the principle axes vary along the chain due to axial inhomogeneity of the RF potential) to be "untwisted". In our experiment, all segments of the same RF blades are electrically connected to each other so the RF field is homogeneous along the chain, hence the ion chain is not twisted.

To be able to rotate the principle axes, the trap must be rectangular $R_x \neq R_y$, meaning the tip-to-tip electrode distances are different in x and y. Then applying DC voltages on the RF blades or different DC voltages on the end-cap DC segments will generates different DC confinements for x and y, as shown in Eq. (3.7), and rotate the radial principal axes [77]. The rotation angle is given by the DC voltages applied and also the geometry of the blades.

3.4 Ion Loading, Doppler Cooling, State Initialization, Detection

3.4.1 Ion Loading and Doppler Cooling

We load Yb ions from an oven enriched with ^{171}Yb (see Section 2.5.2 of Ref. [1] for details on the oven). The hot atoms are ionized by the 399 nm laser from $^1S_0$ to $^1P_1$ then by the 369 nm laser or 355 pulsed laser (any photons with wavelength shorter than 394 nm will be sufficient) from $^1P_1$ to the continuum.

After the two step ionization, the cloud of ions is trapped by the RF field and is relatively hot ($\sim$ 200 m/s). To cool them down to the temperature where they can form the Coulomb crystal, we use Doppler cooling [94] on the $S_{1/2}$ to $P_{1/2}$ transition (369.5 nm) together with the so-called "Recrystalization" procedure, where the RF amplitude is lowered momentarily for faster cooling and raised again to form a 1D chain. "Recrystalization" takes about 1 to 3 seconds, depending on how well the Doppler cooling and trapping parameters are optimized.

For cooling during ion loading, we use mainly two beams: one high power 300 MHz red-detuned ("protection") and one weaker 10 MHz red-detuned ("main cooling") beam. The saturated "protection" beam slows down the hot ions (whose transitions are Doppler shifted by $\vec{k}\cdot\vec{v} \approx 500$ MHz or less), then the unsaturated "main cooling" further cools them down close to the Doppler limit.

The idea of Doppler cooling is that when an atom absorbs a photon coming from the opposite direction its momentum is reduced by the amount equivalent to the photon's momentum $\hbar k$. Vice versa, when the atom spontaneously emits a photon, its momentum

increases (recoil). Since the absorption is directional while the emission's direction is random, on average the atom cools down. Therefore, if the atom is free, we will need three pairs of counter-propagating beam to cool it down. However, for a harmonically trapped atom (ion) with an oscillation period much longer than the decay time (hence more than 1 photon is scattered every period), we only need one beam that has projection on all 3 axes [94] (the ion does not fly away, it keeps coming back against the cooling beam). The more photons scattered, the more the atom cools down. So to achieve fast cooling, a transition with a short lifetime τ, i.e., large natural linewidth ($\gamma \sim 1/\tau$) is desirable. The cooling stops when the momentum gain from recoil is the same as the momentum loss from absorption. The lowest temperature reachable by this method for a harmonically bound ion is

$$T_D = f\frac{\hbar\gamma}{k_B}, \tag{3.17}$$

where $\hbar$ is the Planck constant divided by 2π, k_B is the Boltzmann constant, $f < 1$ depends on the number of cooling beams and the beams' orientation with respect to each principal axis [94]. In our experiment, we never get very close to this limit.

The laser frequency and polarization are shown in Fig. 3.5a. The cooling beams are red-detuned from the transition from $^2S_{1/2}$ $F = 1$ to $^2P_{1/2}$ $F = 0$ with a weaker sideband of $12.643 + 2.105 = 14.748$ GHz (generated by the second-order sideband of a 7.374 GHz modulation from an EOM[1]) added to address the transition from $^2S_{1/2}$ $F = 1$ to $^2P_{1/2}$ $F = 0$. The ions can get out of these cooling transitions via a decay from $^2P_{1/2}$ to $^2D_{3/2}$. Therefore, the 935 nm ("repump") is added to excite the ions to the bracket state

[1] New Focus, model 4851

$^3D[3/2]_{1/2}$. From there they decay back to the $^2S_{1/2}$ manifolds and continue the cooling cycle. The 935 repump beam also needs a $2.2095 + 0.8638 = 3.0733$ GHz sideband[2] to address all the hyperfine states of $^2D_{3/2}$.

All 369 beams, for cooling, initialization and detection, are derived from the second harmonics of a 740 nm doubled laser system[3]. Their frequencies are 300 MHz red-detuned to $^2S_{1/2}$ $F = 1$ to $^2P_{1/2}$ $F = 0$ transition. The light is split up after the laser and the beam on the cooling path goes through the 7.374 GH EOM then an AOM[4] ("cool" AOM) before going through various mirrors and/or fibers to the vacuum chamber. The protection beam is the zeroth order of the cool AOM, while the main cooling beam is the first order, with the input RF at 290 MHz. More details on the setup for the cooling beam can be found in Section 2.4 of Ref. [1].

3.4.2 State Initialization and Detection

The two qubit states are realized in the hyperfine-split ground level of $^{171}\mathrm{Yb}^+$, $|0\rangle = |^2S_{1/2}\ F = 0, m_F = 0\rangle$ and $|1\rangle = |^2S_{1/2}\ F = 1, m_F = 0\rangle$.

We used optical pumping to initialize the ions to $|0\rangle$ as shown in Fig. 3.5b. Optical pumping is done using the 2.105 GHz first-order sideband on the $^2S_{1/2}$ $F = 1$ to $^2P_{1/2}$ $F = 0$ transition. The beam has high enough power so that after 5 μs of pumping, at least 99.7% of the time, the ions end up in state $|0\rangle$. The pump beam, after split up from detect beam, goes through the 2.105 GHz EOM then an AOM[5] ("pump" AOM). The input RF for the

[2]EOSpace PM-0S5-12-PFU-PFU-935-UL

[3]TOPTICA DLC TA-SHG pro

[4]IntraAction ASM-3002B8-13

[5]IntraAction ASM-3002B8-13

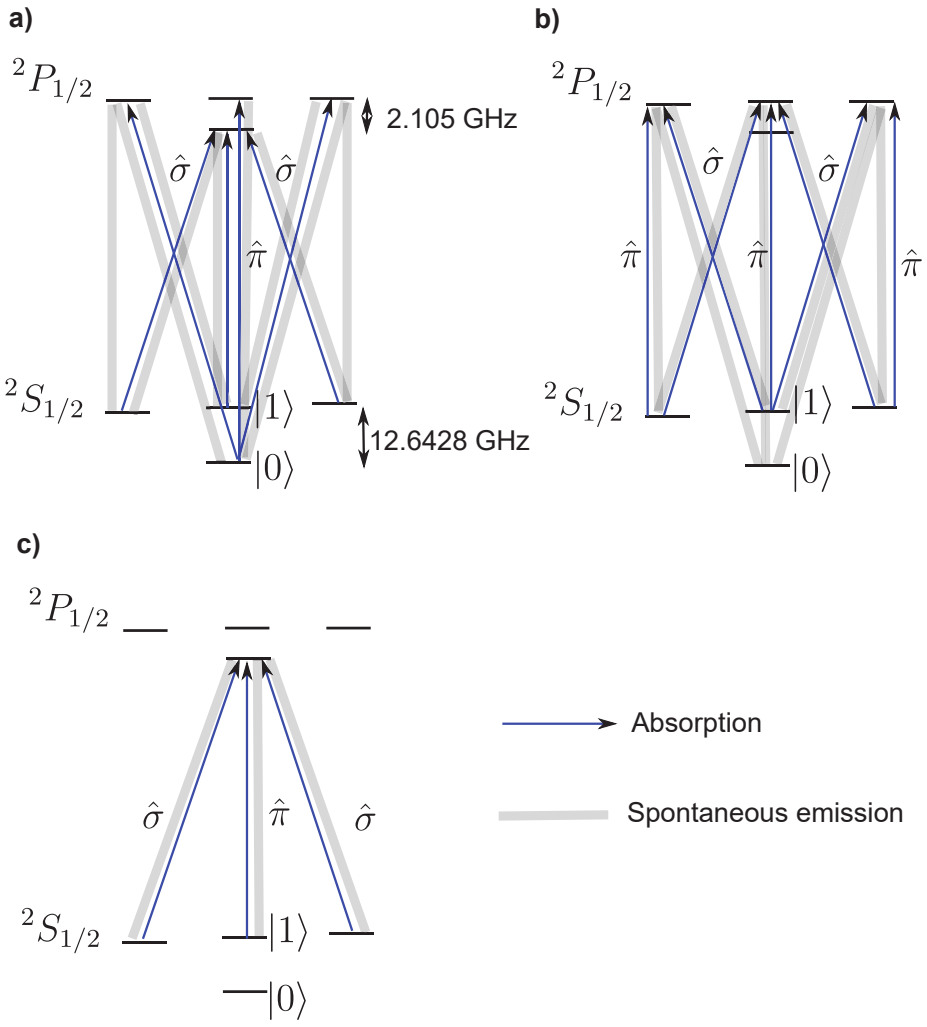

Figure 3.5: Cooling (a), optical pumping (b) and detection (c) via $S_{1/2}$ to $P_{1/2}$ transition in $^{171}Yb^{+}$. Image adapted from Ref. [1]

pump AOM is at 295 MHz, which is 5 MHz red-detuned from resonant (so as not to heat the ions).

Detection is done based on the fact that $^2S_{1/2}$ $F = 0$ to $^2P_{1/2}$ $F = 0$ is a forbidden transition. Therefore only when the ion is in $|1\rangle$ it continuously scatters 369 photons. The detect beam has no sideband and is on resonant with $^2S_{1/2}$ $F = 1$ to $^2P_{1/2}$ $F = 0$ transition (Fig. 3.5c). Therefore we only need an AOM ("detect") on the detect beam path. The input RF is set to be 300 MHz so that the first order is on resonant. The first order beams of the pump AOM and detect AOM are combined before coupled to the "pump/detect" fiber.

The photons emitted from the ions are collected by an custom designed objective (NA = 0.38) and imaged onto a 32-channel PMT[6] and a CCD camera[7] by a series of off-the-shelf lenses. The objective corrects for aberrations caused by the vacuum window and forms a collimated beam (infinity-corrected) so that adding more lenses after the objective only changes the magnification of the system, not the aberration. The collimating beam after the objective is focused by a tube lens (singlet best form lens[8]) to form an intermediate image at the aperture. A focusing cylindrical lens (L1[9]) is added to compensate for astigmatism from the tilt of the vacuum window [1]. Details on the design of the objective and the lenses are in Section 4.1 of Ref. [1].

Photons collected by the 32-channel PMT are amplified by a factor of 100 by a two-stage amplifier and then discriminated against a $\sim$ 1 V reference by a digitizing FPGA

[6]Hamamatsu H7260-200

[7]PCO Sensicam dicam pro

[8]Thorlabs LBF254-200-A

[9]Thorlabs LJ4530RM-A

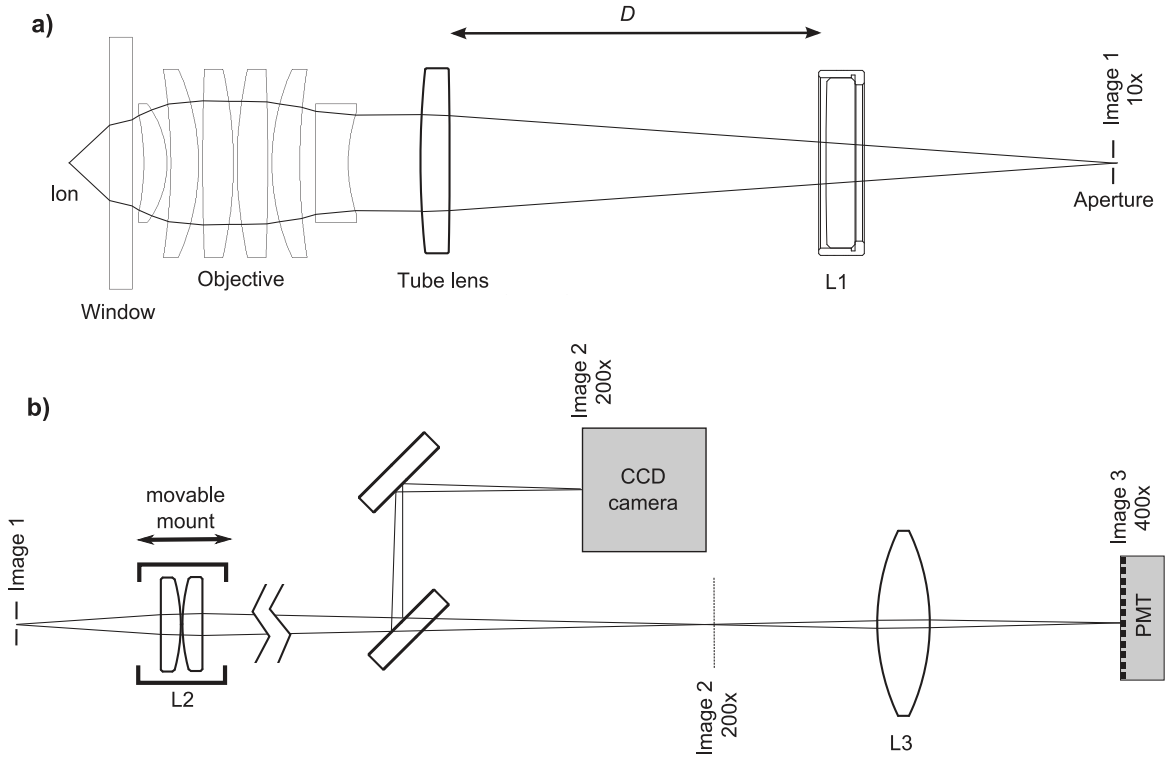

Figure 3.6: Optics for individual detection, $D = 167$ mm to compensate for astigmatism. Image adapted from Ref. [1]

to become a TTL signal. The digitizing FPGA also stretches the TTL pulse to 40 ns to avoid double counting. The stretched TTL pulses are then sent to the PMT FPGA to be counted. More details can be found in Section 4.1 of Ref. [1] and Section 2.5.4 of Ref. [85]. During the 150 μs window for detection, the ion scatters on average 9 photons if it is in $|1\rangle$ and 0 photons if it is in $|0\rangle$.

3.5 Sideband Cooling and Coherent Operations

In this section, we discuss the ideas behind resolved sideband cooling and Raman transitions with continuous wave (CW) laser beams. Then we briefly describes how the Raman transitions are implemented in our setup using pulsed laser beams and how to to extend to an 8-level system of $^{171}Yb^{+}$. Here I will mainly summarize the results. More rigorous derivations can be found in Chapter 3 of Ref. [1] and Ref. [2].

3.5.1 Resolved Sideband Cooling

The Doppler cooling limit for our experiment is $T_D \approx 1$ mK, which is about 0.3 mK for each direction (assuming isotropic cooling). This temperature corresponds to about $n_{x,y} \sim 3$ quanta for the two radial motion and about $n_z \sim 30$ quanta for the axial motion. High-fidelity gates require that $n \ll 1$ for all directions. In our experiment, we use sideband cooling to further cool the ions down to the motional ground state $\bar{n} = 0$ for the radial directions while the axial directions are only Doppler cooled.

In sideband cooling, we drive a red-sideband transition between $|g, n+1\rangle$, the electronic ground state in the motional state $n+1$, and $|e, n\rangle$, the electronic excited state in the

motional state n. Spontaneous emission afterwards returns the ion to its electronic ground state $|g, n\rangle$ with one fewer motional quantum than its initial state $|g, n+1\rangle$. Repeating this process brings the ion to its electronic and motional ground state $|g, 0\rangle$.

However, this technique only works if we drive $|g, n+1\rangle$ to $|e, n\rangle$ without driving to $|e, n+1\rangle$ (carrier transition) or $|e, n+2\rangle$ (blue-sideband transition) and the recoil energy from spontaneous emission is smaller than the motional energy [95, 96]

$$E_r = \frac{\hbar^2 k^2}{2m} \ll \hbar\omega_m, \tag{3.18}$$

where $k = 2\pi/\lambda$ with λ is the wavelength of the transition from $|e\rangle$ to $|g\rangle$. To fulfill the first condition, a) the natural linewidth γ of the transition from $|g\rangle$ to $|e\rangle$ needs to be smaller than the motional energy, b) the laser needs to be able to resolve the different levels of harmonic motion n (and the natural linewidth γ for effective driving)

$$\Delta\omega_L \lesssim \gamma \ll \omega_m, \tag{3.19}$$

c) the ion needs to be cold enough so that linewidth broadening due to Doppler effect is smaller than the motional frequency ω

$$\vec{k} \cdot \vec{v} \ll \omega_m. \tag{3.20}$$

To fulfill 1a) and 1b), we just need to choose a narrow-linewidth transition. These transitions are abundant in $^{171}\mathrm{Yb}^+$ ($^2S_{1/2}$ to $^2D_{3/2}$ or $^2D_{5/2}$ or $^2F_{7/2}$), but driving them is not necessarily easy because (ironically) they are narrow. 2c) can be fulfilled with Doppler cooling since in the limit where $v \sim \omega_m/k$ the ion's temperature in one direction is about 12 mK, which is an order of magnitude higher than the Doppler limit. The recoil energy condition is also easily fulfilled for our experiment where $\omega_m/2\pi \approx 3$ MHz and $E_r/(2\pi\hbar) \sim 10$

kHz.

In our experiment, we choose to do sideband cooling on the qubit transition, so $|g\rangle = |0\rangle$ and $|e\rangle = |1\rangle$, since we will also need to setup a coherent drive for the qubit. Since the qubit transition is electric dipole forbidden, there is no spontaneous decay between $|1\rangle$ and $|0\rangle$, i.e., $\gamma = 0$. Therefore we need to use optical pumping to get the qubit from $|1\rangle$ to $|0\rangle$. We drive the red sideband transition using a Raman process, which will be discussed in details in the next section. We alternate between the Raman drive of the red sideband and optical pumping until the ions reach their motional ground state. As discussed in Chapter 2, the Rabi frequency of the sidebands depend on n, $\Omega_{n,n+1} = \Omega_{n,n}\sqrt{n+1}$. Therefore the duration of the red sideband transitions need to be varied accordingly for optimal cooling.

3.5.2 Coherent Driving of Qubits Using a Raman Transition

We can drive the qubits with microwave or a two-photon transition through the excited states, also known as Raman transition. We choose the later for driving gates because we can individually address the qubits straight-forwardly by focusing the lasers. Also, to excite the motion, the driving field must change significantly compared to the size of the ion wave package. It is characterized by the Lamb-Dicke parameter $\eta = \Delta k x_0$. The microwave has $\eta \sim 10^{-6}$ while the Raman counter-propagating beams have $\eta \sim 0.01$.

A Raman transition coherently transfers the population between two electric-dipole forbidden levels $|g_1\rangle$, $|g_2\rangle$ with two laser beams by weakly exciting dipole allowed transitions between the two states and an excited state $|e\rangle$ (see Fig. 3.7a). One laser drives the transition between $|g_1\rangle$ and $|e\rangle$ with frequency ω_{L1} and Rabi frequency Ω_1 while the other

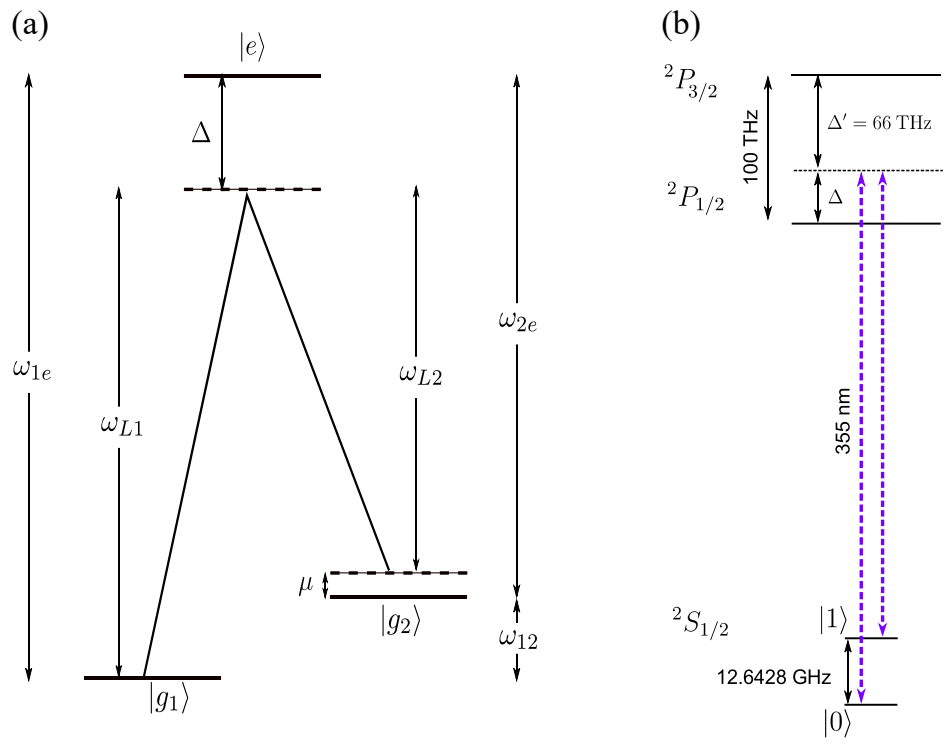

Figure 3.7: (a) A 3-level Raman transition with a Λ system. (b) A Raman transition between the qubit states through the $^2P_{1/2}$ and $^2P_{3/2}$ levels in $^{171}\mathrm{Yb}^+$.

drives the transition between $|g_2\rangle$ and $|e\rangle$ with frequency ω_{L2} and Rabi frequency Ω_2. The frequency difference between the lasers is tuned close to the frequency difference ω_{12} between $|g_1\rangle$ and $|g_2\rangle$, $\omega_{L1} - \omega_{L2} = \omega_{12} + \mu \approx \omega 12$, and both need to be far detuned from the excited state so that this state is never significantly occupied, $\Delta \gg \Gamma$, where Γ is the lifetime of $|e\rangle$. The effective two-photon Rabi frequency is given by [97]

$$\Omega_{2\mathrm{ph}} = \frac{\Omega_1 \Omega_2^*}{2\Delta}. \tag{3.21}$$

A standard Raman transition involves only 3 levels but it can be extended to 4 levels (driving through 2 excited states) or more (if considering all the hyperfine and Zeeman splittings). In our experiment, we detune the lasers to between the $^2P_{1/2}$ and $^2P_{3/2}$ levels so that the two-photon (or differential AC) Stark shifts caused by off-resonantly driving

these transitions are cancelled out [98]. The lasers are 33 THz blue detuned from $^2P_{1/2}$ and 66 THz red detuned from $^2P_{3/2}$ to be exact (about 355 nm, as shown in Fig. 3.7b. The two laser beams must have frequency difference equal to the qubit splitting of 12.6 GHz. Since the transition is very far detuned from both excited state levels, we need a high power laser to achieve the desired two-photon Rabi frequency.

To fulfill these requirements, we need a high power 355 nm laser that is tunable in the GHz range. It is hard to find a CW laser that satisfies all these requirements. So we use a 4 W pulsed (Vanadate mode-locked) laser[10] that emits 355 nm pulses. Since a single pulse is too weak to drive the above Raman transition, many pulses are required [98, 99]. In this regime, it is easier to understand the effect of the pulsed laser on the qubit if we go to the frequency domain. We can think of a pulsed laser as a frequency comb with a finite envelope. The width of the envelope is given by the pulse duration and the spacing between the comb teeth is given by the repetition (rep) rate of the laser, which is inversely proportional to the time between two consecutive pulses (see Fig. 3.8b). Our pulsed laser has a bandwidth of 125 GHz (8 ps pulse width) and a rep rate of $\omega_r/2\pi = 118.314$ MHz. Since the bandwidth is larger than the qubit splitting, we can drive the qubit using any two comb teeth as long as the frequency difference between them is equal to the qubit splitting. We can drive a Raman transition with just one beam (pairs of comb teeth from the same beam) or with two beams (pairs of comb teeth from two different beams) [98]. In the case of one beam, the qubit splitting must be an integer multiples of the rep rate. For the case of two beams, their frequencies can be shifted by an AOM so that the difference between certain two comb teeth is the qubit splitting. The beams can be aligned so that the net

[10] Coherent Paladin Compact 355-4000

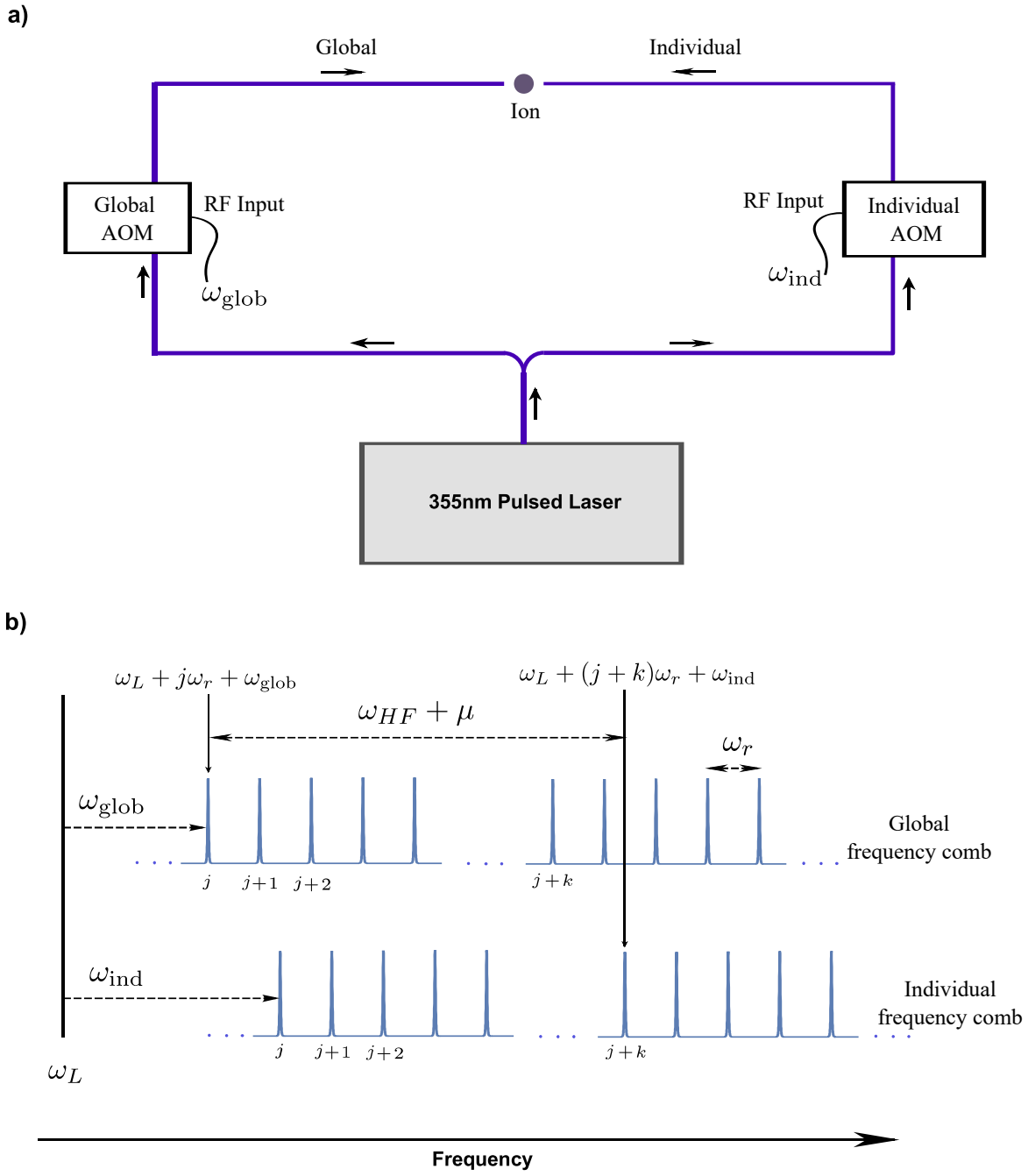

Figure 3.8: Driving Raman transitions with a pulsed laser. (a) The pulsed laser is split into 2 beams, called global and individual. Each beam is modulated by their respective AOMs. The optical path length difference is minimized so that the pulses from both beams arrived at the same time at the ions. (b) The frequency combs of global and individual beams. Image adapted from Ref. [1].

momentum kick Δk from two beams is zero or non-zero.

In order to drive the sidebands for the entangling gates, we need a non-zero Δk. So we need two non co-propagating Raman beams. However, it is challenging to keep a stable phase difference between two different beam paths (air current, temperature fluctuation, vibration, optical delay, etc.) so for application that do not require sideband transitions it is best to use co-propagating beams or just one beam.

In our experiment, we use two counter-propagating beams for Raman transition to maximize Δk. This allows us to use less power when driving sideband transitions. However, this increases the laser dephasing for single-qubit gates. In a future upgrade, we can implement a fast switch to drive single-qubit gates with co-propagating beams.

As shown in Fig. 3.1, Fig. 3.8a and Fig. 3.9, the pulsed laser, after going through a half waveplate and PBSs for polarization and power control, is split into two paths, one that addresses all the ions (global) and one that is further split into ten beams to individually address the ions (individual). The two beams have linear polarization that are oriented perpendicular to each other (so-called the lin-perp-lin configuration). This is to create the varying circular polarization that drives the Raman transitions. The global beam goes through an AOM[11] before being shaped and focused into an elliptical beam with 75 μm waist in the Y direction and 10 μm waist in the Z direction.

The individual beams are split into ten beams by a diffractive optic element[12], each of the beam is then focused onto a channel of a 32-channel AOM[13] (Fig. 3.1). The zeroth-ordered beams are dumped while the first orders are expanded by a factor of $m \approx 39$ before

[11] IntraAction ASM-802B8

[12] Holo-Or MS-244-U-Y-A

[13] Harris H-601 Series 32-Channel UV Acousto-Optic Modulator

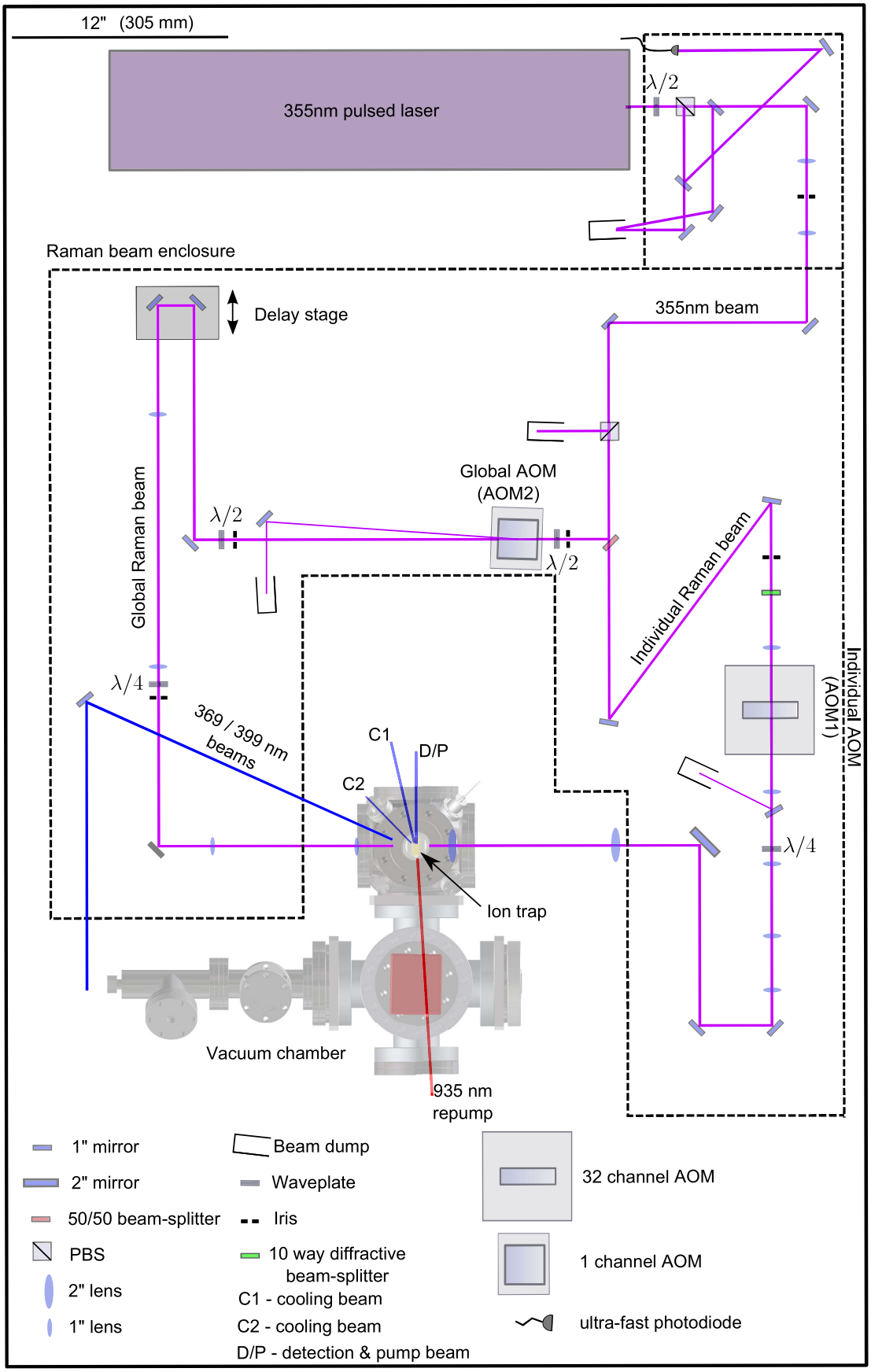

Figure 3.9: Schematic for Raman beam paths. Image adapted from Ref. [1].

being focused by a triplet lens[14] to a 1.5 μm beam waist (in diameter) at the ions. The beams are slightly defocused to be more robust to beam pointing error. The spacing of the focused spots are determined by the focal length $f = 47$ mm of the triple lens, the initial angle of separation $\theta = 4.3$ mrad at the DOE and the magnification factor $m \approx 39$ of the expanding telescopes

$$\Delta z = \frac{f\theta}{m} \approx 5\mu\text{m}. \tag{3.22}$$

More details on the design of the optics for the individual beam path can be found in Section 4.2 of Ref. [1] and the physical lab notebooks.

The global AOM is controlled by an amplified RF signal from an analog generator[15], while each channel of the individual AOM is controlled by a single channel of a multi-channel AWG[16] during gates or a DDS during sideband cooling. The individual RF signals from AWGs or the DDS pass through an RF switchbox before going to the individual AOM. The switchbox functions both as a fast switch and a low-noise amplifier for the control RF signals of the multi-channel AOM. Since each switchbox has five channels, we need two of them to control 9 qubits. For each channel inside the switchbox, the RF signal from an individual AWG channel is combined with the 5-way split DDS signal before going to a fast TTL switch that can be controlled either remotely or manually. Then the signal is attenuated and amplified so that the individual output of the switchbox is at most 27 dBm to avoid damaging the multi-channel AOM.

To drive the transition (on resonant) between $|0\rangle$ and $|1\rangle$ (carrier transition), the RF

[14] Ronar-Smith objective 355nm, FL=47mm, WD=32.7mm

[15] HP8640B

[16] Keysight M3202A

inputs for the two global and individual AOMs must satisfy

$$\omega_{\text{glob}}(t) + k\omega_r(t) - \omega_{\text{ind}} = \omega_{\text{HF}}, \tag{3.23}$$

where k is the number of comb teeth that drive the transition. In our experiment, we choose $k = 108$, $\omega_{\text{glob}}(t)/2\pi \sim 75$ MHz, and $\omega_{\text{ind}}/2\pi = f_c \approx 210$ MHz when driving the carrier, to get the qubit splitting $\omega_{HF}/2\pi \approx 12642.8$ MHz.

Since we do not have control over the rep rate of the pulsed laser, we need to adjust the global beam frequency to account for the fluctuation of the rep rate. This is done by phase locking [100] the frequency of the global AOM's signal generator to a reference signal generated by mixing the 108th beat note $k\omega_r$ with another stable signal generator[17] at 12852.8 MHz ($= \omega_{\text{HF}} + f_c$). The 108th beat note signal is measured (before being split into global and individual paths) by an ultra-fast photo-diode[18] (Fig. 3.9). While the principal of the beat note stabilization is described in [100], more details on an older version of our beat note lock setup, where we feedback on the individual AOM instead of the global AOM, can be found in Section 3.4 of Ref. [1].

By changing the frequency of the input RF signal to the individual AOM, we can also drive sideband transitions

$$\omega_{\text{glob}}(t) + k\omega_r(t) - \omega_{\text{ind}} = \omega_{\text{HF}} + \mu, \tag{3.24}$$

where $\mu = -\omega_m$ for red sidebands and $\mu = \omega_m$ for blue sidebands. For the typical motional mode frequencies of $\omega_m/2\pi \sim 2.92 - 3.06$ MHz, the input RF for the individual channels are $\omega_{\text{ind}}/2\pi = f_r \sim 212.92 - 213.06$ MHz for the red sidebands and $\omega_{\text{ind}}/2\pi = f_b \sim$

[17] Valon 5015 or HP8672 before it broke down

[18] UPD-30-VSG-P

206.94 − 207.08 MHz for the blue sidebands.

Since our qubit has effectively an infinite T_1 time, the coherence time of the gates are determined by the coherence time of the Raman laser, which are determined by the intensity and phase stability of the beams and Stark shifts. Since we are using separate beam paths for the global and individual, the optical paths are subjected to disturbance like air current and vibration of the optical table so they have fluctuations in phase. We minimize these effect of the disturbance by fully enclosing the Raman beam paths, floating the table and turning off the HEPA filter during experiment. The alignment of the beams onto the ions, especially the individual beams, is also important. In our experiment, the ions are not equally spaced (due to not having a quartic potential) while the individual beams are. We mitigate the effect of it by adding extra ions at the ends. However, the best way is still to have functioning DC electrodes to form a equally spaced chain. The final factor is the uncorrected Stark shifts. Although we have the 2-photon Stark shifts from the excited states mostly cancelled out, we still have the 4-photon Stark shifts from the adjacent comb teeth of the same beam (single-beam Stark shift) or from both beams (cross-beam Stark shift). The single-beam Stark shift can be minimized by adjusting the polarization of each beam to be perfectly linear (see Section 3.3 of Ref. [1]). The cross-beam Stark shift can only be minimized by choosing an appropriate rep rate, which requires extensive modification of the pulsed laser [2, 26].

To implement the single-qubit gate $R_i(\theta, \phi)$ described in Chapter 2, we drive the ion i on resonance, with the phase of the individual beam set to ϕ and the duration proportional to θ. The Z rotation is a classical phase advance on the individual beam, and therefore is practically noise free. The two-qubit gate $X_i X_j(\chi)$ is implemented by

applying a two-tone symmetrically detuned red and blue sidebands on both ions i, j with an amplitude/frequency/phase modulation or a combination of them at a pre-determined duration (see Chapter 5). During the gate, the qubits are entangled with the motion (through sideband transitions). Since the motion are shared, any ions addressed by the laser beams can be entangled, no matter the distance. At the end of the gate, the qubits are disentangled from the motion, thereby protecting the information encoded in the qubits. Since the intensity, frequency and phase of the individual beams can be controlled precisely, we can perform any gates on any subset of ions. This capability makes our system a fully-connected programmable quantum computer.

Chapter 4: Experimental Control

Fig. 4.1 describes the software stack that forms the basis of our programmable quantum computer. The software stack offers a user-friendly interface (Fig. 4.4) that allows users to input experiments or quantum circuits into the compiler. This compiler then converts these inputs into a series of RF pulses, which are used to control the laser beams for manipulating the states of ions.

The main user interface together with its back-end modules, such as the compiler, pulse control, etc., are written with WaveMetrics Igor Pro. Only the interface for other minor controls, such as displaying photon counts from the PMT, controlling flags and flip mirrors, are written with Labview. While the software architecture and the Igor program are described in details in Chapter 4 of Ref. [4], we have since upgraded the software and added more capabilities. In this chapter, I will give an overview of the most updated control setup at the time of writing this thesis and discuss in depth the upgrades I am most involved with. These upgrades are extending from 7 qubits to 9 qubits, replacing the Tabor and Chase AWGs with the Keysight AWGs and updating from Igor Pro 6 to Igor Pro 8 together with a control computer upgrade to Windows 10.

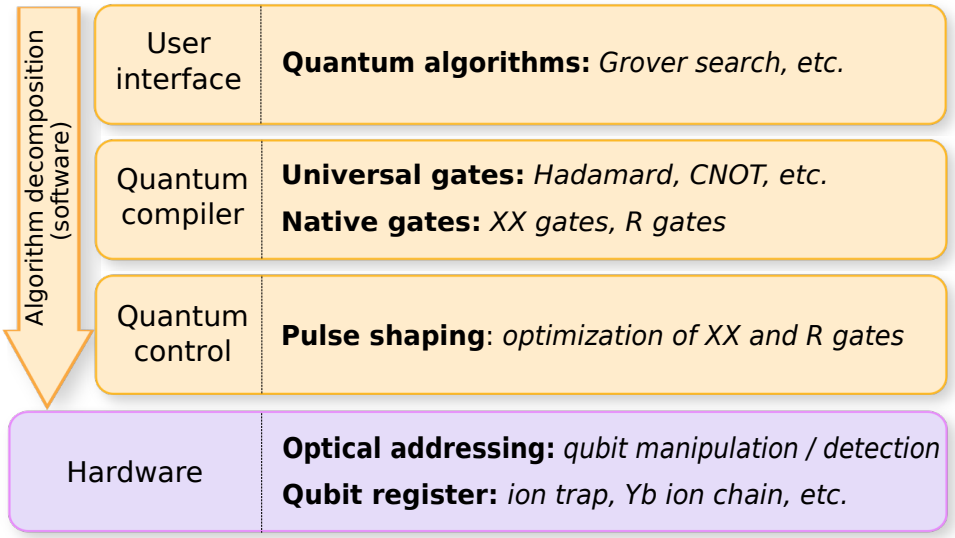

Figure 4.1: The computational architecture of our programmable quantum computer. Image modified from Ref. [3]

.

4.1 Experimental Control Structure

Fig. 4.2 gives an overview of the control setup. The Igor program provides user interfaces for changing the DC voltages of the trap's DC and RF electrodes, setting the amplitude and frequency of the trapping RF field through a DDS FPGA, setting the amplitudes, frequencies and phases of the signal generators (DDS, AWGs, PTSs, etc.) for various AOMs, EOMs and clocks in the experiment, selecting which experiments (Ramsey, Rabi flopping with Microwave or Raman, Algorithms, etc.) to run, the number of repetitions, which PMT channels to collect data from. From the user's inputs about which experiment to perform, Igor creates the instructions for the timings of relevant devices to the specified experiment and for data collection, then sends them to the Sequencer FPGA. If the operation involves AWGs or Raman DDS, Igor also generates the AWG waveforms and DDS commands,

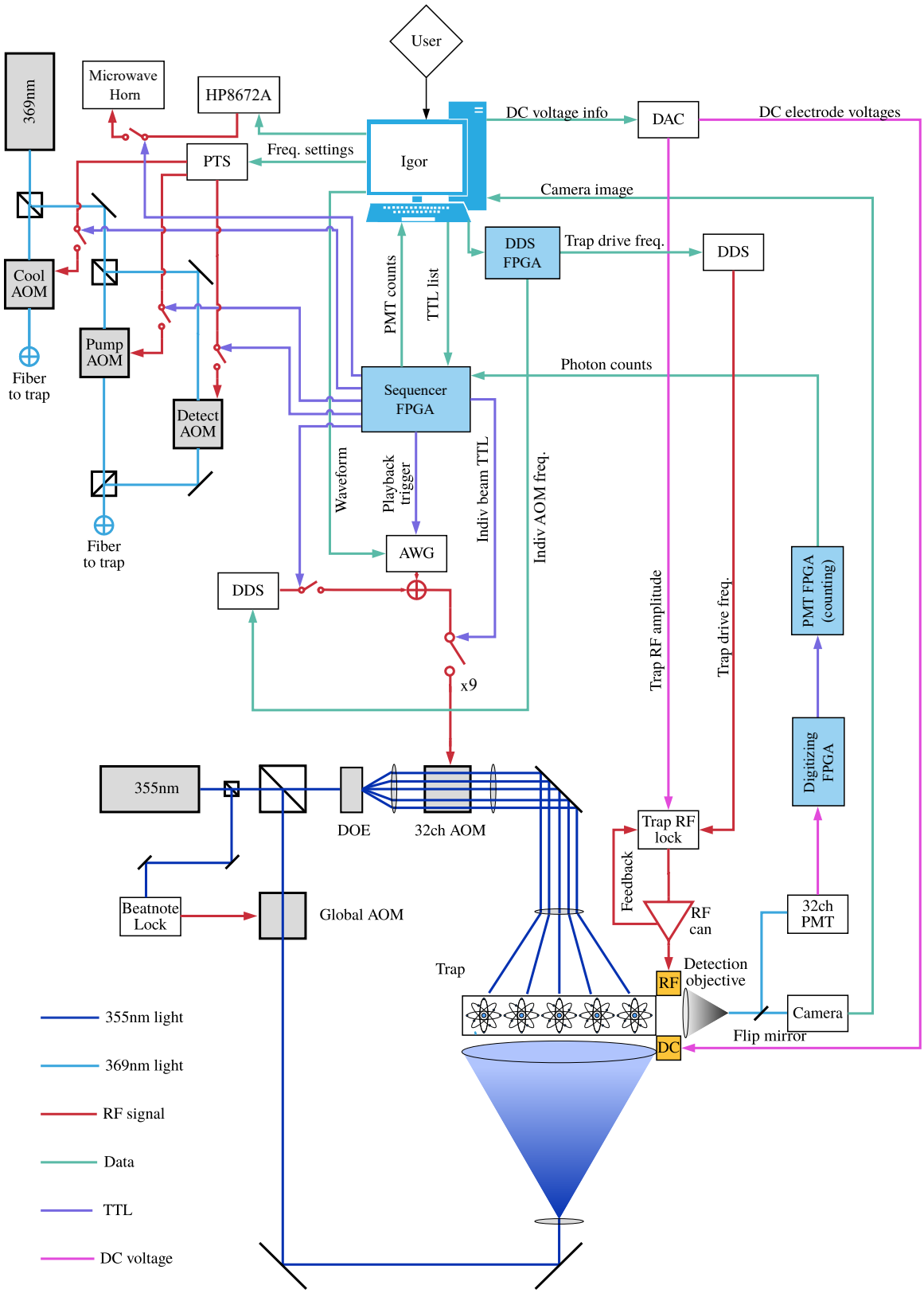

Figure 4.2: A system-level view of the experimental control. Here 5 ions and 5 addressing beams configuration are shown for demonstrative purpose. The experiment can be reconfigured to address up to 9 ions. Image modified from Ref. [4]

sending them to the respective devices. Upon receiving Igor's commands, the Sequencer constructs a sequence of TTL pulses, activating the required devices precisely when needed. It gathers photon counts from the designated qubit data lines, stores them, and repeats the process for the predetermined number of shots. Once all shots are completed, the Sequencer transmits the aggregated photon counts back to Igor. Igor then processes this data, generating and saving plots according to the user's specifications. The timing for the Sequencer FPGA is provided by a 50-MHz clock signal generated by a function generator[1], which in turn is referenced to the Rb atomic clock.

As discussed in Section 3.4.2, during an experiment, photons collected by the PMT are amplified, digitized and stretched. A Labview program receives and displays the counts from the digitizing FPGA, which shows all 32 channels. The Labview program allows the user to select which channels to be sent back to the Sequencer and how to combine them by specifying a mapping between the 32 PMT channels and the 9 qubit data lines. The PMT FPGA combines the photon counts according to this mapping and sent these data to the Sequencer. The Sequencer is currently programmed to work with 9 qubits. The maximum number of qubit is limited by the number of available outputs on the Sequencer FPGA board that can be used as individual qubit addressing TTLs. The current FPGA board only has 24 outputs, 9 of which are currently used for controlling essential devices such as cool, pump, detect and global AOMs, microwave, AWG trigger, DDS trigger, etc. This leaves a maximum of 15 outputs for the qubit addressing TTLs.

Besides the Sequencer and PMT FPGAs, there are also an FPGA to remote control the DDS board (DDS FPGA) and an FPGA (not shown in Fig. 4.2) to control the frequency

[1]Rigor DG4162 2-channel Function/AWG, 160 MHz, 500 MSa/s

of the microwave synthesizer (PTS) with higher precision. Our FPGA boards use the Intel Cyclone II FPGA chip (EP2C5T144C8) that can be programmed with the Quartus software. There are various Verilog programs written by previous graduate students and postdocs (such as Sequencer, DDScontrol, Photon counter, Multitool, Noise-eater, etc) that can be loaded to the FPGA chip via a JTAG cable. The FPGA chip communicates with the computer via a USB port through a USB-to-serial UART interface (FTDI FT232RL chip). For the Igor program to recognize an FPGA board, its USB port must be configured properly, such as the port number must be correct and the baud rate must be the same one as in the loaded Verilog program. For the FPGA board to be recognized by the Labview drivers, the Product Description of the FTDI chip must be the same as the Device Name in the Labview program. Timing for the FPGA chip must be provided by a 50 MHz oscillator (Abracon ACHL-50.000MHZ-EK) or a 50 MHz external clock through an SMA connector for applications that require more stable and precise timing (such as the DDScontrol or the Sequencer). The board is designed to have 24 outputs and 32 inputs. Note that all the inputs and outputs must be 50 Ω terminated to avoid reflections. The board has 5 V and 3.3 V power lines but we mostly use the 5 V power line.

We use a 2-channel DDS board (DDS-AD9912 Rev.4) designed in-house to generate the 23.8167 MHz for the trap RF and the $\sim$ 210 MHZ for individual channels of the 32-channel AOM. The board needs a 1 GHz external clock generated by a PTS (also referenced to the Rb clock) and is controlled using Igor through the DDS FPGA. The RF signal for the 32-channel AOM can be from the DDS or from the AWG. The advantage of the DDS is that it only needs a frequency, amplitude and phase input to generate the signal so even a few-second RF pulse is generated quickly. The AWG requires compilation a time array

of the voltage of the RF signal, which takes a long time for long RF pulses. However, our DDS board cannot switch amplitude very fast ($\sim$ 100 μs) so for doing gates it is simpler to use the AWG. The DDS is mainly used for sideband cooling, sideband spectroscopy and coherence time measurement (the frequency switching and phase switching is $\sim$ 100 ns). The AWGs will be discussed in Section 4.4.

4.2 Igor 6.2 Program

As discussed in the last section, the Igor control program serves as a user interface to control all aspects of the experiment. The code for Igor 6.2 version can be found on gitlab [101]. The code is run with a 32-bit version of Igor since at the time of developing the program, Igor 64-bit version was unstable. An overview of the program backend is given in Section 4.2 of Ref. [4]. Since then we have added the automated algorithm running, gate calibration, motional spectrum fitting and parallel gates on two orthogonal motional modes. In this section, I will explain the organization of the program code and briefly talk about the automation. The parallel gates [44] will be the subject of Yingyue Zhu's thesis.

Our experiment control program is saved as an unpacked experiment file, which has the extension of ".uxp", since it has very large number of internal data (called "waves"). When the ".uxp" file is opened, the experiment control program is loaded. How exactly it is loaded is described in page II-39 of the Igor Pro 6.2 Manual. The important thing to know is that the program is organized into procedure files ending with ".ipf" and the procedure files are only loaded if they are included in the main Procedure Window (accessible with "Ctrl+M") using the "#include" statement (Fig. 4.3) or opened while the ".uxp" file is

opened.

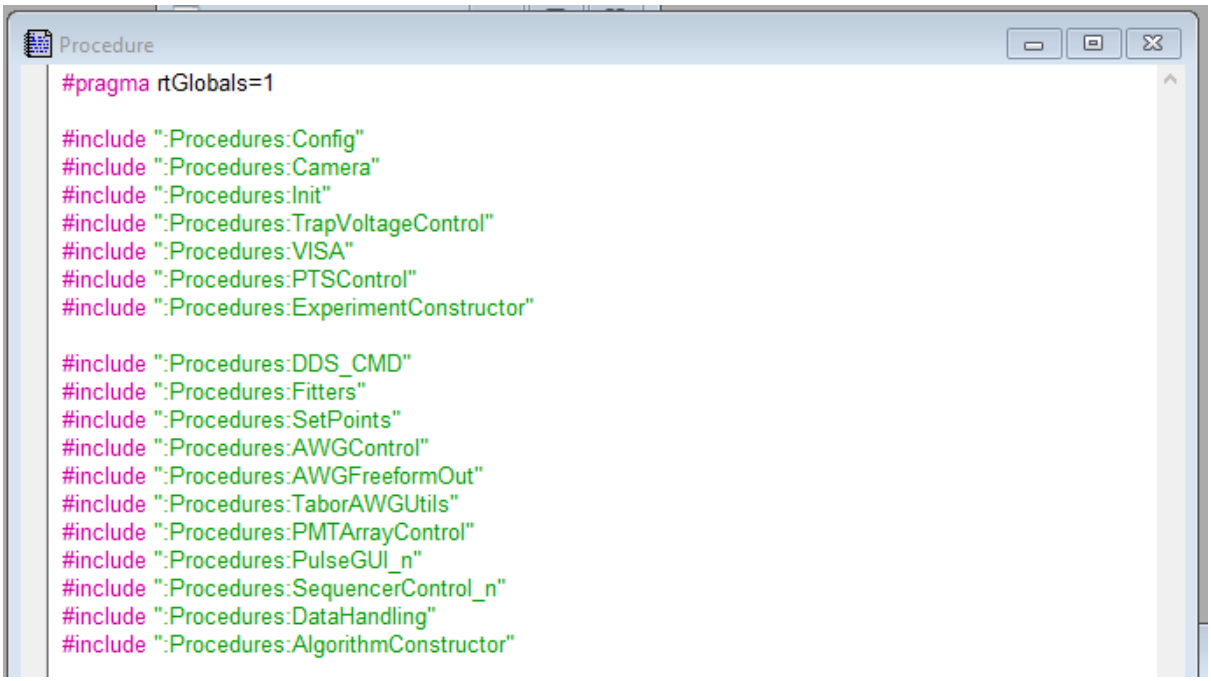

Figure 4.3: Main procedure window of the Igor experimental control program.

TTL hex bits and data line hex bits for communication with the FPGAs are defined in "Config.ipf". Important global parameters, data folders, functions and macros to recreate different GUIs are defined in "Init.ipf". The "ExperimentConstructor.ipf" contains definitions of experiment objects for different experimental operations such cooling, optical pumping, detection or gates. It also contains the "BuildExperiment" function that constructs the experiment sequence based on the user's input and stored it in a structure called "Experiment".

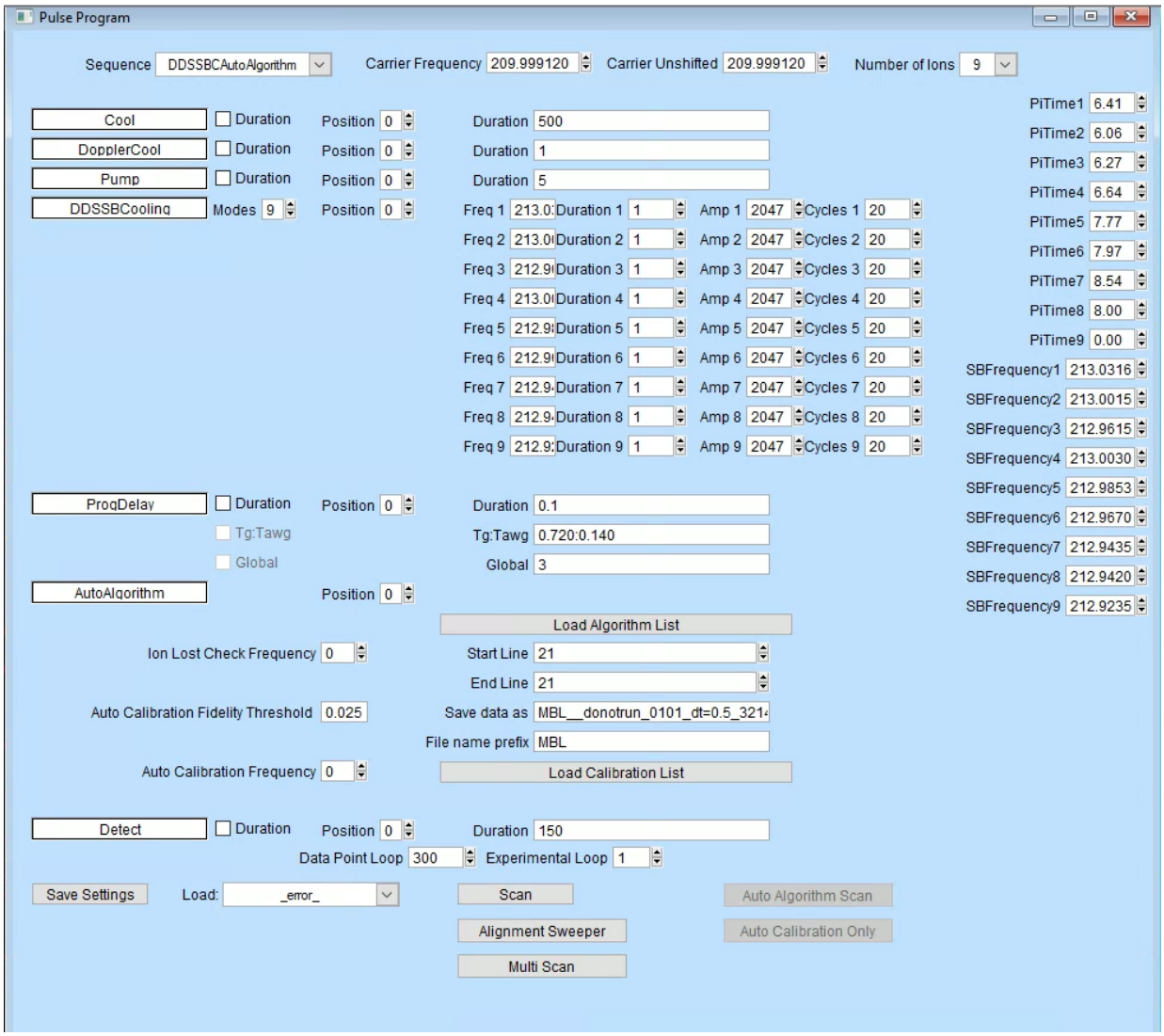

Figure 4.4: The Pulse Program, GUI of Igor when running AutoAlgorithm sequence with a chain of 9 ions, of which 7 are qubits.

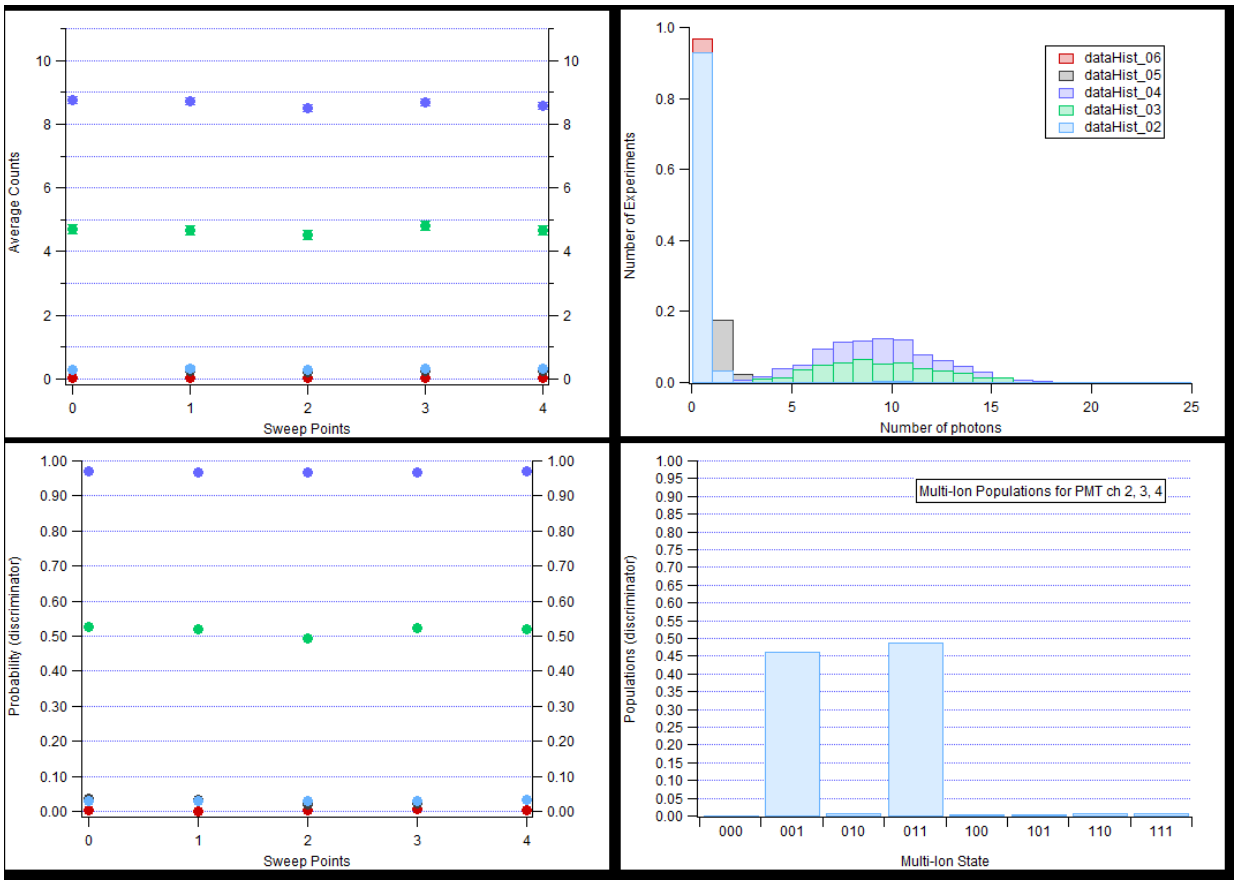

Figure 4.5: Live data visualization by Igor after running an algorithm sweep with 5 qubits, 2 of which are idle.

The "PulseGUI_n.ipf" contains functions related to the main GUI of the Igor program called "Pulse Program" (Fig. 4.4), of which the most important ones are "RunProc", "RunExperiment" and "RunExpValues". The "RunProc" function decides, based on user's input, whether an automatic calibration procedure or an ion-loss check is involved in the experiment sequence and how often. If the calibration result is satisfactory and the ions are not lost (due to collision with the background gas that melts the ionic crystal), the "RunExperiment" function is called. The "RunExperiment" function runs the experiment sequence by calling "RunExpValues", either with changing parameters (a scan) or not (an

alignment sweep), then analyze and plot the data (Fig. 4.5) as specified by the user. The "RunExpValues" function parses through the experiment structure and call functions that construct TTLs for different devices, construct waveforms for the AWGs ("ConstructAWGWaveform"), send the TTLs to the Sequencer ("sendSequence") and the waveforms to the AWGs ("AWGDownloadWaveformTabor" and "AWGUploadWaveformChase"), and collect photon count data from the Sequencer ("runSequence").

As the name suggests, "SequencerControl_n.ipf" contains functions related to the Sequencer, "AWGControl.ipf" for AWG waveforms and Chase AWG, "DataHandling.ipf" for data analysis, visualization and storage, while "TaborAWGUtils.ipf" contains functions specific to Tabor AWG. "AlgorithmConstructor.ipf" is a compiler module translating the gate syntax into relevant experimental operations, which are then converted into pulses by "RunExpValues" function. Details about how the compiler works can be found in Section 4.3 of Ref. [4].

Although the Igor program has enabled us to perform many proof-of-principle demonstrations of potentially useful quantum algorithms [3,43,45,49,53,58,61,68,102–113] along side various scientifically meaningful experiments [43,44,114–118], it has many limitations to scaling up to a larger system, all of which are already discussed in Section 4.4 of Ref. [4]. An immediately pressing limitation is that an "Experiment" structure can only have 100 operations since a structure is allocated on a stack memory, which is only a few MBs. The limit of 100 operations is arbitrarily set to prevent a stack overflow. However, since each of our operation is only about 1 KB or less, we need not worry about this until we reach 1000 operations. Therefore, for now, we can keep appending more "Experiment" structures, each has 100 operations. This is implemented in the newer version of the control

program with Igor 8. For the long term, we will need to rewrite "Experiment" structures as "Experiment" waves, which uses heap memory instead of stack memory. This allows larger memory size but takes longer to access and harder to manage. In general, it will be an overhaul of our current Igor program and will requires a more careful and well-thought-out design.

4.3 Upgrade to 9 Qubits

To upgrade the control system to 9 qubits, we added more TTLs for the individual beams and more qubit data lines for the photon counts. We also found a set of DC voltages that allow for 9 equally spaced ions. To minimize the differences in spacing between the ions, we used 2 end-cap ions at each end of the chain, so we trapped 13 ions for 9 qubits. This is similar to what was done for 7 qubits (trapping 9 ions), as described in Section 2.5 of Ref. [4] and Section 4.4 of Ref. [85]. Then we found the amplitude modulated pulses that performed the entangling gates between the relevant pairs of ions. Details on the pulse shape optimizer can be found in Chapter 4 of [80]. In this section, we focus on the control aspect of the upgrade.

First we upgraded the "photon counter" program for the PMT FPGA to allow for at least 9 outputs instead of just 8 outputs of the previous photon counter program. While the FPGA board allows for up to 24 outputs (organized into 3 sets of 8-pin connectors), the current setup only needs at most 10 outputs for 10 qubits since the number of individual Raman beams is limited to 10 by the diffractive optic element (Section 3.5.2). We chose to extend the outputs to 16 for the PMT FPGA program. We modified the channelize module

(called in the "channelize.v" and the "photon_counter.v") so that it received the mapping information from the Labview program and combined the PMT array counts into at most 16 channels.

Second we updated the "sequencer" program for the Sequencer FPGA to allow for 9 qubit data lines and 2 additional TTL outputs for the individual channels. The functions in "sequencer2.v" that needed modification were "receive_instructions.v" and "send_results.v". As the names suggest, "receive_instructions.v" receives the TTLs information about which channels to turn on and for how long, the number of experiment repetitions and the number of channels to send back photon counts. The "send_results.v" sends the photon counts according to the channels requested.

Third we modified the second RF control box so that 2 more channels were controlled by the AWGs. Note that it is of utmost importance to keep the phase variations between the AOM channels as low as possible. Therefore we used the same electronics components and cables of the same length (to within much less than 1 cm) between corresponding components in different channels (A 200 MHz signal has a wavelength of ~ 1.5 m so a 1 cm different results in a 0.02π phase difference, which is detectable in a Ramsey experiment.)

Finally, we modified the Igor program to add the following features: voltages for trapping 13 ions, voltages for measuring SPAM matrix of 9 qubits, 2 additional TTLs, 2 additional data lines, 2 additional AWG waveforms, and a table to store parameters for entangling gates on 9 qubits. The set of voltages for trapping 13 ions is saved in "CoupledDCVoltageValues13Ions" table under the folder "DCVolt". The set of voltages for measuring SPAM matrix is in "VoltagesFor13IonLocations" table, also under "DCVolt". They are both initialized by "DC_init()" function. The TTL and data hexbits are de-

fined in "Config.ipf", while the values for TTLs and data lines themselves are stored in "ExpParams" folder and initialized by "Param_Init()" function. The pulse shape, gate time, frequency and phase are in "XX13_Params" table, also under "ExpParams". We modified "ConstructAWGSegment" function in "AWGControl.ipf" to compile and upload 2 additional AWG waveforms (a total of 9 AWG waveforms). At the time, we only had 5 independent AWG channels to control 9 qubits, so we multiplexed the waveforms to send to the AWGs. The waveforms for qubits 1 and 7 were combined to a single waveform sent to AWG channel 1. Waveforms for qubits 2 and 6 were combined and sent to channel 2, those of qubits 3 and 8 were sent to channel 3, 4 and 9 to channel 4, while channel 5 was not multiplexed. As a result, we could not perform entangling gates between qubits 1 and 7, 2 and 6, 3 and 8, 4 and 9 without some additional switching schemes, even though we could perform single-qubit gates on the ions sharing AWG channels sequentially by using the TTLs. For the error detection with Shor code (Chapter 6), this was sufficient. For the Schwinger model with 6 qubits (Chapter 7), we needed these gates so we added an additional switch and TTL. We also modified data handling and algorithm running procedures, such as "DataHandler", "AutoCalibrationProc()" and "AutoPiTimeProc()", and the GUIs to be compatible with the added features.

4.4 Upgrade to Keysight AWGs

With the ability to generate arbitrary waveforms, AWGs are the key to performing gates and doing interesting science in our setup. Up until 2023, we used a 1 channel Chase AWG (DA12000-12-4M-PCI) and a 4-channel Tabor AWG (WX1284C). They were sufficient,

until we needed to send $\sim$ 20 ms long waveforms and play them multiple times. The Keysight AWG (M3202A) offers faster data transfer and a larger memory.

Table 4.1: Comparison between different AWGs in our setup

	Keysight	Tabor	Chase
Sampling rate	1GS/s	1.25GS/s	2GS/s
Memory	2GB	64MB	8MB
Data rate	8 GB/s (PCIe 1.0) to 32 GB/s (PCIe 3.0)	60 MB/s (USB 2.0) or 500 MB/s (USB 3.0)	133 MB/s (PCI)

The Keysight AWGs have PXIe interfaces and remote controlled from a computer via a PCIe bus. We installed three Keysight AWG modules, each with four AWG channels, in a PXIe chassis (NI PXIe-1062Q). We installed a host interface card (NI PCIe-8361) on the computer and a remote controller card (NI PXIe-8360) on slot 1 of the PXIe chassis, and connected them with an MXIe cable [119]. A similar setup was used to remote control of the DACs for DC voltages via a PXI chassis (NI PXI-1000) and a remote controller card (NI PXI-8360). For the computer to properly detect the chassis, compatible versions of drivers, such as "NI-PXI Platform Services", "NI-DAQmx", "NI 488.2", etc., were installed [120].

The remote control of Keysight AWGs are done through the "SD1 SFP" (an acronym for Software Development 1 Software Front Panel) included in the "Keysight IO Libraries Suite" and "SD1 3.x Software" packages. Theses packages provide control libraries in common programming languages such as C, C++, Python, etc. However, our programming language of choice, Igor, is not one of them. So an external C++ library (Igor XOP or extension) called KeysightAWGcpp was written to communicate with the Keysight AWGs using

Igor. This XOP [121] acts as a wrapper for the C++ library provided by Keysight. Since the Keysight library is only compatible with 64-bit system, we upgraded our experimental control program to a 64-bit version of Igor, the most stable of which was Igor 8. The XOP was written using Igor XOP Toolkit 8 [122] and Keysight SD1 3.x software package [123] in Visual Studio 2022. To activate the XOP in Igor, a shortcut to "KeysightAWGcpp.xop" was added to "Documents\WaveMetrics\Igor Pro 8 User Files\Igor Extensions (64-bit)".

The RF signal generated by the AWG was amplified by an RF switchbox before going to the 32-channel AOM. Before using the new AWGs, we made sure the amplified power in all the channels were the same and did not exceed 27 dBm by adjusting the amount of attenuation on each channel while setting the AWG output RF signal is to its maximum amplitude of 1.5 V or 3 $V_{pp} \approx 13.5$ dBm. This was done in Igor by calling the function "KeysightFuncGen".

For timing, the Keysight AWG takes a 10 MHz clock signal to the back of the chassis and generates its own 1 GHz clock signal ("CLKSYS") that is phase locked to the 10 MHz input. The AWG "sync mode" was set, by "awgQueueSyncMode" function, to this internal 1 GHz clock (0) instead of the external 10 MHz signal (1) to reduce the AWG jitter to less than a ns. Otherwise, after receiving the TTL trigger, the AWG had to wait up to 100 ns before it saw a rising edge on the clock. A $\sim$ 100 ns jitter randomly changes the length of gates by a significant amount. The "awgQueueSyncMode" currently can only be set in the KeysightAWG XOP not Igor. Other settings include "cyclic" queue mode (set by "KeysightQueueConfig"), so that a wave is played every time there is a trigger, and external trigger on a rising edge (set by "KeysightExtTriggerConfig" to "rise" not "high"). These can be set in Igor.

As mention in Section 4.3, we used RF cables of the same length (within 1 cm) for all channels inside the switchboxes and used cables of the same lengths from the AWGs to both switchboxes. Hence, the timing of the RF pulses were guaranteed to be the same (to much less than a ns) across the channels of the same AWG modules and of different modules. This measure reduced phase variation across the channels since an RF signal at $\sim$ 210 MHz had a $\sim$ 5 ns period, i.e., a ns timing difference could lead to a 0.4π phase difference.

While the laser pulses of the global and individual beam path were guaranteed to overlap at the ion by adjusting the global path with a delay stage (Fig. 3.9), their respective turn-on times might still be different due to the difference in the warm up time of the global and the individual AOMs and the length of the TTL cables. Particularly, the global beam turned on about 0.7 μs later than the individual beams. So we purposely programmed for the global TTL to be 0.676 μs early, a so-called programmable delay (in "ProgDelay" chapter). The exact duration for the delay was determined by overlapping the photo-diode signal from the global beam and individual beams using "ProgDelay".

The AWG signal itself also had a delay turn on time (the time between the trigger and the start of the AWG signal), which was measured to be 218 ns for both short and long pulses for the Keysight AWGs and less than 100 ns for the previous AWGs. Therefore we added padding of 260 ns (instead of 100ns) to the TTL so as not to cut off the AWG signal. The TTL duration could only be a multiple of 320 ns, which was the least common multiple of 20 ns (the FPGA clock) and 64 ns (for unknown reason).

Finally, before getting back to running algorithms, we measured the conversion coefficient from the AWG amplitude to the Rabi frequency seen by the ion. This was determined

in large part by the 32-channel AOM, which was not expected to change significantly. We verified that this coefficient was still 0.86 (also called "calibration coefficient" in the Igor program).

As a result of the upgrade, uploading a waveform from the computer to the AWG is now 12 times faster. Besides the AWG function, the Keysight card also includes an embedded function generator with amplitude, frequency, phase and IQ modulation capabilities. These functions can be helpful for sideband cooling, where using different frequencies on different ions will speed up the cooling cycle. Currently all the individual AOM channels share the same signal from the DDS during sideband cooling, hence they all have the same frequencies. Also for very long circuit, using the function generator capabilities may offer further speedup in terms of compilation and uploading waveform since only the information about the amplitude, phase and frequency needs to be uploaded, not a voltage time series.

4.5 Control Computer Upgrade and Igor 8 Program

Our experiment was started around 2011. It was built over many generations of graduate students and postdocs from 2011-2016 and continuously upgraded to add more capabilities ever since. A problem with any decade old experiment is that the computers and the software that control the experiment get outdated. One of the two control computers in our experiment ,"Decoherence", was still running Windows XP. Its graphic card stopped working so the only way to access the computer was through "Remote Desktop Connection" from the other control computer (called "Coherence"). This one ran Windows 7 but did not fare better. The last few months before the upgrade, it crashed multiple times a day

and stopped connecting to the lab LAN, hence there was no connection to "Decoherence" (where the photon counter Labview program was on) and network drives for data backup. Furthermore, as we needed to compile waveforms with hundreds of frequency components (see Section 5.2) we ran into the CPU's limitation of the computer. This called for a control computer upgrade, replacing "Coherence" with "Alienware" and "Decoherence" with "Oracle", both running Windows 10. This also helped us comply with the school requirement on updating all computers to Windows 10.

As mentioned in the previous section, integrating the Keysight AWGs required updating the Igor control program from its 32-bit version of Igor 6.2 to the 64-bit version of Igor 8. This worked better with Windows 10 and provided a significant speedup to compiling longer waveforms and processing larger data set.

The upgrade was done in three steps: software, computer, and AWG. First we upgraded Igor on the existing control computer, "Coherence", and ensured that all of the current hardware worked with Igor 8. Secondly, we upgraded the computer, and made sure we could detect and control all devices after disconnecting them from "Coherence" and connecting them to the new control computer, "Alienware". Finally we integrated the Keysight AWG modules and verified their operations. The idea of splitting into three steps was that for each step we only changed one aspect of the control system so in case of error we could narrow down the problem and revert the upgrade if necessary. After each step, we ran a standard algorithm on 2-qubit (we chose the two-site Schwinger model simulation) to check the system's operation. This section only focuses on the first two steps of the upgrade. The AWG upgrade is discussed at length in the previous section.

For the software upgrade, we installed the suitable 64-bit versions of drivers for all de-

vices (see Section 4.6 for more details). Then we recompiled the in-house developed XOPs to 64-bit versions compatible with Igor 8 using the provided XOP Toolkit 8. Theses XOPs were "PCOCam.xop" for the PCO camera, "DA12000.xop" the Chase AWG and "ConstructFT-gate.xop" for the Fourier-series based entangling gate. These user-defined XOPs together with shortcuts to others 64-bit WaveMetrics XOPs ("VDT2-64,xop", "NIGPIB2-64.xop", "NIDAQmx64.xop", "VISA64.xop") were placed in the folder "Documents \WaveMatrics \Igor Pro 8 User Files \Igor Extensions (64-bit)". Shortcuts to the WaveMetrics XOPs were placed in "C:\Program Files \WaveMetrics \Igor Pro 8 Folder \Igor Extensions (64-bit)". More details on how to activate XOPs can be found in the XOP manual [122].

To comply with Igor 8's syntax, we updated functions to only return a single value, not a wave, by simply commenting out the lines that return waves since the returned waves were global variables that were updated during the functions' call. Igor 8 also did not allow thread-safe functions to automatically update data in the main thread. Since our camera functions relied on this, the images from the camera was not updated. An attempt to fix the code allowed the camera image to update after a 30-second delay, so we decided to keep running the Camera functions in Igor 6 on "Oracle".

The computer upgrade went smoothly except for two major problems. One was that the NI chassis were not recognized by the originally intended new computer (called "Fault-tolerance", ironically) even though they worked fine during testing. Since all attempts to solve it failed, we switched to a different computer with a similar specification (Dell Alienware) and the NI chassis were again properly recognized. We suspected that some firmware updates were needed for "Fault-tolerance". Secondly, we could not communicate with the GPIB devices using "VISAWrite" when moving to "Alienware" although the "VISAWrite"

function worked fine with the Tabor AWG on the same computer and worked fine with all devices on "Coherence" with Igor 8 64-bit. We used "GPIBWrite2" to communicate with GPIB devices instead.

4.6 Troubleshooting common problems

When you have problems communicating with a device, always check if the device is detected in Windows "Device Manager". If not, check the connection to the device, check if it is powered on, if it has a correct name and if a suitable driver is installed. What counts as a suitable driver depends on its firmware version, the version of the software you used to talk to the device and the operating system you use. For device with serial communication, check the port name, baud rate, parity, stop and start bits. For NI devices such as the PXI/PXIe chassis, DACs and even the Keysight AWGs, check if the device is detected in NI MAX (Fig. 4.6). If it is not detected even though correct drivers ("PXI Platform Services","NI-DAQmx","NI 488.2", etc.) are installed, follow the steps in this troubleshooting guide [124,125]. For the Keysight AWGs, also check if they are detected in the "Keysight Connection Expert" software. If not, check if the compatible firmware and drivers are installed in the "Keysight SD1 SFP". The firmware must be of version 4.02.45 or later.

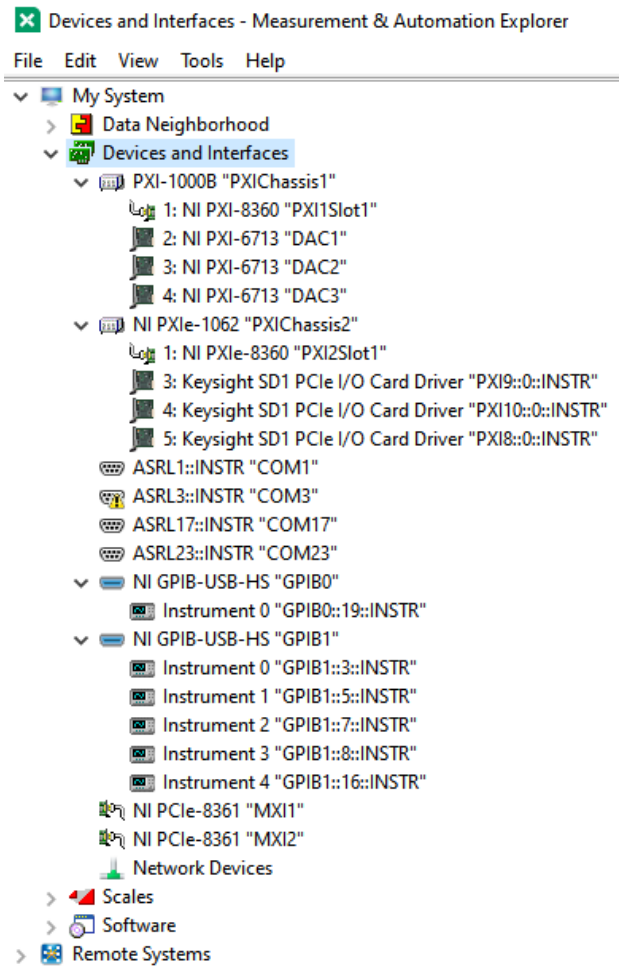

Figure 4.6: NI MAX showing all devices connected to the control computer after the upgrade.

Chapter 5: Entangling Gates in Trapped Ions

The most common entangling gates in trapped-ion use the shared motional modes of the ion chain to mediate interactions between pairs of ions [126–129]. During a gate, the qubit is entangled with the motion. The spin-motion state accumulates a state-dependent geometric phase. At the end of the gate, the spin is disentangled from the motion but the accumulated phase factor remains and becomes a spin flip in another basis. The fidelity of the gate depends on how well the spin and motion are disentangled and the spin and motional coherence during the gates. The majority of the gate optimization consists of finding parameters (gate duration, frequency, amplitude and phase, etc.) that minimize the spin-motion entanglement α.

The gates can be categorized into two kinds: $\hat{\sigma}^z\hat{\sigma}^z$ and $\hat{\sigma}^\phi\hat{\sigma}^\phi$ [81,130]. The first kind is usually induced by applying a spin-dependent Stark shift on the relevant transitions [21,128] and the second kind is usually induced by applying a bi-chromatic (red- and blue-sideband) spin-flip [126, 131]. The first kind is also known as a phase or ZZ gate. The second kind is a Molmer-Sorensen (MS) or XX gate. In this chapter, we focus on the later.

5.1 Molmer-Sorensen (MS) Gate

In the MS gate, the spin-motion entanglement is induced by a bichromatic drive, driving the first-order red and blue sideband simultaneously with the symmetric detuning from the carrier $\mu_i^b = \mu_i = \omega_p + \delta_{ip}$, $\mu_i^r = -\mu_i$ on the ions that you want to entangle. As seen in Section 2.3, the Hamiltonian for ion i in the interaction picture after the first RWA is

$$\hat{H}_i^{\mathrm{rb}} = \frac{\Omega_i}{2}\left(1 + i\sum_{p=1}^{N}\eta_{ip}(\hat{a}_p^\dagger \mathrm{e}^{i\omega_p t} + \hat{a}_p \mathrm{e}^{-i\omega_p t})\right)\left(\mathrm{e}^{-i(\mu_i^b t+\phi_i^b)} + e^{-i(\mu_i^r t+\phi_i^r)}\right)\hat{\sigma}_i^+ + \mathrm{h.c.} \tag{5.1}$$

$$= \Omega_i\left(1 + i\sum_{p=1}^{N}\eta_{ip}\left(\hat{a}_p^\dagger \mathrm{e}^{i\omega_p t} + \hat{a}_p \mathrm{e}^{-i\omega_p t}\right)\right)\cos(\mu_i t - \phi_i^m)\hat{\sigma}_i^+ \mathrm{e}^{-i\phi_i^s} + \mathrm{h.c.} \tag{5.2}$$

$$= \Omega_i \cos(\mu_i t - \phi_i^m)\hat{\sigma}_i^{\phi_i^s} + \Omega_i\sum_{p=1}^{N}\eta_{ip}\cos(\mu_i t - \phi_i^m)\left(\hat{a}_p^\dagger \mathrm{e}^{i\omega_p t} + \hat{a}_p \mathrm{e}^{-i\omega_p t}\right)\hat{\sigma}_i^{\phi_i^s - \pi/2}, \tag{5.3}$$

where $\phi_i^s = (\phi_i^r + \phi_i^b)/2$ is the spin phase, $\phi_i^m = (\phi_i^r - \phi_i^b)/2$ is the motional phase, and $\hat{\sigma}^\phi = \hat{\sigma}^+ \mathrm{e}^{-i\phi} + \hat{\sigma}^- \mathrm{e}^{i\phi} = \hat{\sigma}^x \cos\phi + \hat{\sigma}^y \sin\phi$. Note that the sum over the modes in Eq. (5.3) is only from $p = 1$ to $p = N$ not $p = 3N$ (meaning x radial modes only) since the Raman beams in our setup has mostly projections in the x-y plane and the Rabi frequencies for the sidebands are a lot smaller than the spacings of the x and y radial modes ($\eta_{ip}\Omega_i/2\pi \sim 10$ kHz, while $(\omega_{x,N} - \omega_{y,1})/2\pi \sim 100$ kHz).

We set the phases of the red and blue sideband $\phi_i^r = \pi/2 - \phi_i$, $\phi_i^b = \pi/2 + \phi_i$ so that $\phi_i^s = \pi/2$ and $\phi_i^m = -\phi_i$. Since the $\Omega_i \ll \omega_p$, we can ignore the off-resonant carrier transition (the first term).

$$\hat{H}_i^{\mathrm{rb}} = \Omega_i\sum_{p=1}^{N}\eta_{ip}\cos(\mu_i t + \phi_i)\left(\hat{a}_p^\dagger \mathrm{e}^{i\omega_p t} + \hat{a}_p \mathrm{e}^{-i\omega_p t}\right)\hat{\sigma}_i^x. \tag{5.4}$$

Applying the Hamiltonian above to 2 ions i, j with the same frequency $\mu_i = \mu_j = \mu$ and phase $\phi_i = \phi_j = \phi$. Using the Magnus expansion [132, 133] to obtain the time evolution

under $\hat{H}_i^{\mathrm{rb}}+\hat{H}_j^{\mathrm{rb}}$. Notice that terms with higher order than two are canceled since $[\hat{a},\hat{a}^\dagger]=1$

$$U_{ij}(\tau)=\exp\left[\sum_{i'=i,j}\sum_{p=1}^{N}\left(\alpha_{i'p}(\tau)\hat{a}_p^\dagger-\alpha_{i'p}^*(\tau)\hat{a}_p\right)\hat{\sigma}_i^x+i\chi_{ij}(\tau)\hat{\sigma}_i^x\hat{\sigma}_j^x\right], \tag{5.5}$$

where

$$\alpha_{ip}(\tau)=-i\eta_{ip}\int_0^\tau \Omega_i(t)\cos\left(\mu t+\phi\right)\mathrm{e}^{i\omega_p t}dt \tag{5.6}$$

and

$$\chi_{i,j}(\tau)=\eta_{ip}\eta_{jp}\sum_{p=1}^{N}\int_0^\tau dt\int_0^t dt'\Omega_i(t)\Omega_j(t')\sin(\omega_p(t-t'))\cos(\mu t+\phi)\cos(\mu t'+\phi) \tag{5.7}$$

The Hamiltonian can be rewritten with displacement operator $\hat{D}(\beta)=\mathrm{e}^{\beta\hat{a}^\dagger-\beta^*\hat{a}}$

$$U(\tau)=\left(\prod_{i'=i,j}\prod_{p=1}^{N}\hat{D}\left(\alpha_{i'p}(\tau)\hat{\sigma}_{i'}^x\right)\right)\mathrm{e}^{i\chi_{i,j}(\tau)\hat{\sigma}_i^x\hat{\sigma}_j^x}, \tag{5.8}$$

where the amount of displacement $\beta=\alpha\hat{\sigma}^x$ is spin-dependent. The first term describes residual spin-motion entanglement at the end of the gate. The second term is the geometric phase accumulated during the gate.

We can generalize Eq. (5.4) into

$$\hat{H}_i^{\mathrm{rb}}=\sum_{p=1}^{N}\frac{\eta_{ip}}{2}\hat{\sigma}_i^x(g(t)\hat{a}_p^\dagger\mathrm{e}^{i\omega_p t}+\mathrm{h.c.}), \tag{5.9}$$

where $g(t)$ can be a function of any form not just $g(t)=\Omega_i\mathrm{e}^{i(\mu t+\phi)}$. Now the problem becomes finding a pulse shape $g(t)$ that minimizes the phase space closure while making the maximally entangled state, i.e.,

$$\alpha_{ip}(\tau)=-i\eta_{ip}\int_0^\tau g(t)\mathrm{e}^{i\omega_p t}dt=0 \tag{5.10}$$

for all N modes, and

$$\chi_{ij}=\sum_{p=1}^{N}\eta_{ip}\eta_{ip}\int_0^\tau dt_2\int_0^{t_2}dt_1 g(t_2)g(t_1)\sin[\omega_p(t_2-t_1)]=\frac{\pi}{4}. \tag{5.11}$$

The traditional method in our experiment is with amplitude modulation [131]. The pulse is divided into L segments, each has a constant amplitude, but the amplitude of one segment is different from the next while the frequency and phase is the same for all segments. Details on the pulse optimization procedure and the implementation of this amplitude modulated scheme on our setup can be found in previous theses [1, 4, 80].

5.2 Fourier-Transformed (FT) Gates

In this section, we present an experimental implementation of new pulse optimization methods, where the amplitude, frequency and phase are simultaneously modulated. These methods allow for the construction of robust and power optimal entangling gate pulses for a pair of ions in a long chain without involving costly optimization. These methods are both computationally efficient and flexible due to the built-in trade-off between laser power, gate speed-up and robustness to motional drift. The performance of the pulses on our experiment agrees very well with the theoretical prediction when taking into account of imperfection in the confining potential for the ions. The results for this gate implementation are published in [117].

The pulses of Fourier transformed (FT) gates are first proposed by Blumel et al [134] and have been demonstrated in [117, 134]. Ref. [134] implements the pulses with a DDS, which is limited in number of frequencies or tones it can produce. Therefore, they have to demodulate the pulses (see Section 5.2.2) and implement them in the time domain. While Ref. [117] uses an AWG, therefore is able to implement the pulses directly in the frequency domain. In this section, we mainly discuss the implementation used in Ref. [117].

In the frequency domain, an FT gate is a sum of Fourier-sine series. For a gate of duration τ and N_A frequency components.

$$g(t) = \sum_n^{N_A} A_n \sin\left(\frac{2\pi nt}{\tau}\right), \tag{5.12}$$

Each frequency component $f_n = n/\tau$ has a different amplitude that is either in-phase ($A_n > 0$) or out-of-phase ($A_n < 0$) with each other.

To achieve a high-fidelity gate, we need to require that A_n satisfy two constraints. The first constraint is phase-space closure as in Eq. (5.10), which together with Eq. (5.12) becomes

$$\alpha_{ip}(\tau) = -i\eta_{ip} \sum_n^{N_A} A_n \int_0^\tau \sin\left(\frac{2\pi nt}{\tau}\right) \mathrm{e}^{i\omega_p t} dt = -i\eta_{ip} \sum_n^{N_A} M_{pn} A_n = 0 \tag{5.13}$$

or

$$\sum_n^{N_A} M_{pn} A_n = M\vec{A} = 0, \tag{5.14}$$

where $M_{pn} = \int_0^\tau \sin\left(\frac{2\pi nt}{\tau}\right) \mathrm{e}^{i\omega_p t} dt$.

The second constraint is stability against the fluctuation of ω_p up to an order K

$$\left(\frac{\partial^k}{\partial \omega_p^k}\right) \alpha_{ip}(\tau) = -\left(\frac{\partial^k}{\partial \omega_p^k}\right) i\eta_{ip} \int_0^\tau g(t) \mathrm{e}^{i\omega_p t} dt = 0 \tag{5.15}$$

or

$$\sum_n^{N_A} M_{pn}^{(k)} A_n = 0, \tag{5.16}$$

where $k = 1, 2, ..., K$. Together these make $Q = N(K+1)$ constraints. As long as $N_A > Q$ there exists a solution that satisfies all the constraint. Let $\vec{A}^\gamma$, $\gamma = 1, 2, ..., N_A - Q$, be a set of linearly independent solution that spans the solution space of Eq. (5.14) and Eq. (5.16),

i.e., null space of M. In general, any solutions of Eq. (5.14) and Eq. (5.16) can be written as a linear combination of $\vec{A}^\gamma$,

$$\vec{A} = \sum_{\gamma=1}^{N_A-Q} c_\gamma \vec{A}^\gamma. \tag{5.17}$$

Additionally, for practical purpose, the power required to achieve the maximally entangled angle $\chi_0 = \pi/4$ should be as small as possible. Subtitute Eq. (5.12) into Eq. (5.11)

$$\chi_{ij} = \sum_{p=1}^{N} \eta_p^i \eta_p^j \int_0^\tau dt_2 \int_0^{t_2} dt_1 \sum_n^{N_A} A_n \sin\left(\frac{2\pi n t_2}{\tau}\right) \sum_m^{N_A} A_m \sin\left(\frac{2\pi m t_1}{\tau}\right) \sin[\omega_p(t_2 - t_1)] \tag{5.18}$$

$$= \vec{A}^{\,T} D^{ij} \vec{A} = \frac{\pi}{4}, \tag{5.19}$$

where

$$D_{nm}^{ij} = \sum_{p=1}^{N} \eta_p^i \eta_p^j \int_0^\tau dt_2 \int_0^{t_2} dt_1 \sin\left(\frac{2\pi n t_2}{\tau}\right) \sin\left(\frac{2\pi m t_1}{\tau}\right) \sin[\omega_p(t_2 - t_1)]. \tag{5.20}$$

We can rewrite χ_{ij} using $\vec{A}^\gamma$

$$\chi_{ij} = \sum_{\gamma\gamma'} c_\gamma c_{\gamma'} \vec{A^\gamma}^{\,T} D^{ij} \vec{A^{\gamma'}} = \sum_{\gamma\gamma'} c_\gamma c_{\gamma'} B_{\gamma\gamma'} = \vec{c}^{\,T} B \vec{c}, \tag{5.21}$$

where $B_{\gamma\gamma'} = \vec{A^\gamma}^{\,T} D^{ij} \vec{A^{\gamma'}}$.

Again, we can expand $\vec{c}$ in the basis $\vec{v}_\beta$ of B, $\vec{c} = \sum_\beta b_\beta \vec{v}_\beta$ where $B\vec{v}_\beta = \lambda_\beta \vec{v}_\beta$

$$\chi_{ij} = \sum_{\beta\beta'} b_\beta b_{\beta'}\ \vec{v}_\beta{}^T B_{\beta\beta'} \vec{v}_{\beta'} = \sum_{\beta\beta'} b_\beta b_{\beta'}\ \lambda_\beta \delta_{\beta\beta'} = \sum_\beta b_\beta^2 \lambda_\beta \le \sum_\beta b_\beta^2 \lambda_{\max} \tag{5.22}$$

where we assume, without loss of generality, $\lambda_1 = \lambda_{\max}$ is the largest eigenvalue of B corresponding to $\vec{v}_1$. We can rewrite the maximally entangled angle χ_0 in term of the

average power

$$\bar{P} = \frac{1}{\tau}\int_0^\tau g^2(t)dt = \frac{1}{2}\sum_{n=1}^{N_A} A_n^2 = \frac{1}{2}\vec{A}^{\,T}\vec{A} = \frac{1}{2}\sum_\beta b_\beta^2, \tag{5.23}$$

$$\chi_0 = \chi_{ij} \leq 2\bar{P}\lambda_{\max} \tag{5.24}$$

If we require the average power to be minimum then

$$\bar{P}_{\min} = \frac{\chi_0}{2\lambda_{\max}} \tag{5.25}$$

when $\chi_{ij} = (1/2)b_1^2\lambda_{\max}$ and $\vec{c} = b_1\vec{v}_1$.

Since the ion number N does not occur explicitly other than in the vector space size, the method is naturally scalable to any number of ions. And since solving for $\vec{A}$ involves only linear algebra, the method is computationally efficient and straightforward to implement. However, if more conditions are added, the size of the null-space contracts, and with it the number of accessible degrees of freedom, which leads to an increase in the power required. Conversely, for a set of constraints and a given power budget, $\bar{P}$, there is a minimum gate-duration, $\tau_{\min}$, which roughly follows $\tau_{\min} \sim 1/\bar{P}$. Thus, there is a trade-off between power requirement and gate duration.

The two-qubit gate infidelity $\mathcal{I}$ at zero temperature is given by

$$\mathcal{I} = \frac{4}{5}\vec{A}^T\bar{F}\vec{A} = \frac{4}{5}\sum_{p=1}^{N}\left(|\alpha_{i,p}|^2 + |\alpha_{j,p}|^2\right), \tag{5.26}$$

where the matrix

$$\bar{F}_{nm} = \sum_{p=1}^{N}[(\eta_{ip})^2 + (\eta_{jp})^2]\hat{\sigma}_{np}\hat{\sigma}_{mp} \tag{5.27}$$

is the infidelity matrix and $\hat{\sigma}_{np} = \int_0^\tau \sin(2\pi nt/\tau)\exp(i\omega_p t)dt$ [135].

5.2.1 Power, Gate Speed and Fidelity Trade-off

If the conditions in Eqs. (5.14) and (5.16) are satisfied exactly then we call this method **Exact AMFM**. Otherwise, we also allow Eqs. (5.14) and (5.16) to be satisfied approximately by including, in the null space of M, eigenvectors with non-zero eigenvalues, as long as their moduli are smaller than a pre-determined, non-zero value. We name this the extended null-space method or **ENS AMFM**.

Figure 5.1(a) shows the power requirement of the optimal, exact AMFM method for various qubit pairs (i, j) and degrees of stabilization K as a function of gate duration τ for a 15-ion chain, with an inter-ion spacing of 5 μm and the 11 central ions used as qubits. We see that the power requirement dramatically increases as we decrease τ, exhibiting a step-like transition, whose location is nearly independent of the specific ion-pair gate combinations. The reason is the following. To operate a two-qubit gate at low power, it is necessary that the basis frequencies, $2\pi nt/\tau$, have a good overlap with the motional-mode frequencies, typically capped at $\omega_p \lesssim 2\pi \times 3\,\mathrm{MHz}$. As τ decreases, more and more basis frequencies are pushed out of the frequency range of the motional modes, effectively reducing the dimension of the null-space from which the power-optimal solutions are drawn. The step in power results when we run out of null-space vectors with good motional-mode frequency overlap. Since increasing K reduces the null-space dimension even further, the power step happens at larger gate times τ for larger K. Similarly to [136], our scheme cancels carrier excitation to first order due to the sinusoidal nature of our basis functions. While Figure 5.1 shows gates $< 100\mu$s, which approximately are still in the Lamb-Dicke regime, further investigation is needed to ensure the standard MS formalism with its perturbative expansions of the

Hamiltonian is still valid in this short-pulse regime.

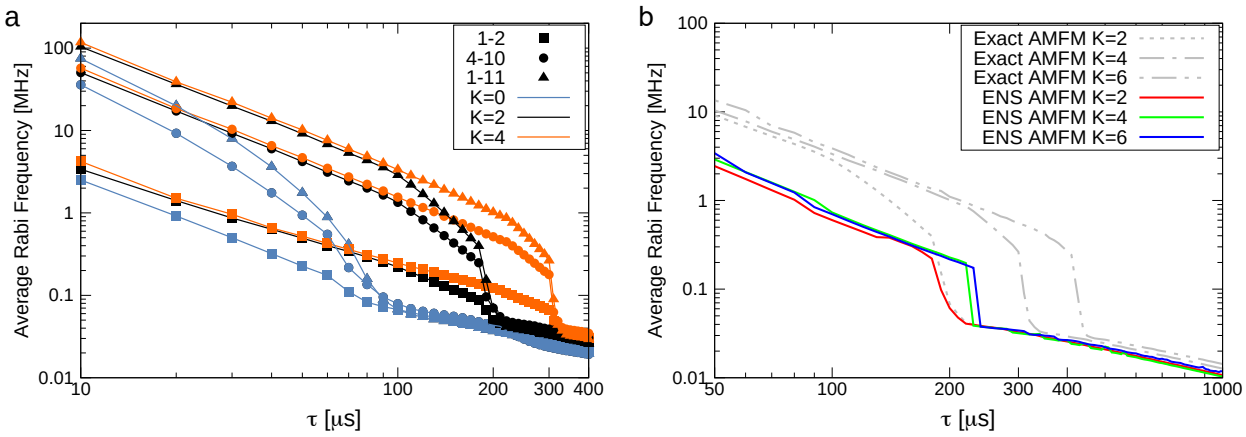

Figure 5.1: Properties of gate pulses generated for a 15-ion, 11-qubit chain. (a) Power requirement of the exact AMFM gate as a function of gate time τ for three different qubit pairs, $(1, 2)$ (squares), $(4, 10)$ (circles), and $(1, 11)$ (triangles), and three different degrees of stability $K = 0$ (blue), $K = 2$ (black), and $K = 4$ (orange). (b) Average power requirement as a function of τ for different degrees of stabilization K for the ENS protocol (colored, solid lines) with $\mathcal{I} \leq 10^{-4}$. Red, green, and blue lines are for $K = 2$, $K = 4$, and $K = 6$, respectively. For comparison, the results for the exact AMFM for $K = 2$ (dotted line) and $K = 4$ (dot-dashed line) are imported from (a) without change, and $K = 6$ (dot-dot-dashed line) is added to illustrate the trend.

In Figure 5.1(b) we compare the pulse-power requirements of stabilized pulses produced according to the exact AMFM method and the ENS method, which allows for straightforward implementation of the stability conditions. Over a large span of gate times, the ENS method offers significant power savings for stabilized pulses. In particular, we find that, for stability degree $K = 6$ and gate duration $\tau = 250\,\mu$s, the power saving can be as

large as a factor of 15.

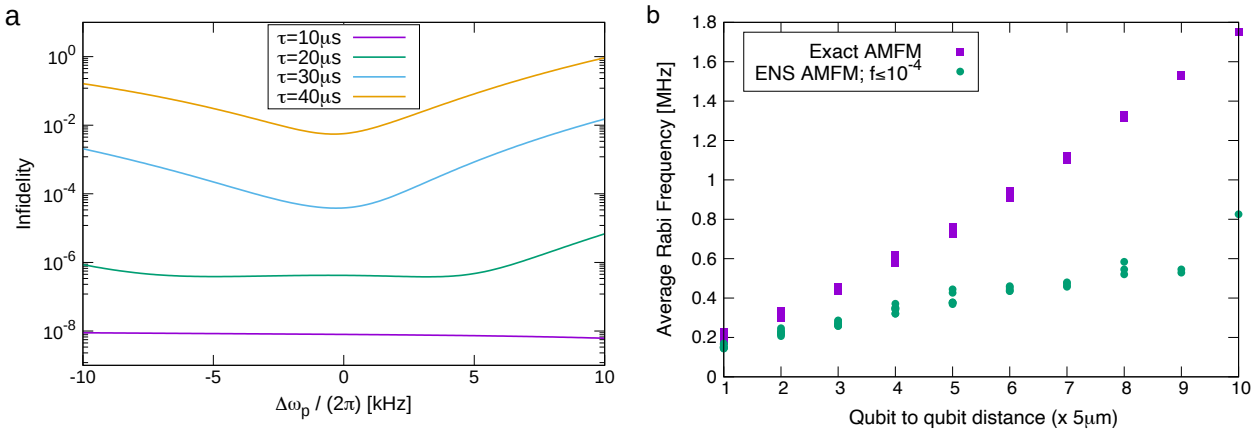

Figure 5.2: Trade space for a 15-ion, 11-qubit chain. (a) Infidelity $\mathcal{I}$ as a function of uniform mode-frequency drift $\omega_p \to \omega_p + \Delta\omega_p$ on qubits $(1, 11)$ for four different gate times τ. (b) Average power requirement as a function of distance between the qubits for a τ=50 μs gate. Purple squares: exact AMFM; green circles: ENS AMFM.

We note that faster gates come with exponentially decreasing infidelity and increased natural stability against mode-frequency drifts, even in the absence of active stabilization. We illustrate this in Figure 5.2(a), which shows that increasing the gate speed from 40 μs to 10 μs reduces the infidelity by about 6 orders of magnitude, reaching below $f = 10^{-8}$ over a drift-frequency range larger than ± 10 kHz at $\tau = 10\,\mu$s. While pulses this short may not be practical, the stability they provide can be propagated to longer gates at the cost of power optimality by reducing the power and repeating the pulse sequence multiple times.

According to Figure 5.1(a), qubit pairs whose constituent ions are further apart from each other require more power. Therefore, given a fixed power budget, instead of trading the power savings afforded by our pulse design for gate duration, we can alternatively

trade the savings for better qubit connectivity. This power-connectivity trade-off can play a critical role in harnessing the power of quantum computation since matching hardware and application connectivity is crucial to performance in a future quantum operating system [102]. In Figure 5.2(b) we show the power requirement for $\tau = 50\,\mu$s as a function of qubit distance for the exact AMFM and ENS AMFM. We see that the ENS AMFM requires factors of about 2 to 4 smaller power when compared to the exact AMFM counterparts.

5.2.2 Demodulation of The FT Gates

In the time domain, the gate is equivalent to an amplitude and frequency modulated pulse [117, 134]

$$g(t) = \Omega(t) \sin\Big(\int \mu(t')dt' \Big) = \Omega(t) \sin(\Psi(t)). \tag{5.28}$$

The procedure to obtain $\Omega(t)$ and $\mu(t')$ is described in details in the supplementary section S9 of Ref. [134]. It can be summarized as following: Assume the envelope $\Omega(t)$ is non-zero (which reduces the power required for a maximally entangled gate), then $g(t) = 0$ only when $\Psi(t) = j\pi$ where $j \in \Re$. Let ζ_j be the solutions of $\Psi(t) = 0$. Approximate $\mu(t')$ to be constant between ζ_j then

$$\pi = \int_{\zeta_j}^{\zeta_{j+1}} \mu(t')dt' \approx \mu(\zeta_j)(\zeta_{j+1} - \zeta_j).$$

Then

$$\mu(\zeta_j) = \frac{\pi}{\zeta_{j+1} - \zeta_j}. \tag{5.29}$$

We can obtain $\Omega(t)$ by evaluating $g'(\zeta_j)$

$$\Omega(\zeta_j) = \left| (-1)^j \frac{g'(\zeta_j)}{\mu(\zeta_j)} \right|. \tag{5.30}$$

Figures 5.6 and 5.7 show the pulse shapes used to implement the two-qubit gates on our seven-ion, five-qubit trapped-ion quantum computer.

5.2.3 Experimental Performance of the FT Gates

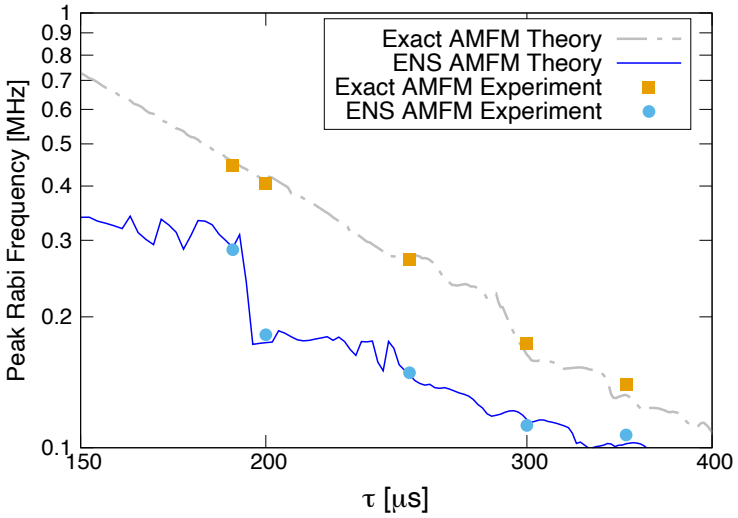

Figure 5.3: Comparison of peak power requirements of ENS gates (blue solid line) with exact AMFM gates (grey dashed line) on qubits $(4, 5)$ as a function of gate time τ ($K = 4$) for $\mathcal{I} \leq 10^{-4}$ on a seven-ion, five-qubit chain. Experimental results at five different gate times, i.e., 190μs, 200μs, 250μs, 300μs, and 350μs, implementing pulses constructed according to the exact AMFM and ENS protocols, are shown as orange squares and blue circles, respectively. The experimental error bars are smaller than the plot symbols.

Figure 5.3 shows the theoretical predictions and experimentally measured power requirements as a function of gate duration for exact AMFM and ENS-based pulses. We chose infidelity $\mathcal{I} = 10^{-4}$ to determine the ENS since the gates are limited to 10^{-2} by other imperfections. We chose to stabilize these pulses to degree $K = 4$.

Due to the limited amplitude resolution of the AWG (14-bit DAC), the relative amplitudes of basis frequencies smaller than 10^{-4} are neglected in the experimental implementation. We confirm numerically that this does not significantly impact the theoretical fidelity and stability of the resulting gates. We verify a successful implementation of a pulse by observing a continuous coherent transfer of population between the $|00\rangle$ and $|11\rangle$ states when the applied laser power is varied. We then calculate the minimal Rabi frequency $\Omega_0 = s\Omega_{\max}$ needed to perform a maximally entangling gate, where $s \leq 1$ is a scale factor and $\Omega_{\max}$ is the maximum Rabi rate available. We further verify the creation of the maximally entangled state by measuring the parity contrast for some of the pulses.

All the experimentally determined Rabi frequencies for the two-qubit gates using either the ENS- or the exact AMFM protocols fall within $\pm 10\%$ of the respective theoretically predicted values. The small discrepancies between experimental values and theory predictions are due to uncertainties in the Lamb-Dicke parameters and mode frequencies. We note that shorter gates at higher Rabi frequency may suffer from more noise, and thus higher infidelity due to, e.g., acoustic vibrations, which do not get averaged out over the gate application.

To accurately determine the experimental Rabi frequencies for every two-qubit gate presented in Figure 5.3, we employ the following procedure. To eliminate the effect of beam alignments and laser power fluctuation on the Rabi frequencies, for each experiment, we measure the carrier Rabi frequencies of each qubit at the scale $s = 1$. We then scan the scale to observe coherent population transfer between $|00\rangle$ and $|11\rangle$, a signature of the MS gate. From this scan, we can determine the scale for maximally entangling gate. We perform the gate at this scale with 10000 data points and correct for state-preparation and

measurement (SPAM) errors in post-processing to obtain a good estimate of the scale, and therefore the Rabi rate Ω_0.

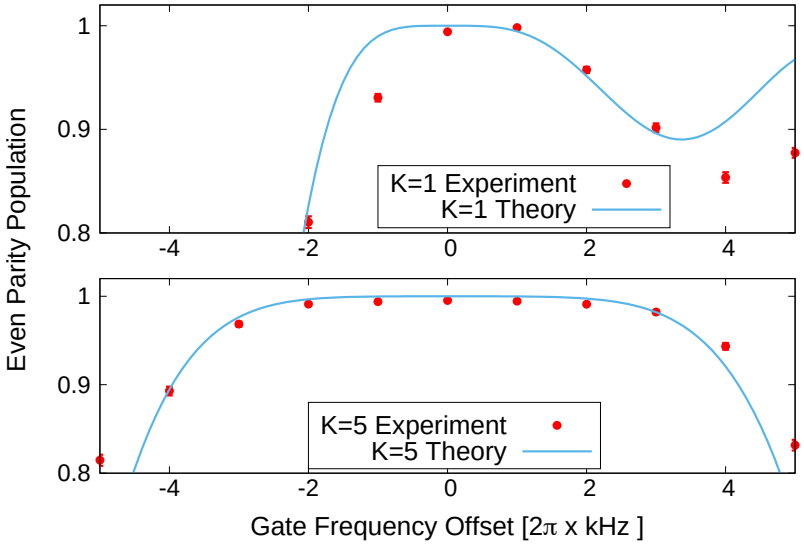

Figure 5.4: Experimental demonstration of the K-order stabilized two-qubit gates for qubit pair (4,5) on our seven-ion, five-qubit system. The ENS AMFM pulse sequence satisfying $\mathcal{I} \leq 10^{-4}$ at no frequency offset with $K = 1$ (top) and $K = 5$ (bottom), corresponds to a maximally entangling gate. The experimentally measured even-parity population is plotted as a function of the gate frequency. The blue lines show the gate fidelity according to the analytical expression for $\mathcal{F}$, valid in the low-error limit. The width of the detuning-robust region is larger for the the pulse with the higher stabilization order ($K = 5$ vs. $K = 1$).

We demonstrate the benefit of stabilizing the gates with respect to fluctuations in the motional-mode frequencies by applying pulses with two different stabilization orders, i.e., $K = 1$ and $K = 5$, to qubits (4,5) on our seven-ion, five-qubit quantum computer. The two ENS AMFM pulses are constructed with $\mathcal{I} = 10^{-4}$ at zero gate-frequency offset. To systematically control the detuning error, we offset the gate frequency from the original

intended gate frequency, which is equivalent to uniformly offsetting the motional-mode frequencies in the opposite direction. We apply the pulses to the initial state $|00\rangle$ and measure the even-parity populations when $P_{00} \approx P_{11}$, akin to performing a maximally entangling gate.

Figure 5.4 shows the even-parity population $P_{\text{even}} = P_{00} + P_{11}$, which is the quantity stabilized by the gate. Since this does not measure coherent errors, we checked the parity contrast for some of the pulses as for the previous measurement. The experimentally measured values with their associated error bars are marked in red. The error bars are 1σ confidence intervals, sampled from a binomial distribution, and each point represents 4000 experimental shots. The blue line shows the analytical fidelity $\mathcal{F} = 1 - \frac{4}{5}\sum_p (|\alpha_{i,p}|^2 + |\alpha_{j,p}|^2)$, follow from Eq. (5.26), which is valid in the low-infidelity limit [135]. As expected, the width of the detuning-robust region is larger for the pulse with the higher stabilization order.

5.2.4 Measuring the Lamb-Dicke Parameters

A carefully designed protocol for accurately determining the motional mode frequencies as well as the Lamb-Dicke parameters η_{ip} is necessary to achieve a good agreement between predicted and observed Rabi rates needed for a maximally entangling gate. Here, we present the details of the protocol we implement in terms of experimental procedures and post processing steps. Experimentally, we aim to measure the mode frequencies and the magnitude of the Lamb-Dicke parameters through sideband spectroscopy.

After ground-state cooling and initialization, we scan the frequencies across the blue sideband for each ion, one ion at a time, with square pulses at a fixed laser power and pulse

duration before detecting the population in $|1\rangle$ state.

For each normal mode and each ion, we can define a sideband Rabi frequency as $\Omega_i^p = \sqrt{\bar{n}+1}\Omega_i\eta_i^p$, where Ω_i is the Rabi frequency of the qubit transition. When Ω_i^p is much smaller than the splitting between motional mode frequencies, the transitions with frequency in the vicinity of the motional mode frequency ω_p can be modeled as a two-level system and the final $|1\rangle$ state population after a pulse with a duration t_{bsb} can be approximated as

$$P_{|1\rangle} = \frac{\Omega_i^{p2}}{\Omega_i^{p2} + \delta\omega_p^2/4} \sin^2\left(t_{\mathrm{bsb}}\sqrt{\Omega_i^{p2} + \frac{\delta\omega_p^2}{4}}\right) , \tag{5.31}$$

where $\delta\omega_p$ is the difference between the mode frequency ω_p and the frequency of the sideband pulse. Thus, with enough frequency points scanned near each mode, we can fit the qubit $|1\rangle$ state population as a function of frequency to (5.31) and extract ω_p and $|\Omega_i^p|$. Note that we choose the pulse duration and the Rabi frequency of the qubit transition with care so that $P_{|1\rangle} \lesssim 50\%$ to minimize the effect of the thermal distribution of the mode phonon population. Using the Rabi frequency of the qubit transition, which can be measured in a straightforward fashion, the magnitude of the Lamb-Dicke parameter is given by $|\eta_i^p| = |\Omega_i^p|/\sqrt{\bar{n}+1}\Omega_i$. After measuring them for all modes and addressable ions, we fit the magnitudes and the mode frequencies to a simple theoretical model of a linear ion chain and obtain theoretically fitted η_i^p, including their signs. The model includes the Coulomb interaction between ions and individual harmonic confinements for each ion along the direction that is perpendicular to the chain. The inter-ion spacing and the spring constants for the harmonic confinements are the fit parameters. An example of the fitted Lamb-Dicke parameters is shown in Figure 5.5, which shows the quality of the fit is excellent.

For increasingly small η_i^p values, measuring them precisely and accurately becomes difficult, since the BSB Rabi frequencies Ω_i^p are smaller than the frequency resolution of the scan (which is 1.5 kHz), and the measurements become dominated by RF noises of the trap. Therefore, it is more appropriate to use the theoretically fitted Lamb-Dicke parameters for the pulse-shaping calculations.

The mode frequencies used to generate the pulses are reported in Table 5.1.

Mode	$\omega_p/2\pi$ (MHz)
1	2.951
2	2.973
3	2.993
4	3.010
5	3.025
6	3.038
7	3.054

Table 5.1: Mode frequencies of the motional modes of our seven-ion chain.

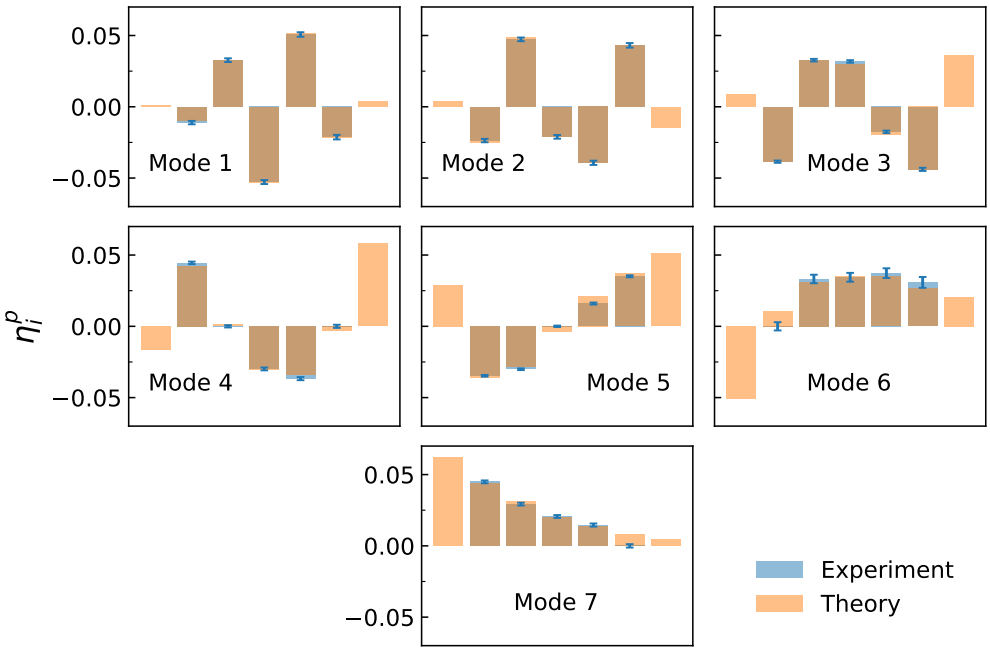

Figure 5.5: Comparison between experimentally extracted Lamb-Dicke parameters and theoretically fitted ones. The signs of the experimentally extracted Lamb-Dicke parameters are forced to be the same as the theoretically predicted ones since we can only extract the magnitude of the Lamb-Dicke parameters using sideband spectroscopy. The blue bars are experimental measurements. The blue error bars are statistical errors propagated through the fitting routines by bootstrap. The error bars do not account for systematic errors such as mode drift, heating and motional decoherence during the measurements. Only the middle five ions are accessible by Raman lasers thus there is not any data for the two ions at the ends of the chain. The orange bars represent the fitted result using the simple theoretical model described below. The modes are indexed in the order of increasing mode frequency, as shown in Tb. 5.1.

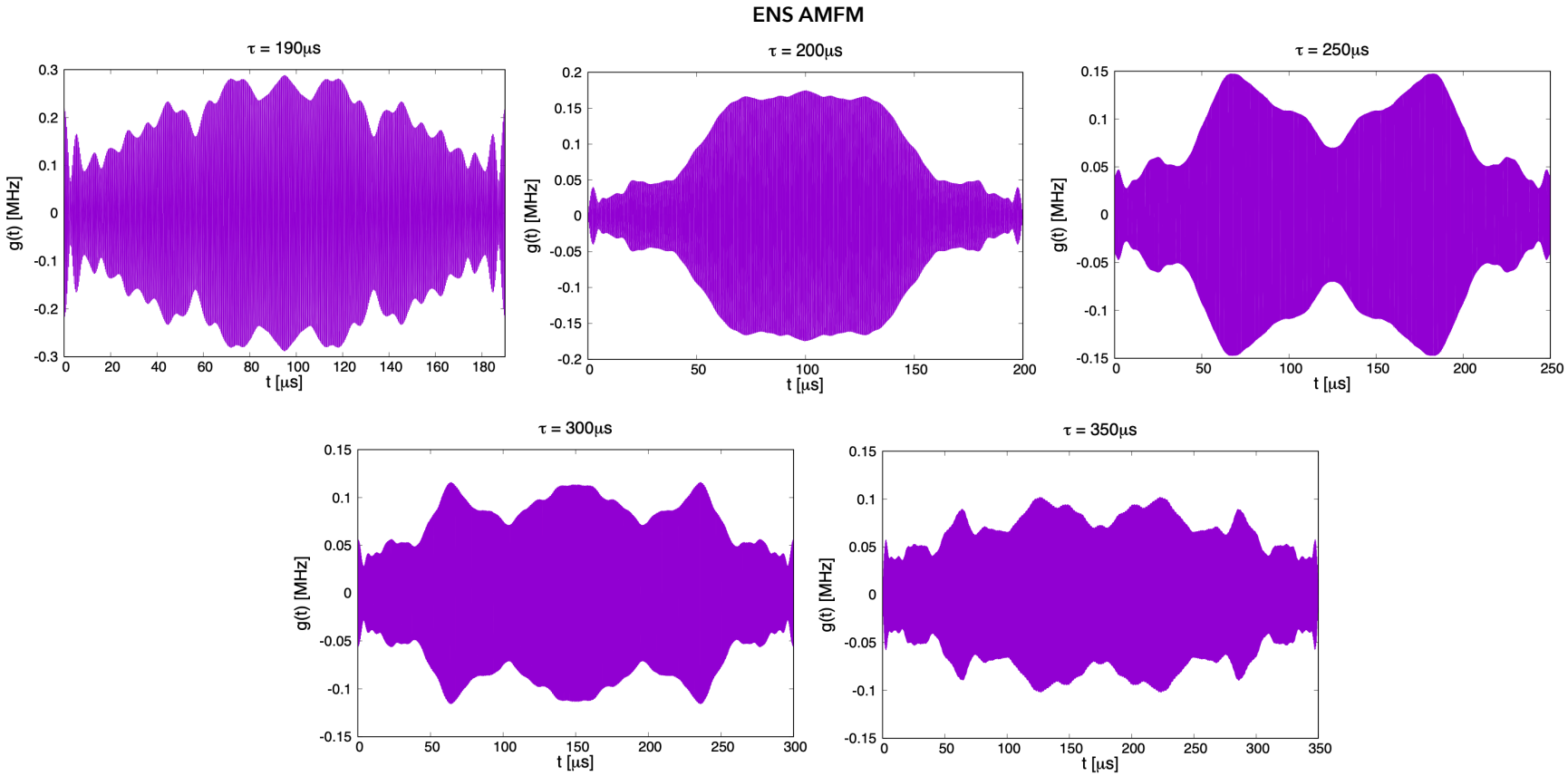

Figure 5.6: Pulse shapes for two-qubit gates on qubits 4, 5 computed according to the extended null-space AMFM protocol.

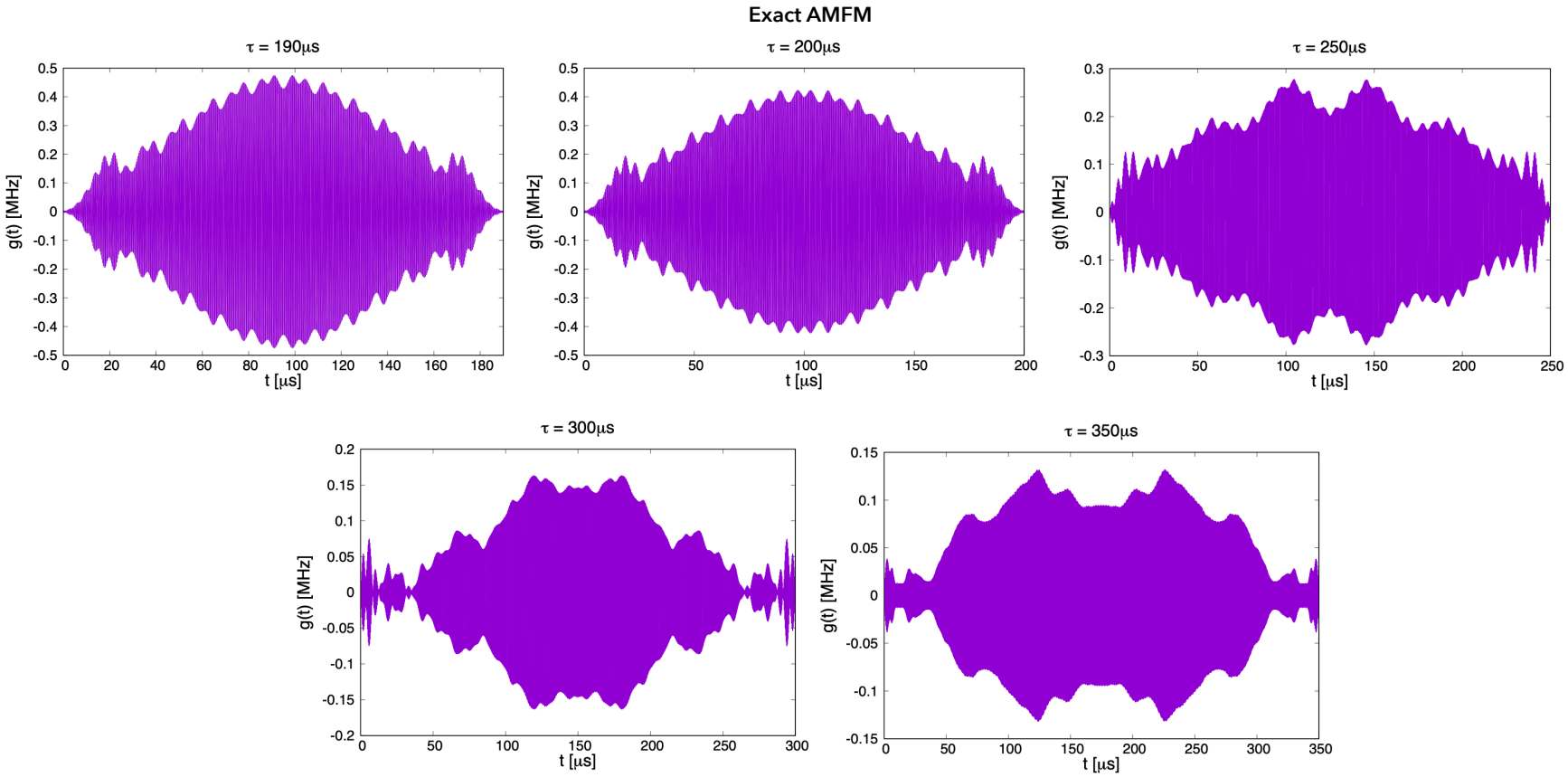

Figure 5.7: Pulse shapes for two-qubit gates on qubits 4, 5 computed according to the exact AMFM protocol.

5.3 Gate Fidelity Limitation

There are several factors that limit the gate fidelity, which we quantify by measuring the state population and parity contrast in our experiment. Assuming that the best efforts are spent to achieve a high fidelity gate in our setup, this means that the individual beams are aligned as well as they can be, sideband cooling are optimized so that $\bar{n} \approx 0.1$, an optimized pulse shape is found with minimal residual spin-motion entanglement, the following are the limiting factors that prevent us to achieve 99.99% fidelity gates in our setup.

The leading factor is the laser intensity fluctuation due to beam misalignment at the ions. The fluctuation in the laser intensity leads to errors in the rotation angles of the gates. As mentioned in Section 3.2, we cannot make a chain of equally spaced ions. However, the individual addressing beams generated by the DOE are equally spaced. This limits our ability to align the beams to the ions. Other sources of misalignment are vibrations affecting the optical table, which we try to minimize to our best ability, and axial micromotion. In principle, there is no micromotion along the trap axis. However, due to defects on the trap blades, we have axial micromotion, which can only be cancelled for one ion in the chain.

Another leading factor for gate infidelity in our experiment is the fluctuation in the motional mode frequency even though the slow drift in the RF amplitude is already stabilized. The cause of the fluctuation is not exactly known but we speculate that it is due to noises in the trap RF. To minimize this effect, we look for a gate solution that is the most robust against such drift. Eventually, to reduce the fluctuation, we need to identify the cause and correct for it. A measurement of motional coherence in our setup shows a relatively short coherence time of 1 ms, which is about four gates. This can contribute to

the fluctuation. To increase the motional coherence time, we need to reduce the noise in the amplifying circuit for the trap RF by using a low-noise RF source and design a better amplifying circuit.

Besides these factors, the gate fidelity is also affected by laser phase stability. While the Raman laser phase is stable because it phase locked to an atomic frequency standard, the optical path length fluctuation causes instability in the laser phase. It is exacerbated by having two counter-propagating beams that travel long distance from the laser head to the trap. In the future, this effect can be minimized by implementing the phase insensitive scheme for the Raman transition [81].

Other factors like heating, off-resonant carrier excitation, spontaneous scattering, etc. make small contributions to the gate infidelity in our experiments. These factors may become more relevant when scaling up the system.

Chapter 6: Towards Fault-Tolerant Quantum Computing

Fault-tolerant logical qubit encoding and fault-tolerant operations are required for executing quantum algorithms of sufficient depth to solve relevant problems [137–139]. Fault-tolerant operations, such as state preparation, syndrome measurement, error correction, logical gates, and measurements are designed such that any physical-level error they introduce is corrected at the logical level [140]. When the physical error rate is below a certain threshold, the logical error can be made arbitrarily small by concatenation, i.e. using multiple layers of encoding [141], or taking advantage of natural robustness within the system [142]. The optimal method for fault-tolerant quantum computation is unknown and current methods offer trade-offs between encoding rate, threshold [143, 144], and the number of available fault-tolerant gates [145–147]. The same is true for near-term quantum error correction where only a limited amount of protection from physical-level errors will be available.

The Shor code [148] protects against all physical single-qubit Pauli errors. While the canonical $[[9, 1, 3]]$ code[1] is based on triple modular redundancy, larger $[[m^2, 1, m]]$

[1] [[n,k,d]] means encoding k logical qubits in n physical qubits with a code distance d

Shor codes can be generated using m-modular redundancy, where m is the number of physical qubits in each module. The Shor code, together with the rotated surface code [149] and the Bacon-Shor subsystem code [150], are examples of compass codes [151]. The surface code has high memory and circuit-level thresholds, and treats phase- and bit-flip errors equivalently [152–154]. The Bacon-Shor code has no asymptotic threshold with m for either X or Z errors [155]. The Shor code on the other hand has a memory threshold of 50% for Z errors and no threshold for X errors as m increases. In practice, this means that, for any physical error rate, there is an optimal size for the Shor and Bacon-Shor codes [155]. These optimal codes can then be concatenated in a modular fashion to further improve performance [156]. Theoretical investigations comparing the 17-qubit rotated surface code [149] to a compass code on a 3×3 qubit lattice find the latter to have much better performance in a realistic ion trap error model [157]. In this chapter, we report our result on the optimal size m of the Shor code implemented in our trapped-ion quantum computer described in Chapter 3 and show how measurements on a few qubits can predict the performance of larger systems. Specifically, we prepare m-qubit GHZ states on our trapped-ion system and extrapolate the logical error rate classically in order to emulate state preparation and measurement of an $[[m^2, 1, m]]$ Shor code, where $m = 3, 4, 5, 6, 7$. This emulation yields the optimal code size for our current system. We then compare the emulated $m = 3$ results to the full 3×3 code state preparation on nine physical qubits.

6.1 The Shor Code

An $[[m^2, 1, m]]$ Shor code uses $m \times m$ physical qubits to encode a single logical qubit with distance m, i.e. any two orthogonal logical states differ by at least m bit- or phase-flips. It is constructed from the concatenation of an m-bit repetition code that corrects X errors with an m-bit repetition code that corrects Z errors [148]. Since all Pauli errors can be described as combinations of Z and X errors, measuring the stabilizers returns one of the potential syndromes, which give the location and type of the physical errors. These can then be remedied by applying suitable X and/or Z correction operations. For the $[[9, 1, 3]]$ Shor code only a single physical error can be diagnosed unambiguously, since it has distance 3.

State preparation starts by fault-tolerantly creating a logical basis state, followed by fault-tolerant logical gates to generate a desired logical state $|\psi\rangle_L$. For an $[[m^2, 1, m]]$ Shor code, the logical basis is given by $|\pm\rangle_L = \underbrace{|\mathrm{GHZ}_m^{\pm}\rangle \otimes |\mathrm{GHZ}_m^{\pm}\rangle \otimes ... \otimes |\mathrm{GHZ}_m^{\pm}\rangle}_{m} = |\mathrm{GHZ}_m^{\pm}\rangle^{\otimes m}$, where $|\mathrm{GHZ}_m^{\pm}\rangle = \frac{1}{\sqrt{2^m}}(|\underbrace{00...0}_{m}\rangle \pm |\underbrace{11...1}_{m}\rangle) = \frac{1}{\sqrt{2^m}}(|0\rangle^{\otimes m} \pm |1\rangle^{\otimes m})$ and $|\psi\rangle^{\otimes m}$ denotes m qubits, each of which is prepared in state $|\psi\rangle$. Since the $|\pm\rangle_L$ are product states of $|\mathrm{GHZ}_m^{\pm}\rangle$, we can prepare and measure many copies of a single $|\mathrm{GHZ}_m^{\pm}\rangle$ and randomly sample from these copies to artificially construct results corresponding to an $m \times m$ logical state. For example, with $m = 3$, the logical states are $|+\rangle_L = \frac{1}{2\sqrt{2}}(|000\rangle + |111\rangle)^{\otimes 3} = \bigotimes_{i=1,2,3} |\mathrm{GHZ}_3^{+}\rangle_i$ and $|-\rangle_L = \frac{1}{2\sqrt{2}}(|000\rangle - |111\rangle)^{\otimes 3} = \bigotimes_{i=1,2,3} |\mathrm{GHZ}_3^{-}\rangle_i$. The circuit for encoding the $|+\rangle_L$ separates into three independent sub-circuits for creating three 3-qubit GHZ states, see Fig. 6.1. This is also the case for state preparation of the Bacon-Shor subsystem code [26]. This up-sampling allows us to study an $m \times m$-qubit Shor code with only m qubits. However,

some physical errors that come with larger system sizes such as cross-talk and others [28] are underestimated.

For a $[[9, 1, 3]]$ Shor code, there are eight stabilizers, six Z stabilizers, which detect X errors, and two X stabilizers, which detect Z errors [157]. Therefore the code is better at detecting X errors than Z errors. To detect a single bit-flip within any GHZ sub-group, we measure the Z stabilizers $Z_j Z_{j+1}$ for the physical qubit index $j = 1, 2, 4, 5, 6, 7$. To detect a single phase-flip error, we measure the X stabilizers $X_1X_2X_3X_4X_5X_6$ and $X_4X_5X_6X_7X_8X_9$. These error detection measurements can be done in a non-destructive way by projecting the parity onto an ancilla qubit and measuring it without disturbing the code qubits [158]. In our experiment we directly perform the projective measurement on the physical qubits and perform the error detection or correction procedure in post-processing. While not realizing a full error correction scheme, we still observe how logical errors scale with the number of physical qubits and gates used for state preparation.

6.2 Scaling of the Shor Code

We use the circuit in Fig. 6.2 to create $|\mathrm{GHZ}_m^{\pm}\rangle$ states using our native gate set. The results of measuring in the Z-basis for $m = 3$ are shown in Fig. 6.3 (a). To measure in the X-basis, we apply $H^{\otimes m}$ before detection which creates an equal superposition of all even- and odd-parity computational states for $|\mathrm{GHZ}_m^{+}\rangle$ and $|\mathrm{GHZ}_m^{-}\rangle$, respectively, i.e. $\langle X^{\otimes m}\rangle = 1$ and -1. The results for $m = 3$ are shown in Fig. 6.3 (b). The probability of measuring the $|\mathrm{GHZ}_m^{\pm}\rangle$ in the Z or X basis, shown in Fig. 6.4 (a), is given by summing the relevant measured state populations, $\mathcal{F}_z = P_{00\ldots0} + P_{11\ldots1}$ and $\mathcal{F}_x^{\pm} = \sum_{s\ \mathrm{even}\atop \mathrm{odd}} P_s$, respectively.

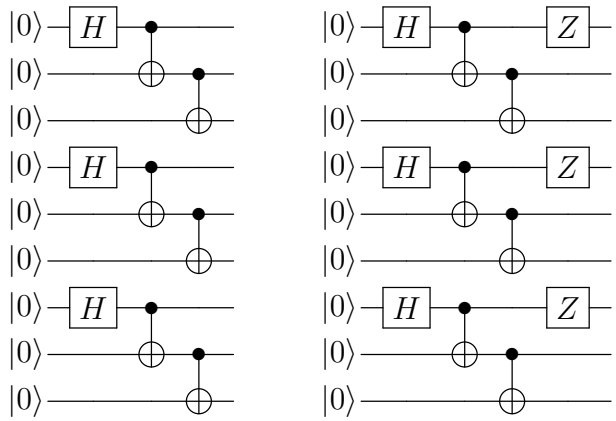

Figure 6.1: Circuits for fault-tolerant preparation of logical states (a) $|+\rangle_L$ and (b) $|-\rangle_L$ of the $[[m^2, 1, m]]$ Shor code for $m = 3$. The circuit separates into m groups, each preparing a $|\mathrm{GHZ}_m^{\pm}\rangle$ state.

.

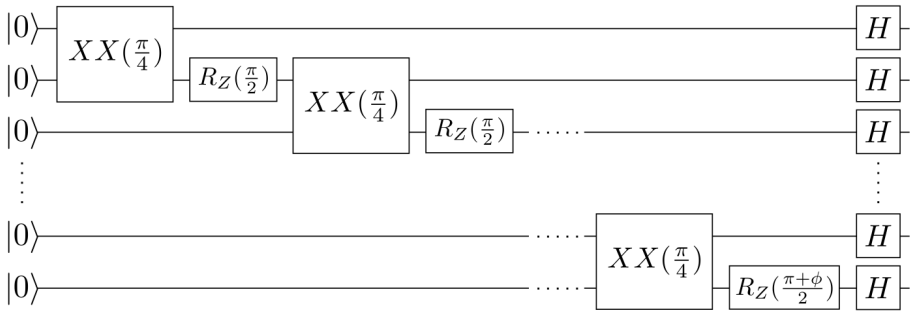

Figure 6.2: The circuit to prepare a $|\mathrm{GHZ}_m^{\pm}\rangle$ on a trapped-ion quantum computer, with $\phi = 0$ for $|\mathrm{GHZ}_m^{+}\rangle$ and $\phi = \pi$ for $|\mathrm{GHZ}_m^{-}\rangle$.

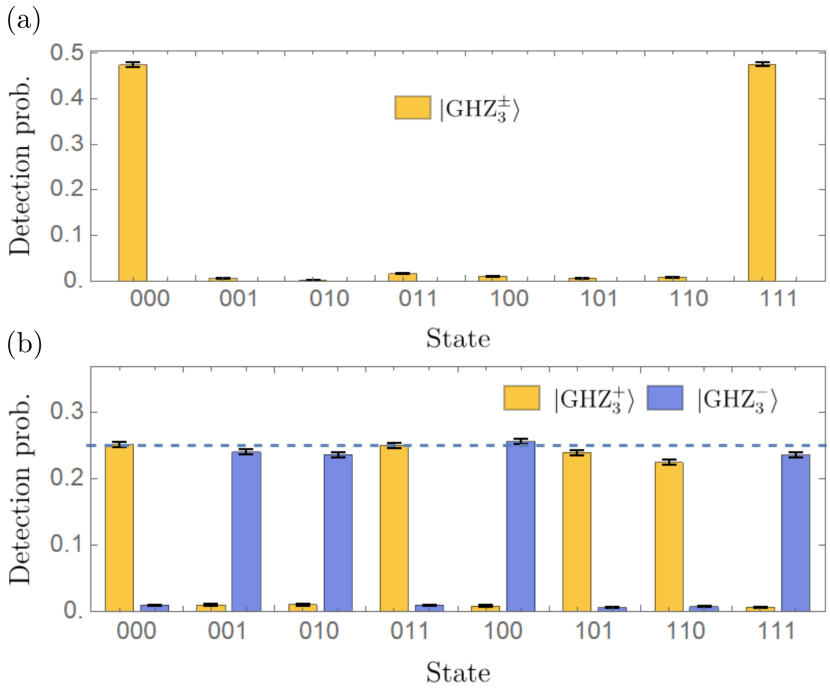

Figure 6.3: Measurement of $|\mathrm{GHZ}_3^{\pm}\rangle$ in the (a) Z basis and (b) X basis. In the Z basis, $\mathrm{GHZ}_3^{\pm}$ have the same measurement outcomes. The dashed line gives the ideal target population of 0.25.

We sample a group of m experimental shots from $|\mathrm{GHZ}_m^{\pm}\rangle$ to construct an artificial shot corresponding to the measurement of an $m \times m$ logical state $|\pm\rangle_L$, which we read out by majority voting. For even m, ties are assigned randomly. Repeating this N/m times, where N is the total number of experimental repetitions, we arrive at the fidelities $\mathcal{F}_L^{\pm}$ for $m = 3, 4, 5, 6, 7$ shown in Fig. 6.4 (b) and Table 6.1.

For large N, the up-sampled logical fidelities are given by

$$\mathcal{F}_L^{\pm} = \sum_{k=(m+1)/2}^{m} \binom{m}{k} (\mathcal{F}_x^{\pm})^k (1 - \mathcal{F}_x^{\pm})^{m-k} \tag{6.1}$$

for odd m, and

$$\mathcal{F}_L^{\pm} = \sum_{k=(m+2)/2}^{m} \binom{m}{k} (\mathcal{F}_x^{\pm})^k (1 - \mathcal{F}_x^{\pm})^{m-k} + \frac{1}{2}\binom{m}{m/2} (\mathcal{F}_x^{\pm})^{m/2} (1 - \mathcal{F}_x^{\pm})^{m/2} \tag{6.2}$$

for even m, due to the random assignment of ties.

Assuming depolarizing errors dominate, the physical qubit fidelity is roughly $f = \mathcal{F}_x^{\pm}/m$ [155] and therefore the logical fidelity is

$$\mathcal{F}_L^{\pm} = \sum_{k=\lceil m/2 \rceil}^{m} \binom{m}{k} (mf)^k (1-mf)^{m-k}. \tag{6.3}$$

Fig. 6.5 plots the dependence of the logical error rate, which is $1 - \mathcal{F}_L^{\pm}$, on the physical error rate, which is $1 - f$, for different code sizes $m = 3, 5, 7, 9$ as in Eq. (6.3). There is a cross-over point in the physical error rate where deeper encoding compensates for the larger number of gate errors that can arise when preparing larger GHZ states. The experimental results presented in Table 6.1 and Fig. 6.4 follow the estimated fidelity given by Eqs. (6.1) and (6.2).

Although the fidelity to prepare five-qubit GHZ states is lower than that of the three-qubit GHZ states, the up-sampled logical states for the $[[25, 1, 5]]$ code has a higher fidelity than that for the up-sampled $[[9, 1, 3]]$ code after majority voting. This hints at the onset of fault-tolerance, since it demonstrates that deeper encoding can compensate for the increase in physical errors caused by employing more qubits and gates, leading to a lower logical error than a shallower code. This increase is not replicated when going to $[[49, 1, 7]]$, which shows that the state preparation errors have increased substantially as seen in the drop in the fidelity of $\mathrm{GHZ}_7^{\pm}$ (Fig. 6.4). The random assignment of ties leads to a lower probability for $m = 4, 6$ in Fig. 6.4 (b).

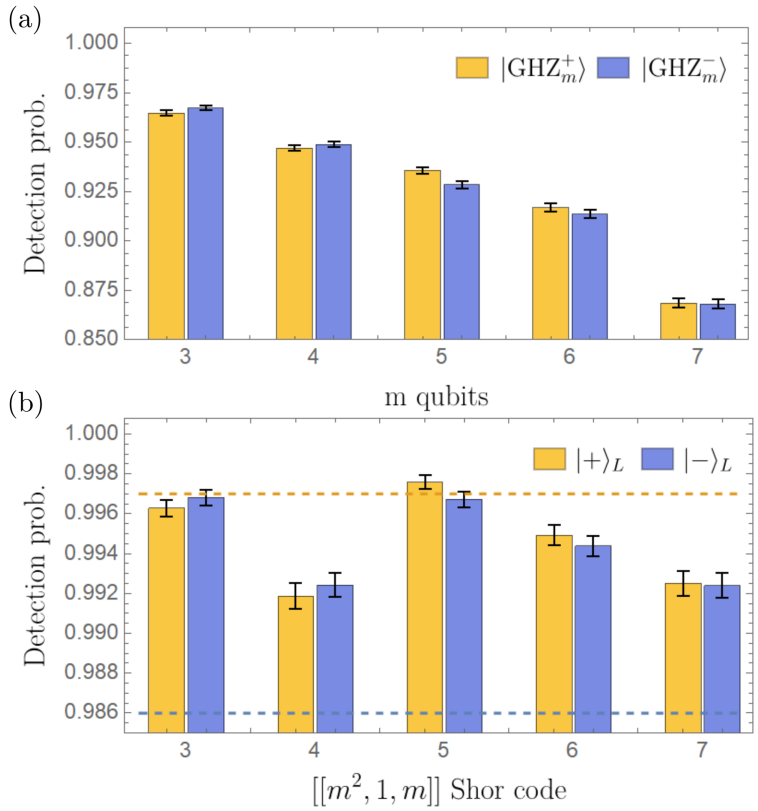

Figure 6.4: (a) $|\mathrm{GHZ}_m^{\pm}\rangle$ fidelity measured on m trapped-ion qubits. (b) Up-sampled logical state fidelity of $[[m^2, 1, m]]$ Shor codes after majority voting. For even m, ties are assigned randomly, hence the drop in state fidelity after majority voting. The dashed yellow (blue) line is the state preparation and measurement fidelity for state $|+\rangle$ ($|-\rangle$) of the physical qubit. Note that the vertical ranges for (a) and (b) are different. The increase in logical fidelity from $m = 3$ to $m = 5$ shows how deeper encoding can offer increased protection against physical errors. This advantage does not carry over to $m = 7$ due to increase in the number of gates and gate errors for larger m.

Table 6.1: Fidelity of state preparation and measurement for $|\mathrm{GHZ}_m^{\pm}\rangle$ (Measure) and logical states of $[[m^2, 1, m]]$ Shor codes constructed by up-sampling with majority voting (Majority vote). Data are taken with $N = 20000$ shots. The uncertainty is given by the standard deviation of the binomial distribution $\sqrt{\mathcal{F}(1-\mathcal{F})/N}$.

m	Prep.	Z Meas.	X Meas.		Majority vote	
		$\mathcal{F}_z$	$\mathcal{F}_x^+$	$\mathcal{F}_x^-$	$\mathcal{F}_L^+$	$\mathcal{F}_L^-$
3	+	0.951(1)	0.965(1)	0.035(1)	0.9963(4)	0.0037(1)
	−		0.033(1)	0.967(1)	0.0032(1)	0.9968(4)
4	+	0.917(2)	0.947(2)	0.053(1)	0.9919(6)	0.0081(1)
	−		0.051(1)	0.949(2)	0.0076(1)	0.9924(6)
5	+	0.882(2)	0.936(2)	0.064(1)	0.9976(3)	0.0024(1)
	−		0.072(1)	0.928(2)	0.0033(1)	0.9967(4)
6	+	0.806(2)	0.917(2)	0.083(1)	0.9949(5)	0.0051(1)
	−		0.086(1)	0.914(2)	0.0056(1)	0.9944(5)
7	+	0.723(2)	0.869(2)	0.131(1)	0.9925(6)	0.0075(1)
	−		0.132(1)	0.868(2)	0.0076(1)	0.9924(6)

.

The additional errors in the logical state preparation and measurement (SPAM) process mainly come from an increase in single- and two-qubit gate errors for longer ion chains, and read-out errors because of cross-talk between photo-multiplier tube channels, i.e. physical SPAM errors. Physical readout cross-talk accounts for $1 - 5\%$ infidelity in the Z -measurements, depending on m. The rest is from two-qubit gates, which corresponds to

Table 6.2: Fidelity of logical states of $[[m^2, 1, m]]$ after discarding non-unanimous results (Error detect) and the success probability (Yield). Data are taken with $N = 20000$ shots.

m	Prepare	Error detect		Yield
		+	−	
3	+	0.99995(1)	0.00005(1)	0.898(4)
	−	0.00003(1)	0.99997(1)	0.905(4)
4	+	0.99999(1)	0.00001(1)	0.804(6)
	−	0.000009(1)	0.999991(1)	0.810(6)
5	+	0.999998(1)	0.000002(1)	0.717(3)
	−	0.000003(1)	0.999997(1)	0.690(4)
6	+	0.9999996(2)	0.0000004(1)	0.594(5)
	−	0.0000010(1)	0.9999990(1)	0.581(5)
7	+	0.999997(1)	0.000003(1)	0.373(6)
	−	0.000002(1)	0.999998(1)	0.371(6)

an average of 0.9% error per gate for $m = 3$, 1.3% for $m = 4$, 1.6% for $m = 5$, 1.7% for $m = 6$ and 2.2% for $m = 7$. These errors come from the increased beam mismatch.

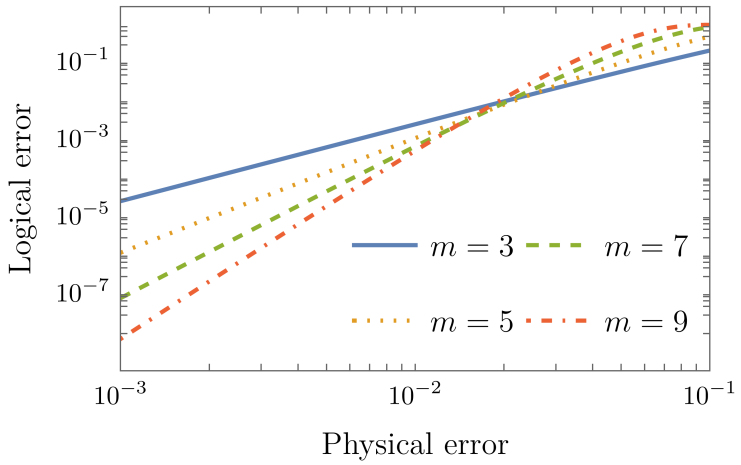

Figure 6.5: Scaling of the $[[m^2, 1, m]]$ Shor code given by a depolarizing error model, Eq. (6.3).

The fidelity for both single- and two-qubit gates is mainly limited by beam misalignment, beam-pointing instabilities, imperfect Stark-shift compensation and axial micromotion for all but the center ion. In our setup, we do not have the ability to apply a quartic axial potential in order to space the ions equally. As a result, the alignment of the equally-spaced individual addressing beams worsens for larger numbers of ions in the trap. We mitigate this effect to some degree by using up to two additional ions at the each end of the chain. For five qubits, we trap seven ions; for seven qubits, we trap nine ions; for nine qubits, we trap thirteen ions. Trap imperfections also cause an unwanted axial radio-frequency (RF) field component that leads to axial micromotion. Therefore, in our setup, the single-qubit and two-qubit gate fidelities tend to decrease with the number of ions. The average fidelity for single-qubit gates (except R_z) in our experiment is 99.0(5)% after correcting for state-preparation-and-measurement (SPAM) error. Typical fidelities for two-qubit gates are 99% for a five-qubit system, 98.5% for a seven-qubit system and

98% for a nine-qubit system.

The Shor code can also be used as an error detection code, where non-unanimous votes are discarded rather than corrected, which leads to a finite yield. The fidelity and yield of the logical states after this procedure are presented in Table 6.2. The fidelities are higher than for the correction scheme since all m qubits have to flip for a logical error to occur. For large N, the yield can be estimated by $(\mathcal{F}_x^{\pm})^m + (1-\mathcal{F}_x^{\pm})^m$. The optimal code size has increased to 6, which is a valid size since ties don't play a role in the detection code.

Using Eq. (6.1) we can estimate the minimal $|\mathrm{GHZ}_m^{\pm}\rangle$ fidelities needed in order for the up-sampled $m \times m$-qubit logical state to have the same fidelity as that of the 3×3-qubit logical state. For $m = 5$, it is 0.93; for $m = 7$ qubits, it is 0.895, which translates to an average infidelity of 1.7% per two-qubit gate.

6.3 Experimental Encoding of a Logical Qubit with 13 Ions

We also perform the full $[[9, 1, 3]]$ encoding with nine qubits in a 13-ion chain. In this experiment we directly generate and read out logical states $|\pm\rangle_L$ of the $[[9, 1, 3]]$ Shor code. We also characterize the individual $|\mathrm{GHZ}_3^{\pm}\rangle$ states with measurements in the X-basis. The results are presented in Table 6.3 and Fig. 6.6.

The fidelity of the logical states $|\pm\rangle_L$ is at the level of the physical state $|-\rangle$ and hence falls short of the average performance of the physical qubit $|\pm\rangle$. Using Eq. (6.1), we estimate that the fidelity of each $|\mathrm{GHZ}_3^{+}\rangle$ state must be increased to 0.968 in order to achieve the same logical fidelity as our physical qubit $|+\rangle$. It is worth noting that the

fidelities of the $|\mathrm{GHZ}_3^{\pm}\rangle$ triplet on nine qubits are very similar to each other. This indicates a high level of uniformity among the qubits and gates.

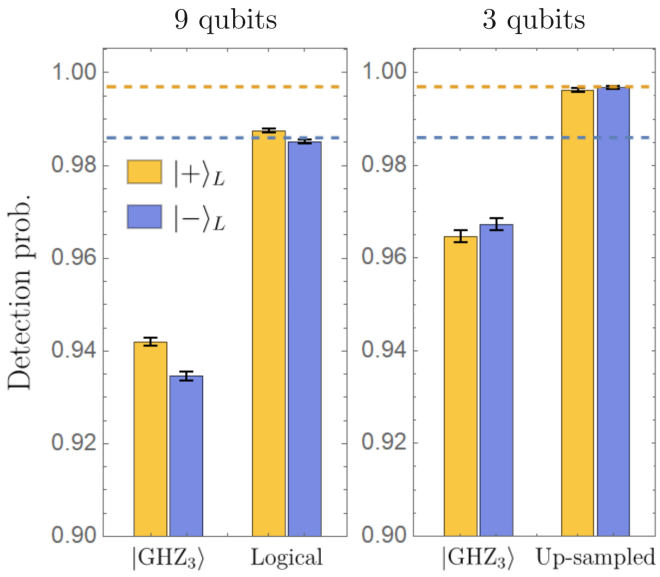

Figure 6.6: A full $[[9, 1, 3]]$ Shor code logical state measurement with nine trapped-ion qubits (Left). We also show the average fidelity of the $|\mathrm{GHZ}_3^{\pm}\rangle$ states. For comparison, we show again the up-sampled results with three qubits from Fig. 6.4 (Right). The dashed yellow (blue) line is the state preparation and measurement fidelity for state $|+\rangle$ ($|-\rangle$) of the physical qubit.

Notice that the fidelities of both the $|\mathrm{GHZ}_3^{\pm}\rangle$ states and logical $|\pm\rangle_L$ states are lower than their corresponding counterparts in the up-sampled experiment with three qubits in a chain of seven ions (see Fig. 6.4). The additional errors reduce the fidelity compared to the up-sampled version by about 1%.

Table 6.3: Fidelity of state preparation and measurement for three sets of $|\mathrm{GHZ}_3^{\pm}\rangle$ labeled as $1, 2, 3$ and the logical state $|\pm\rangle_L$ of [[9,1,3]]] code on a thirteen-ion chain.

	Prepare	Measure	
		+	−
Logical	+	0.988(1)	0.012(1)
	−	0.015(1)	0.985(1)
$\|\mathrm{GHZ}_3^{\pm}\rangle_1$	+	0.942(1)	0.058(1)
	−	0.050(1)	0.950(1)
$\|\mathrm{GHZ}_3^{\pm}\rangle_2$	+	0.942(1)	0.058(1)
	−	0.079(1)	0.921(1)
$\|\mathrm{GHZ}_3^{\pm}\rangle_3$	+	0.942(1)	0.058(1)
	−	0.068(1)	0.932(1)

6.4 Discussion

Our preparation and sampling of $|\mathrm{GHZ}_m^{\pm}\rangle$ states to synthetically construct $m \times m$ logical Shor code states shows experimentally that deeper encoding can compensate for additional physical errors from logical state preparation. For our specific setup, the $|\mathrm{GHZ}_5^{\pm}\rangle$ state projects the best logical fidelities. The increase in physical errors with larger m we observe is due to hardware limitations, most of which can be solved by better engineering. For example, detection cross-talk can be eliminated by independent photon-detectors [26, 159, 160]. The beam-ion alignment can be improved by traps with more control electrodes, such

as micro-fabricated surface traps [161] or blade traps with more segments [162]. Alternatively, near-perfect ion addressing can be achieved with integrated optics [163,164] or beam steering using a micro-electro-mechanical system of mirrors [165]. Axial RF stray fields, and hence axial micromotion is also greatly reduced in precision-fabricated surface or 3D traps [166, 167].

The comparison of the emulated 9-qubit Shor state to a direct preparation of the 9-qubit Shor code states shows a 2% decrease in the fidelity of individual $|\mathrm{GHZ}_m^{\pm}\rangle$ states and a 1% decrease in the SPAM logical fidelity. This result points toward future work where parts of quantum error corrected codes can be used as benchmarks for system scalability and uniformity. Recent work has emphasized that physical errors are not uniform over the Pauli operators [151, 168–170]. Although the $m \times m$ Shor code has no threshold for one type of Pauli error, it matches the classical threshold for the other Pauli error. This makes the Shor code an exciting choice for quantum memories with asymmetric errors. Further work on asymmetric Shor codes and how they interact with bias-preserving gates is warranted [171].

Chapter 7: Digital Simulation of the Schwinger Model

An exciting prospect for quantum computers is the simulation of complex physical systems [5, 172]. Digital quantum computers can simulate a wide range of physical Hamiltonians since one can often find efficient circuit decompositions to approximate their dynamics. However, the number of qubits and the achievable circuit depth in experiments are limited. In particular, it is challenging to simulate larger systems for longer time while maintaining the fidelity of the simulations. To address this challenge, there has been substantial theoretical research on finding optimal simulation algorithms with improved theoretical error bounds [173–180] and better empirical performance [181, 182], as well as efficient circuit decomposition with resource analysis for a range of problems [138, 182–197]. Furthermore, symmetry-protection schemes have emerged to suppress algorithmic and experimental errors [198–205], along with noise-mitigation schemes for extrapolating to the noiseless limit of observables [206–214]. As a result, it is of great interest to study how well these recent algorithmic advances, which mostly concern asymptotic regimes with a large number of qubits and long evolution times, apply in a current experiment. The data presented in this chapter is also published in [68].

7.1 The Lattice Schwinger Model

The physical system we consider is a low-dimensional lattice gauge theory. Gauge field theories are the underlying formalism describing interactions among elementary particles in the Standard Model, and are prime candidates for modeling physics beyond the Standard Model. They further provide a powerful theoretical framework for describing low-energy excitations in condensed-matter systems. There has been tremendous progress in applying non-perturbative methods to solve lattice gauge theories in various systems and coupling regimes [215–220]. However, evaluating the real-time dynamics of gauge field theories remains challenging in the strong-coupling regime, where a notorious sign problem halts Monte-Carlo-based classical simulations [221]. Both fermionic and bosonic degrees of freedom in gauge theories, when defined on a discretized spacetime, can be mapped to spins and, in principle, efficiently simulated using quantum simulators. A simple Abelian low-dimensional gauge theory is quantum electrodynamics in 1+1 dimensions, or the Schwinger model [222]. It exhibits non-trivial dynamics similar to those seen in quantum chromodynamics in 3+1 dimensions, i.e., the theory of the strong force in nature, including particle-antiparticle pair creation, chiral symmetry breaking, confinement, and a non-trivial θ-vacuum [223, 224]. The Hamiltonian formulation of the lattice Schwinger model, i.e., the Schwinger model defined in a discretized space and with continuous time, has served as a testbed for numerous computational techniques in recent years, including quantum simulation and computation. In particular, there have been several theoretical proposals for analog quantum simulation [225–231] and gate-based quantum algorithms [191,193,232–239] of the Schwinger model, along with experimental implementations on various quantum platforms

such as trapped ions [56, 67], Rydberg atoms [229, 240], ultracold atoms [241, 242], and superconducting qubits [233, 243].

Inspired by the first digital simulation of the Schwinger model in Ref. [67], we revisit the simulation to answer the following questions: i) Are larger and longer simulations of lattice gauge theories viable on present hardware? ii) Given recent progress in quantifying the theoretical and empirical bounds on simulation algorithms, what are the resource requirements of simulating the lattice Schwinger model in the purely fermionic formulation with long-range interactions versus the fermion-boson formulation with only local interactions? iii) What are the theoretical considerations in decomposing the time evolution operator using product formulas, e.g., how does the Trotter error depend on the ordering of terms in each Trotter step of the evolution, what order of the product formula should one use, and how small should the Trotter steps be, considering the anticipated size of the experimental error? iv) Can recent cost-efficient symmetry protection protocols provide insights into the nature of experimental errors?

To address these questions, we realize experimentally the time dynamics of the lattice Schwinger model in its staggered formulation [244], and within its purely fermionic representation, for two-, four-, and six-site theories. Along with the experimental demonstration, different term orderings and product formulas are studied, and the gate complexity of the algorithm used here is compared with another algorithm in the local formulation of the same theory [191]. The symmetry protection of Ref. [198] is implemented for the first time in experiment, in addition to a simple symmetry-inspired post-selection.

In the staggered formulation of the lattice Schwinger model introduced by Kogut and Susskind [244], the two-component matter field at one spatial site is split into two

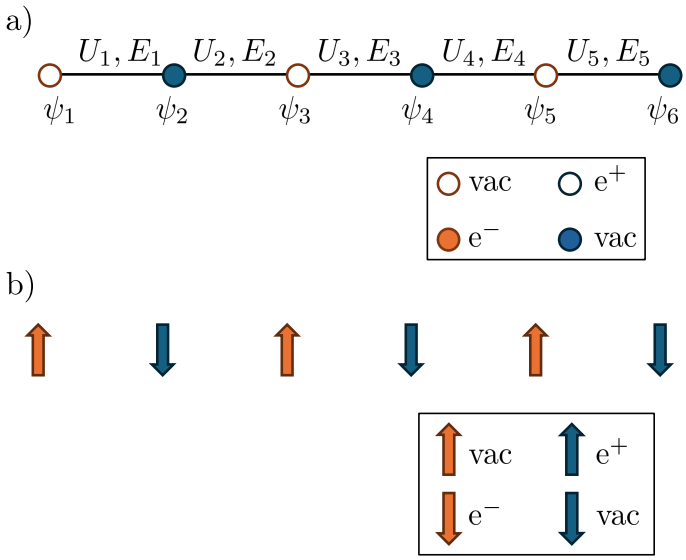

Figure 7.1: (a) Illustration of the staggered formulation of the Schwinger model on a one-dimensional lattice where the fermions (electrons) are at the odd sites, the anti-fermions (positrons) are at the even sites and the vector bosons (electric fields) are the links between sites. (b) The lattice Schwinger model after the fermions and anti-fermions are mapped to spins. The bosons are not shown since they can be rewritten in terms of the long-range interaction between fermions and anti-fermions using Gauss's laws.

one-component fields, $\hat{\psi}$, each occupying one site of the staggered lattice. This staggering corresponds to placing electrons at odd sites and positrons at even sites. The electric field, $\hat{E}$, and the corresponding gauge-link variable, $\hat{U}$, are defined on the link connecting the two adjacent staggered sites. The Hamiltonian in natural units is:

$$\hat{H}_{\mathrm{KS}} = \frac{i}{2a}\sum_{n=1}^{N-1}(\hat{\psi}_n^\dagger \hat{U}_n \hat{\psi}_{n+1} - \mathrm{H.c.}) + \frac{g^2 a}{2}\sum_{n=1}^{N-1}\hat{E}_n^2 + \frac{m}{2}\sum_{n=1}^{N}(-1)^n \hat{\psi}_n^\dagger \hat{\psi}_n, \qquad (7.1)$$

where N is the number of staggered sites, m is the mass of the fermions, a denotes the lattice spacing, and g is the coupling constant. The first term in the Hamiltonian involves gauge-boson-assisted fermionic hopping between nearest-neighbor sites. The second term

is the energy stored in the electric field. The last term represents the rest mass of the fermions in the staggered formulation. The theory exhibits a local gauge symmetry, which leads to a Gauss's law constraint on the allowed physical states $|\phi\rangle_{\text{phys}}$. This constraint enforces the net electric field at each site to be balanced by the electric charge present at the site, i.e., $\hat{G}_n |\phi\rangle_{\text{phys}} = 0$ with $\hat{G}_n = \hat{E}_n - \hat{E}_{n-1} - \hat{\psi}_n^\dagger \hat{\psi}_n + \frac{\mathbb{1}}{2}[1-(-1)^n]$ for all n.

The matter-field operators in Eq. (7.1) can be mapped to spin operators by the Jordan-Wigner transformation: $\hat{\psi}_n = \prod_{l<n}(i\hat{\sigma}_l^z)\hat{\sigma}_n^-$ and $\hat{\psi}_n^\dagger = \prod_{l<n}(-i\hat{\sigma}_l^z)\hat{\sigma}_n^+$, with $\hat{\sigma}_n^\pm = \frac{1}{2}(\hat{\sigma}_n^x \pm i\hat{\sigma}_n^y)$. With open boundary conditions (OBCs), the gauge links and the electric fields can be eliminated upon a gauge transformation and the application of Gauss's law [245]. Without loss of generality, the electric field coming into the lattice is set to zero, and the resulting spin Hamiltonian reads[1]

$$\begin{aligned}\hat{H} &= x\sum_{n=1}^{N-1}(\hat{\sigma}_n^x\hat{\sigma}_{n+1}^x + \hat{\sigma}_n^y\hat{\sigma}_{n+1}^y) + \frac{1}{4}\sum_{n=1}^{N-1}\left[\sum_{m=1}^{n}\left(\hat{\sigma}_m^z + (-1)^m \times \mathbb{1}_2\right)\right]^2 + \mu\sum_{n=1}^{N}(-1)^n\frac{\hat{\sigma}_n^z + \mathbb{1}_2}{2} \\ &\equiv \hat{H}^x + \hat{H}^{zz} + \hat{H}^z + \text{const.}\end{aligned} \tag{7.2}$$

Here, the original Hamiltonian is rescaled by $\frac{2}{ag^2}$, i.e., $\hat{H} = \frac{2}{ag^2}\hat{H}_{\text{KS}}$, so that $\hat{H}$ in Eq. (7.2) is dimensionless with parameters $x = \frac{1}{g^2a^2}$ and $\mu = \frac{2m}{ag^2}$. $\hat{H}^x$ denotes the term proportional to the coupling x, $\hat{H}^{zz}$ consists of (nearly) all-to-all spin-spin interactions proportional to $\hat{\sigma}_n^z\hat{\sigma}_m^z$, and $\hat{H}^z$ is the sum of the terms proportional to $\hat{\sigma}_n^z$. The constant terms are ignored in the following as they do not affect the evolution. By convention, $\hat{\sigma}^z|0\rangle = |0\rangle, \hat{\sigma}^z|1\rangle = -|1\rangle$, and the presence of a particle (antiparticle) is encoded as $|1\rangle$ ($|0\rangle$) at an odd (even) site. Therefore, for an N-site system, the bare-vacuum state, i.e., the ground state of the theory in the $x = 0$ limit, is $|\psi_0\rangle \equiv (|01\rangle)^{\otimes N/2}$.

[1] $\mathbb{1}_2$ is the 2×2 identity matrix.

The goal is to study the real-time dynamics of bare-vacuum fluctuations and particle-antiparticle pair creation. One can therefore perform a quench experiment where the simulation is initiated in the bare-vacuum state, $|\psi(0)\rangle = |\psi_0\rangle$, which is then evolved via the Hamiltonian in Eq. (7.2) with $x \neq 0$. The survival probability of the bare-vacuum state is

$$P_{\text{vac}}(t) = |\langle\psi(0)|\psi(t)\rangle|^2 = \left|\langle\psi(0)|\, \mathrm{e}^{-it\hat{H}}\, |\psi(0)\rangle\right|^2, \tag{7.3}$$

and the particle-number density is $\nu(t) = \frac{1}{N}\sum_{n=1}^{N} \nu_n(t)$ with

$$\nu_n(t) = \langle\psi(t)|\frac{(-1)^n\hat{\sigma}_n^z + \mathbb{1}_2}{2}|\psi(t)\rangle. \tag{7.4}$$

In the limit of $N \to \infty$, the two quantities are related to each other via $\nu(t) = -\frac{1}{N}\log(P_{\text{vac}})$ [222]. The local charge density is defined as

$$Q_n(t) \equiv \langle\psi(t)|\frac{\hat{\sigma}_n^z + (-1)^n \times \mathbb{1}_2}{2}|\psi(t)\rangle \tag{7.5}$$

$$= \langle\psi(t)|\hat{E}_n - \hat{E}_{n-1}|\psi(t)\rangle, \tag{7.6}$$

where the particle's (antiparticle's) charge is -1 (1). The local charge density is related to the local particle-number density by $Q_n(t) = (-1)^n\nu_n(t)$. As there is no interaction in the Hamiltonian that changes the total net charge of the system, $\sum_n Q_n$ is conserved. Therefore, the model has a global symmetry operator $\hat{S}_z = \sum_n \hat{\sigma}_n^z$, which is consistent with the symmetry of an XXZ Heisenberg spin Hamiltonian.

7.2 The Simulation Algorithm

To perform the unitary evolution $\hat{\mathcal{U}}(t) = \mathrm{e}^{-it\hat{H}}$ with $\hat{H} \equiv \sum_{k=1}^{K} \hat{h}_k$ on a quantum computer, with non-commuting Hamiltonian terms $\hat{h}_k$, the evolution can be broken into r smaller

time steps of size $\delta t = t/r$. For each time step, the unitary $\hat{\mathcal{U}}(\delta t)$ is approximated by a product formula, which can then be implemented in terms of the available native gates. For the first-order product formula,

$$\hat{\mathcal{S}}_1(\delta t) = \prod_{k=1}^{K} \mathrm{e}^{-i\delta t\, \hat{h}_k}, \tag{7.7}$$

while for the second-order product formula,

$$\hat{\mathcal{S}}_2(\delta t) = \prod_{k=1}^{K} \mathrm{e}^{-i\frac{\delta t}{2}\hat{h}_k} \prod_{k=K}^{1} \mathrm{e}^{-i\frac{\delta t}{2}\hat{h}_k}, \tag{7.8}$$

where the second product is realized in reversed order. Higher-order formulas $\hat{\mathcal{S}}_p(\delta t)$ can also be constructed recursively for even integers p [246].

While it is generally difficult to obtain an exact estimate for the Trotter error in the pth-order product formula, progress in recent years has resulted in tighter error bounds for them. For example, a nearly optimal bound is derived in Ref. [173], expressed in terms of the nested commutators between different $\hat{h}_k$ terms. For the error of the second-order formula:

$$\begin{aligned}\left\|\hat{\mathcal{U}}(\delta t) - \hat{\mathcal{S}}_2(\delta t)\right\| \leq \frac{(\delta t)^3}{24} \sum_{k_1=1}^{K-1} \left\| \left[\hat{h}_{k_1}, \left[\hat{h}_{k_1}, \sum_{k_2=k_1+1}^{K} \hat{h}_{k_2}\right]\right]\right\| + \\ \frac{(\delta t)^3}{12} \sum_{k_1=1}^{K-1} \left\| \left[\sum_{k_3=k_1+1}^{K} \hat{h}_{k_3}, \left[\sum_{k_2=k_1+1}^{K} \hat{h}_{k_2}, \hat{h}_{k_1}\right]\right]\right\|.\end{aligned} \tag{7.9}$$

The norms of non-vanishing nested commutators can be further upper-bounded using the triangle inequality $\|[A, B]\| \leq 2\,\|A\|\,\|B\|$, resulting in closed-form, albeit looser, error bounds. Based on this approach, an upper bound for the pth-order formulas in simulating a two-body Hamiltonian can be obtained,

$$\left\|\hat{\mathcal{U}}(\delta t) - \hat{\mathcal{S}}_p(\delta t)\right\| \leq \kappa_p \gamma \lambda^p (\delta t)^{p+1}, \tag{7.10}$$

where $\kappa_p = (4 \times 5^{p/2-1})^{p+1}$ is a constant, λ is the maximum strength of the sum of the interactions that involve any particular site, and $\gamma = \sum_{k=1}^{K-1} \|\hat{h}_k\|$. Since γ only involves the first $K-1$ terms of the Hamiltonian, labeling the index k such that $\hat{h}_K$ is the term with the largest norm typically results in the smallest error bound.

Given a small δt, a higher-order formula results in a smaller simulation error. However, since the gate count of $\hat{\mathcal{S}}_p(\delta t)$ scales as $\mathcal{O}\left(5^{p/2}\right)$, increasing p increases the gate complexity of the simulation exponentially. The optimal choice for p is a balance between the gate depth, the evolution time t, and the error tolerance of the simulation. Since the experimental error can dominate the Trotter error at long evolution times, the first-order product formula, which minimizes the gate count per Trotter step, turns out to be a more suitable choice for the experiment in this work.

7.2.1 Term Ordering

Generally, the Hamiltonian terms in Eq. (7.2) do not commute. Therefore, one needs to find the optimal ordering in the application of the product formula to minimize the Trotter error. There are two typical orderings of the terms in a nearest-neighbor Heisenberg spin model. The odd-even ordering is defined as having the odd-leading two-spin terms, e.g., $\hat{\sigma}^{\tau}_{2k-1}\hat{\sigma}^{\tau}_{2k}$ with $\tau = X, Y, Z$ and $1 \leq k \in \mathbb{Z}$, applied first, then applying the even-leading two-spin terms, e.g., $\hat{\sigma}^{\tau}_{2k}\hat{\sigma}^{\tau}_{2k+1}$, followed by the single-body terms (if any). In the XYZ ordering, the terms involving $\hat{\sigma}^{x}$ are applied first, followed by the terms involving $\hat{\sigma}^{y}$, and finally those involving $\hat{\sigma}^{z}$. It is known that the odd-even ordering introduces less Trotter error than the XYZ ordering [181]. Here, we investigate whether the odd-even ordering is also

a better choice for simulating the Schwinger model, which includes both nearest-neighbor and (nearly) all-to-all spin-spin interactions.

Since $\hat{H}^x$ in the Hamiltonian in Eq. (7.2) includes only nearest-neighbor interactions, one way to define an odd-even-ordered product formula is to apply the odd-even ordering to terms in $\hat{H}^x$ only. Defining $\hat{H}^x_{n,m}$ to be the term in $\hat{H}^x$ acting on sites n and m, and, similarly, $\hat{H}^{zz}_{n,m}$ to be the term in $\hat{H}^{zz}$ acting on sites n and m, this ordering can be written as:

$$\hat{\mathcal{S}}_1^{\mathrm{oe1}}(\delta t) = \mathrm{e}^{-i\delta t\,\hat{H}^z}\mathrm{e}^{-i\delta t\,\hat{H}^{zz}} \times \prod_{k=1}^{(N/2)-1} \mathrm{e}^{-i\delta t\,\hat{H}^x_{2k,2k+1}} \prod_{k=1}^{N/2} \mathrm{e}^{-i\delta t\,\hat{H}^x_{2k-1,2k}}. \tag{7.11}$$

Alternatively, the odd-even ordering can be applied to both $\hat{H}^x$ and the nearest-neighbor terms in $\hat{H}^{zz}$, followed by the application of the non-nearest neighbor terms in $\hat{H}^{zz}$ as well as $\hat{H}^z$,

$$\begin{aligned}\hat{\mathcal{S}}_1^{\mathrm{oe2}}(\delta t) = \mathrm{e}^{-i\delta t\,\hat{H}^z} &\prod_{n=1}^{N-1}\prod_{m=1}^{n-2} \mathrm{e}^{-i\delta t\,\hat{H}^{zz}_{m,n}} \\ &\times \prod_{k=1}^{(N/2)-1} \mathrm{e}^{-i\delta t\,\hat{H}^{zz}_{2k,2k+1}}\mathrm{e}^{-i\delta t\,\hat{H}^x_{2k,2k+1}} \\ &\times \prod_{k=1}^{N/2} \mathrm{e}^{-i\delta t\,\hat{H}^{zz}_{2k-1,2k}}\mathrm{e}^{-i\delta t\,\hat{H}^x_{2k-1,2k}}.\end{aligned} \tag{7.12}$$

The two odd-even-ordered evolution operators are related by a rotation around the Z-axis:

$$\hat{\mathcal{S}}_1^{\mathrm{oe1}} = \left(\prod_{k=1}^{N/2} \mathrm{e}^{-i\delta t\,\hat{H}^{zz}_{2k-1,2k}}\right)\hat{\mathcal{S}}_1^{\mathrm{oe2}}\left(\prod_{k=1}^{N/2} \mathrm{e}^{i\delta t\,\hat{H}^{zz}_{2k-1,2k}}\right). \tag{7.13}$$

As a result, if the state is initialized and measured in the Z-basis, one arrives at the same measurement outcome using either scheme. Therefore, in the following we will only consider $\hat{\mathcal{S}}_1^{\mathrm{oe1}}$ because it requires implementing fewer single-qubit gates.

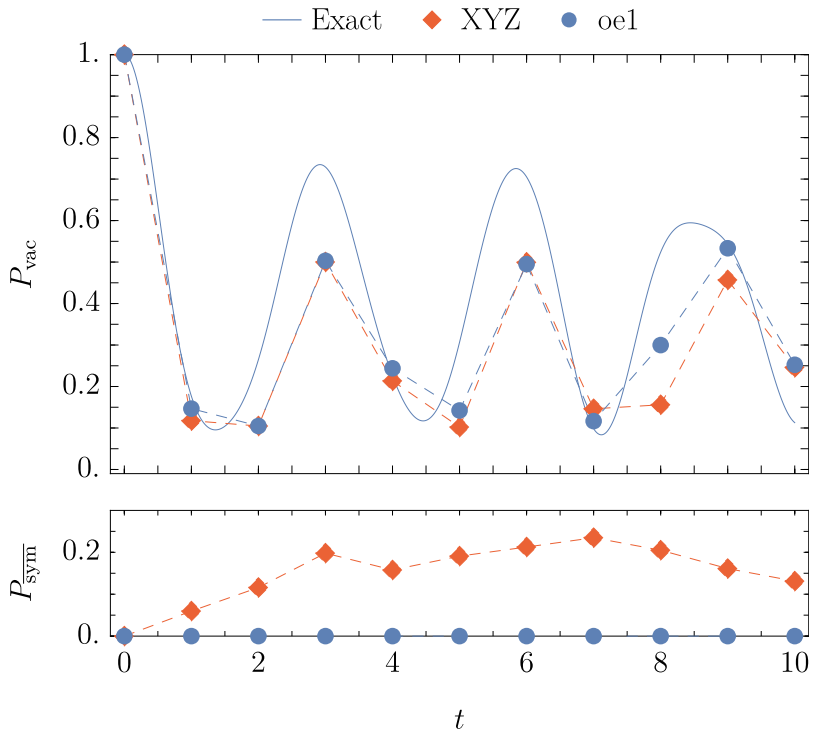

Figure 7.2: Numerical simulation of the projection on the bare-vacuum state $P_{\rm vac}$ (upper panel) and the population of symmetry-forbidden states $P_{\overline{\rm sym}}$ (lower panel) when the system is initialized in the bare-vacuum state for $N = 6$, $\mu = 0.1$ and $x = 0.6$. Different term orderings for the Trotterized evolution are considered: the odd-even ordering defined in Eq. (7.11) (blue dots) and the XYZ ordering defined in Eq. (7.14) (red diamonds). The blue line denotes the exact evolution. The odd-even ordering (oe1) has smaller Trotter errors than the XYZ ordering. More importantly, oe1 ordering preserves the symmetry of the Hamiltonian while XYZ does not (lower panel).

The symmetry operator $\hat{S}_z$ commutes with $\hat{\sigma}^x_n\hat{\sigma}^x_{n+1} + \hat{\sigma}^y_n\hat{\sigma}^y_{n+1} = \hat{\sigma}^+_n\hat{\sigma}^-_{n+1} + \text{H.c.}$, which is not broken up by the odd-even ordering scheme. Therefore, this ordering does not result in any leakage to the symmetry-forbidden subspace. This is unlike the XYZ ordering that

implements

$$\hat{\mathcal{S}}_1^{XYZ}(\delta t) = \mathrm{e}^{-i\delta t\,\hat{H}^z}\mathrm{e}^{-i\delta t\,\hat{H}^{zz}} \times \prod_{k=1}^{N-1} \mathrm{e}^{-i\delta t\,\hat{H}^{(yy)}_{k,k+1}} \prod_{k=1}^{N-1} \mathrm{e}^{-i\delta t\,\hat{H}^{(xx)}_{k,k+1}} \ , \tag{7.14}$$

where $\hat{H}^{(xx)}_{k,k+1}$ and $\hat{H}^{(yy)}_{k,k+1}$ are the terms in the Hamiltonian in Eq. (7.2) proportional to $\hat{\sigma}^x_k\hat{\sigma}^x_{k+1}$ and $\hat{\sigma}^y_k\hat{\sigma}^y_{k+1}$, respectively. The size of the leakage to the symmetry-forbidden subspace for both schemes are verified numerically in Fig. 7.2.

7.2.2 Gate Complexity

There are different approaches to digitally simulating the Schwinger model. Ref. [191] truncates the gauge-boson degrees of freedom in the electric-field basis, $|E| \leq \Lambda$. The electric-field Hilbert space at each link is then encoded using $\log_2(2\Lambda + 1)$ qubits. With OBCs and a zero incoming electric-field flux, the exact theory is recovered for $\Lambda = N/2$. To simulate the model with N sites for time t, this approach requires $\mathcal{O}(N + N\log_2 N)$ qubits and, up to logarithmic corrections, $\mathcal{O}\left(N^{5/2}t^{3/2}\right)$ two-qubit gates, using the second-order Suzuki-Trotter formula. In contrast, our approach integrates out the gauge bosons, leaving only the fermionic degree of freedom associated with the matter fields [67, 245]. Therefore, it requires $\mathcal{O}(N\log_2 N)$ fewer qubits to simulate the same model. However, in this approach, one trades the local gauge-matter interactions for long-range matter-matter interactions that correspond to a Coulomb force. Here, we investigate whether this purely fermionic model increases the gate complexity of the simulation compared with the local formulation involving both fermions and bosons.

Given a fixed error tolerance, one can use Eq. (7.10) to estimate the required number of Trotter steps in the purely fermionic formulation for simulation time t, system size N,

and at fixed x and μ:

$$\mathcal{O}\left(\lambda\gamma^{1/p}t^{1+1/p}\right) = \mathcal{O}\left(N^{2+1/p}t^{1+1/p}\right), \tag{7.15}$$

Here, $\lambda = \mathcal{O}(N^2)$, which is determined by the interactions in $\hat{H}^{zz}$, and $\gamma = \mathcal{O}(N)$, which results from summing over only the interactions in $\hat{H}^{x}$.[2] Since each Trotter step requires $\mathcal{O}(N^2)$ two-qubit gates, the gate complexity of the pth-order product formula is $\mathcal{O}\left(N^{4+1/p}t^{1+1/p}\right)$. For the second-order product formula ($p = 2$), the gate complexity reduces to $N^{9/2}t^{3/2}$, which is a factor of N^2 larger than the scaling of Ref. [191].

The bound on the Trotter error derived above is an upper bound and the required gate count may be much smaller in practice. In Fig. 7.3, we plot the empirical value of the number of two-qubit gates required for simulating the time-evolution operator in the purely fermionic formulation using the second-order formula for time $t = N$. The empirical gate count is obtained through a binary search for the minimum number of Trotter steps such that the difference between the Trotterized and the exact evolution is at most $\epsilon = 0.01$. This value is compared to two bounds: the commutator bound obtained from Eq. (7.10), following the discussion above, and the exact commutator bound derived from computing the norms of the nested commutators in Eq. (7.9) exactly. The gate complexity $\mathcal{O}(N^{6.2})$ from the commutator bound agrees with our earlier estimate of $\mathcal{O}(N^6)$ for this formulation of the model. However, Fig. 7.3 shows that this bound, obtained by applying the triangle inequality on the norms of the nested commutators, is rather loose. Instead, by computing Eq. (7.9) exactly, hence invoking cancellations between the commutators, the

[2] We group the interactions in $\hat{H}^{zz}$ and $\hat{H}^{z}$ into the Kth term in the estimation of the Trotter error in Eq. (7.10). Since the terms in $\hat{H}^{zz}$ and $\hat{H}^{z}$ commute, further Trotterizing the evolution under $\hat{H}^{zz}$ and $\hat{H}^{z}$ into one- and two-qubit gates introduces no additional Trotter error.

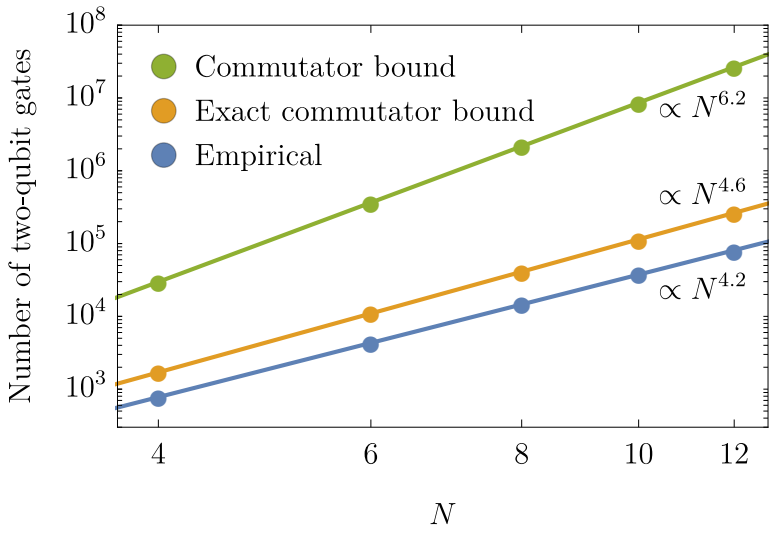

Figure 7.3: The number of two-qubit gates required to simulate the time evolution under the Hamiltonian in Eq. (7.2) on an N-site lattice for time $t = N$ given an error tolerance $\epsilon = 0.01$, and using the second-order product formula in Eq. (7.8). The commutator bound on the gate complexity (green dots) is estimated from the error bound in Eq. (7.10). We also obtain a tighter estimate (orange dots) by exactly computing the nested commutators in Eq. (7.9). Finally, the empirical gate count (blue dots) is obtained through a binary search for the minimum number of time steps $t/\delta t$ such that the total error is at most ϵ. The straight lines are linear fits that result in the polynomial scaling given in the figure.

gate complexity reduces to $\mathcal{O}\left(N^{4.6}\right)$, very close to the empirical scaling of $\mathcal{O}\left(N^{4.2}\right)$. Notably, the empirical scaling is nearly the same as the scaling of Ref. [191] for the fermion-boson formulation. However, we note that one may also be able to obtain tighter error bounds on the algorithm of Ref. [191] empirically.

7.2.3 Symmetry Protection

Digitizing a quantum evolution may introduce errors that populate states forbidden by the symmetry of the target system. Ref. [198] proposes a method to reduce this leakage when using product formulas and applies it to the fermion-boson formulation of the Schwinger model. In this section, we discuss whether the proposed method is effective at protecting the symmetry of the purely fermionic formulation, and in reducing the Trotter error.

The Schwinger-model Hamiltonian in Eq. (7.2) is invariant under a global rotation around the Z axis of the qubits, i.e., $[\hat{H}, \hat{S}_z] = 0$. Hence, the expectation value of $\hat{S}_z$ is conserved if the evolution is exact. However, due to Trotterization errors, $\langle \hat{S}_z \rangle$ may deviate from its initial value during the simulation. To mitigate this error, we can insert rotations generated by the symmetry, i.e., $\hat{C}(\alpha) = \mathrm{e}^{-i\alpha \hat{S}_z}$, in between the Trotter steps [198]:

$$\hat{\mathcal{U}}(t) = \prod_{k=1}^{t/\delta t} \hat{\mathcal{U}}_k(\delta t) \longrightarrow \prod_{k=1}^{t/\delta t} \hat{C}^\dagger(\alpha_k) \hat{\mathcal{U}}_k(\delta t) \hat{C}(\alpha_k). \tag{7.16}$$

By choosing suitable angles α_k for different Trotter steps, the errors from each step that do not commute with $\hat{S}_z$ are rotated by different amounts and can interfere destructively. This results in smaller leakage to the sector with the global charges that differ from the initial state. Therefore, the method mitigates errors in symmetry-violating Trotterization schemes, such as the XYZ ordering. Errors that commute with $\hat{S}_z$ remain intact under these rotations $\hat{C}(\alpha_k)$. As the result, this method has no effect on symmetry-preserving Trotterization schemes, such as the odd-even ordering. Additionally, since the symmetry operator $\hat{S}_z$ is diagonal in the measurement basis for the observables considered here, one can simply mitigate symmetry-violating errors by post-selecting on measurement outcomes

that preserve $\langle \hat{S}_z \rangle$. We compare the two mitigation methods in the following.

For simplicity, the angles α_k in Eq. (7.16) can be chosen such that $\alpha_k = k\alpha_1$, where for each t, α_1 is determined by numerically minimizing the leakage to the symmetry-forbidden subspace after $t/\delta t$ steps, as detailed in Appendix B.

As a result, the optimal value of α_1 depends on the number of Trotter steps and the simulation time. The top panel in Fig. 7.4 plots the leakage to the symmetry-forbidden sector for the odd-even ordering, the XYZ ordering before and after post-selection, as well as the XYZ ordering with symmetry protection but without post-selection. As expected, the odd-even ordering results in no population in the symmetry-forbidden states, and the leakage seen in the XYZ ordering trivially goes to zero after post-selection. Importantly, the symmetry-protected XYZ ordering leads to a strong suppression of the leakage.

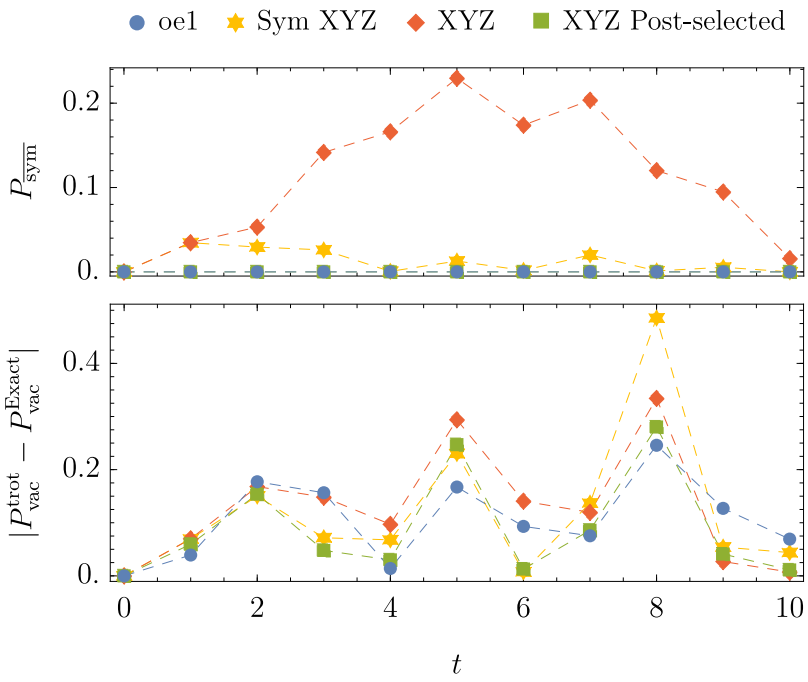

Figure 7.4: The leakage to the symmetry-forbidden sector, $P_{\overline{\text{sym}}}$, defined as the population in the states with a non-vanishing total charge given a bare-vacuum initial state (upper panel), as well as the error in the bare-vacuum population (lower panel) are shown for the odd-even ordering (blue dots), the XYZ ordering before (red diamonds) and after (green squares) post-selection, as well as the XYZ ordering with symmetry protection but without post-selection (yellow stars). The parameters used for the plot are $\mu = 0.1$, $x = 0.6$, $N = 4$ and $\delta t = 1$. The optimal angles for the symmetry-protected simulation are provided in Appendix B.

However, this improvement in preserving the symmetry does not guarantee a smaller Trotter error. Given two operators $\mathcal{E}_{\text{sym}}$ and $\mathcal{E}_{\overline{\text{sym}}}$, corresponding to the symmetry-preserving and symmetry-violating errors in the simulation, respectively, it is generally not true that $\|\mathcal{E}_{\text{sym}}\| < \|\mathcal{E}_{\text{sym}} + \mathcal{E}_{\overline{\text{sym}}}\|$. In particular, depending on the observable of interest, the effect of the two types of errors may interfere destructively. Therefore, eliminating $\mathcal{E}_{\overline{\text{sym}}}$ may

actually increase the error in the expectation value of the observable. For example, as shown in the lower panel of Fig. 7.4, the symmetry protection sometimes increases the error in the population of the bare-vacuum state instead of decreasing it. Overall, symmetry protection does not improve the accuracy of the XYZ-ordering scheme over the odd-even ordering scheme. Notably, post-selection is more successful than the symmetry-protection scheme at mitigating the Trotter error in P_{vac}.

According to Ref. [198], the symmetry protection scheme mitigates time-correlated experimental errors as well. Since the errors in our experiment are expected to be dominated by uncorrelated noise, it is interesting to investigate how well the scheme performs in the experimental implementation. To isolate the effects of symmetry protection on experimental rather than Trotter errors, we implement the odd-even ordering, which preserves the symmetry. The results are presented at the end of the next section.

7.3 Experimental Results

To simulate the evolution under the Hamiltonian in Eq. (7.2), the product formula needs to be decomposed into the native gates in the experiment. Specifically, to implement the $Y_iY_j(\chi) = \mathrm{e}^{-i\chi\hat{\sigma}_i^y\hat{\sigma}_j^y}$ ($Z_iZ_j(\chi) = \mathrm{e}^{-i\chi\hat{\sigma}_i^z\hat{\sigma}_j^z}$) gate, each qubit is rotated around the Z (Y) axis before and after applying an $X_iX_j(\chi)$ gate. For the odd-even ordering, i.e., $\mathcal{S}_1^{\text{oe1}}$ given in Eq. (7.11), the circuit can be broken down into three parts: $\mathrm{e}^{-i\delta t\hat{H}^x}$, $\mathrm{e}^{-i\delta t\hat{H}^{zz}}$, and $\mathrm{e}^{-i\delta t\hat{H}^z}$. An example of the circuit for the Trotterized evolution with $N = 6$ is shown in Fig. 7.5. The number of gates needed in each Trotter step for the different values of N in the experiment are summarized in Table 7.1. While the number of single-qubit rotations can be further

reduced in the circuits, such an optimization is not considered here since they have much lower error rates than the two-qubit gates.

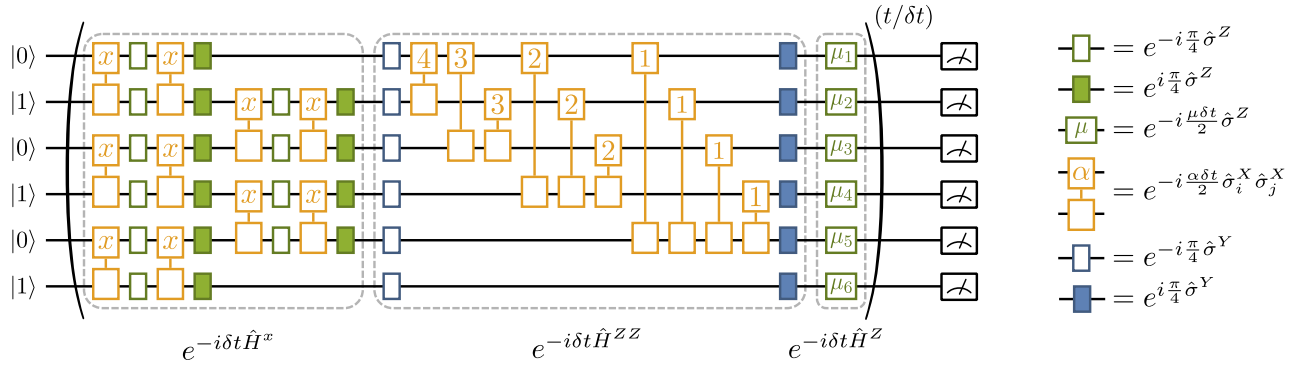

Figure 7.5: Circuit for the Trotterized evolution according to the Hamiltonian in Eq. (7.2) for $N = 6$ lattice sites, with odd-even ordering of the Trotter decomposition introduced in Eq. (7.11). The interaction term $\mathrm{e}^{-i\delta t\hat{H}^x}$ is implemented with nearest-neighbor X_iX_{i+1} and Y_iY_{i+1} gates. The $\mathrm{e}^{-i\delta t\hat{H}^{zz}}$ term is implemented with X_iX_j and R_i rotations. The $\mathrm{e}^{-i\delta t\hat{H}^z}$ term involves only Z_i rotations, with the angles $\mu_1 = -(\mu+3)\delta t$, $\mu_2 = (\mu-2)\delta t$, $\mu_3 = -(\mu+2)\delta t$, $\mu_4 = (\mu-1)\delta t$, $\mu_5 = -(\mu+1)\delta t$, and $\mu_6 = \mu\delta t$. Qubits are initialized in the bare-vacuum state $|010101\rangle$, then evolved by repeating the circuit in the parentheses $t/\delta t$ times, and measured individually in the Z basis in the end.

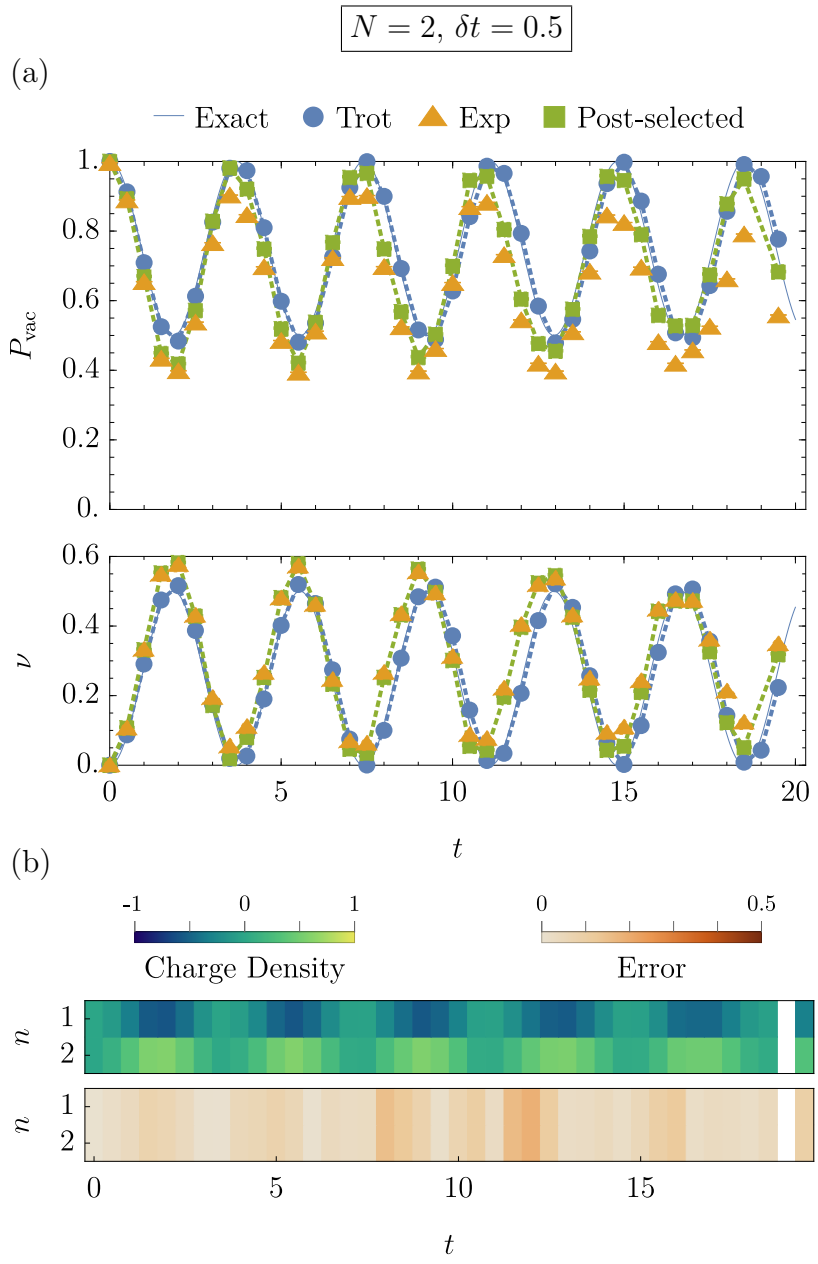

Figure 7.6: Experimental results for $N = 2$ and $\delta t = 0.5$. (a) The upper plot shows fluctuation in the bare-vacuum population, P_{vac}, while the lower plot shows particle-number density, ν, as a function of time, indicating the creation and annihilation of the particle-antiparticle pairs. The dashed lines are a guide to the eye. (b) The upper plot shows the local charge density Q_n as measured in the experiment after post-selection, while the lower plot shows its deviation from theory as a function of time.

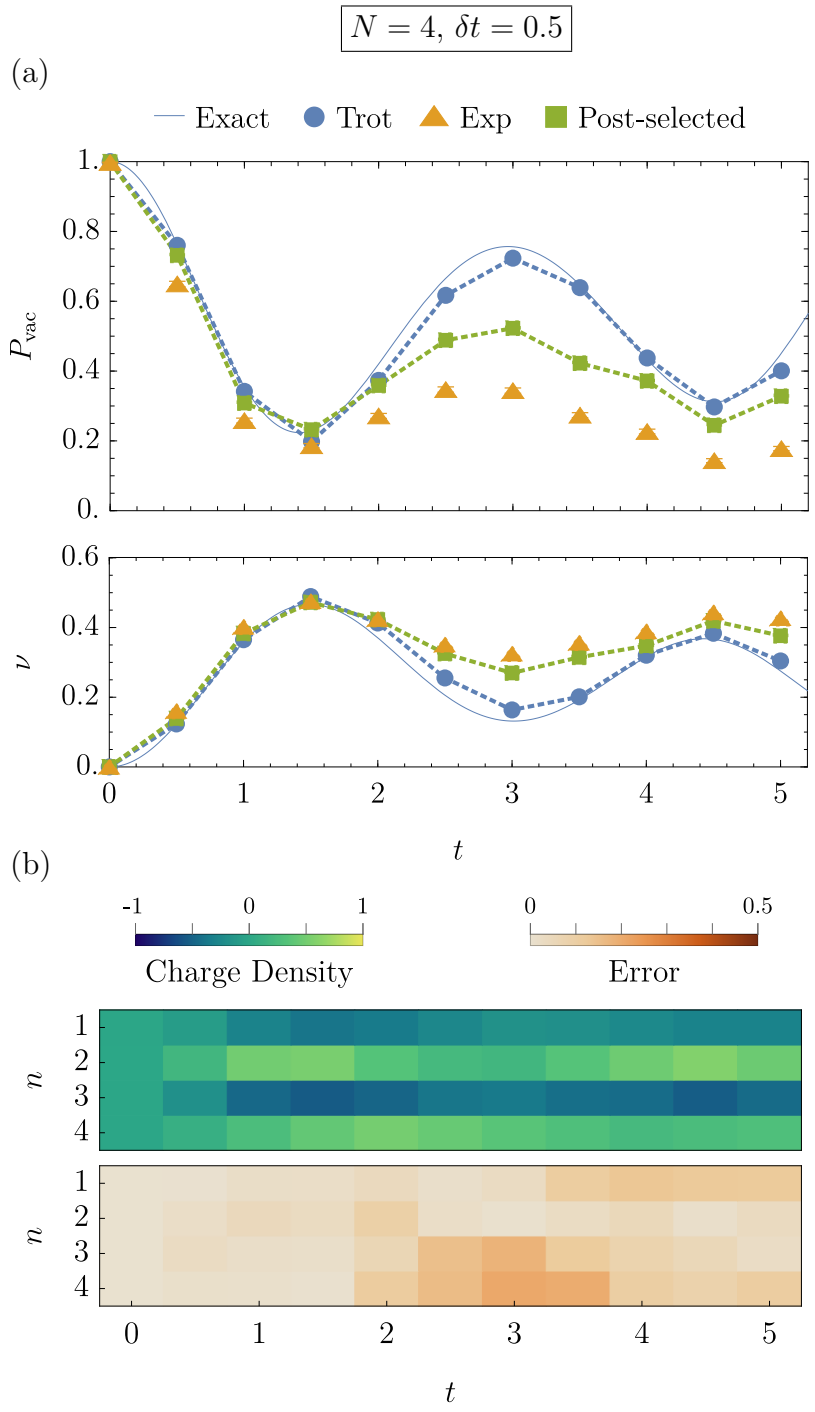

Figure 7.7: Experimental results for $N = 4$ and $\delta t = 0.5$. (a) The upper plot shows fluctuation in the bare-vacuum population, $P_{\text{vac}}(t)$, while the lower plot shows particle-number density, $\nu(t)$. (b) The upper plot shows the local charge density $Q_n(t)$ as measured in the experiment after post-selection, while the lower plot shows its deviation from theory.

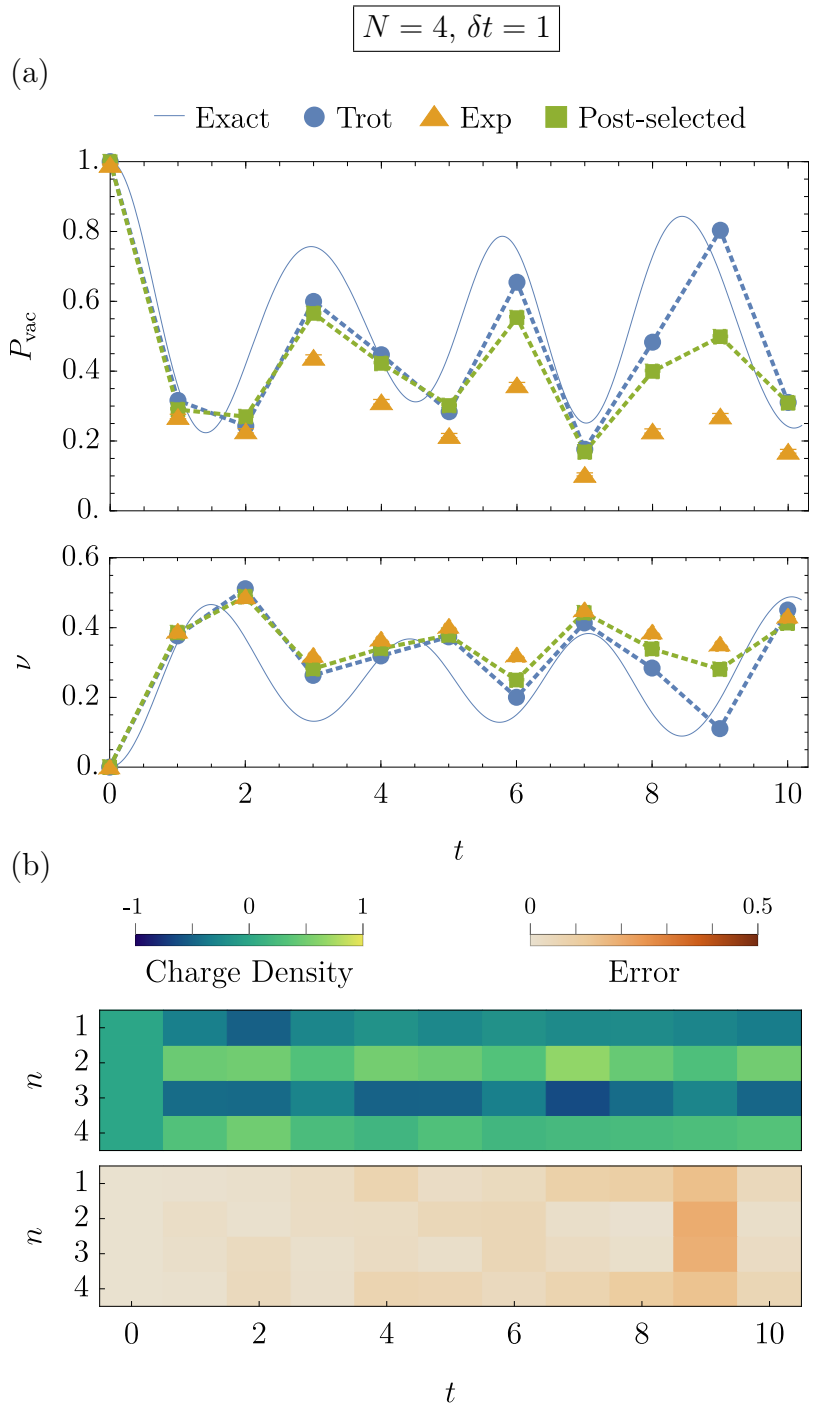

Figure 7.8: Experimental results for $N = 4$ and $\delta t = 1$. (a) The upper plot shows fluctuation in the bare-vacuum population, $P_{\text{vac}}(t)$, while the lower plot shows particle-number density, $\nu(t)$. (b) The upper plot shows the local charge density $Q_n(t)$ as measured in the experiment after post-selection, while the lower plot shows its deviation from theory.

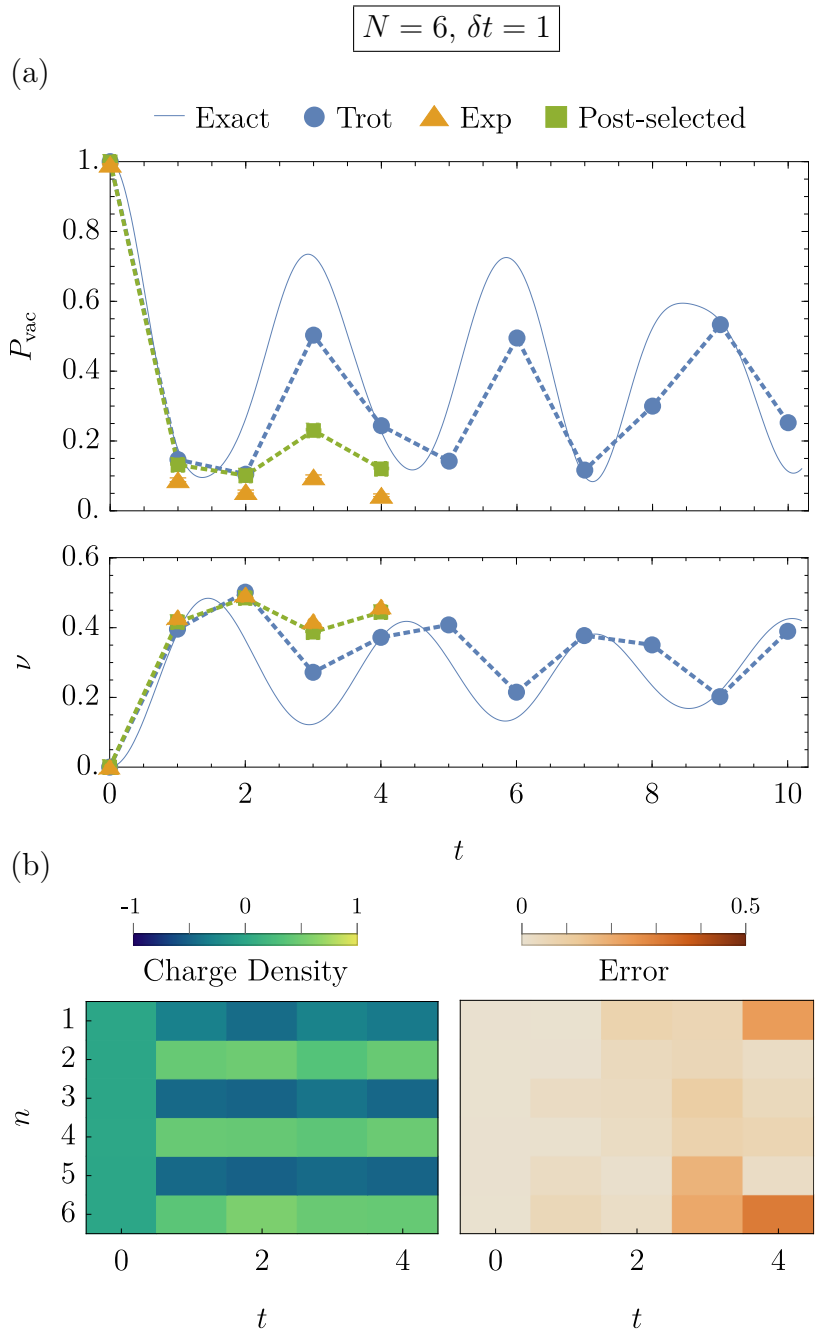

Figure 7.9: Experimental results for $N = 6$ and $\delta t = 1$. (a) The upper plot shows fluctuation in the bare-vacuum population, $P_{\text{vac}}(t)$, while the lower plot shows particle-number density, $\nu(t)$. (b) The left plot shows the local charge density $Q_n(t)$ as measured in the experiment after post-selection, while the right plot shows its deviation from theory. At $t = 4$, we reach the gate-depth limit of the hardware.

The experiment starts by preparing the qubits in the vacuum state of the Hamiltonian in the limit of $x = 0$, $|\text{vac}\rangle = |\psi_0\rangle$, using $R_i(\pi, 0)$ on alternate qubits. The model parameters are set to $\mu = 0.1$ and $x = 0.6$ to ensure non-trivial dynamics starting from the bare vacuum. We measure all the qubits in the Z basis to get the state populations. The state preparation and measurement errors are corrected by applying the inverse of an independently measured state-transfer matrix. The observables of interest are then calculated from the state populations using Eqs. (7.3)-(7.5).

Table 7.1: Gate counts for simulating each Trotter step of the time evolution in the Schwinger model with the odd-even term ordering in Eq. (7.11), along with the largest number of Trotter steps $t/\delta t$ implemented in the experiment for $N = 2, 4, 6$ staggered sites.

N	$X_iX_j(\chi)$	$R_i(\theta, \phi)$	$Z_i(\theta)$	$t/\delta t$
2	2	0	6	39
4	9	8	16	10
6	20	12	26	4

Algorithmic and experimental errors can, in principle, produce measurement results that break the global charge conservation of the system. This means that starting from the bare-vacuum state, the probability amplitude for evolving to states with non-vanishing total charge may not be negligible. Therefore, to improve the results, one can post-select the measurements so that only outcomes in the relevant symmetry sector are kept. Since the odd-even ordering implemented in the experiment does not violate the global charge conservation, these errors result entirely from the experimental imperfections.

Fig. 7.6(a) plots the bare-vacuum population P_{vac}, Eq. (7.3), and the particle-number density ν, Eq. (7.4), as a function of time for $N = 2$ and $\delta t = 0.5$. For $\delta t = 0.5$, the theoretical Trotterized evolution (blue dots) has no significant deviation from the exact evolution (blue line). The experimental results after post-selection agree well with the theory even after 39 Trotter steps corresponding to $t = 19.5$. Post-selection is shown to significantly mitigate the experimental errors for P_{vac}, especially at long evolution times. However, it does not appear as effective for the particle-number density or the survival amplitude of other initial states in general, as plotted in Appendix C. Fig. 7.6(b) plots the local charge density Q_n, Eq. (7.5), derived from post-selected measurement results and their deviation from the theoretical expectation for the same set of parameters. The local-charge profile is consistent with the global dynamics shown in Fig. 7.6(a) as the pair creation coincides with the destruction of the bare vacuum.

Fig. 7.7 plots the same observables as a function of time for $N = 4$ and $\delta t = 0.5$. Compared with the $N = 2$ case, each Trotter step for $N = 4$ requires seven extra two-qubit gates, see Table 7.1, and we only perform ten Trotter steps for this case. Since the experimental error dominates the Trotter error after a few Trotter steps for $\delta t = 0.5$, the Trotter step size is increased to $\delta t = 1$ in Fig. 7.8, doubling the simulation time. Even though the Trotter error is larger in Fig. 7.8 than in Fig. 7.7, the Trotterized evolution still qualitatively follows the exact solution. In both cases, the experimental data after post-selection agree reasonably well with the numerical simulation.

Next, we increase the number of staggered sites to $N = 6$, with the results displayed in Fig. 7.9. Since each Trotter step now requires 20 two-qubit gates and 38 single-qubit gates, only four Trotter steps could be run before decoherence dampens the evolution. Nev-

ertheless, the qualitative behavior, including the first revival of the bare-vacuum amplitude, can still be observed from the results.

Finally, we study the effect of active symmetry protection by inserting rotations generated by the symmetry operator $\hat{S}_z$, as discussed in Sec. 7.2. In the numerical study of Sec. 7.2, a set of optimal angles was found to minimize the leakage to the symmetry-forbidden subspace caused by algorithmic error. Since such an optimal set cannot be found a priori, a straightforward strategy is to use a random angle at each Trotter step to average out the leakage after many Trotter steps [198]. Since the effectiveness of the scheme depends on the nature of the experimental error, it is interesting to see if symmetry protection can improve our experimental implementation.

Figure 7.10 plots the result of an experiment using the odd-even term ordering. As before, the initial state is the bare vacuum. The unitaries $\mathrm{e}^{-i\alpha_k \hat{S}_z}$, with random angles α_k given in Appendix B, are inserted between Trotter steps k and $k+1$. While the population in states forbidden by the symmetry, denoted as $P_{\overline{\mathrm{sym}}}$ in the upper panel, decreases with symmetry protection, this reduction is not significant. Furthermore, while the deviation of the bare-vacuum population from the Trotterized theory generally decreases, post-selecting symmetry-preserving measurements appears more effective in mitigating the error in this quantity than the symmetry protection as shown in the lower panel of the figure. This indicates that the experiment is dominated by noise that is not correlated in time. Note that by construction, the symmetry-protection scheme only mitigates time-correlated errors.

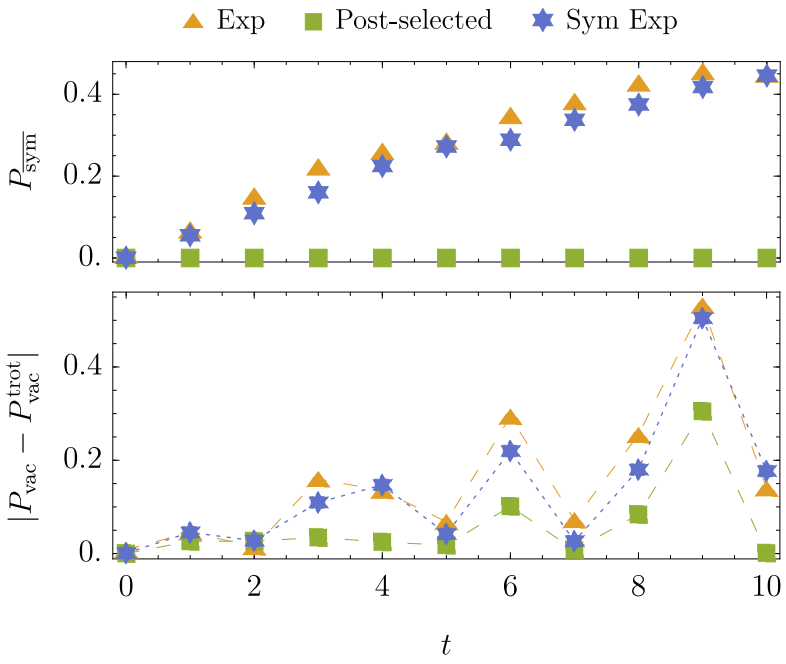

Figure 7.10: Leakage to the symmetry-forbidden subspace (upper panel) and deviation of the experimental results from theory for the bare-vacuum population (lower panel) when different schemes to mitigate errors are applied: no mitigation (orange triangles), post-selection (green squares), and symmetry protection (blue stars). Note that by definition, the leakage to the symmetry-forbidden subspace is zero after post-selection. In both plots, $N = 4$ and $\delta t = 1.0$, the system is initiated in the bare-vacuum state, and is evolved via the odd-even ordering scheme.

7.4 Discussion

We have digitally simulated the time evolution of the lattice Schwinger model with up to six qubits using the purely fermionic formulation. For a four-qubit simulation, we observe four oscillations of the particle density, and the simulated time is almost four times longer than previously demonstrated using a Trotterized scheme [67, 233]. Given the long circuit depths required for dynamical gauge-theory simulations, gate fidelity, rather than qubit

number, is the main limitation of our implementation. Efforts to overcome such a technical limitation are well underway [26]. To mitigate the time-correlated errors, we have applied a symmetry-protection scheme [198] but found negligible effects in suppressing the errors. This symmetry-protection investigation indicates that the dominant noise in experiment is incoherent and uncorrelated. Incoherent errors can be mitigated by post-selection of the experimental measurements using symmetry considerations. Better-motivated and further-tailored schemes for mitigating incoherent errors are desired in future simulations. Furthermore, it is found that the symmetry-violating and symmetry-preserving errors can destructively contribute to given quantities, and removing only one of these errors can decrease the overall accuracy. It is therefore important to also develop and apply symmetry-preserving error-suppression schemes in future experiments.

An avenue for improving the simulation quality is reducing the gate depth, e.g., by performing gates in parallel instead of sequentially. In our model, $\mathrm{e}^{-i\delta t\hat{H}^x}$, consisting of only nearest-neighbor interactions, can be applied in a fixed circuit depth of 4 instead of $2N$ by performing all $X_{2i}X_{2i+1}$ terms, then all $X_{2i+1}X_{2i+2}$ terms, in parallel. The all-to-all interactions in $\mathrm{e}^{-i\delta t\hat{H}^{zz}}$ can be reduced to depth of N instead of N^2 if gates X_iX_{i+n}, for all i and fixed n, are performed in parallel. With trapped ions, parallel operations can be done either in multi-zone architectures [30, 32], or in linear chains with advanced control schemes [43, 44].

Alternatively, the gate depth can be reduced by using M-body Mølmer-Sørensen gates $\mathrm{MS}(\chi, M) \equiv \mathrm{e}^{-i\chi\sum_{i=1}^{M}\sum_{j=i+1}^{M}\hat{\sigma}_i^x\hat{\sigma}_j^x}$ [126, 127, 129]. This approach was implemented in Ref. [67] to reduce the number of MS operations in the simulation of the Schwinger model from $\mathcal{O}(N^2)$ to $\mathcal{O}(N)$. In general, a non-trivial optimization of both frequency and

amplitude modulation of the beams may be required to implement an M-body gate with desired rotation angles, as demonstrated in Ref. [228]. Furthermore, one should note that since an M-body MS gate has roughly comparable fidelity as that of M 2-body MS (X_iX_j) gates [247], the overall fidelity of the simulation would likely be similar for both schemes.

When the fermion-boson formulation of the lattice Schwinger model is concerned, a trapped-ion-specific approach to reduce the gate count is to encode the gauge degrees of freedom into the motion of the ions as explained in Ref. [237] and Chapter 8. Besides the standard set of gates, the proposed hybrid digital-analog scheme involves both spin-phonon and phonon-phonon gates. This approach leads to a reduction in both the number of qubits and the number of entangling gates compared with a fully-digital algorithm involving the gauge bosons [191].

To make implementations of more complex gauge theories possible, including non-Abelian and higher-dimensional models, unifying physics insights, algorithm optimization, hardware implementation, and post-processing is required, as demonstrated in this work. In this context, it would be interesting to investigate whether more resource-efficient encodings of such theories exist, if optimal Trotter decompositions and term ordering schemes can be found, to what degree these preserve local gauge symmetries, whether information regarding the initial state and the symmetries can be incorporated to further tighten the algorithmic error bounds [239, 248–253], how to balance these errors with experimental errors, and whether symmetry-protection schemes are advantageous in suppressing algorithmic and experimental errors. While progress along these lines is already being made [192, 193, 196, 199, 201, 205, 236, 254–262], further technological advances in quantum hardware are essential to enable advanced gauge-theory simulations in the upcoming years.

Chapter 8: Hybrid Analog-Digital Quantum Simulation of the Yukawa Model

Encoding the bosonic dofs into qubits is expensive since a boson has an infinite number of levels while a qubit only has two. Given a cutoff Λ, where the maximum excitation number is Λ, $\lceil \log_2(\Lambda + 1) \rceil$ qubits are required to encode a boson. Therefore encoding bosons using qubits is costlier than directly mapping them to the intrinsic bosons of the experimental system. However, only a few experimental hardware for quantum computing and simulation have an accessible intrinsic bosonic dofs with controllable coupling between the bosons and the qubits. These intrinsic bosonic dofs are either photons generated from a cavity (a microwave cavity/resonator in the case of superconducting qubits [263], an optical cavity in the case of atoms [264]) or phonons originated from the quantized vibration of particles in a shared confining potential [79, 265, 266]. In trapped-ion simulators, the native bosons are phonons, i.e., quantized excitations of the ionic Coulomb crystal.

Over the past few years, there has been a significant improvement in the ability to control and engineer spin-phonon and phonon-phonon couplings in trapped ions as well as the ability to prepare and read out complex phonon states with high fidelities [267–270]. The bosonic dofs in trapped ion systems have been employed to perform quantum error-

correction with bosonic codes [271–273], quantum simulation for chemistry [69, 71, 72] and quantum field theories (QFTs) [274]. However, there has not been a demonstration of utilizing the phonon dofs in trapped ions in a programmable and scalable way to perform quantum simulation of QFTs, even though there have been many theoretical proposals [237, 275, 276]. Specifically, the fermionic dofs are encoded in the spins or internal states of the ions while the bosonic dofs are encoded in the phonons or external dofs of the ions. The interactions between the spins are performed digitally (gate-based and universal) while the spin-phonon and phonon-phonon interactions can be performed semi-digitally (gate-based but the gates have not been proved to form a universal set). This method is named hybrid simulation. Here, we present our experimental attempt of bridging this gap with the simulation of the 1+1 D Yukawa model following the theoretical framework laid out in Ref. [237].

In this chapter, we briefly describe the ideas for hybrid simulation proposed in Ref. [237] with application to the Yukawa model, an effective field theory proposed by Hideki Yukawa to describe the interaction between fermions (nucleons) through the exchange of a scalar boson (pion). We detail the steps that we took and what still needs to be done to implement these ideas in the laboratory.

8.1 1D Lattice Yukawa Model

One of the simplest models in nuclear and high-energy physics (NHEP) that involves interacting bosons and fermions is the Yukawa model [277,278]. The Yukawa model describes the interaction between fermions and scalar (spin-0) bosons. An example of Yukawa interaction

is the interaction between nucleons (protons and neutrons) by exchanging pions. This force dominates the long-range component of the nuclear force arising from strong interactions in nature. Since nucleons and pions come in different flavors or species, each species has a different spin and isospin, the Yukawa interactions among them are complicated. Here, we restrict ourselves to the study of interactions between a single species of nucleons and pions, in particular the interactions between nucleons under the exchange of one pion (one-boson-exchange model). Such a Yukawa coupling can lead to one-boson-exchange potential of the form e^{-mr}/r, where m is the mass of the scalar boson. In nature, pions also self interact. Nonetheless, at low energies, their interactions contribute less significantly to the nuclear potential and can be ignored. We further restrict ourselves to the Yukawa interaction at low energies in 1+1 D. As this model has no boson-boson interaction, its implementation in current experiment is easier compared with the Schwinger model [237].

In this section, we follow the derivations of the Hamiltonian and the transformation to a basis more applicable to a trapped ion quantum computer for the 1+1 D Lattice Yukawa model outlined in Ref. [237].

8.1.1 The Fermionic-Bosonic Basis

Since we are performing a quantum simulation, it is more straight forward to use the Hamiltonian formulation rather than the Lagrangian formulation. We consider a 1+1 D N-site lattice with lattice spacing b that has fermions at the odd sites, anti-fermions at the even sites (in the staggered formulation of lattice fermions), and scalar bosons $\hat{\varphi}_j$ at every

site. The Hamiltonian for the lattice Yukawa model has the three following terms:

$$\hat{H}^{(I)} = \sum_{j=1}^{N} \left[\frac{i}{2b} (\hat{\psi}_j^\dagger \hat{\psi}_{j+1} - \hat{\psi}_{j+1}^\dagger \hat{\psi}_j) + m_\psi (-1)^j \hat{\psi}_j^\dagger \hat{\psi}_j \right], \tag{8.1}$$

$$\hat{H}^{(II)} = b \sum_{j=1}^{N} \left[\frac{\hat{\Pi}_j^2}{2} + \frac{(\nabla \hat{\varphi}_j)^2}{2} + \frac{m_\varphi^2}{2} \hat{\varphi}_j^2 \right], \tag{8.2}$$

$$\hat{H}^{(III)} = gb \sum_{j=1}^{N} \hat{\psi}_j^\dagger \hat{\varphi}_j \hat{\psi}_j, \tag{8.3}$$

where g is the coupling constant, and m_ψ and m_φ are masses of fermions and bosons, respectively. The periodic boundary conditions (PBCs) are assumed, i.e., $\hat{\psi}_{N+1} \equiv \hat{\psi}_1$ and $\hat{\varphi}_{N+1} \equiv \hat{\varphi}_1$. $\hat{\Pi}_j$ is the canonical momentum (an equivalent of time-derivatives) of the bosonic field $\hat{\varphi}_i$ [279]. The first term given by Eq. (8.1) describes the dynamics of the fermionic fields which comprises of two parts: the hopping dynamics and the mass of the fermions. The second term, Eq. (8.2), describes the bosonic fields' dynamics which comprises of the kinetic energy (time and space derivatives of the fields) and the potential energy due to the mass of the bosons. The third term, Eq. (8.3), describes the interaction between fermionic and bosonic fields through Yukawa interaction.

Expanding the bosonic fields in the momentum basis with the momentum eigenvalues $p_k \equiv 2\pi k/(Nb)$ and energy eigenvalues $\varepsilon_k = \sqrt{p_k^2 + m_\varphi^2}$[1] gives:

$$\hat{\varphi}_j = \frac{1}{\sqrt{Nb}} \sum_{k=-N/2}^{N/2-1} \frac{1}{\sqrt{2\varepsilon_k}} \left(\hat{d}_k^\dagger \mathrm{e}^{-i2\pi kj/N} + \hat{d}_k \mathrm{e}^{i2\pi kj/N} \right), \tag{8.4}$$

$$\hat{\Pi}_j = \frac{i}{\sqrt{Nb}} \sum_{k=-N/2}^{N/2-1} \sqrt{\frac{\varepsilon_k}{2}} \left(\hat{d}_k^\dagger \mathrm{e}^{-i2\pi kj/N} - \hat{d}_k \mathrm{e}^{i2\pi kj/N} \right). \tag{8.5}$$

[1]This is true for the continuous model, for a lattice, the energy is $\varepsilon_k^2 = 4\sin^2(p_k b/2)/b^2 + m_\varphi^2$. We will work in a small lattice-spacing limit in which this relation holds.

We can rewrite the bosonic term as

$$\hat{H}^{(II)} = \sum_{k=-N/2}^{N/2-1} \varepsilon_k (\hat{d}_k^\dagger \hat{d}_k + \frac{1}{2}\mathbb{1}_\infty), \tag{8.6}$$

where $\mathbb{1}_\infty$ is the identity matrix of infinite dimension, and the Yukawa interaction term as

$$\hat{H}^{(III)} = g\sqrt{\frac{b}{N}} \sum_{j=1}^{N} \sum_{k=-N/2}^{N/2-1} \frac{1}{\sqrt{2\varepsilon_k}} \hat{\psi}_j^\dagger \hat{\psi}_j \left(\hat{d}_k^\dagger \mathrm{e}^{-i2\pi kj/N} + \hat{d}_k \mathrm{e}^{i2\pi kj/N} \right) \tag{8.7}$$

(for details, see Appendix D). From here on, we will work with the Yukawa Hamiltonian in the momentum basis, i.e., Eqs. (8.1), (8.6) and (8.7).

8.1.2 The Spin-Bosonic Basis

The Hamiltonian terms in Eqs. (8.1), (8.6) and (8.7) can be mapped to spins and bosons following the procedure in Ref. [237]. Explicitly, we use Jordan-Wigner (JW) transformation to convert fermionic operators to spin operators $\hat{\psi}_j = \prod_{l=1}^{j-1}(i\hat{\sigma}_l^z)\hat{\sigma}_j^-$ and $\hat{\psi}_j^\dagger = \prod_{l=1}^{j-1}(-i\hat{\sigma}_l^z)\hat{\sigma}_j^+$. Then, the fermionic hopping in $\hat{H}^{(I)}$ becomes

$$\begin{aligned} &\sum_{j=1}^{N-1} \left[\frac{i}{2b} (\hat{\psi}_j^\dagger \hat{\psi}_{j+1} - \hat{\psi}_{j+1}^\dagger \hat{\psi}_j) \right] + \frac{i}{2b} (\hat{\psi}_N^\dagger \hat{\psi}_1 - \hat{\psi}_1^\dagger \hat{\psi}_N) \\ &= \frac{1}{2b} \sum_{j=1}^{N-1} (\hat{\sigma}_j^+ \hat{\sigma}_{j+1}^- + \hat{\sigma}_{j+1}^+ \hat{\sigma}_j^-) - \frac{1}{2b} (\hat{\sigma}_N^+ \hat{\sigma}_1^- + \hat{\sigma}_1^+ \hat{\sigma}_N^-) \prod_{l=1}^{N} (i\hat{\sigma}_l^z) \end{aligned} \tag{8.8}$$

(for details, see Appendix A). Similarly for the mass term in $\hat{H}^{(I)}$,

$$\sum_j m_\psi (-1)^j \hat{\psi}_j^\dagger \hat{\psi}_j = \sum_j \frac{m_\psi}{2} (-1)^j (\hat{\sigma}_j^z + \mathbb{1}_2). \tag{8.9}$$

Using $\hat{\sigma}_j^+ \hat{\sigma}_{j+1}^- + \hat{\sigma}_{j+1}^+ \hat{\sigma}_j^- = \frac{1}{2}(\hat{\sigma}_j^x \hat{\sigma}_{j+1}^x + \hat{\sigma}_j^y \hat{\sigma}_{j+1}^y)$, $\hat{H}^{(I)}$ in Eq. (8.1) becomes, up to a constant,

$$\hat{H'}^{(I)} = \frac{1}{4b} \sum_{j=1}^{N-1} (\hat{\sigma}_j^x \hat{\sigma}_{j+1}^x + \hat{\sigma}_j^y \hat{\sigma}_{j+1}^y) - \frac{1}{4b} (\hat{\sigma}_1^x \hat{\sigma}_N^x + \hat{\sigma}_1^y \hat{\sigma}_N^y) \prod_{l=1}^{N} (i\hat{\sigma}_l^z) + \frac{m_\psi}{2} \sum_{j=1}^{N} (-1)^j \hat{\sigma}_j^z. \tag{8.10}$$

The product $\prod_{l=1}^{N}(i\hat{\sigma}_l^z)$ with $N > 1$ is a constant that depends on the initial state and number of sites N because the Hamiltonian conserves the number of particles. Specifically, for even N, $\prod_{l=1}^{N}(i\hat{\sigma}_l^z)$ is either 1 or -1. $\hat{H}^{(II)}$ of Eq. (8.6) does not change under the JW transformation since it does not involve fermions. $\hat{H}^{(III)}$ in Eq. (8.7) becomes

$$\hat{H'}^{(III)} = \sqrt{\frac{g^2 b}{2N}} \sum_{j=1}^{N} \sum_{k=-N/2}^{N/2-1} \frac{1}{\sqrt{\varepsilon_k}} \frac{1}{2} (\hat{\sigma}_j^z + \mathbb{1}_2) \left(\hat{d}_k^\dagger \mathrm{e}^{-i2\pi kj/N} + \hat{d}_k \mathrm{e}^{i2\pi kj/N} \right). \tag{8.11}$$

In Section 8.2, we show how to implement the three terms in Eqs. (8.10), (8.6) and (8.11) with trapped ions.

8.1.3 Mapping to Trapped Ions

As discussed in Chapter 2, trapped ions have the internal (spin) and external (motion) degrees of freedom. We have shown throughout the dissertation how to encode the quantum information in the spins and perform computation. Specifically, in Chapter 7, we use the spins to perform a quantum simulation of the lattice Schwinger model where the bosonic degrees of freedom encoding the electric field are rewritten into long-range interactions between the spins. Generally, boson degrees of freedom cannot be eliminated from the formulation, so it is important to find efficient quantum-simulation strategies for fermion-bosonic field theories. Moreover, the fully fermionic formulation of the Schwinger model increases the number of gates required to simulate the model of N lattice site by $\mathcal{O}(N^2)$ (because of all-to-all interactions among the fermions). The alternative is to encode the bosons into spins, which in turn increases the number of qubits required. Here, we take advantage of the existing bosonic degrees of freedom in trapped ion systems, their motion, to simulate the bosons in the model. We show an example of this mapping for the low

energy Yukawa model in 1+1 D, which has the spin-boson interaction but not the boson-boson interaction as in the Schwinger model.

When we map the bosons to the collective motion of the ions, i.e., the normal phonons, the bosonic operators become $\hat{d}_k \rightarrow \hat{a}_{k+N/2+1} = \hat{a}_m$ and $\hat{d}_k^\dagger \rightarrow \hat{a}_{k+N/2+1}^\dagger = \hat{a}_m^\dagger$. $\hat{H}^{(II)}$ of Eq. (8.6) is rewritten as

$$\hat{H}''^{(II)} = \sum_{m=1}^{N} \varepsilon_m (\hat{a}_m^\dagger \hat{a}_m + \frac{1}{2}\mathbb{1}_2). \tag{8.12}$$

Using the same mapping, $\hat{H}^{(III)}$ of Eq. (8.7) becomes

$$\hat{H}''^{(III)} = \sqrt{\frac{g^2 b}{2N}} \sum_{j=1}^{N} \sum_{m=1}^{N} \frac{1}{\sqrt{\varepsilon_m}} \frac{1}{2} (\hat{\sigma}_j^z + \mathbb{1}_2) \Big(\hat{a}_m^\dagger \mathrm{e}^{-i2\pi j/N(m-N/2-1)} + \hat{a}_m \mathrm{e}^{i2\pi j/N(m-N/2-1)} \Big). \tag{8.13}$$

As discussed latter in Section 8.3, since we start in the pure state with no bosons, no fermions and no anti-fermions, the spin state is $|\psi_{0,N}\rangle_{sp} = |\underbrace{0,1,0,1,...,0,1}_{N}\rangle_s |\underbrace{0,0,...,0}_{N}\rangle_p$, hence $\prod_{l=1}^{N}(i\hat{\sigma}_l^z) = 1$. This can be proved by induction. For $N = 2$, the initial state is $|\psi_{0,2}\rangle_{sp} = |0,1\rangle_s |0,0\rangle_p$, hence $\prod_{l=1}^{2}(i\hat{\sigma}_l^z) = (i)(-i) = 1$. For $N = 4$, the initial state is $|\psi_{0,4}\rangle_{sp} = |0,1,0,1\rangle_s |0,0,0,0\rangle_p$, hence $\prod_{l=1}^{4}(i\hat{\sigma}_l^z) = (i)(-i)(i)(-i) = 1$. Going from N to $N+2$ adds an extra fermionic field and anti-fermionic field (together with two bosonic fields), $|\psi_{0,N+2}\rangle_{sp} = |\psi_{0,N}\rangle_{sp} \otimes |0,1\rangle_s |0,0\rangle_p$. As a result, the spin string for $N+2$ is the spin string for N multiplied with a factor of $(i)^2(\hat{\sigma}_{N+1}^z)(\hat{\sigma}_{N+2}^z) = (i)(-i) = 1$, therefore $\prod_{l=1}^{N+2}(i\hat{\sigma}_l^z) = \prod_{l=1}^{N}(i\hat{\sigma}_l^z) = 1$. $\hat{H}'^{(I)}$ in Eq. (8.10) then becomes

$$\hat{H}''^{(I)} = \frac{1}{4b} \sum_{j=1}^{N-1} (\hat{\sigma}_j^x \hat{\sigma}_{j+1}^x + \hat{\sigma}_j^y \hat{\sigma}_{j+1}^y) - \frac{1}{4b} (\hat{\sigma}_1^x \hat{\sigma}_N^x + \hat{\sigma}_1^y \hat{\sigma}_N^y) + \frac{m_\psi}{2} \sum_{j=1}^{N} (-1)^j \hat{\sigma}_j^z. \tag{8.14}$$

As shown in in Chapter 7, similar to the Schwinger model Hamiltonian given by Eq. (7.2), this term can be implemented with our universal gate set.

$\hat{H}''^{(II)}$ of Eq. (8.12) can be implemented as a phase shift in the phonon degree of freedom when moving to the right rotating frame. In particular, we move into the rotating frame of

$$\hat{U}_R = \exp\left(-it\sum_m \varepsilon_m \hat{a}_m^\dagger \hat{a}_m\right). \tag{8.15}$$

In this frame, $\hat{a}_m \to \hat{a}_m e^{-i\epsilon_m t}$, $\hat{a}_m^\dagger \to \hat{a}_m^\dagger e^{i\epsilon_m t}$. The first term $\hat{H}'^{(I)}$ of Eq. (8.14) is unaffected, we can relabel $\tilde{H}^{(I)} = \hat{H}''^{(I)}$. The second term $\hat{H}''^{(II)}$ of Eq. (8.12) vanishes. The third term $\hat{H}''^{(III)}$ of Eq. (8.13), becomes

$$\tilde{H}^{(III)} = \sqrt{\frac{g^2 b}{2N}}\sum_{j=1}^{N}\sum_{m=1}^{N}\frac{1}{\sqrt{\varepsilon_m}}\frac{1}{2}(\hat{\sigma}_j^z + \mathbb{1}_2)\left(\hat{a}_m^\dagger \mathrm{e}^{-i2\pi j/N(m-N/2-1)+i\varepsilon_m t} + \hat{a}_m \mathrm{e}^{i2\pi j/N(m-N/2-1-i\varepsilon_m t)}\right). \tag{8.16}$$

As we shall see in Section 8.2, this term, up to some single-qubit rotations, is a sum of spin-dependent forces $\hat{\sigma}_j^x(\hat{a}_m^\dagger + \hat{a}_m)$ on ion j mode m with an ancillary ion $\mathbb{1}_2(\hat{a}_m^\dagger + \hat{a}_m)$. If we have very good control of the lasers and the motion, Eq. (8.16) can be implemented as one gate. Therefore, using the phonons to encode the bosons and the spins to encode the fermions, we only need $N+1$ ions and a number of gates on the order of N to implement the simulation of an N-site theory. Compared to the fully digital method where the bosons are truncated to Λ and mapped to spins, this hybrid method requires fewer qubits $(N+1)$ compared to $N + N\log(\Lambda+1))$ and fewer gates to reach similar accuracy.

8.2 Implementation of Spin-Phonon Gates

The spin-phonon gates on qubit i, motional mode k and duration τ are defined as

$$\mathrm{SNPx}ik(\phi_{ik},\delta_k,\tau)=\hat{U}_{ik}^{\mathrm{SNPx}}(\tau)=\exp[-i\tau\hat{H}_{ik}^{\mathrm{SNPx}}(\phi_{ik},\delta_k)], \tag{8.17}$$

$$\mathrm{SNPy}ik(\phi_{ik},\delta_k,\tau)=\hat{U}_{ik}^{\mathrm{SNPy}}(\tau)=\exp[-i\tau\hat{H}_{ik}^{\mathrm{SNPy}}(\phi_{ik},\delta_k)], \tag{8.18}$$

$$\mathrm{SNPz}ik(\phi_{ik},\delta_k,\tau)=\hat{U}_{ik}^{\mathrm{SNPz}}(\tau)=\exp[-i\tau\hat{H}_{ik}^{\mathrm{SNPz}}(\phi_{ik},\delta_k)], \tag{8.19}$$

with the Hamiltonians defined as

$$\hat{H}_{ik}^{\mathrm{SNPx}}(\phi_{ik},\delta_k)=\frac{\eta_{ik}\Omega_i}{2}\left(\mathrm{e}^{-i\delta_k t+i\phi_{ik}}\hat{a}_k+\mathrm{e}^{i\delta_k t-i\phi_{ik}}\hat{a}_k^\dagger\right)\hat{\sigma}_i^x, \tag{8.20}$$

$$\hat{H}_{ik}^{\mathrm{SNPy}}(\phi_{ik},\delta_k)=-\frac{\eta_{ik}\Omega_i}{2}\left(\mathrm{e}^{-i\delta_k t+i\phi_{ik}}\hat{a}_k+\mathrm{e}^{i\delta_k t-i\phi_{ik}}\hat{a}_k^\dagger\right)\hat{\sigma}_i^y. \tag{8.21}$$

$$\hat{H}_{ik}^{\mathrm{SNPz}}(\phi_{ik},\delta_k)=-\frac{\eta_{ik}\Omega_i}{2}\left(\mathrm{e}^{-i\delta_k t+i\phi_{ik}}\hat{a}_k+\mathrm{e}^{i\delta_k t-i\phi_{ik}}\hat{a}_k^\dagger\right)\hat{\sigma}_i^z. \tag{8.22}$$

Notice that Eqs. (8.20) and (8.21) are similar to Eq. (5.3) where we apply symmetrically detuned red ($\omega_{L,i}^r=\omega_0-\mu_i$) and blue ($\omega_{L,i}^b=\omega_0+\mu_i$) sidebands on ion i. The spin phase is set by the sum of the red and blue sidebands' phases $\phi_i^s=(\phi_i^r+\phi_i^b)/2$, while the motional phase is set by the red and blue sidebands' phase difference $\phi_i^m=(\phi_i^r-\phi_i^b)/2$. The bichromatic Hamiltonian is

$$\hat{H}_i^{\mathrm{rb}}=\Omega_i\sum_{p=1}^{N}\eta_{ip}\cos(\mu_i t-\phi_i^m)\left(\hat{a}_p^\dagger\mathrm{e}^{i\omega_p t}+\hat{a}_p\mathrm{e}^{-i\omega_p t}\right)\hat{\sigma}_i^{\phi_i^s-\pi/2}. \tag{8.23}$$

We set the detuning close to a mode k, $\mu_i=\omega_k-\delta_k$ with $|\delta_k|<|\omega_k-\omega_{k\pm1}|$. Assuming that the Rabi frequency is small enough compared to the spacing of the modes, $\eta_{ik}\Omega_i<|\omega_k-\omega_{k\pm1}|$, we can ignore the other modes and the terms that rotate at $\mathrm{e}^{\pm i2\omega_k t}$. The Hamiltonian becomes

$$\hat{H}_i^{\mathrm{rb}}\approx\frac{\eta_{ik}\Omega_i}{2}\left(\mathrm{e}^{-i\delta_k t-i\phi_i^m}\hat{a}_k+\mathrm{e}^{i\delta_k t+i\phi_i^m}\hat{a}_k^\dagger\right)\hat{\sigma}_i^{\phi_i^s-\pi/2} \tag{8.24}$$

To implement the $\hat{\sigma}^x$ spin-phonon Hamiltonian $\hat{H}_{ik}^{\mathrm{SNPx}}(\phi_{ik}, \delta_k)$ given in Eq. (8.20), we implement the bichromatic Hamiltonian above and set $\phi_i^r = \pi/2 - \phi_{ik}$, $\phi_i^b = \pi/2 + \phi_{ik}$, hence, $\phi_i^s = \pi/2$, $\hat{\sigma}_i^{\phi_i^s - \pi/2} = \hat{\sigma}_i^x$ and $\phi_i^m = -\phi_{ik}$. To implement the $\hat{\sigma}^y$ spin-phonon Hamiltonian $\hat{H}_{ik}^{\mathrm{SNPy}}(\phi_{ik}, \delta_k)$ given in Eq. (8.21), we set the laser phases of $\hat{H}_i^{\mathrm{rb}}$ to $\phi_i^r = -\pi/2 - \phi_{ik}$ and $\phi_i^b = -\pi/2 + \phi_{ik}$, hence, $\phi_i^s = 0$, $\hat{\sigma}_i^{\phi_i^s - \pi/2} = -\hat{\sigma}_i^y$, $\phi_i^m = -\phi_{ik}$. To implement the $\hat{\sigma}^z$ spin-phonon gate SNPz$ik(\phi_{ik}, \delta_k, \tau)$, we apply the $\hat{\sigma}^x$ or $\hat{\sigma}^y$ spin-phonon gate sandwiched between two single-qubit rotations ($R_y(\pm\pi/2)$ or $R_x(\pm\pi/2)$). Notice that under the Hamiltonian $\hat{H}_i^{\mathrm{rb}}$ only ion i undergoes the spin-dependent phase-space displacement. The other unaddressed ions $j \neq i$ have phase-space displacement independent of their spin states which is described by $\frac{\eta_{ik}\Omega_i}{2}\left(\mathrm{e}^{-i\delta_k t - i\phi_i^m}\hat{a}_k + \mathrm{e}^{i\delta_k t + i\phi_i^m}\hat{a}_k^\dagger\right) \otimes \mathbb{1}_2$.

Similar to Section 5.1, we can use the Magnus expansion to obtain the analytic form of the unitary operators of the spin-phonon gates. Consider the $\hat{\sigma}^x$ spin-phonon gate on ion i, mode k, its unitary evolution is

$$\hat{U}_{ik}^{\mathrm{SNPx}}(\tau) = \exp[-i\tau\hat{H}_{ik}^{\mathrm{SNPx}}(\phi_{ik}, \delta_k)] = \hat{D}\left(\alpha_{ik}(\tau)\hat{\sigma}_i^x\right)\mathrm{e}^{i\chi_{ik}(\tau)}, \tag{8.25}$$

with the displacement operator $\hat{D}(\beta_{ik}) = \mathrm{e}^{\beta_{ik}\hat{a}_k^\dagger - \beta_{ik}^*\hat{a}_k}$, the displacement angle $\beta_{ik} = \alpha_{ik}(\tau)\hat{\sigma}_i^x$,

$$\alpha_{ik}(\tau) = -i\frac{\eta_{ik}\Omega_i}{2}\int_0^\tau dt\ \mathrm{e}^{i\delta_k t - i\phi_{ik}} = \frac{1}{2}\eta_{ik}\Omega_i\mathrm{e}^{-i\phi_{ik}}\frac{1 - \mathrm{e}^{i\delta_k\tau}}{\delta_k}, \tag{8.26}$$

and the geometric phase angle

$$\chi_{ik}(\tau) = \frac{1}{4}\eta_{ik}^2\Omega_i^2\int_0^\tau dt_1\int_0^{t_1} dt_2\ \sin(\delta_k(t_1 - t_2)) = \frac{1}{4}\eta_{ik}^2\Omega_i^2\ \frac{\sin(\delta_k\tau) - \delta_k\tau}{\delta_k^2}. \tag{8.27}$$

Eq. (8.25) is similar to Eq. (5.5) except that the second factor containing χ_{ik} is now a pure phase, not a spin-spin entanglement since there is only one ion involved. The first term shows spin-motion entanglement since the displacement angle β_{ik} is spin-dependent.

Rewriting the displacement operator in terms of $\hat{x} = \frac{\hat{a}+\hat{a}^\dagger}{\sqrt{2}}$ and $\hat{p} = \frac{\hat{a}-\hat{a}^\dagger}{i\sqrt{2}}$, we have (where indices are suppressed for brevity)

$$\hat{D}(\beta) = \exp\left[\hat{x}\ \frac{\beta-\beta^*}{\sqrt{2}} - i\hat{p}\ \frac{\beta+\beta^*}{\sqrt{2}}\right] = \exp(i\hat{x}\Delta p - i\hat{p}\Delta x). \tag{8.28}$$

We can see that the spin-phonon gate provides a momentum kick of magnitude $\Delta p = \sqrt{2}\,\mathrm{Im}(\beta)$ and a translation by $\Delta x = \sqrt{2}\,\mathrm{Re}(\beta)$. A similar conclusion can be drawn for the $\hat{\sigma}^y$ spin-phonon gate, the corresponding displacement angle is $\beta_{ik} = -\alpha_{ik}(\tau)\hat{\sigma}_i^y$.

To test the implementation of the spin-phonon gates, first we consider the case of $\phi_{ik} = 0$ and observe that the dynamics depend on the detuning δ_k from the mode k.

- Test 1 (Detuning test): We prepare the ion i in the state $|0\rangle$, which is a superposition of the basis states $|\pm\rangle$ of the $\hat{\sigma}^x$ spin-phonon gate. Then we apply the $\hat{\sigma}^x$ spin-phonon gate for different duration τ and measure the overlap of the ion state $|\psi_i(\tau)\rangle$ with the bright state $|\langle 1|\psi_i(\tau)\rangle|^2$. For different δ_k, we should see dips with a period of $2\pi/\delta_k$. The bright probability is given by

$$\begin{aligned}
|\langle 1|\psi_i(\tau)\rangle|^2 &= |\,\langle 1|\,\hat{U}_{ik}^{\mathrm{SNPx}}(\tau)\,|0\rangle\,|^2 = |\,\langle 1|\,\hat{D}\left(\alpha_{ik}(\tau)\hat{\sigma}_i^x\right)\mathrm{e}^{i\chi_{ik}(\tau)}\,|0\rangle\,|^2 \\
&= \frac{1}{2}\left(1 - \mathrm{e}^{-2|\alpha_{ik}(\tau)|^2}\right) \\
&= \frac{1}{2}\left\{1 - \exp\left[-\left(\frac{2\eta_{ik}\Omega_i}{\delta_k}\right)^2 \sin^2\left(\frac{\delta_k\tau}{2}\right)\right]\right\}.
\end{aligned} \tag{8.29}$$

- Test 2 (Phase counting test): We repeat the same experiments above but instead of varying τ, we apply M $\hat{\sigma}^x$ spin-phonon gates, each with duration $\Delta t = \tau/M$. We should see similar results as the first experiment for different δ_k with a small deviation coming from Trotterization (since we are approximating the long pulse with many short pulses and the Hamiltonian at different times do not commute).

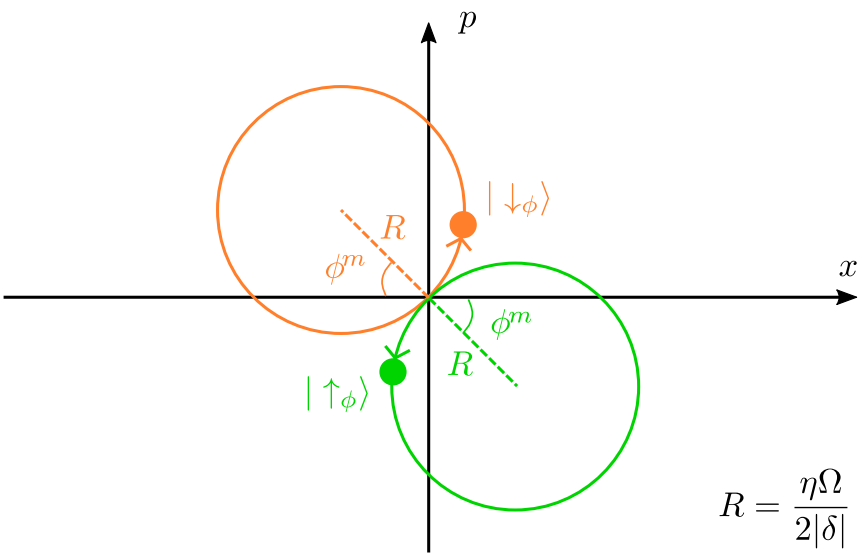

Figure 8.1: Phase space evolution of an ion in a single-ion chain under the $\hat{\sigma}^\phi$ spin-phonon gate of detuning δ, phase ϕ^m and duration τ. The ion is initialized in $\psi_0 = \frac{1}{2}(|\uparrow_\phi\rangle + |\downarrow_\phi\rangle)$. The evolution is described by $\hat{U}^{\mathrm{SNP}\phi}(\tau) = \hat{D}(\beta(\tau))\mathrm{e}^{i\chi(\tau)}$, where $\beta(\tau) = \hat{\sigma}^\phi \frac{\eta\Omega}{2\delta}\mathrm{e}^{-i\phi^m}(1-\mathrm{e}^{i\delta\tau})$ is spin-dependent, $\chi(\tau) = \left(\frac{\eta\Omega}{2\delta}\right)^2(\sin(\delta\tau) - \delta\tau)$. The ion follows the orange (green) trajectory if it is in $|\downarrow_\phi\rangle$ ($|\uparrow_\phi\rangle$). $\phi = 0$ for $\hat{\sigma}^x$, $\phi = \frac{\pi}{2}$ for $\hat{\sigma}^y$. $\hat{\sigma}^\phi|\uparrow_\phi\rangle = |\uparrow_\phi\rangle$, $\hat{\sigma}^\phi|\downarrow_\phi\rangle = -|\downarrow_\phi\rangle$.

Then we consider the case of $\phi_{ik} \neq 0$ and observe how the dynamics depend on the phase ϕ_{ik} of the displacement. We note that an addition of π to the phase of a spin-phonon gate turns the gate into its inverse.

- Test 3 (Phonon coherence test): We prepare the ion i in the state $|0\rangle$ and apply a $\hat{\sigma}^x$ spin-phonon gate with phase $\phi_{ik} = 0$, and a certain detuning and duration. Then we wait for time t to apply its inverse, which is a pulse with the same duration and detuning but a phase $\phi_{ik} = \pi$. This experiment also shows any decoherence in the motional degrees of freedom. We repeat this experiment for different values of detuning and duration.

- Test 4 (Phonon phase test): We repeat the same experiment above but with the phase

of the first spin-phonon gate set to $\phi_{ik} = \phi'$ and the phase of the second spin-phonon gate set to $\phi_{ik} = \phi' + \pi$. The result of the experiment should be independent of ϕ' if both pulses are applied, but be dependent on ϕ' if only the first pulse is applied.

8.2.1 Preliminary Experimental Results of the Tests

For all the tests, the ion is initialized in state $|0\rangle$ (dark).

Test 1: Applying a long pulse of $\hat{\sigma}^x$ spin-phonon and vary the duration, then measure in the probability of the final state $|\psi_i(\tau)\rangle$ to be in the bright state $|1\rangle$ as given by Eq. (8.29).

Eq. (8.29) shows that the spin-motion is disentangled at the interval of $2\pi/\delta_k$, at which the ion returns to its initial state and the bright probability vanishes. This is useful for finding uncorrected Stark shifts to the motional mode when applying the spin-phonon gate. Between the intervals, the ion is in a spin-motion entangled state, $|\psi_i(\tau)\rangle = \frac{1}{\sqrt{2}}(|+\rangle\,|\alpha_{ik}(\tau)\rangle + |-\rangle\,|-\alpha_{ik}(\tau)\rangle)$, hence has a non-zero probability of being bright.

The experimental data in Fig. 8.2 show the expected dips but not at the intervals corresponding to the set detuning, which indicates that there is inaccuracy in determining the motional mode frequencies in the experiment. The amplitudes of the dips also decrease for longer pulses. This loss of contrast cannot be explained by motional heating or imperfect cooling (where $\bar{n} \neq 0$). It can partially be explained by adding a variance to the motional mode frequencies, i.e., the detuning follows a Gaussian distribution with mean μ_{δ_k} and variance $\sigma^2_{\delta_k}$. By averaging the probability given by Eq. (8.29) for different detunings δ_k sampled from the distribution with μ_{δ_k} and σ_{δ_k} as fit parameters (Table 8.1), we obtain fitting curves in Fig. 8.2.

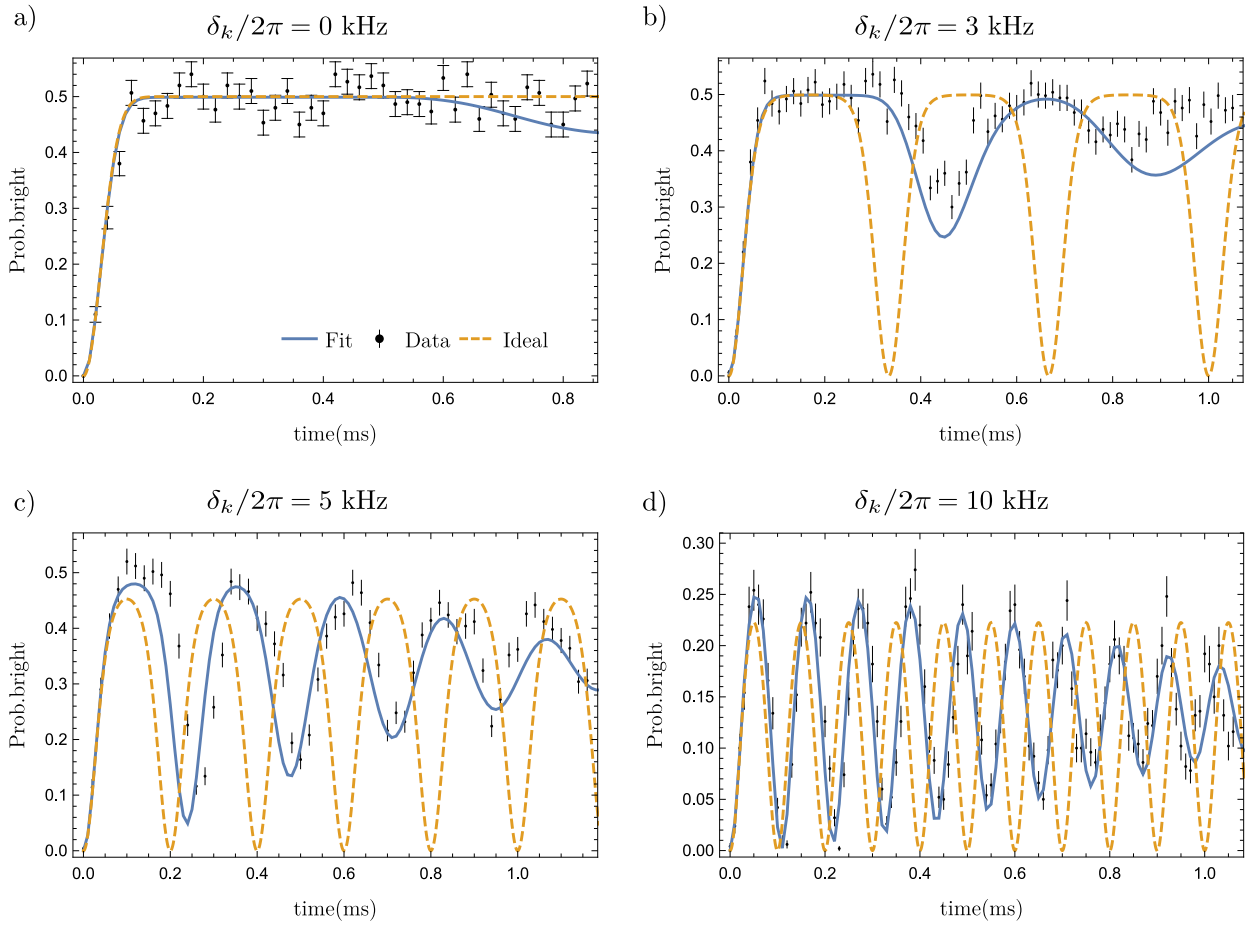

Figure 8.2: Experimental results for $|\langle 1|\psi_i(\tau)\rangle|^2$ when applying a single pulse of $\hat{\sigma}^x$ spin-phonon gates on a single ion. The spin-phonon phase is $\phi_m = 0$, the detuning is set to $\delta_k/2\pi = 0$ kHz (a), $\delta_k/2\pi = 3$ kHz (b), $\delta_k/2\pi = 5$ kHz (c), $\delta_k/2\pi = 10$ kHz (d) and the duration is scanned. The ideal curves (yellow dashed lines) are given by Eq. (8.29) while the fits (blue lines) are based on the error model described in the preceding text. The fit parameters are given in Table 8.1. Mismatch in the dips' positions between ideal curves and the fit suggest an inaccuracy in determining motional frequencies due to uncompensated Stark shifts. The reduction in the contrast of the dips can be explained by the fluctuation of the motional frequencies.

The variance corresponds to the fluctuation of the mode frequencies in the experiment.

However, the fits do not agree very well with the experiment data in Fig. 8.2a,b,c. In particular, it seems that the interval of the dips are not uniform, which indicates a drift in the mean of the distribution for the detuning.

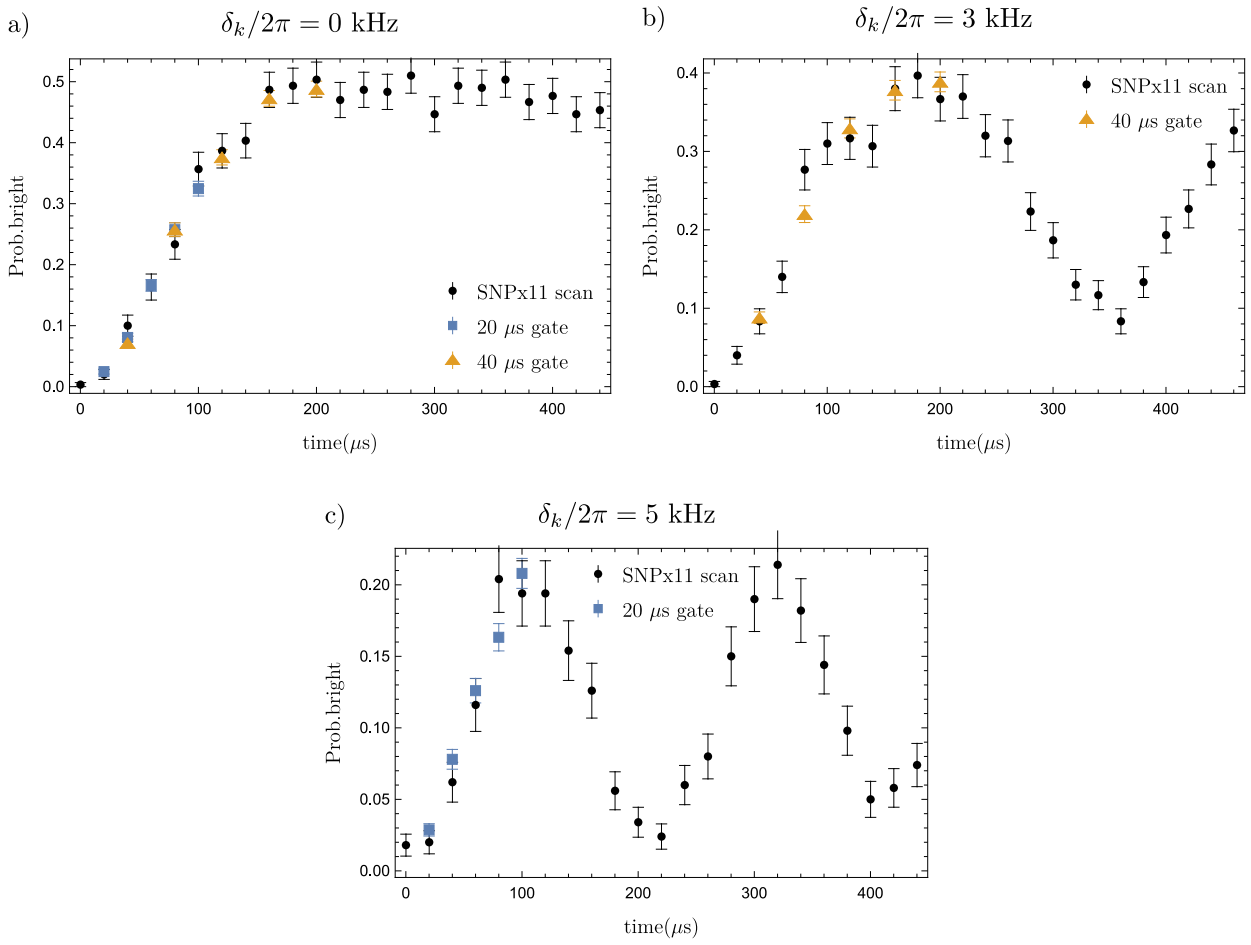

Figure 8.3: Experimental results for $|\langle 1|\psi_i(\tau)\rangle|^2$ when applying many short pulses of fixed durations ($\tau = 20$ μs for blue, $\tau = 40$ μs for orange) compared to one long pulse with variable durations (SNPxik, black). The pulse is a $\hat{\sigma}^x$ spin-phonon gate on the first ion in a 3-ion chain, using COM mode ($i = 1, k = 1$). The spin-phonon phase $\phi_{ik} = 0$, the detunings are $\delta_k/2\pi = 0$ kHz (a), $\delta_k/2\pi = 3$ kHz (b), $\delta_k/2\pi = 5$ kHz (c). The dynamics under many short pulses is the same as the dynamics under a long pulse, which indicates that phase coherence is maintained between pulses.

Test 2: Repeat Test 1 with short pulses. This test is to verify if there is phase coherence between spin-phonon gates. If it is, the results of the experiment done with the short pulses should be identical to those done with long pulses (Fig. 8.3). The phase coherence between gates (for both spin gates and spin-phonon gates) are maintained by keeping track of the phases of the driving fields, also known phase counting. If the driving fields are generated by an analog oscillator, the phase counting is done automatically as the oscillator advances in time. If the driving fields are generated digitally by an AWG (like in our case, we create a time series of the amplitude of the fields), the phase counting must be done programmatically by calculating and storing the phases of the waveforms. For a multi-tone driving field, the phase of each tone advances at the rate of the tone's frequency. To implement Eq. (8.7), we need to store the phases of $2N(N+1)$ tones for the sidebands and N tones for the carriers (each ion has a different phase). This is the experimental version of moving into the interaction picture. Figure 8.3 shows that the phase counting is indeed performed correctly in our experiment.

Table 8.1: Fit parameters used in Fig. 8.2

Fig.	$\delta_k/2\pi$(kHz)	$\mu_{\delta_k}/2\pi$(kHz)	$\sigma_{\delta_k}/2\pi$(kHz)
a	0	-1	0.25
b	3	2.2	0.25
c	5	4.1	0.25
d	10	9	0.25

Test 3: Verify the control of the spin-phonon phase and the phonon coherence for $\phi_{ik} = 0$. We evolve the ion forward under the spin-phonon gate with detuning $\delta_k/2\pi = 0$

kHz (a spin-dependent momentum kick) at a certain duration then evolve backward by applying the same gate with π added phase (kick-back). The ion should return to its initial state ($|0\rangle$) after the second pulse. We experimentally confirmed this (Fig. 8.4).

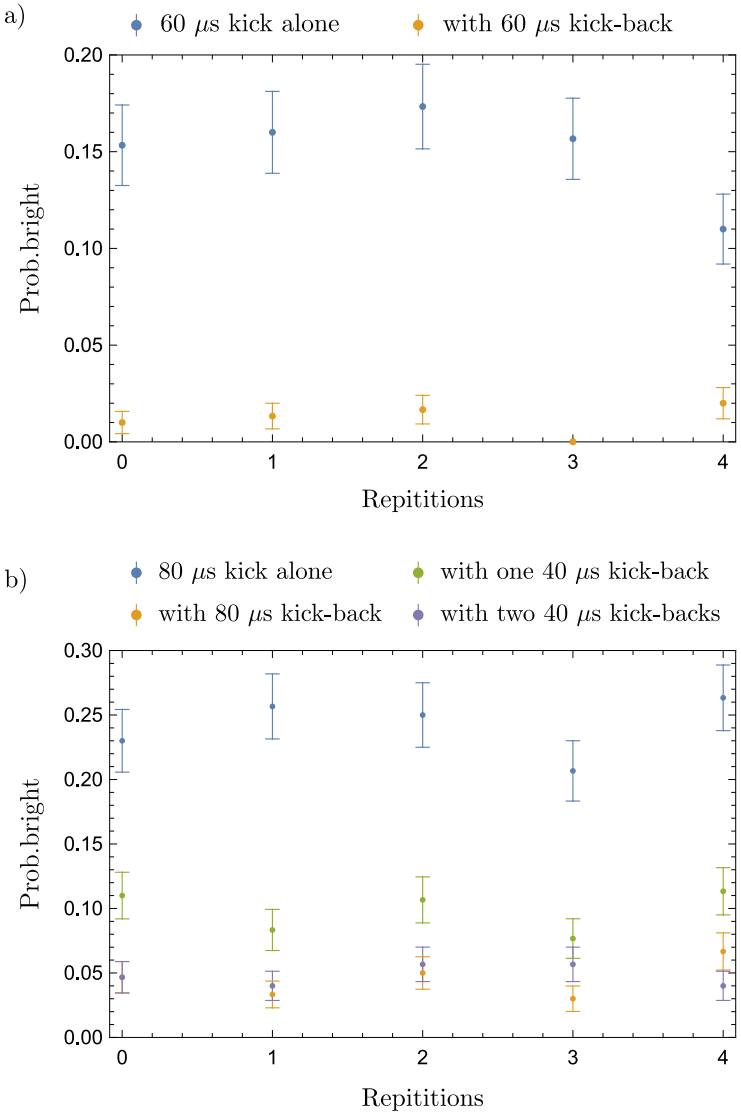

Figure 8.4: Experimental results for $|\langle 1|\psi_i(\tau)\rangle|^2$ when applying a spin-phonon gate with detuning $\delta_k/2\pi = 0$ kHz (a spin-dependent momentum kick) and its inverse (kick-back) at different durations. a) 60 μs kick and kick-back. b) 80 μs kick, with a 80 μs kick-back, a 40 μs kick-back, and two 80 μs kick-backs. The phase kick-back is experimentally shown to reverse the time evolution of the kick, which indicates a good control of the phonon phase.

Test 4: Verify the control of the spin-phonon phase for $\phi_{ik} \neq 0$. This test is ongoing. In principle, it is the general case of Test 3 and should work straightforwardly.

8.3 Dynamical Generation of Fermionic Mass with Realistic Parameters

In Section 8.2, we have seen how the Hamiltonian describing the Yukawa interaction at low energies can be engineered using native interactions of trapped ions. In this section, we explore the interesting physical phenomena that can be observed when a system of fermions and bosons evolves under this Hamiltonian and whether the regimes of interest in the model are within the control of our trapped-ion experiment.

One fascinating phenomenon is the generation of mass of the fermions under the Yukawa interaction even when the system starts at zero bare fermionic mass. The initial state of the system is the ground state of the non-interacting Hamiltonian ($g = 0$), which means there are no anti-fermions (odd sites are occupied), no fermions (even sites are unoccupied) and no bosons, i.e.,

$$|\psi_0\rangle_{fb} = |\underbrace{1,0,1,0,...,1,0}_{N}\rangle_f |\underbrace{0,0,...,0}_{N}\rangle_b \tag{8.30}$$

Since the Jordan-Wigner transformation maps ψ_i to σ_i^-, $|1\rangle_f$ is mapped to $|\uparrow\rangle = \begin{pmatrix} 1 \\ 0 \end{pmatrix} =$ $|0\rangle_s$ and $|0\rangle_f$ is mapped to $|\downarrow\rangle = \begin{pmatrix} 0 \\ 1 \end{pmatrix} = |1\rangle_s$. Hence in the spin-phonon basis,

$$|\psi_0\rangle_{sp} = |\underbrace{0,1,0,1,...,0,1}_{N}\rangle_s |\underbrace{0,0,...,0}_{N}\rangle_p. \tag{8.31}$$

We then perform a quench, i.e., applying the Hamiltonian with the interaction $g \neq 0$ and let the system evolve. We measure the overlap with the initial state $|\langle\psi_0|\psi(t)\rangle|^2$, also known as the Loschmidt echo, and the boson number $\langle N_d \rangle$, where

$$N_d = \frac{1}{N} \sum_{k=-N/2}^{N/2-1} \hat{d}_k^\dagger \hat{d}_k. \tag{8.32}$$

8.3.1 Quantum Simulation via Trotterization

To perform the unitary evolution of the Yukawa model, we employ the first-order Trotterization, where $\hat{\mathcal{U}}(t) = \prod_{k=1}^{t/\delta t} \hat{\mathcal{U}}_k(\delta t)$. Following the odd-even ordering of terms as discussed in Section 7.2.1, we have

$$\begin{aligned}\hat{\mathcal{U}}(\delta t) &= \mathrm{e}^{-i\delta t\left(\tilde{H}^{(I)}+\tilde{H}^{(III)}\right)} \\ &\approx \mathrm{e}^{-i\delta t\,\hat{H}^z} \times \prod_{j}^{N+1} \prod_{m=1}^{N} \mathrm{e}^{-i\delta t\,\hat{H}_{ik}^{\mathrm{SNPz}}(\phi_{ik},\varepsilon_m)} \times \prod_{j=1}^{(N/2)} \mathrm{e}^{-i\delta t\,\hat{H}_{2j,2j+1}^{h}} \prod_{j=1}^{N/2} \mathrm{e}^{-i\delta t\,\hat{H}_{2j-1,2j}^{h}},\end{aligned} \tag{8.33}$$

where

$$\hat{H}^z = \frac{m_\psi}{2} \sum_{j=1}^{N} (-1)^j \hat{\sigma}_i^z, \tag{8.34}$$

$$\hat{H}_{j,j+1}^h = \frac{1}{4b} (\hat{\sigma}_i^x \hat{\sigma}_{j+1}^x + \hat{\sigma}_i^y \hat{\sigma}_{j+1}^y). \tag{8.35}$$

The angles for the spin gates are

$$\theta_{j(j+1)}^h = \begin{cases} \frac{\delta t}{4b}, & \text{if } 1 \leq j < N \\ -\frac{\delta t}{4b} = \theta_{N1}^h, & \text{if } j = N \end{cases} \tag{8.36}$$

$$\theta_i^z = m_\psi (-1)^j \delta t. \tag{8.37}$$

Notice that since our gate definition is $R_i^z = \mathrm{e}^{-i\theta_i^z/2\sigma_i^z}$ our angle θ_i^z is twice as large as given in [237]. Angles for the spin-phonon gates are

$$\theta_{ik}^{\mathrm{SNPz}} = \theta_{N+1,m}^{\mathrm{SNPz}} = \sqrt{\frac{g^2 b}{8N\varepsilon_m}}\delta t, \tag{8.38}$$

$$\varepsilon_m = \sqrt{\left(\frac{2\pi}{Nb}(m - N/2 - 1)\right)^2 + m_\varphi^2}, \tag{8.39}$$

$$\phi_{ik} = \frac{2\pi j}{N}(m - N/2 - 1). \tag{8.40}$$

When we apply a spin-phonon gate in the rotating frame, we also unintentionally apply $\sum_m \varepsilon_m \hat{a}_m^\dagger \hat{a}_m$. Therefore when we apply $N+1$ spin-phonon gates we apply $\sum_m (N+1)\,\varepsilon_m \hat{a}_m^\dagger \hat{a}_m$. Hence we need to divide the added detuning of the rotating frame by $N+1$.

8.3.2 Feasibility of the parameters

In all of the above discussion, we did not specify the length scale and time scale of the interaction. We need to look into this to evaluate whether the range of control in the trapped ion experiment is good enough to cover the relevant range of parameters in the model. For a spin-phonon gate on ion j and mode m whose gate time τ is determined by the available Rabi frequency Ω_i and Lamb-Dicke parameter η_{ik}, the angle of the spin-phonon gate is given by

$$\theta_{ik}^{\mathrm{SNPz}} = \frac{\eta_{ik}\Omega_i}{2}\tau. \tag{8.41}$$

This angle $\theta_{ik}^{\mathrm{SNPz}}$ can also be related to the model parameters by Eq. (8.38). The detuning of the gate $\tilde{\varepsilon}$ must satisfies $\tilde{\varepsilon}\tau = \varepsilon\delta t$, where ε is the energy of a boson and δt is the time step in the model.

In our experiment, $\tilde{\varepsilon}$ can vary from 100 Hz to 100 kHz, and τ from 1 μs to 1 ms.

That means $10^{-4} \leq \varepsilon\delta t \leq 10^{2}$. If we take $\varepsilon \approx 1$ MeV, then $10^{-4}(\text{MeV})^{-1} \leq \delta t \leq 10^{2}(\text{ MeV})^{-1}$. Since $(\text{MeV})^{-1} \approx 10^{-22}$ s, it follows that 10^{-26} s $\leq \delta t \leq 10^{-20}$s. The timescale of the interaction is on the order of 10^{-23} s, therefore consistent with intrinsic timescale of strong interactions in nature (although our model is a simplified 1+1 D model of Yukawa interactions).

8.3.3 Example of a Two-Site Theory

For $N = 2$, we have 1 fermionic field, 1 anti-fermionic field, and 2 bosonic fields. Together with the ancilla, in total, we need 3 ions. Table 8.2 shows the values of parameters that give rise to interesting dynamics. For now, we focus on the first set of parameters. The initial state is $|\psi_0\rangle_{sp} = |0,1\rangle_s |0,0\rangle_p$. As seen from Fig. 8.5, $\delta t = 1$ is small enough to observe the important features of the evolution. From Eq. (8.1), we see that for $N = 2$, there is no fermion hopping.

Table 8.2: Parameters for $N = 2$. The first four columns are input parameters for the model. The last column shows the maximum boson population of all times. It is the maximum of $\langle N_d \rangle$, the boson population per mode on average according to Eq. (8.32), multiplied by the number of modes N.

No.	b	g	m_φ	m_ψ	$N \times \langle N_d \rangle$
1	1	2	1.5	1	≤ 1.5
2	1	0.5	1.0	1	≤ 1
3	1	5	2	1	≤ 3.5

Table 8.3: Angles (rad) for the first set of parameters for $N = 2$, $\delta t = 1$

No.	b	g	m_φ	m_ψ	δt	θ^h_{12}	θ^z_i	$\theta^{\text{SNPz}}_{j,1}$	$\theta^{\text{SNPz}}_{j,2}$	$\phi_{j,1}$	$\phi_{j,2}$
1	1	2	1.5	1	1	0.25	$(-1, 1)$	0.267977	0.408248	$(-\pi, -2\pi)$	(0, 0)

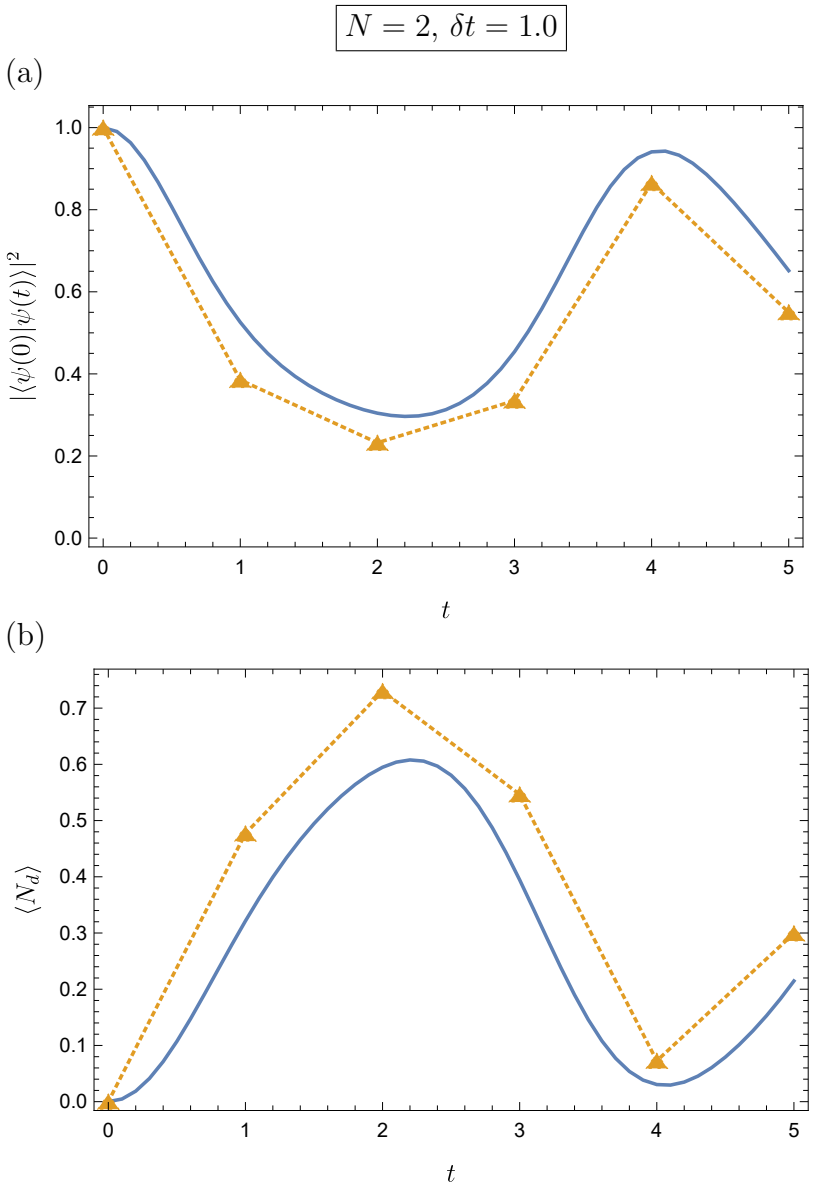

Figure 8.5: Numerical simulation of the 1D Lattice Yukawa model for $N = 2, g = 2, b = 1, m_\varphi = 1.5, m_\psi = 1$ with exact diagonalization (solid line) and Trotterization with $\delta t = 1$ (triangles). The numerics are done with the bosonic cutoff $\Lambda = 7$.

The dynamics for the two-site theory comes purely from fermion-boson interaction since the fermion hopping term, Eq. (8.8), cancels out for $N = 2$ due to the PBCs. If the Trotter step size is reduced to $\delta t = 0.5$, the Trotter errors are further reduced and the Trotterized evolution gets closer to the exact evolution (Fig. 8.6).

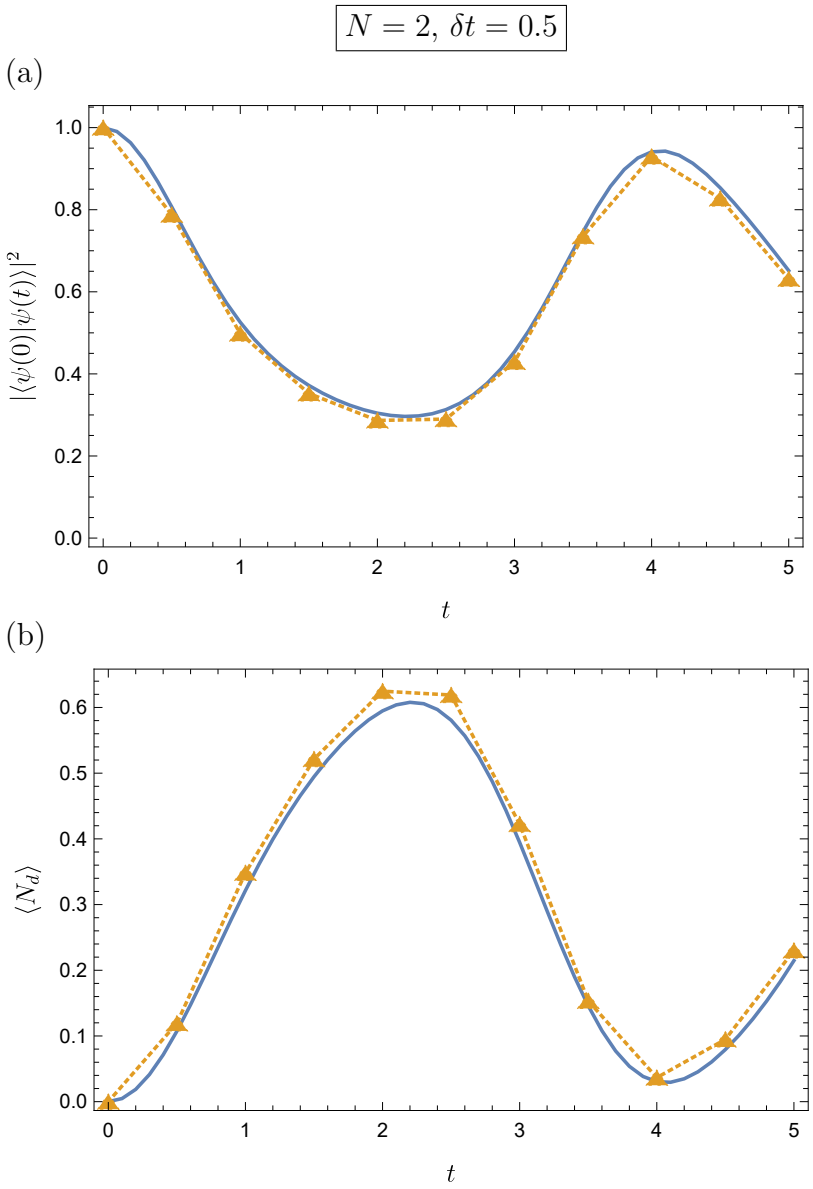

Figure 8.6: Numerical simulation of the 1D Lattice Yukawa model for $N = 2, g = 2, b = 1, m_\varphi = 1.5, m_\psi = 1$ with exact diagonalization (solid line) and Trotterization with $\delta t = 0.5$ (triangles). The numerics are done with the bosonic cutoff $\Lambda = 7$.

We choose the bosonic cutoff of $\Lambda = 7$ (the boson becomes an 8-level system) to make sure that the observed dynamics is unaffected by the cutoff. As we can see from the last column Table 8.2, the number of bosons generated is fewer than 1.5, hence will not be affected by the cutoff of 7.

8.3.4 Example of a Four-Site Theory

For $N = 4$, we have 2 fermionic fields, 2 anti-fermionic fields, and 4 bosonic fields. Together with the ancilla, in total, we need 5 ions. The initial state is $|\psi_0\rangle_{sp} = |0,1,0,1\rangle_s |0,0,0,0\rangle_p$. Note that Eq. (8.1) shows that for $N > 2$, there is fermion hopping dynamics. Therefore we expect some qualitative difference in the Loschmidt echo between the two-site ($N = 2$) and four-site ($N = 4$) theories. Using the first set of parameters in Table 8.2, we perform the numerical simulation of the Yukawa interaction. We choose the bosonic cutoff of 7 ($\Lambda = 8$) to make sure that the observed dynamics is unaffected by the cutoff. As we see in Figs. 8.7 and 8.8, the number of bosons generated is $N \times \langle N_d \rangle = 2.4$, hence the dynamics is unaffected by the cutoff.

The numerical results show that for $N = 4$, the Trotter step of $\delta = 1$ causes too much Trotter errors for both the fermion (Loschmidt echo) and the boson ($\langle N_d \rangle$) dynamics (Fig. 8.7). If we reduce the Trotter step to $\delta = 0.5$, Trotter errors are significantly reduced (Fig. 8.8).

The next step is to perform these experiments and see whether the experimental data agree with the Trotterized evolution. If they do not, we need to understand why and what to improve to obtain the expected results. Then using the experiment we can perform

the (real) quantum simulation with model parameters that are inaccessible to a classical computer, such as ones that result in higher number of bosons generated demanding larger cutoffs.

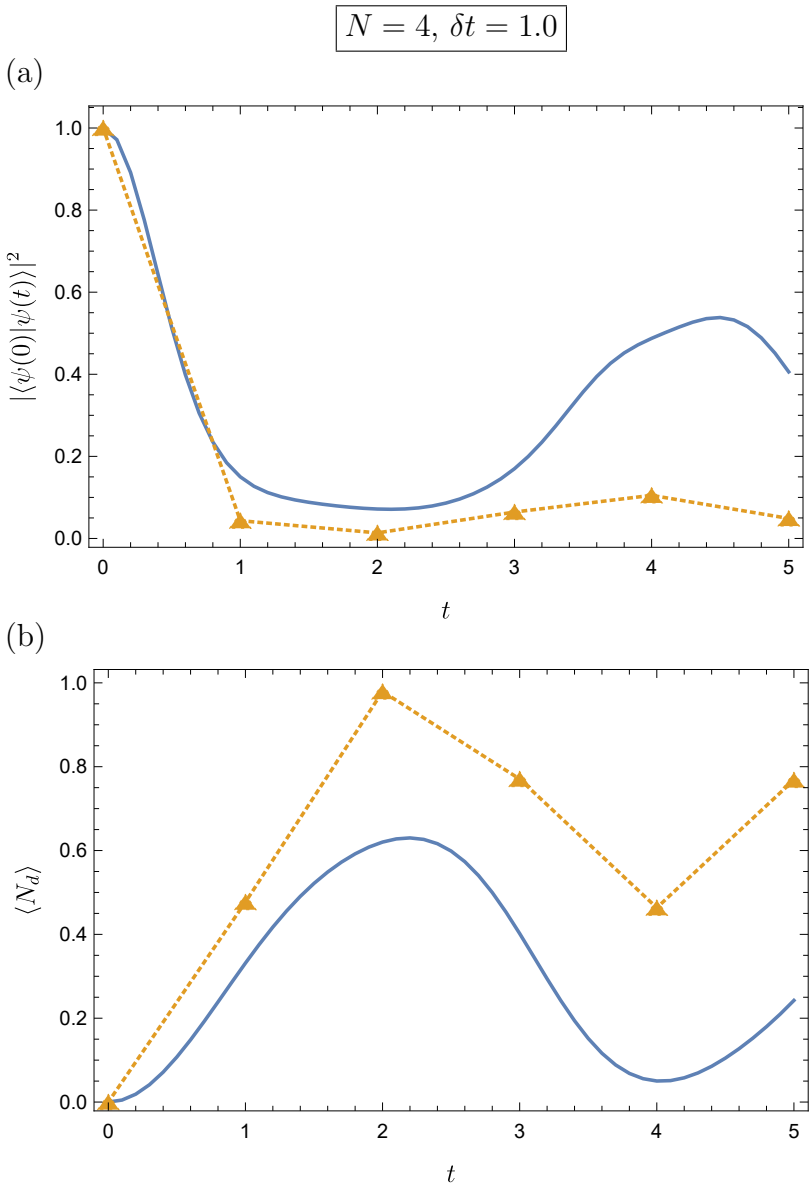

Figure 8.7: Numerical simulation of the 1D Lattice Yukawa model for $N = 4, g = 2, b = 1, m_\varphi = 1.5, m_\psi = 1$ with exact diagonalization (solid line) and Trotterization with $\delta t = 1$ (triangles). The numerics are done with the bosonic cutoff $\Lambda = 7$.

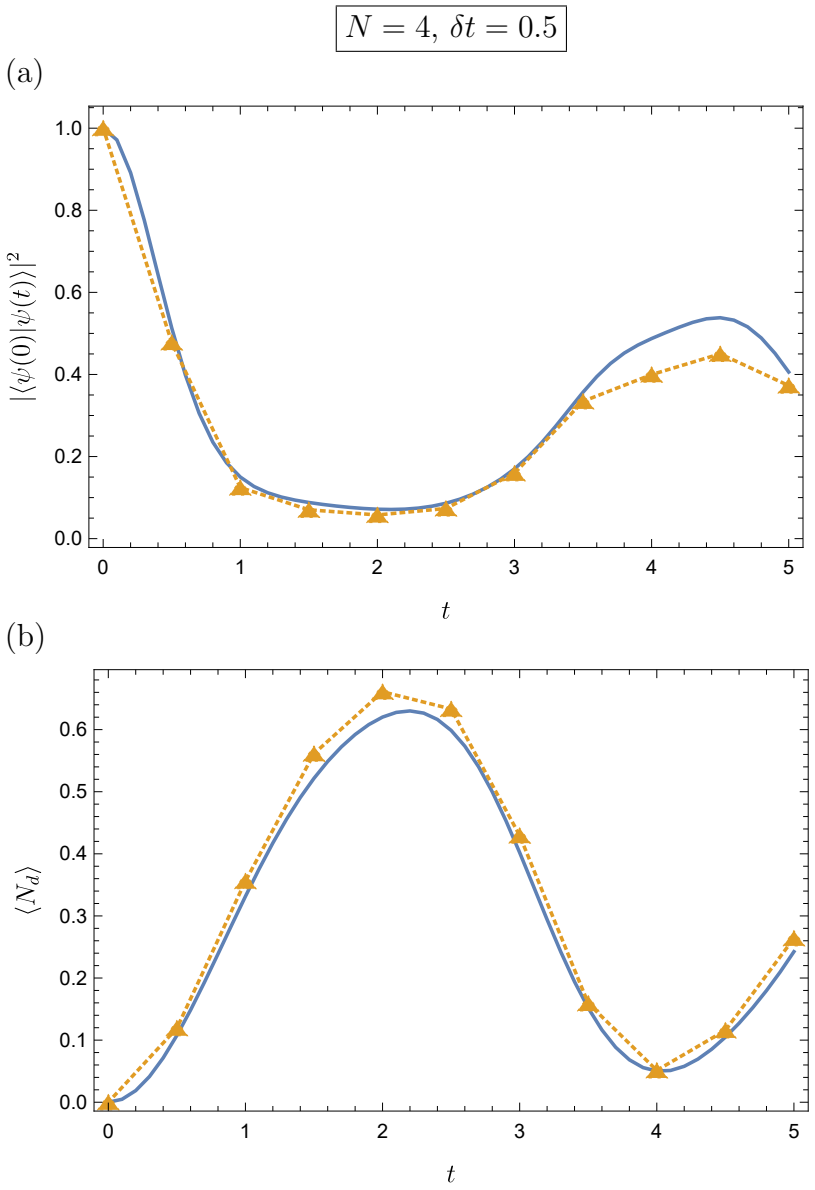

Figure 8.8: Numerical simulation of the 1D Lattice Yukawa model for $N = 4, g = 2, b = 1, m_\varphi = 1.5, m_\psi = 1$ with exact diagonalization (solid line) and Trotterization with $\delta t = 0.5$ (triangles). The numerics are done with the bosonic cutoff $\Lambda = 7$.

Chapter 9: Outlook

As we explore new frontiers with quantum simulations using trapped ions, we are entering an exciting phase that could change both quantum computing and many areas of science. This dissertation has laid the groundwork by exploring the manipulation of quantum information encoded in ions, developing techniques for high-fidelity entanglement, and advancing the simulation of complex quantum phenomena, such as those described by the Schwinger model and the Yukawa model in high-energy and nuclear physics. Looking forward, the challenge lies in transcending the limitations of current ion-trap architectures, harnessing advanced error correction techniques, and integrating scalable designs that can accommodate more qubits. This pursuit is not merely technical but a quest for deeper understanding of atomic and optical physics, of quantum information and of the algorithms that will tackle classically intractable problems. As we refine our control over trapped ions, we edge closer to realizing the full potential of quantum computing, heralding a new era of scientific exploration and technological innovation.

Chapter A: Jordan-Wigner Transformation

This appendix shows the derivation of Hamiltonian terms that involve the fermionic fields under the Jordan-Wigner (JW) transformation, which is relevant to Chapters 7 and 8. The JW transformation converting a fermionic operator to a string of spin operators is given by

$$\hat{\psi}_j = \prod_{l=1}^{j-1}(i\hat{\sigma}_l^z)\hat{\sigma}_j^- \tag{A.1}$$

$$\hat{\psi}_j^\dagger = \prod_{l=1}^{j-1}(-i\hat{\sigma}_l^z)\hat{\sigma}_j^+ \tag{A.2}$$

A.1 Fermionic Hopping Terms

The fermionic hopping terms with open boundary condition (OBC) is

$$\sum_{j=1}^{N} i(\hat{\psi}_j^\dagger\hat{\psi}_{j+1} - \hat{\psi}_{j+1}^\dagger\hat{\psi}_j) \tag{A.3}$$

After JW

$$\hat{\psi}_j^\dagger\hat{\psi}_{j+1} = \prod_{l=1}^{j-1}(-i\hat{\sigma}_l^z)\hat{\sigma}_j^+\prod_{l'=1}^{j}(i\hat{\sigma}_{l'}^z)\hat{\sigma}_{j+1}^- \tag{A.4}$$

Since $[\hat{\sigma}_l^z, \hat{\sigma}_j^\pm] = [\hat{\sigma}_l^z, \hat{\sigma}_j^z] = 0$ for $l \neq j$, $(\hat{\sigma}_l^z)^2 = \mathbb{1}_2$ and $\hat{\sigma}_j^+\hat{\sigma}_j^z = -\hat{\sigma}_j^+ = -\hat{\sigma}_j^z\hat{\sigma}_j^+$

$$\hat{\psi}_j^\dagger\hat{\psi}_{j+1} = \hat{\sigma}_j^+(i\hat{\sigma}_j^z)\hat{\sigma}_{j+1}^- = -i\hat{\sigma}_j^+\hat{\sigma}_{j+1}^- \tag{A.5}$$

Similarly, $\hat{\sigma}_j^- \hat{\sigma}_j^z = \hat{\sigma}_j^- = -\hat{\sigma}_j^z \hat{\sigma}_j^-$

$$\hat{\psi}_{j+1}^\dagger \hat{\psi}_j = \prod_{l=1}^{j} (-i\hat{\sigma}_l^z) \hat{\sigma}_{j+1}^+ \prod_{l'=1}^{j-1} (i\hat{\sigma}_{l'}^z) \hat{\sigma}_j^- \tag{A.6}$$

$$= \hat{\sigma}_{j+1}^+ (-i\hat{\sigma}_j^z) \hat{\sigma}_j^- = i\hat{\sigma}_{j+1}^+ \hat{\sigma}_j^- \tag{A.7}$$

Therefore

$$i(\hat{\psi}_j^\dagger \hat{\psi}_{j+1} - \hat{\psi}_{j+1}^\dagger \hat{\psi}_j) = (\hat{\sigma}_j^+ \hat{\sigma}_{j+1}^- + \hat{\sigma}_{j+1}^+ \hat{\sigma}_j^-) \tag{A.8}$$

With periodic boundary condition (PBC) we have the extra term

$$i(\hat{\psi}_N^\dagger \hat{\psi}_1 - \hat{\psi}_1^\dagger \hat{\psi}_N) = i \prod_{l=1}^{N-1} (-i\hat{\sigma}_l^z) \hat{\sigma}_N^+ \hat{\sigma}_1^- - i\hat{\sigma}_1^+ \prod_{l=1}^{N-1} (i\hat{\sigma}_l^z) \hat{\sigma}_N^- \tag{A.9}$$

$$= -i\hat{\sigma}_N^+ \hat{\sigma}_1^- \prod_{l=1}^{N-1} (-i\hat{\sigma}_l^z) - i\hat{\sigma}_1^+ \hat{\sigma}_N^- \prod_{l=1}^{N-1} (i\hat{\sigma}_l^z) \tag{A.10}$$

$$= -i\hat{\sigma}_N^+ \hat{\sigma}_1^- \prod_{l=1}^{N-1} (-i\hat{\sigma}_l^z) \left(\frac{-i\hat{\sigma}_N^z}{i} \right) - i\hat{\sigma}_1^+ \hat{\sigma}_N^- \prod_{l=1}^{N-1} (i\hat{\sigma}_l^z) \left(\frac{i\hat{\sigma}_N^z}{i} \right) \tag{A.11}$$

$$= -\hat{\sigma}_N^+ \hat{\sigma}_1^- \prod_{l=1}^{N} (-i\hat{\sigma}_l^z) - \hat{\sigma}_1^+ \hat{\sigma}_N^- \prod_{l=1}^{N} (i\hat{\sigma}_l^z) \tag{A.12}$$

$$= -(\hat{\sigma}_N^+ \hat{\sigma}_1^- (-1)^N + \hat{\sigma}_1^+ \hat{\sigma}_N^-) \prod_{l=1}^{N} (i\hat{\sigma}_l^z) \tag{A.13}$$

We use $\hat{\sigma}_N^+ \hat{\sigma}_N^z = -\hat{\sigma}_N^+$ and $\hat{\sigma}_N^- \hat{\sigma}_N^z = \hat{\sigma}_N^-$ to go from Eq. (A.10) to Eq. (A.11). Since N is even (N must be even for the Hamiltonian under PBCs to be Hermitian)

$$i(\hat{\psi}_N^\dagger \hat{\psi}_1 - \hat{\psi}_1^\dagger \hat{\psi}_N) = -(\hat{\sigma}_N^+ \hat{\sigma}_1^- + \hat{\sigma}_1^+ \hat{\sigma}_N^-) \prod_{l=1}^{N} (i\hat{\sigma}_l^z) \tag{A.14}$$

A.2 Fermionic Mass Term

$$\hat{\psi}_j^\dagger \hat{\psi}_j = \left(\prod_{l=1}^{j-1} (-i\hat{\sigma}_l^z) \hat{\sigma}_j^+ \right) \left(\prod_{l'=1}^{j-1} (i\hat{\sigma}_{l'}^z) \hat{\sigma}_j^- \right) \tag{A.15}$$

$$= \prod_{l=1}^{j-1} \prod_{l'=1}^{j-1} (-i\hat{\sigma}_l^z)(i\hat{\sigma}_{l'}^z) \hat{\sigma}_j^+ \hat{\sigma}_j^- \tag{A.16}$$

$$= \frac{1}{2}(\hat{\sigma}_j^z + \mathbb{1}_2) \tag{A.17}$$

since $(\hat{\sigma}_j^z)^2 = \mathbb{1}_2$ and $\hat{\sigma}_j^+ \hat{\sigma}_j^- = \frac{1}{2}(\hat{\sigma}_j^z + \mathbb{1}_2)$.

Chapter B: Optimal and Random Angles for Symmetry Protection

This appendix gives more details on how we choose the angles of the random unitaries used in the symmetry protection protocol of Chapter 7.

In Fig. 7.4, we study how well the symmetry-protected time evolution given in Eq. (7.16) suppresses the symmetry-breaking Trotter errors for a simulation with the XYZ ordering with $\mu = 0.1$, $x = 0.6$, $N = 4$ and $\delta t = 1$. For the time evolution with a particular t, the angle of rotation, α_k, for the k-th Trotter step depends on α_1 in the first Trotter step as $\alpha_k = k\alpha_1$, where $0 \leq \alpha_1 < 2\pi$. We choose α_1 to be the smallest angle with which the leakage to the symmetry-broken subspace at time t is minimized.

Figure B.1 displays a few examples of how the leakage varies as a function of α_1 for selected times t. As shown in the plot, there are several values of α_1 that minimize the leakage and the number of minima tends to increase with increasing t. The optimal value of α_1 is determined from the smallest minimum found at each t. These values are listed in Table B.1.

Meanwhile, the angles α_k for the symmetry-protected evolution in the experiment in Fig. 7.10 are chosen at random from a uniform distribution in the interval $[0, 2\pi]$. These

angles are listed in Table B.2.

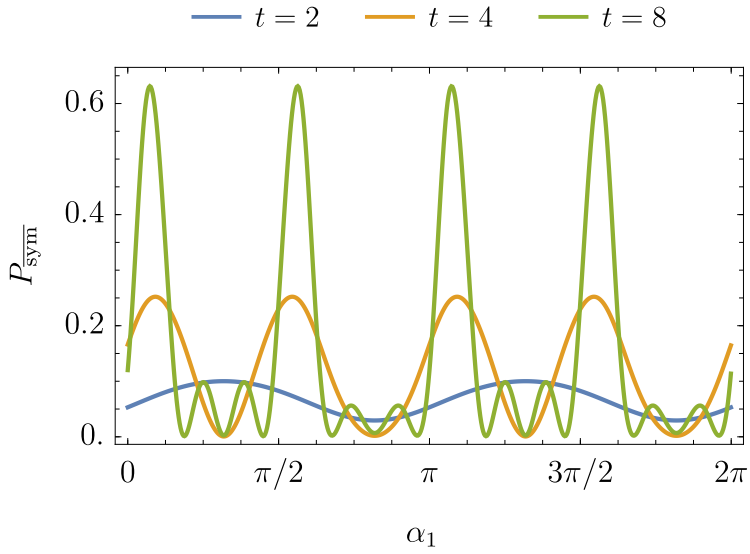

Figure B.1: The population of the symmetry-forbidden subspace as a function of the angles α_1 for $t = 2, 4, 8$, for $\mu = 0.1$, $x = 0.6$, $N = 4$ and $\delta t = 1$. We choose α_1 to be the smallest angle that minimizes $P_{\overline{\text{sym}}}$ at each t.

Table B.1: Values of α_1 used for the symmetry-protected XYZ ordering in Fig. 7.4 at different times t, together with the corresponding leakage to the symmetry-forbidden subspace.

t	α_1	$P_{\overline{\text{sym}}}$
1	0	0.0346
2	0.8184π	0.0294
3	0.8184π	0.0260
4	0.3183π	0.0006
5	0.8811π	0.0128
6	0.2314π	0.0018
7	0.4370π	0.0201
8	0.1875π	0.0011
9	0.8496π	0.0055
10	0.9887π	0.0000

Table B.2: Randomly chosen values of α_k used in the experiment to study the effect of symmetry protection on experimental error. The result is presented in Fig. 7.10.

t	α_1	α_2	α_3	α_4	α_5	α_6	α_7	α_8	α_9	α_{10}
1	0.9559π	—	—	—	—	—	—	—	—	—
2	1.1461π	0.2987π	—	—	—	—	—	—	—	—
3	0.0150π	0.6927π	1.6279π	—	—	—	—	—	—	—
4	0.5861π	0.0333π	0.0787π	0.1613π	—	—	—	—	—	—
5	1.7496π	1.7986π	0.4505π	1.4374π	0.3222π	—	—	—	—	—
6	1.7205π	0.0706π	1.0666π	1.5912π	1.0554π	0.8444π	—	—	—	—
7	0.2499π	0.2990π	0.1212π	0.6793π	0.9988π	0.9218π	1.8565π	—	—	—
8	1.7974π	0.7531π	0.0548π	0.4236π	1.8081π	1.7279π	0.4253π	0.8807π	—	—
9	0.8880π	0.3908π	1.7202π	1.7779π	1.1028π	1.7425π	1.6552π	0.0604π	0.2346π	—
10	0.7112π	1.1025π	1.3913π	0.5387π	1.7179π	1.0585π	0.2870π	0.8636π	1.6639π	1.5434π

Chapter C: State populations

This appendix provides more details on the effect of the symmetry (Gauss's law) based post-selection procedure used in Chapter 7 on different subspaces of the physical state $e^{-it\hat{H}}|\psi\rangle$. It shows that post-selection does not significantly affect the dynamics of the model since post-selection is based on the symmetry of the Hamiltonian.

The population in the bare vacuum as a function of time is displayed in Fig. 7.8 of the main text. For completeness, we also plot in Fig. C.1 the population of all allowed states as a function of time for the case of $N = 4$ and $\delta t = 1.0$. Additionally, the cumulative population in the symmetry-forbidden sector, $P_{\overline{\text{sym}}}$, is shown, demonstrating the rate at which the leakage to the symmetry-forbidden sector grows.

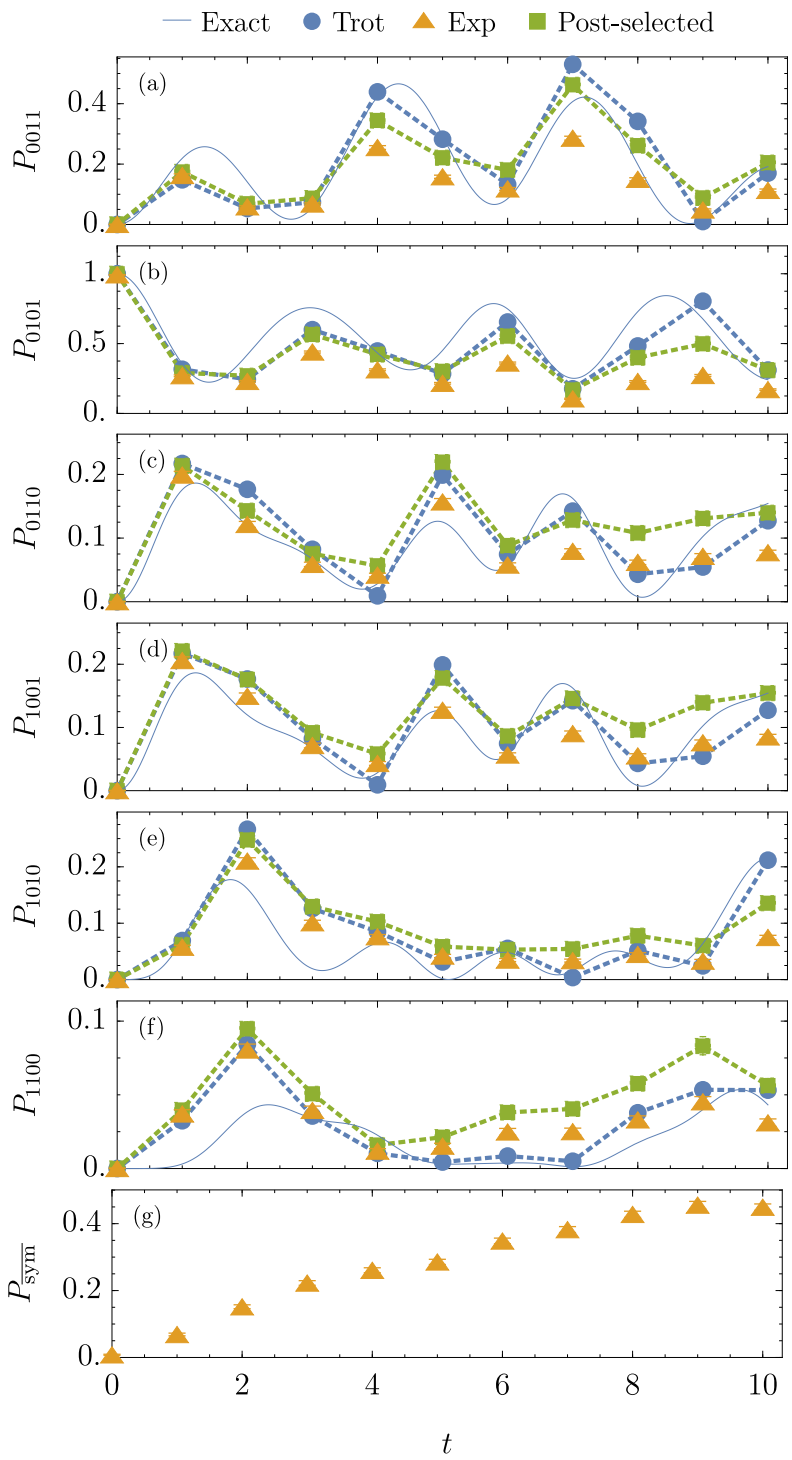

Figure C.1: Evolution of states characterized by the quantity $P_\Psi \equiv |\langle\Psi|e^{-it\hat{H}}|\psi_0\rangle|^2$ in the symmetry-allowed (a-f) and symmetry-forbidden (g) subspace for $N = 4$ and $\delta t = 1.0$ starting from the bare-vacuum state $|\psi_0\rangle$. $P_{0101} \equiv P_{\text{vac}}$ is also plotted in Figure 7.8. The effectiveness of post-selection in mitigating errors is both quantity- and time-dependent. In some cases, it ceases to improve the agreement with theory at larger times.

Chapter D: Hamiltonian for free scalar bosons

This appendix provides the derivations for transforming the Hamiltonian term for the scalar bosons' dynamics, Eq. (8.3), from the position basis to the momentum basis. This appendix is relevant to Chapter 8.

The Hamiltonian for free scalar bosons of mass m_φ on a 1D lattice with spacing b is [279]

$$\hat{H}^{(II)} = b\sum_{j=1}^{N}\left[\frac{\hat{\Pi}_j^2}{2} + \frac{(\nabla\hat{\varphi}_j)^2}{2} + \frac{m_\varphi^2}{2}\hat{\varphi}_j^2\right] \tag{D.1}$$

In the momentum basis, the bosonic field operator $\hat{\varphi}_j$ and its canonical momentum $\hat{\Pi}_j$ at each site j are given by [237]

$$\hat{\varphi}_j = \frac{1}{\sqrt{Nb}}\sum_{k=-N/2}^{N/2-1}\frac{1}{\sqrt{2\varepsilon_k}}\left(\hat{d}_k^\dagger \mathrm{e}^{-ip_kjb} + \hat{d}_k\mathrm{e}^{ip_kjb}\right) \tag{D.2}$$

$$\hat{\Pi}_j = \frac{i}{\sqrt{Nb}}\sum_{k=-N/2}^{N/2-1}\sqrt{\frac{\varepsilon_k}{2}}\left(\hat{d}_k^\dagger \mathrm{e}^{-ip_kjb} - \hat{d}_k\mathrm{e}^{ip_kjb}\right) \tag{D.3}$$

with $p_k = 2\pi k/(Nb)$ and $\varepsilon_k^2 = 4\sin^2(p_k b/2)/b^2 + m_\varphi^2$. The first term in Eq. (D.1) is

$$\frac{b}{2}\sum_j \hat{\Pi}_j^2 = -\frac{1}{2N}\sum_j\sum_{k,k'}\frac{\sqrt{\varepsilon_k\varepsilon_{k'}}}{2}\Big(\hat{d}_k^\dagger\hat{d}_{k'}^\dagger \mathrm{e}^{-i(p_k+p_{k'})jb} + \hat{d}_k\hat{d}_{k'}\mathrm{e}^{i(p_k+p_{k'})jb} \\ -\hat{d}_k^\dagger\hat{d}_{k'}\mathrm{e}^{-i(p_k-p_{k'})jb} - \hat{d}_k\hat{d}_{k'}^\dagger\mathrm{e}^{i(p_k-p_{k'})jb}\Big). \tag{D.4}$$

Since

$$\sum_j \mathrm{e}^{\pm 2i(p_k+p_{k'})jb} = N\delta_{-k,k'}, \tag{D.5}$$

$$\sum_j \mathrm{e}^{\pm 2i(p_k-p_{k'})jb} = N\delta_{k,k'}, \tag{D.6}$$

and $\varepsilon_{-k} = \varepsilon_k$,

$$\frac{b}{2}\sum_j \hat{\Pi}_j^2 = -\frac{1}{2}\sum_{k,k'}\frac{\sqrt{\varepsilon_k\varepsilon_{k'}}}{2}\Big(\hat{d}_k^\dagger\hat{d}_{k'}^\dagger\delta_{-k,k'} + \hat{d}_k\hat{d}_{k'}\delta_{-k,k'} - \hat{d}_k^\dagger\hat{d}_{k'}\delta_{k,k'} - \hat{d}_k\hat{d}_{k'}^\dagger\delta_{k,k'}\Big) \tag{D.7}$$

$$= -\frac{1}{2}\sum_k\frac{\varepsilon_k}{2}\Big(\hat{d}_k^\dagger\hat{d}_{-k}^\dagger + \hat{d}_k\hat{d}_{-k} - \hat{d}_k^\dagger\hat{d}_k - \hat{d}_k\hat{d}_k^\dagger\Big). \tag{D.8}$$

Similarly,

$$\frac{b}{2}\sum_j \hat{\varphi}_j^2 = \frac{1}{2}\sum_j\sum_{k,k'}\frac{1}{2\sqrt{\varepsilon_k\varepsilon_{k'}}}\Big(\hat{d}_k^\dagger\hat{d}_{k'}^\dagger \mathrm{e}^{-i(p_k+p_{k'})jb} + \hat{d}_k\hat{d}_{k'}\mathrm{e}^{i(p_k+p_{k'})jb} \\ + \hat{d}_k^\dagger\hat{d}_{k'}\mathrm{e}^{-i(p_k-p_{k'})jb} + \hat{d}_k\hat{d}_{k'}^\dagger\mathrm{e}^{i(p_k-p_{k'})jb}\Big) \tag{D.9}$$

$$= \frac{1}{2}\sum_k\frac{1}{2\varepsilon_k}\Big(\hat{d}_k^\dagger\hat{d}_{-k}^\dagger + \hat{d}_k\hat{d}_{-k} + \hat{d}_k^\dagger\hat{d}_k + \hat{d}_k\hat{d}_k^\dagger\Big). \tag{D.10}$$

The spatial derivative in 1D is

$$\nabla\hat{\varphi}_j = \frac{\hat{\varphi}_{j+1} - \hat{\varphi}_j}{(j+1)b - jb} = \frac{\hat{\varphi}_{j+1} - \hat{\varphi}_j}{b}. \tag{D.11}$$

Therefore

$$\sum_j(\nabla\hat{\varphi}_j)^2 = \frac{1}{b^2}\sum_j(\hat{\varphi}_{j+1}^2 - \hat{\varphi}_{j+1}\hat{\varphi}_j - \hat{\varphi}_j\hat{\varphi}_{j+1} + \hat{\varphi}_j^2) \tag{D.12}$$

$$= \frac{1}{b^2}\sum_j(2\hat{\varphi}_j^2 - \hat{\varphi}_{j+1}\hat{\varphi}_j - \hat{\varphi}_j\hat{\varphi}_{j+1}) \tag{D.13}$$

since $\sum_j \hat{\varphi}_{j+1}^2 = \sum_j \hat{\varphi}_j^2$ due to the PBC. Equation (8.2) becomes

$$\hat{H}^{(II)} = \frac{b}{2}\sum_{j=1}^{N}\left[\hat{\Pi}_j^2 + \left(\frac{2}{b^2} + m_\varphi^2\right)\hat{\varphi}_j^2 - \frac{1}{b^2}\left(\hat{\varphi}_{j+1}\hat{\varphi}_j + \hat{\varphi}_j\hat{\varphi}_{j+1}\right)\right] \tag{D.14}$$

$$\sum_j \hat{\varphi}_{j+1}\hat{\varphi}_j = \frac{1}{Nb}\sum_j\sum_{k,k'}\frac{1}{2\sqrt{\varepsilon_k\varepsilon_{k'}}}\Big(\hat{d}_k^\dagger\hat{d}_{k'}^\dagger \mathrm{e}^{-i(p_k+p_{k'})jb-ip_kb} + \hat{d}_k\hat{d}_{k'}\mathrm{e}^{i(p_k+p_{k'})jb+ip_kb}$$
$$+ \hat{d}_k^\dagger\hat{d}_{k'}\mathrm{e}^{-i(p_k-p_{k'})jb-ip_kb} + \hat{d}_k\hat{d}_{k'}^\dagger\mathrm{e}^{i(p_k-p_{k'})jb+ip_kb}\Big) \tag{D.15}$$
$$= \frac{1}{b}\sum_{k,k'}\frac{1}{2\sqrt{\varepsilon_k\varepsilon_{k'}}}\Big(\hat{d}_k^\dagger\hat{d}_{k'}^\dagger\delta_{-k,k'}\mathrm{e}^{-ip_kb} + \hat{d}_k\hat{d}_{k'}\delta_{-k,k'}\mathrm{e}^{ip_kb} + \hat{d}_k^\dagger\hat{d}_{k'}\delta_{k,k'}\mathrm{e}^{-ip_kb}$$
$$+ \hat{d}_k\hat{d}_{k'}^\dagger\delta_{k,k'}\mathrm{e}^{ip_kb}\Big) \tag{D.16}$$
$$= \frac{1}{b}\sum_k\frac{1}{2\varepsilon_k}\Big(\hat{d}_k^\dagger\hat{d}_{-k}^\dagger\mathrm{e}^{-ip_kb} + \hat{d}_k\hat{d}_{-k}\mathrm{e}^{ip_kb} + \hat{d}_k^\dagger\hat{d}_k\mathrm{e}^{-ip_kb} + \hat{d}_k\hat{d}_k^\dagger\mathrm{e}^{ip_kb}\Big) \tag{D.17}$$

$$\sum_j \hat{\varphi}_j\hat{\varphi}_{j+1} = \frac{1}{Nb}\sum_j\sum_{k,k'}\frac{1}{2\sqrt{\varepsilon_k\varepsilon_{k'}}}\Big(\hat{d}_k^\dagger\hat{d}_{k'}^\dagger\mathrm{e}^{-i(p_k+p_{k'})jb-ip_{k'}b} + \hat{d}_k\hat{d}_{k'}\mathrm{e}^{i(p_k+p_{k'})jb+ip_{k'}b}$$
$$+ \hat{d}_k^\dagger\hat{d}_{k'}\mathrm{e}^{-i(p_k-p_{k'})jb+ip_{k'}b} + \hat{d}_k\hat{d}_{k'}^\dagger\mathrm{e}^{i(p_k-p_{k'})jb-ip_{k'}b}\Big) \tag{D.18}$$
$$= \frac{1}{b}\sum_{k,k'}\frac{1}{2\sqrt{\varepsilon_k\varepsilon_{k'}}}\Big(\hat{d}_k^\dagger\hat{d}_{k'}^\dagger\delta_{-k,k'}\mathrm{e}^{-ip_{k'}b} + \hat{d}_k\hat{d}_{k'}\delta_{-k,k'}\mathrm{e}^{ip_{k'}b} + \hat{d}_k^\dagger\hat{d}_{k'}\delta_{k,k'}\mathrm{e}^{ip_{k'}b}$$
$$+ \hat{d}_k\hat{d}_{k'}^\dagger\delta_{k,k'}\mathrm{e}^{-ip_{k'}b}\Big) \tag{D.19}$$
$$= \frac{1}{b}\sum_k\frac{1}{2\varepsilon_k}\Big(\hat{d}_k^\dagger\hat{d}_{-k}^\dagger\mathrm{e}^{ip_kb} + \hat{d}_k\hat{d}_{-k}\mathrm{e}^{-ip_kb} + \hat{d}_k^\dagger\hat{d}_k\mathrm{e}^{ip_kb} + \hat{d}_k\hat{d}_k^\dagger\mathrm{e}^{-ip_kb}\Big). \tag{D.20}$$

We can also see that since $[\hat{\varphi}_j, \hat{\varphi}_{j'}] = 0$, $\hat{\varphi}_j\hat{\varphi}_{j+1} = \hat{\varphi}_{j+1}\hat{\varphi}_j$. We can rewrite Eq. (D.14) as

$$\begin{aligned}
\hat{H}^{(II)} &= -\frac{1}{2}\sum_k \frac{\varepsilon_k}{2}\Big(\hat{d}_k^\dagger\hat{d}_{-k}^\dagger + \hat{d}_k\hat{d}_{-k} - \hat{d}_k^\dagger\hat{d}_k - \hat{d}_k\hat{d}_k^\dagger\Big) \\
&+ \Big(\frac{2}{b^2} + m_\varphi^2\Big)\frac{1}{2}\sum_k \frac{1}{2\varepsilon_k}\Big(\hat{d}_k^\dagger\hat{d}_{-k}^\dagger + \hat{d}_k\hat{d}_{-k} + \hat{d}_k^\dagger\hat{d}_k + \hat{d}_k\hat{d}_k^\dagger\Big) \\
&- \frac{1}{2b^2}\sum_k \frac{1}{2\varepsilon_k}\Big(\hat{d}_k^\dagger\hat{d}_{-k}^\dagger \mathrm{e}^{-ip_kb} + \hat{d}_k\hat{d}_{-k}\mathrm{e}^{ip_kb} + \hat{d}_k^\dagger\hat{d}_k\mathrm{e}^{-ip_kb} + \hat{d}_k\hat{d}_k^\dagger\mathrm{e}^{ip_kb}\Big) \\
&- \frac{1}{2b^2}\sum_k \frac{1}{2\varepsilon_k}\Big(\hat{d}_k^\dagger\hat{d}_{-k}^\dagger \mathrm{e}^{ip_kb} + \hat{d}_k\hat{d}_{-k}\mathrm{e}^{-ip_kb} + \hat{d}_k^\dagger\hat{d}_k\mathrm{e}^{ip_kb} + \hat{d}_k\hat{d}_k^\dagger\mathrm{e}^{-ip_kb}\Big) \qquad \text{(D.21)} \\
&= \frac{1}{4}\sum_k \frac{1}{\varepsilon_k}\Big(m_\varphi^2 + \frac{2}{b^2} - \frac{\mathrm{e}^{-ip_kb} + \mathrm{e}^{ip_kb}}{b^2} - \varepsilon_k^2\Big)\Big(\hat{d}_k^\dagger\hat{d}_{-k}^\dagger + \hat{d}_k\hat{d}_{-k}\Big) \\
&+ \frac{1}{4}\sum_k \frac{1}{\varepsilon_k}\Big(m_\varphi^2 + \frac{2}{b^2} - \frac{\mathrm{e}^{-ip_kb} + \mathrm{e}^{ip_kb}}{b^2} + \varepsilon_k^2\Big)\Big(\hat{d}_k^\dagger\hat{d}_k + \hat{d}_k\hat{d}_k^\dagger\Big). \qquad \text{(D.22)}
\end{aligned}$$

Since $\mathrm{e}^{-ip_kb} + \mathrm{e}^{ip_kb} = 2\cos(p_kb)$ and $1 - \cos(p_kb) = 2\sin^2(p_kb/2)$,

$$m_\varphi^2 + \frac{2}{b^2} - \frac{\mathrm{e}^{-ip_kb} + \mathrm{e}^{ip_kb}}{b^2} - \varepsilon_k^2 = m_\varphi^2 + \frac{4}{b^2}\sin^2\Big(\frac{p_kb}{2}\Big) - \varepsilon_k^2 = 0, \qquad \text{(D.23)}$$

$$m_\varphi^2 + \frac{2}{b^2} - \frac{\mathrm{e}^{-ip_kb} + \mathrm{e}^{ip_kb}}{b^2} + \varepsilon_k^2 = m_\varphi^2 + \frac{4}{b^2}\sin^2\Big(\frac{p_kb}{2}\Big) + \varepsilon_k^2 = 2\varepsilon_k^2. \qquad \text{(D.24)}$$

Using $[\hat{d}_k, \hat{d}_k^\dagger] = \mathbb{1}_\infty$, Eq. (D.22) becomes

$$\hat{H}^{(II)} = \frac{1}{4}\sum_k 2\varepsilon_k\Big(\hat{d}_k^\dagger\hat{d}_k + \hat{d}_k\hat{d}_k^\dagger\Big) = \sum_k \varepsilon_k\Big(\hat{d}_k^\dagger\hat{d}_k + \frac{1}{2}\mathbb{1}_\infty\Big). \qquad \text{(D.25)}$$

Bibliography

[1] Shantanu Debnath. *A Programmable Five Qubit Quantum Computer Using Trapped Atomic Ions*. PhD thesis, University of Maryland, College Park, 2016.

[2] Laird Nicholas Egan. *Scaling Quantum Computers With Long Chains Of Trapped Ions*. PhD thesis, University of Maryland, College Park, 2021.

[3] S. Debnath, N. M. Linke, C. Figgatt, K. A. Landsman, K. Wright, and C. Monroe. Demonstration of a small programmable quantum computer with atomic qubits. *Nature*, 536(7614):63–66, aug 2016.

[4] Caroline Margaret Figgatt. *Building and Programming a Universal Ion Trap Quantum Computer*. PhD thesis, University of Maryland, College Park, 2018.

[5] R. P. Feynman. Simulating Physics with Computers. *Int. J. Theor. Phys.*, 21:467–488, June 1982.

[6] Peter W. Shor. Polynomial-time algorithms for prime factorization and discrete logarithms on a quantum computer. *SIAM Journal on Computing*, 26(5):1484–1509, 1997.

[7] Lov K. Grover. Quantum mechanics helps in searching for a needle in a haystack. *Physical Review Letters*, 79:325–328, 1997.

[8] A. Ambainis. Quantum search algorithms. *ACM SIGACT News*, 35(2):22–35, 2004. Available online at https://arxiv.org/abs/quant-ph/0504012.

[9] Andris Ambainis. Quantum walks and their algorithmic applications. *International Journal of Quantum Information*, 1:507–518, 2003.

[10] Edward Farhi, Jeffrey Goldstone, Sam Gutmann, and Michael Sipser. Quantum computation by adiabatic evolution, 2000.

[11] Edward Farhi, Jeffrey Goldstone, Sam Gutmann, Joshua Lapan, Andrew Lundgren, and Daniel Preda. A quantum adiabatic evolution algorithm applied to random instances of an np-complete problem. *Science*, 292(5516):472–475, 2001.

[12] Edward Farhi, Jeffrey Goldstone, and Sam Gutmann. A quantum approximate optimization algorithm, 2014.

[13] Tameem Albash and Daniel A. Lidar. Adiabatic quantum computation. *Rev. Mod. Phys.*, 90:015002, Jan 2018.

[14] Madelyn Cain, Sambuddha Chattopadhyay, Jin-Guo Liu, Rhine Samajdar, Hannes Pichler, and Mikhail D. Lukin. Quantum speedup for combinatorial optimization with flat energy landscapes, 2023.

[15] A. Aspuru-Guzik, A. D. Dutoi, P. J. Love, and M. Head-Gordon. Simulated quantum computation of molecular energies. *Science*, 309:1704, 2005.

[16] L. Veis and J. Pittner. Quantum computing applied to calculations of molecular energies: Ch2 benchmark. *J. Chem. Phys.*, 133:194106, 2010.

[17] L. Veis and J. Pittner. Quantum computing approach to nonrelativistic and relativistic molecular energy calculations. In Sabre Kais, editor, *Quantum Information and Computation for Chemistry*, volume 154, page 107. John Wiley and Sons, New York, 2014.

[18] Vera von Burg, Guang Hao Low, Thomas Häner, Damian S. Steiger, Markus Reiher, Martin Roetteler, and Matthias Troyer. Quantum computing enhanced computational catalysis. *Phys. Rev. Res.*, 3:033055, Jul 2021.

[19] Michael A. Nielsen and Isaac Chuang. *Quantum Computation and Quantum Information*. Cambridge University Press, Cambridge, 2010.

[20] J. P. Gaebler, T. R. Tan, Y. Lin, Y. Wan, R. Bowler, A. C. Keith, S. Glancy, K. Coakley, E. Knill, D. Leibfried, and D. J. Wineland. High-Fidelity Universal Gate Set for $^{9}Be^{+}$ Ion Qubits. *Phys. Rev. Lett.*, 117(6):060505, August 2016.

[21] C. J. Ballance, T. P. Harty, N. M. Linke, M. A. Sepiol, and D. M. Lucas. High-Fidelity Quantum Logic Gates Using Trapped-Ion Hyperfine Qubits. *Phys. Rev. Lett.*, 117(6):060504, August 2016.

[22] Craig R. Clark, Holly N. Tinkey, Brian C. Sawyer, Adam M. Meier, Karl A. Burkhardt, Christopher M. Seck, Christopher M. Shappert, Nicholas D. Guise, Curtis E. Volin, Spencer D. Fallek, Harley T. Hayden, Wade G. Rellergert, and Kenton R.

Brown. High-fidelity bell-state preparation with $^{40}ca^{+}$ optical qubits. *Phys. Rev. Lett.*, 127:130505, Sep 2021.

[23] V. M. Schäfer, C. J. Ballance, K. Thirumalai, L. J. Stephenson, T. G. Ballance, A. M. Steane, and D. M. Lucas. Fast quantum logic gates with trapped-ion qubits. *Nature*, 555(7694):75–78, March 2018.

[24] Philipp Schindler, Daniel Nigg, Thomas Monz, Julio T Barreiro, Esteban Martinez, Shannon X Wang, Stephan Quint, Matthias F Brandl, Volckmar Nebendahl, Christian F Roos, Michael Chwalla, Markus Hennrich, and Rainer Blatt. A quantum information processor with trapped ions. *New Journal of Physics*, 15(12):123012, dec 2013.

[25] Thomas Monz, Daniel Nigg, Esteban A. Martinez, Matthias F. Brandl, Philipp Schindler, Richard Rines, Shannon X. Wang, Isaac L. Chuang, and Rainer Blatt. Realization of a scalable shor algorithm. *Science*, 351:1068–1070, 2016.

[26] Laird Egan, Dripto M. Debroy, Crystal Noel, Andrew Risinger, Daiwei Zhu, Debopriyo Biswas, Michael Newman, Muyuan Li, Kenneth R. Brown, Marko Cetina, and Christopher Monroe. Fault-tolerant control of an error-corrected qubit. *Nature*, 598(7880):281–286, Oct 2021.

[27] I. Pogorelov, T. Feldker, Ch. D. Marciniak, L. Postler, G. Jacob, O. Krieglsteiner, V. Podlesnic, M. Meth, V. Negnevitsky, M. Stadler, B. Höfer, C. Wächter, K. Lakhmanskiy, R. Blatt, P. Schindler, and T. Monz. Compact ion-trap quantum computing demonstrator. *PRX Quantum*, 2:020343, Jun 2021.

[28] M. Cetina, L.N. Egan, C. Noel, M.L. Goldman, D. Biswas, A.R. Risinger, D. Zhu, and C. Monroe. Control of transverse motion for quantum gates on individually addressed atomic qubits. *PRX Quantum*, 3:010334, Mar 2022.

[29] D.J. Wineland, C. Monroe, W.M. Itano, D. Leibfried, B.E. King, and D.M. Meekhof. Experimental issues in coherent quantum-state manipulation of trapped atomic ions. *Journal of Research of the National Institute of Standards and Technology*, 103(3):259, may 1998.

[30] D. Kielpinski, C. Monroe, and D. J. Wineland. Architecture for a large-scale ion-trap quantum computer. *Nature*, 417(6890):709–711, jun 2002.

[31] J. M. Pino, J. M. Dreiling, C. Figgatt, J. P. Gaebler, S. A. Moses, M. S. Allman, C. H. Baldwin, M. Foss-Feig, D. Hayes, K. Mayer, C. Ryan-Anderson, and B. Neyenhuis. Demonstration of the trapped-ion quantum CCD computer architecture. *Nature*, 592(7853):209–213, apr 2021.

[32] C. Ryan-Anderson, J. G. Bohnet, K. Lee, D. Gresh, A. Hankin, J. P. Gaebler, D. Francois, A. Chernoguzov, D. Lucchetti, N. C. Brown, T. M. Gatterman, S. K. Halit, K. Gilmore, J. Gerber, B. Neyenhuis, D. Hayes, and R. P. Stutz. Realization of real-time fault-tolerant quantum error correction. *arXiv:2107.07505*, jul 2021.

[33] S. A. Moses, C. H. Baldwin, M. S. Allman, R. Ancona, L. Ascarrunz, C. Barnes, J. Bartolotta, B. Bjork, P. Blanchard, M. Bohn, J. G. Bohnet, N. C. Brown, N. Q. Burdick, W. C. Burton, S. L. Campbell, J. P. Campora, C. Carron, J. Chambers, J. W. Chan, Y. H. Chen, A. Chernoguzov, E. Chertkov, J. Colina, J. P. Curtis,

R. Daniel, M. DeCross, D. Deen, C. Delaney, J. M. Dreiling, C. T. Ertsgaard, J. Esposito, B. Estey, M. Fabrikant, C. Figgatt, C. Foltz, M. Foss-Feig, D. Francois, J. P. Gaebler, T. M. Gatterman, C. N. Gilbreth, J. Giles, E. Glynn, A. Hall, A. M. Hankin, A. Hansen, D. Hayes, B. Higashi, I. M. Hoffman, B. Horning, J. J. Hout, R. Jacobs, J. Johansen, L. Jones, J. Karcz, T. Klein, P. Lauria, P. Lee, D. Liefer, S. T. Lu, D. Lucchetti, C. Lytle, A. Malm, M. Matheny, B. Mathewson, K. Mayer, D. B. Miller, M. Mills, B. Neyenhuis, L. Nugent, S. Olson, J. Parks, G. N. Price, Z. Price, M. Pugh, A. Ransford, A. P. Reed, C. Roman, M. Rowe, C. Ryan-Anderson, S. Sanders, J. Sedlacek, P. Shevchuk, P. Siegfried, T. Skripka, B. Spaun, R. T. Sprenkle, R. P. Stutz, M. Swallows, R. I. Tobey, A. Tran, T. Tran, E. Vogt, C. Volin, J. Walker, A. M. Zolot, and J. M. Pino. A race-track trapped-ion quantum processor. *Phys. Rev. X*, 13:041052, Dec 2023.

[34] Mohsin Iqbal, Nathanan Tantivasadakarn, Ruben Verresen, Sara L. Campbell, Joan M. Dreiling, Caroline Figgatt, John P. Gaebler, Jacob Johansen, Michael Mills, Steven A. Moses, Juan M. Pino, Anthony Ransford, Mary Rowe, Peter Siegfried, Russell P. Stutz, Michael Foss-Feig, Ashvin Vishwanath, and Henrik Dreyer. Non-abelian topological order and anyons on a trapped-ion processor. *Nature*, 626:505–511, 2024.

[35] L.-M. Duan, B. B. Blinov, D. L. Moehring, and C. Monroe. Scalable trapped ion quantum computation with a probabilistic ion-photon mapping. *Quant. Inf. Comp.*, 4:165, 2004.

[36] C. Monroe and J. Kim. Scaling the ion trap quantum processor. *Science*, 339:1164, 2013.

[37] P. Maunz, S. Olmschenk, D. Hayes, D. N. Matsukevich, L.-M. Duan, and C. Monroe. Heralded quantum gate between remote quantum memories. *Phys. Rev. Lett.*, 102:250502, Jun 2009.

[38] L. J. Stephenson, D. P. Nadlinger, B. C. Nichol, S. An, P. Drmota, T. G. Ballance, K. Thirumalai, J. F. Goodwin, D. M. Lucas, and C. J. Ballance. High-rate, high-fidelity entanglement of qubits across an elementary quantum network. *Phys. Rev. Lett.*, 124:110501, Mar 2020.

[39] Lukas Postler, Sascha Heußen, Ivan Pogorelov, Manuel Rispler, Thomas Feldker, Michael Meth, Christian D. Marciniak, Roman Stricker, Martin Ringbauer, Rainer Blatt, Philipp Schindler, Markus Müller, and Thomas Monz. Demonstration of fault-tolerant universal quantum gate operations. *Nature*, 605:675–680, 2022.

[40] Daiwei Zhu, Gregory D. Kahanamoku-Meyer, Laura Lewis, Crystal Noel, Or Katz, Bahaa Harraz, Qingfeng Wang, Andrew Risinger, Lei Feng, Debopriyo Biswas, Laird Egan, Alexandru Gheorghiu, Yunseong Nam, Thomas Vidick, Umesh Vazirani, Norman Y. Yao, Marko Cetina, and Christopher Monroe. Interactive cryptographic proofs of quantumness using mid-circuit measurements. *Nat. Phys.*, 19:1725–1731, 2023.

[41] Matthew DeCross, Eli Chertkov, Megan Kohagen, and Michael Foss-Feig. Qubit-reuse compilation with mid-circuit measurement and reset. *Phys. Rev. X*, 13:041057, Dec 2023.

[42] Michael Foss-Feig, Arkin Tikku, Tsung-Cheng Lu, Karl Mayer, Mohsin Iqbal, Thomas M. Gatterman, Justin A. Gerber, Kevin Gilmore, Dan Gresh, Aaron Hankin, Nathan Hewitt, Chandler V. Horst, Mitchell Matheny, Tanner Mengle, Brian Neyenhuis, Henrik Dreyer, David Hayes, Timothy H. Hsieh, and Isaac H. Kim. Experimental demonstration of the advantage of adaptive quantum circuits, 2023.

[43] C. Figgatt, A. Ostrander, N. M. Linke, K. A. Landsman, D. Zhu, D. Maslov, and C. Monroe. Parallel entangling operations on a universal ion-trap quantum computer. *Nature*, 572(7769):368–372, August 2019.

[44] Yingyue Zhu, Alaina M. Green, Nhung H. Nguyen, C. Huerta Alderete, Elijah Mossman, and Norbert M. Linke. Pairwise-parallel entangling gates on orthogonal modes in a trapped-ion chain. *Advanced Quantum Technologies*, 6(11):2300056, 2023.

[45] Norbert M. Linke, Mauricio Gutierrez, Kevin A. Landsman, Caroline Figgatt, Shantanu Debnath, Kenneth R. Brown, and Christopher Monroe. Fault-tolerant quantum error detection. *Sci. Adv.*, 3(10):e1701074, October 2017.

[46] Nhung H. Nguyen, Muyuan Li, Alaina M. Green, C. Huerta Alderete, Yingyue Zhu, Daiwei Zhu, Kenneth R. Brown, and Norbert M. Linke. Demonstration of shor encoding on a trapped-ion quantum computer. *Phys. Rev. Appl.*, 16:024057, Aug 2021.

[47] C. Ryan-Anderson, N. C. Brown, M. S. Allman, B. Arkin, G. Asa-Attuah, C. Baldwin, J. Berg, J. G. Bohnet, S. Braxton, N. Burdick, J. P. Campora, A. Chernoguzov, J. Esposito, B. Evans, D. Francois, J. P. Gaebler, T. M. Gatterman, J. Gerber,

K. Gilmore, D. Gresh, A. Hall, A. Hankin, J. Hostetter, D. Lucchetti, K. Mayer, J. Myers, B. Neyenhuis, J. Santiago, J. Sedlacek, T. Skripka, A. Slattery, R. P. Stutz, J. Tait, R. Tobey, G. Vittorini, J. Walker, and D. Hayes. Implementing fault-tolerant entangling gates on the five-qubit code and the color code, 2022.

[48] Daniel Gottesman. An Introduction to Quantum Error Correction and Fault-Tolerant Quantum Computation, April 2009.

[49] C. Figgatt, D. Maslov, K. A. Landsman, N. M. Linke, S. Debnath, and C. Monroe. Complete 3-qubit grover search on a programmable quantum computer. *Nature Communications*, 8(1):1918, 2017.

[50] Jarrod R McClean, Jonathan Romero, Ryan Babbush, and Alán Aspuru-Guzik. The theory of variational hybrid quantum-classical algorithms. *New Journal of Physics*, 18:023023, 2016.

[51] J Cohn, A Safavi-Naini, R J Lewis-Swan, J G Bohnet, M Gärttner, K A Gilmore, J E Jordan, A M Rey, J J Bollinger, and J K Freericks. Bang-bang shortcut to adiabaticity in the dicke model as realized in a penning trap experiment. *New Journal of Physics*, 20(5):055013, may 2018.

[52] Guido Pagano, Aniruddha Bapat, Patrick Becker, Katherine S. Collins, Arinjoy De, Paul W. Hess, Harvey B. Kaplan, Antonis Kyprianidis, Wen Lin Tan, Christopher Baldwin, Lucas T. Brady, Abhinav Deshpande, Fangli Liu, Stephen Jordan, Alexey V. Gorshkov, and Christopher Monroe. Quantum approximate optimization of the long-

range ising model with a trapped-ion quantum simulator. *Proceedings of the National Academy of Sciences*, 117(41):25396–25401, 2020.

[53] Yingyue Zhu, Zewen Zhang, Bhuvanesh Sundar, Alaina M Green, C Huerta Alderete, Nhung H Nguyen, Kaden R A Hazzard, and Norbert M Linke. Multi-round qaoa and advanced mixers on a trapped-ion quantum computer. *Quantum Science and Technology*, 8(1):015007, nov 2022.

[54] Man-Hong Yung, Jorge Casanova, Antonio Mezzacapo, Jarrod McClean, Lucas Lamata, Alán Aspuru-Guzik, and Enrique Solano. From transistor to trapped-ion computers for quantum chemistry. *Scientific Reports*, 4:3589, 2014.

[55] Cornelius Hempel, Christine Maier, Jonathan Romero, Jarrod McClean, Thomas Monz, Heng Shen, Petar Jurcevic, Ben P. Lanyon, Peter Love, Ryan Babbush, Alán Aspuru-Guzik, Rainer Blatt, and Christian F. Roos. Quantum chemistry calculations on a trapped-ion quantum simulator. *Phys. Rev. X*, 8:031022, Jul 2018.

[56] C. Kokail, C. Maier, R. van Bijnen, T. Brydges, M. K. Joshi, P. Jurcevic, C. A. Muschik, P. Silvi, R. Blatt, C. F. Roos, and P. Zoller. Self-verifying variational quantum simulation of lattice models. *Nature*, 569(7756):355–360, may 2019.

[57] Nicolai Friis, Oliver Marty, Christine Maier, Cornelius Hempel, Milan Holzäpfel, Petar Jurcevic, Martin B. Plenio, Marcus Huber, Christian Roos, Rainer Blatt, and Ben Lanyon. Observation of entangled states of a fully controlled 20-qubit system. *Phys. Rev. X*, 8:021012, Apr 2018.

[58] D. Zhu, S. Johri, N. M. Linke, K. A. Landsman, C. Huerta Alderete, N. H. Nguyen, A. Y. Matsuura, T. H. Hsieh, and C. Monroe. Generation of thermofield double states and critical ground states with a quantum computer. *Proceedings of the National Academy of Sciences*, 117(41):25402–25406, 2020.

[59] Kévin Hémery, Khaldoon Ghanem, Eleanor Crane, Sara L. Campbell, Joan M. Dreiling, Caroline Figgatt, Cameron Foltz, John P. Gaebler, Jacob Johansen, Michael Mills, Steven A. Moses, Juan M. Pino, Anthony Ransford, Mary Rowe, Peter Siegfried, Russell P. Stutz, Henrik Dreyer, Alexander Schuckert, and Ramil Nigmatullin. Measuring the loschmidt amplitude for finite-energy properties of the fermi-hubbard model on an ion-trap quantum computer, 2023.

[60] Or Katz, Lei Feng, Diego Porras, and Christopher Monroe. Observing topological insulator phases with a programmable quantum simulator, 2024.

[61] K. A. Landsman, C. Figgatt, T. Schuster, N. M. Linke, B. Yoshida, N. Y. Yao, and C. Monroe. Verified quantum information scrambling. *Nature*, 567(7746):61–65, March 2019.

[62] Manoj K. Joshi, Andreas Elben, Benoît Vermersch, Tiff Brydges, Christine Maier, Peter Zoller, Rainer Blatt, and Christian F. Roos. Quantum information scrambling in a trapped-ion quantum simulator with tunable range interactions. *Phys. Rev. Lett.*, 124:240505, Jun 2020.

[63] Eli Chertkov, Justin Bohnet, David Francois, John Gaebler, Dan Gresh, Aaron Hankin, Kenny Lee, David Hayes, Brian Neyenhuis, Russell Stutz, Andrew C. Potter, and

Michael Foss-Feig. Holographic dynamics simulations with a trapped-ion quantum computer. *Nature Physics*, 18(9):1074–1079, aug 2022.

[64] Florian Kranzl, Stefan Birnkammer, Manoj K. Joshi, Alvise Bastianello, Rainer Blatt, Michael Knap, and Christian F. Roos. Observation of magnon bound states in the long-range, anisotropic heisenberg model. *Phys. Rev. X*, 13:031017, Aug 2023.

[65] Alexander Schuckert, Or Katz, Lei Feng, Eleanor Crane, Arinjoy De, Mohammad Hafezi, Alexey V. Gorshkov, and Christopher Monroe. Observation of a finite-energy phase transition in a one-dimensional quantum simulator, 2023.

[66] L. Feng, O. Katz, C. Haack, M. Maghrebi, A. V. Gorshkov, Z. Gong, M. Cetina, and C. Monroe. Continuous symmetry breaking in a trapped-ion spin chain. *Nature*, 623:713, 2023.

[67] E. A. Martinez, C. A. Muschik, P. Schindler, D. Nigg, A. Erhard, M. Heyl, P. Hauke, M. Dalmonte, T. Monz, P. Zoller, and R. Blatt. Real-time dynamics of lattice gauge theories with a few-qubit quantum computer. *Nature*, 534(7608):516–519, June 2016.

[68] Nhung H. Nguyen, Minh C. Tran, Yingyue Zhu, Alaina M. Green, C. Huerta Alderete, Zohreh Davoudi, and Norbert M. Linke. Digital quantum simulation of the schwinger model and symmetry protection with trapped ions. *PRX Quantum*, 3:020324, May 2022.

[69] Dylan J Gorman, Boerge Hemmerling, Eli Megidish, Soenke A. Moeller, Philipp Schindler, Mohan Sarovar, and Hartmut Haeffner. Engineering vibrationally assisted

energy transfer in a trapped-ion quantum simulator. *Phys. Rev. X*, 8:011038, Mar 2018.

[70] Yangchao Shen, Yao Lu, Kuan Zhang, Junhua Zhang, Shuaining Zhang, Joonsuk Huh, and Kihwan Kim. Quantum optical emulation of molecular vibronic spectroscopy using a trapped-ion device. *Chem. Sci.*, 9:836–840, 2018.

[71] Jacob Whitlow, Zhubing Jia, Ye Wang, Chao Fang, Jungsang Kim, and Kenneth R. Brown. Quantum simulation of conical intersections using trapped ions. *Nature Chemistry*, 15:1509–1514, 2023.

[72] C. H. Valahu, V. C. Olaya-Agudelo, R. J. MacDonell, T. Navickas, A. D. Rao, M. J. Millican, J. B. Pérez-Sánchez, J. Yuen-Zhou, M. J. Biercuk, C. Hempel, T. R. Tan, and I. Kassal. Direct observation of geometric-phase interference in dynamics around a conical intersection. *Nature Chemistry*, 15(11):1503–1508, August 2023.

[73] K. Seetharam, D. Biswas, C. Noel, A. Risinger, D. Zhu, O. Katz, S. Chattopadhyay, M. Cetina, C. Monroe, E. Demler, and Dries Sels. Digital quantum simulation of nmr experiments. *Science Advances*, 9:eadh259, 2023.

[74] Philip Richerme, Melissa C. Revelle, Christopher G. Yale, Daniel Lobser, Ashlyn D. Burch, Susan M. Clark, Debadrita Saha, Miguel Angel Lopez-Ruiz, Anurag Dwivedi, Jeremy M. Smith, Sam A. Norrell, Amr Sabry, and Srinivasan S. Iyengar. Quantum computation of hydrogen bond dynamics and vibrational spectra. *The Journal of Physical Chemistry Letters*, 14(32):7256–7263, aug 2023.

[75] Bjoern Lekitsch et al. Blueprint for a microwave trapped ion quantum computer. *Sci. Adv.*, 3:e1601540, 2017.

[76] W. Paul. Quadrupole mass filter. *Z. Naturforsch. A*, 8:448, 1953.

[77] M. J. Madsen, W. K. Hensinger, D. Stick, J. A. Rabchuk, and C. Monroe. Planar ion trap geometry for microfabrication. *Applied Physics B*, 78:639, 2004.

[78] C. Marquet, F. Schmidt-Kaler, and D. James. Phonon–phonon interactions due to non-linear effects in a linear ion trap. *Appl Phys B*, 76:199–208, 2003.

[79] D.F.V. James. Quantum dynamics of cold trapped ions with application to quantum computation. *Applied Physics B: Lasers and Optics*, 66(2):181–190, feb 1998.

[80] Timothy Andrew Manning. *Quantum Information Processing With Trapped Ion Chains*. PhD thesis, University of Maryland, College Park, 2014.

[81] Patricia J. Lee. *Quantum Information Processing with Two Trapped Cadmium Ions*. PhD thesis, University of Michigan, 2006.

[82] K. E. Cahill and R. J. Glauber. Ordered expansions in boson operators. *Physical Review*, 177:1857, 1969.

[83] Christian Felix Roos. *Controlling the quantum state of trapped ions*. PhD thesis, Leopold-Franzens-Universität Innsbruck, 2000.

[84] Thomas P. Harty. *High-Fidelity Microwave-Driven Quantum Logic in Intermediate-Field 43Ca+*. PhD thesis, University of Oxford, 2013.

[85] Kevin Antony Landsman. *CONSTRUCTION, OPTIMIZATION, AND APPLICATIONS OF A SMALL TRAPPED-ION QUANTUM COMPUTER*. PhD thesis, University of Maryland, College Park, 2019.

[86] Th. Hannemann, D. Reiss, Ch. Balzer, W. Neuhauser, P. E. Toschek, and Ch. Wunderlich. Self-learning estimation of quantum states. *Phys. Rev. A*, 65:050303, May 2002.

[87] Chr. Balzer, A. Braun, T. Hannemann, Chr. Paape, M. Ettler, W. Neuhauser, and Chr. Wunderlich. Electrodynamically trapped yb^+ ions for quantum information processing. *Phys. Rev. A*, 73:041407, Apr 2006.

[88] S. Olmschenk, K. C. Younge, D. L. Moehring, D. N. Matsukevich, P. Maunz, and C. Monroe. Manipulation and detection of a trapped Yb + hyperfine qubit. *Phys. Rev. A*, 76(5):052314, November 2007.

[89] P. K. Ghosh. *Ion Traps*. Clarendon Press, 1995.

[90] D. J. Berkeland, J. D. Miller, J. C. Bergquist, W. M. Itano, and D. J. Wineland. Minimization of ion micromotion in a paul trap. *Journal of Applied Physics*, 83(10):5025–5033, may 1998.

[91] Jonathan Albert Mizrahi. *Ultrafast Control of Spin and Motion in Trapped Ions*. PhD thesis, University of Maryland, 2013.

[92] Michael Drewsen. Ion coulomb crystals. *Physica B: Condensed Matter*, 460:105–113, 2015. Special Issue on Electronic Crystals (ECRYS-2014).

[93] D. G. Enzer, M. M. Schauer, J. J. Gomez, M. S. Gulley, M. H. Holzscheiter, P. G. Kwiat, S. K. Lamoreaux, C. G. Peterson, V. D. Sandberg, D. Tupa, A. G. White, R. J. Hughes, and D. F. V. James. Observation of power-law scaling for phase transitions in linear trapped ion crystals. *Phys. Rev. Lett.*, 85:2466–2469, Sep 2000.

[94] Wayne M. Itano and D. J. Wineland. Laser cooling of ions stored in harmonic and penning traps. *Phys. Rev. A*, 25:35–54, Jan 1982.

[95] W. M. Itano, J. C. Bergquist, J. J. Bollinger, and D. J. Wineland. Laser cooling of trapped ions. pages 519–537, 1993.

[96] Wayne M Itano, J C Bergquist, J J Bollinger, and D J Wineland. Cooling methods in ion traps. *Physica Scripta*, 1995(T59):106, jan 1995.

[97] Daniel Adam Steck. Quantum and atom optics. https://atomoptics.uoregon.edu/~dsteck/teaching/quantum-optics/, 2024. Accessed: 2024-02-12.

[98] J. Mizrahi, B. Neyenhuis, K.G. Johnson, et al. Quantum control of qubits and atomic motion using ultrafast laser pulses. *Applied Physics B*, 114(1):45–61, 2014.

[99] D. Hayes, D. N. Matsukevich, P. Maunz, D. Hucul, Q. Quraishi, S. Olmschenk, W. Campbell, J. Mizrahi, C. Senko, and C. Monroe. Entanglement of atomic qubits using an optical frequency comb. *Phys. Rev. Lett.*, 104:140501, Apr 2010.

[100] R. Islam, W. C. Campbell, T. Choi, S. M. Clark, C. W. S. Conover, S. Debnath, E. E. Edwards, B. Fields, D. Hayes, D. Hucul, I. V. Inlek, K. G. Johnson, S. Korenblit, A. Lee, K. W. Lee, T. A. Manning, D. N. Matsukevich, J. Mizrahi, Q. Quraishi,

C. Senko, J. Smith, and C. Monroe. Beat note stabilization of mode-locked lasers for quantum information processing. *Opt. Lett.*, 39(11):3238–3241, Jun 2014.

[101] Gates lab experiment control igor pro 6.2. https://gitlab.com/linkelab/gates-lab-experiment-control-coherence. Accessed: 2024-01-14.

[102] Norbert M. Linke, Dmitri Maslov, Martin Roetteler, Shantanu Debnath, Caroline Figgatt, Kevin A. Landsman, Kenneth Wright, and Christopher Monroe. Experimental comparison of two quantum computing architectures. *Proceedings of the National Academy of Sciences*, 114(13):3305–3310, 2017.

[103] Neal Solmeyer, Norbert M Linke, Caroline Figgatt, Kevin A Landsman, Radhakrishnan Balu, George Siopsis, and C Monroe. Demonstration of a bayesian quantum game on an ion-trap quantum computer. *Quantum Science and Technology*, 3(4):045002, jul 2018.

[104] N. M. Linke, S. Johri, C. Figgatt, K. A. Landsman, A. Y. Matsuura, and C. Monroe. Measuring the rényi entropy of a two-site fermi-hubbard model on a trapped ion quantum computer. *Phys. Rev. A*, 98:052334, Nov 2018.

[105] D. Zhu, N. M. Linke, M. Benedetti, K. A. Landsman, N. H. Nguyen, C. H. Alderete, A. Perdomo-Ortiz, N. Korda, A. Garfoot, C. Brecque, L. Egan, O. Perdomo, and C. Monroe. Training of quantum circuits on a hybrid quantum computer. *Science Advances*, 5(10):eaaw9918, 2019.

[106] O. Shehab, K. Landsman, Y. Nam, D. Zhu, N. M. Linke, M. Keesan, R. C. Pooser, and C. Monroe. Toward convergence of effective-field-theory simulations on digital quantum computers. *Phys. Rev. A*, 100:062319, Dec 2019.

[107] C Huerta Alderete, Shivani Singh, Nhung H Nguyen, Daiwei Zhu, Radhakrishnan Balu, Christopher Monroe, C M Chandrashekar, and Norbert M Linke. Quantum walks and dirac cellular automata on a programmable trapped-ion quantum computer. *Nature Communications*, 11(1):3720, July 2020.

[108] Prakash Murali, Norbert M. Linke, Margaret Martonosi, Ali Javadi Abhari, Nhung Hong Nguyen, and Cinthia Huerta Alderete. Architecting noisy intermediate-scale quantum computers: A real-system study. *IEEE Micro*, 40(3):73–80, 2020.

[109] D. Zhu, S. Johri, N. H. Nguyen, C. Huerta Alderete, K. A. Landsman, N. M. Linke, C. Monroe, and A. Y. Matsuura. Probing many-body localization on a noisy quantum computer. *Phys. Rev. A*, 103:032606, Mar 2021.

[110] Erik Gustafson, Yingyue Zhu, Patrick Dreher, Norbert M. Linke, and Yannick Meurice. Real-time quantum calculations of phase shifts using wave packet time delays. *Phys. Rev. D*, 104:054507, Sep 2021.

[111] Akhil Francis, Daiwei Zhu, Cinthia Huerta Alderete, Sonika Johri, Xiao Xiao, James K. Freericks, Christopher Monroe, Norbert M. Linke, and Alexander F. Kemper. Many-body thermodynamics on quantum computers via partition function zeros. *Science Advances*, 7(34):eabf2447, 2021.

[112] Alaina M. Green, A. Elben, C. Huerta Alderete, Lata Kh Joshi, Nhung H. Nguyen, Torsten V. Zache, Yingyue Zhu, Bhuvanesh Sundar, and Norbert M. Linke. Experimental measurement of out-of-time-ordered correlators at finite temperature. *Phys. Rev. Lett.*, 128:140601, Apr 2022.

[113] Austin K. Daniel, Yingyue Zhu, C. Huerta Alderete, Vikas Buchemmavari, Alaina M. Green, Nhung H. Nguyen, Tyler G. Thurtell, Andrew Zhao, Norbert M. Linke, and Akimasa Miyake. Quantum computational advantage attested by nonlocal games with the cyclic cluster state. *Phys. Rev. Res.*, 4:033068, Jul 2022.

[114] S. Debnath, N. M. Linke, S.-T. Wang, C. Figgatt, K. A. Landsman, L.-M. Duan, and C. Monroe. Observation of hopping and blockade of bosons in a trapped ion spin chain. *Phys. Rev. Lett.*, 120:073001, Feb 2018.

[115] Pak Hong Leung, Kevin A. Landsman, Caroline Figgatt, Norbert M. Linke, Christopher Monroe, and Kenneth R. Brown. Robust 2-qubit gates in a linear ion crystal using a frequency-modulated driving force. *Phys. Rev. Lett.*, 120:020501, Jan 2018.

[116] K. A. Landsman, Y. Wu, P. H. Leung, D. Zhu, N. M. Linke, K. R. Brown, L. Duan, and C. Monroe. Two-qubit entangling gates within arbitrarily long chains of trapped ions. *Phys. Rev. A*, 100:022332, Aug 2019.

[117] Reinhold Blümel, Nikodem Grzesiak, Nhung H. Nguyen, Alaina M. Green, Ming Li, Andrii Maksymov, Norbert M. Linke, and Yunseong Nam. Efficient stabilized two-qubit gates on a trapped-ion quantum computer. *Phys. Rev. Lett.*, 126:220503, Jun 2021.

[118] C. Huerta Alderete, Alaina M. Green, Nhung H. Nguyen, Yingyue Zhu, B. M. Rodríguez-Lara, and Norbert M. Linke. Experimental realization of para-particle oscillators, 2021.

[119] National Instruments. Pxi remote control and system expansion. https://www.ni.com/pdf/product-flyers/pxi-remote-control-and-system-expansion.pdf. Accessed: 2024-01-14.

[120] National Instruments. Ni hardware and software operating system compatibility. https://www.ni.com/en/support/documentation/compatibility/21/ni-hardware-and-operating-system-compatibility.html#section_01. Accessed: 2024-01-27.

[121] Keysight awg xop 8. https://gitlab.com/linkelab/KeysightAWGcpp. Accessed: 2024-01-14.

[122] WaveMetrics. Xop toolkit. https://www.wavemetrics.com/products/xoptoolkit. Accessed: 2024-01-14.

[123] https://www.keysight.com/us/en/lib/software-detail/instrument-firmware-software/sd1-3x-software-3120392.html. Accessed: 2024-01-14.

[124] National Instruments. Pxi/pxie system not correctly recognized or unidentified in ni max. https://knowledge.ni.com/KnowledgeArticleDetails?id=kA00Z000001DbP3SAK&l=en-US. Accessed: 2024-01-27.

[125] National Instruments. Mxi-express compatibility and connectivity troubleshooting guide. https://knowledge.ni.com/KnowledgeArticleDetails?id=kA03q000000x0MKCAY&l=en-US. Accessed: 2024-01-27.

[126] Anders Sorensen and Klaus Molmer. Quantum computation with ions in thermal motion. *Phys. Rev. Lett.*, 82(9):1971–1974, mar 1999.

[127] G. J. Milburn, S. Schneider, and D. F. V. James. Ion trap quantum computing with warm ions. *Fortschritte der Physik*, 48(9-11):801–810, 2000.

[128] C. A. Sackett, D. Kielpinski, B. E. King, C. Langer, V. Meyer, C. J. Myatt, M. Rowe, Q. A. Turchette, W. M. Itano, D. J. Wineland, and C. Monroe. Experimental entanglement of four particles. *Nature*, 404(6775):256–259, mar 2000.

[129] E. Solano, R. L. de Matos Filho, and N. Zagury. Deterministic Bell states and measurement of the motional state of two trapped ions. *Phys. Rev. A*, 59(4):R2539–R2543, apr 1999.

[130] Christian F. Roos. Ion trap quantum gates with amplitude-modulated laser beams. *New J. Phys.*, 10(1):013002, jan 2008.

[131] T. Choi, S. Debnath, T. A. Manning, C. Figgatt, Z.-X. Gong, L.-M. Duan, and C. Monroe. Optimal quantum control of multimode couplings between trapped ion qubits for scalable entanglement. *Phys. Rev. Lett.*, 112:190502, May 2014.

[132] Wilhelm Magnus. On the exponential solution of differential equations for a linear operator. *Communications on Pure and Applied Mathematics*, VII:649–673, 1954.

[133] Sergio Blanes, Fernando Casas, Jose A. Oteo, and Jose Ros. The magnus expansion and some of its applications. *Physics Reports*, 470(5-6):151–238, Jan 2009.

[134] Reinhold Blümel, Nikodem Grzesiak, Neal Pisenti, Kenneth Wright, and Yunseong Nam. Power-optimal, stabilized entangling gate between trapped-ion qubits. *npj Quantum Information*, 7(1):147, Oct 2021.

[135] Yukai Wu, Sheng-Tao Wang, and L.-M. Duan. Noise analysis for high-fidelity quantum entangling gates in an anharmonic linear paul trap. *Phys. Rev. A*, 97:062325, Jun 2018.

[136] V. M. Schäfer, C. J. Ballance, K. Thirumalai, L. J. Stephenson, T. G. Ballance, A. M. Steane, and D. M. Lucas. Fast quantum logic gates with trapped-ion qubits. *Nature*, 555(7694):75–78, Mar 2018.

[137] Craig Gidney and Martin Ekerå. How to factor 2048 bit RSA integers in 8 hours using 20 million noisy qubits. *Quantum*, 5:433, April 2021.

[138] Vera von Burg, Guang Hao Low, Thomas Häner, Damian S. Steiger, Markus Reiher, Martin Roetteler, and Matthias Troyer. Quantum computing enhanced computational catalysis. *Phys. Rev. Res.*, 3:033055, Jul 2021.

[139] Alexander F. Shaw, Pavel Lougovski, Jesse R. Stryker, and Nathan Wiebe. Quantum Algorithms for Simulating the Lattice Schwinger Model. *Quantum*, 4:306, August 2020.

[140] Michael A. Nielsen and Isaac L. Chuang. *Quantum Computation and Quantum Information*. Cambridge University Press, USA, 10 edition, 2011.

[141] E. Knill, R. Laflamme, and W. Zurek. Threshold Accuracy for Quantum Computation, October 1996.

[142] A. Yu Kitaev. Fault-tolerant quantum computation by anyons. *Ann Phys*, 303(1):2–30, January 2003.

[143] Alexey A. Kovalev and Leonid P. Pryadko. Quantum kronecker sum-product low-density parity-check codes with finite rate. *Phys. Rev. A*, 88:012311, Jul 2013.

[144] M. Li and T. J. Yoder. A numerical study of bravyi-bacon-shor and subsystem hypergraph product codes. In *IEEE Int. Conf. Quant. Comp. Eng. (QCE)*, pages 109–119, 2020.

[145] Markus S. Kesselring, Fernando Pastawski, Jens Eisert, and Benjamin J. Brown. The boundaries and twist defects of the color code and their applications to topological quantum computation. *Quantum*, 2:101, October 2018.

[146] M. Gutiérrez, M. Müller, and A. Bermúdez. Transversality and lattice surgery: Exploring realistic routes toward coupled logical qubits with trapped-ion quantum processors. *Phys. Rev. A*, 99:022330, Feb 2019.

[147] Anirudh Krishna and David Poulin. Fault-tolerant gates on hypergraph product codes. *Phys. Rev. X*, 11:011023, Feb 2021.

[148] Peter W. Shor. Scheme for reducing decoherence in quantum computer memory. *Phys. Rev. A*, 52(4):R2493–R2496, October 1995.

[149] Yu Tomita and Krysta M. Svore. Low-distance surface codes under realistic quantum noise. *Phys. Rev. A*, 90(6):062320, December 2014.

[150] Dave Bacon. Operator quantum error-correcting subsystems for self-correcting quantum memories. *Phys. Rev. A*, 73(1):012340, January 2006.

[151] Muyuan Li, Daniel Miller, Michael Newman, Yukai Wu, and Kenneth R. Brown. 2D Compass Codes. *Phys. Rev. X*, 9(2):021041, May 2019.

[152] Robert Raussendorf and Jim Harrington. Fault-Tolerant Quantum Computation with High Threshold in Two Dimensions. *Phys. Rev. Lett.*, 98(19):190504, May 2007.

[153] Austin G. Fowler, Adam C. Whiteside, and Lloyd C. L. Hollenberg. Towards Practical Classical Processing for the Surface Code. *Phys. Rev. Lett.*, 108(18):180501, May 2012.

[154] Ashley M. Stephens. Fault-tolerant thresholds for quantum error correction with the surface code. *Phys. Rev. A*, 89(2):022321, February 2014.

[155] John Napp and John Preskill. Optimal bacon-shor codes, September 2012.

[156] Panos Aliferis and Andrew W. Cross. Subsystem Fault Tolerance with the Bacon-Shor Code. *Phys. Rev. Lett.*, 98(22):220502, May 2007.

[157] Dripto M Debroy, Muyuan Li, Shilin Huang, and Kenneth R Brown. Logical performance of 9 qubit compass codes in ion traps with crosstalk errors. *Quantum Science and Technology*, 5(3):034002, apr 2020.

[158] Muyuan Li, Daniel Miller, and Kenneth R. Brown. Direct measurement of Bacon-Shor code stabilizers. *Phys. Rev. A*, 98(5):050301(R), November 2018.

[159] D. H. Slichter, V. B. Verma, D. Leibfried, R. P. Mirin, S. W. Nam, and D. J. Wineland. Uv-sensitive superconducting nanowire single photon detectors for integration in an ion trap. *Opt. Express*, 25(8):8705–8720, Apr 2017.

[160] Stephen Crain, Clinton Cahall, Geert Vrijsen, Emma E. Wollman, Matthew D. Shaw, Varun B. Verma, Sae Woo Nam, and Jungsang Kim. High-speed low-crosstalk detection of a 171 Yb + qubit using superconducting nanowire single photon detectors. *Commun. Phys.*, 2(1):1–6, August 2019.

[161] Peter Lukas Wilhelm Maunz. High optical access trap 2.0., 1 2016.

[162] G Pagano, P W Hess, H B Kaplan, W L Tan, P Richerme, P Becker, A Kyprianidis, J Zhang, E Birckelbaw, M R Hernandez, Y Wu, and C Monroe. Cryogenic trapped-ion system for large scale quantum simulation. *Quantum Science and Technology*, 4(1):014004, oct 2018.

[163] Karan K. Mehta, Chi Zhang, Maciej Malinowski, Thanh-Long Nguyen, Martin Stadler, and Jonathan P. Home. Integrated optical multi-ion quantum logic. *Nature*, 586(7830):533–537, October 2020.

[164] R. J. Niffenegger, J. Stuart, C. Sorace-Agaskar, D. Kharas, S. Bramhavar, C. D. Bruzewicz, W. Loh, R. T. Maxson, R. McConnell, D. Reens, G. N. West, J. M. Sage, and J. Chiaverini. Integrated multi-wavelength control of an ion qubit. *Nature*, 586(7830):538–542, October 2020.

[165] Ye Wang, Stephen Crain, Chao Fang, Bichen Zhang, Shilin Huang, Qiyao Liang, Pak Hong Leung, Kenneth R. Brown, and Jungsang Kim. High-Fidelity Two-Qubit Gates Using a Microelectromechanical-System-Based Beam Steering System for Individual Qubit Addressing. *Phys. Rev. Lett.*, 125(15):150505, October 2020.

[166] Karsten Pyka, Norbert Herschbach, Jonas Keller, and Tanja E. Mehlstäubler. A high-precision segmented paul trap with minimized micromotion for an optical multiple-ion clock. *Applied Physics B*, 114(1):231–241, Jan 2014.

[167] Chiara Decaroli, Roland Matt, Robin Oswald, Christopher Axline, Maryse Ernzer, Jeremy Flannery, Simon Ragg, and Jonathan P Home. Design, fabrication and characterization of a micro-fabricated stacked-wafer segmented ion trap with two x-junctions. *Quantum Science and Technology*, 6(4):044001, jul 2021.

[168] Shruti Puri, Lucas St-Jean, Jonathan A. Gross, Alexander Grimm, N. E. Frattini, Pavithran S. Iyer, Anirudh Krishna, Steven Touzard, Liang Jiang, Alexandre Blais, Steven T. Flammia, and S. M. Girvin. Bias-preserving gates with stabilized cat qubits. *Sci. Adv.*, 6(34):eaay5901, August 2020.

[169] J. Pablo Bonilla Ataides, David K. Tuckett, Stephen D. Bartlett, Steven T. Flammia, and Benjamin J. Brown. The xzzx surface code. *Nature Communications*, 12(1):2172, Apr 2021.

[170] David K. Tuckett, Stephen D. Bartlett, Steven T. Flammia, and Benjamin J. Brown. Fault-tolerant thresholds for the surface code in excess of 5% under biased noise. *Phys. Rev. Lett.*, 124(13):130501, March 2020.

[171] Christopher Chamberland, Kyungjoo Noh, Patricio Arrangoiz-Arriola, Earl T. Campbell, Connor T. Hann, Joseph Iverson, Harald Putterman, Thomas C. Bohdanowicz, Steven T. Flammia, Andrew Keller, Gil Refael, John Preskill, Liang Jiang, Amir H. Safavi-Naeini, Oskar Painter, and Fernando G.S.L. Brandão. Building a fault-tolerant quantum computer using concatenated cat codes. *PRX Quantum*, 3:010329, Feb 2022.

[172] Seth Lloyd. Universal quantum simulators. *Science*, 273(5278):1073–1078, 1996.

[173] Andrew M. Childs, Yuan Su, Minh C. Tran, Nathan Wiebe, and Shuchen Zhu. Theory of Trotter Error with Commutator Scaling. *Phys. Rev. X*, 11(1):011020, February 2021.

[174] Andrew M Childs and Nathan Wiebe. Hamiltonian simulation using linear combinations of unitary operations. *Quantum Inf. Comput.*, 12:901–921, 2012.

[175] Dominic W. Berry, Andrew M. Childs, Richard Cleve, Robin Kothari, and Rolando D. Somma. Simulating Hamiltonian dynamics with a truncated Taylor series. *Phys. Rev. Lett.*, 114(9):090502, 2015.

[176] Guang Hao Low and Isaac L. Chuang. Optimal hamiltonian simulation by quantum signal processing. *Phys. Rev. Lett.*, 118:010501, Jan 2017.

[177] Guang Hao Low and Isaac L. Chuang. Hamiltonian simulation by qubitization. *Quantum*, 3:163, July 2019.

[178] Shantanav Chakraborty, András Gilyén, and Stacey Jeffery. The Power of Block-Encoded Matrix Powers: Improved Regression Techniques via Faster Hamiltonian

Simulation. In Christel Baier, Ioannis Chatzigiannakis, Paola Flocchini, and Stefano Leonardi, editors, *46th International Colloquium on Automata, Languages, and Programming (ICALP 2019)*, volume 132 of *Leibniz International Proceedings in Informatics (LIPIcs)*, pages 33:1–33:14, Dagstuhl, Germany, 2019. Schloss Dagstuhl–Leibniz-Zentrum fuer Informatik.

[179] András Gilyén, Yuan Su, Guang Hao Low, and Nathan Wiebe. Quantum singular value transformation and beyond: exponential improvements for quantum matrix arithmetics. In *Proceedings of the 51st Annual ACM SIGACT Symposium on Theory of Computing*, pages 193–204, 2019.

[180] Amir Kalev and Itay Hen. Quantum algorithm for simulating hamiltonian dynamics with an off-diagonal series expansion. *Quantum*, 5:426, 2021.

[181] Andrew M. Childs and Yuan Su. Nearly Optimal Lattice Simulation by Product Formulas. *Phys. Rev. Lett.*, 123(5):050503, August 2019.

[182] Torin F Stetina, Anthony Ciavarella, Xiaosong Li, and Nathan Wiebe. Simulating effective qed on quantum computers. *arXiv:2101.00111*, 2020.

[183] Joonho Lee, Dominic W. Berry, Craig Gidney, William J. Huggins, Jarrod R. McClean, Nathan Wiebe, and Ryan Babbush. Even more efficient quantum computations of chemistry through tensor hypercontraction. *PRX Quantum*, 2:030305, Jul 2021.

[184] William J. Huggins, Jarrod R. McClean, Nicholas C. Rubin, Zhang Jiang, Nathan Wiebe, K. Birgitta Whaley, and Ryan Babbush. Efficient and noise resilient mea-

surements for quantum chemistry on near-term quantum computers. *npj Quantum Inf.*, 7(1):23, Feb 2021.

[185] Ryan Babbush, Craig Gidney, Dominic W. Berry, Nathan Wiebe, Jarrod McClean, Alexandru Paler, Austin Fowler, and Hartmut Neven. Encoding electronic spectra in quantum circuits with linear t complexity. *Phys. Rev. X*, 8:041015, Oct 2018.

[186] Ryan Babbush, Nathan Wiebe, Jarrod McClean, James McClain, Hartmut Neven, and Garnet Kin-Lic Chan. Low-depth quantum simulation of materials. *Phys. Rev. X*, 8:011044, Mar 2018.

[187] Stephen P Jordan, Keith SM Lee, and John Preskill. Quantum algorithms for quantum field theories. *Science*, 336(6085):1130–1133, 2012.

[188] Natalie Klco and Martin J. Savage. Digitization of scalar fields for quantum computing. *Phys. Rev. A*, 99(5):052335, 2019.

[189] Joao Barata, Niklas Mueller, Andrey Tarasov, and Raju Venugopalan. Single-particle digitization strategy for quantum computation of a ϕ^4 scalar field theory. *Phys. Rev. A*, 103(4):042410, 2021.

[190] Henry Lamm, Scott Lawrence, and Yukari Yamauchi. General Methods for Digital Quantum Simulation of Gauge Theories. *Phys. Rev. D*, 100(3):034518, 2019.

[191] Alexander F. Shaw, Pavel Lougovski, Jesse R. Stryker, and Nathan Wiebe. Quantum Algorithms for Simulating the Lattice Schwinger Model. *Quantum*, 4:306, August 2020.

[192] Anthony Ciavarella, Natalie Klco, and Martin J. Savage. Trailhead for quantum simulation of SU(3) Yang-Mills lattice gauge theory in the local multiplet basis. *Phys. Rev. D*, 103(9):094501, 2021.

[193] Angus Kan and Yunseong Nam. Lattice quantum chromodynamics and electrodynamics on a universal quantum computer. *arXiv:2107.12769*, 2021.

[194] Michael Kreshchuk, William M Kirby, Gary Goldstein, Hugo Beauchemin, and Peter J Love. Quantum simulation of quantum field theory in the light-front formulation. *arXiv:2002.04016*, 2020.

[195] Junyu Liu and Yuan Xin. Quantum simulation of quantum field theories as quantum chemistry. *J. High Energy Phys.*, 2020(12):11, Dec 2020.

[196] Danny Paulson, Luca Dellantonio, Jan F. Haase, Alessio Celi, Angus Kan, Andrew Jena, Christian Kokail, Rick van Bijnen, Karl Jansen, Peter Zoller, and Christine A. Muschik. Simulating 2d effects in lattice gauge theories on a quantum computer. *PRX Quantum*, 2:030334, Aug 2021.

[197] Benjamin Nachman, Davide Provasoli, Wibe A. de Jong, and Christian W. Bauer. Quantum algorithm for high energy physics simulations. *Phys. Rev. Lett.*, 126:062001, Feb 2021.

[198] Minh C. Tran, Yuan Su, Daniel Carney, and Jacob M. Taylor. Faster digital quantum simulation by symmetry protection. *PRX Quantum*, 2:010323, Feb 2021.

[199] Henry Lamm, Scott Lawrence, and Yukari Yamauchi. Suppressing Coherent Gauge Drift in Quantum Simulations. *arXiV:2005.12688*, 5 2020.

[200] Jad C. Halimeh, Haifeng Lang, Julius Mildenberger, Zhang Jiang, and Philipp Hauke. Gauge-symmetry protection using single-body terms. *PRX Quantum*, 2:040311, Oct 2021.

[201] Jad C Halimeh, Haifeng Lang, and Philipp Hauke. Gauge protection in non-abelian lattice gauge theories. *New Journal of Physics*, 24(3):033015, mar 2022.

[202] K. Stannigel, P. Hauke, D. Marcos, M. Hafezi, S. Diehl, M. Dalmonte, and P. Zoller. Constrained dynamics via the Zeno effect in quantum simulation: Implementing non-Abelian lattice gauge theories with cold atoms. *Phys. Rev. Lett.*, 112(12):120406, 2014.

[203] Valentin Kasper, Torsten V. Zache, Fred Jendrzejewski, Maciej Lewenstein, and Erez Zohar. Non-Abelian gauge invariance from dynamical decoupling. *arXiv:2012.08620*, December 2020.

[204] Jesse R. Stryker. Oracles for Gauss's law on digital quantum computers. *Phys. Rev. A*, 99(4):042301, 2019.

[205] Indrakshi Raychowdhury and Jesse R. Stryker. Solving gauss's law on digital quantum computers with loop-string-hadron digitization. *Phys. Rev. Research*, 2:033039, Jul 2020.

[206] Abhinav Kandala, Kristan Temme, Antonio D. Córcoles, Antonio Mezzacapo, Jerry M. Chow, and Jay M. Gambetta. Error mitigation extends the computational reach of a noisy quantum processor. *Nature*, 567(7749):491–495, Mar 2019.

[207] Kristan Temme, Sergey Bravyi, and Jay M. Gambetta. Error mitigation for short-depth quantum circuits. *Phys. Rev. Lett.*, 119:180509, Nov 2017.

[208] Suguru Endo, Simon C. Benjamin, and Ying Li. Practical quantum error mitigation for near-future applications. *Phys. Rev. X*, 8:031027, Jul 2018.

[209] Swamit S. Tannu and Moinuddin K. Qureshi. Mitigating measurement errors in quantum computers by exploiting state-dependent bias. In *Proceedings of the 52nd Annual IEEE/ACM International Symposium on Microarchitecture*, MICRO '52, page 279–290, New York, NY, USA, 2019. Association for Computing Machinery.

[210] Joel J. Wallman and Joseph Emerson. Noise tailoring for scalable quantum computation via randomized compiling. *Phys. Rev. A*, 94:052325, Nov 2016.

[211] Andrew Shaw. Classical-Quantum Noise Mitigation for NISQ Hardware. *arXiv:2105.08701*, 2021.

[212] Andre He, Benjamin Nachman, Wibe A. de Jong, and Christian W. Bauer. Zero-noise extrapolation for quantum-gate error mitigation with identity insertions. *Phys. Rev. A*, 102:012426, Jul 2020.

[213] Piotr Czarnik, Andrew Arrasmith, Patrick J. Coles, and Lukasz Cincio. Error mitigation with clifford quantum-circuit data. *Quantum*, 5:592, Nov 2021.

[214] Joseph Vovrosh, Kiran E. Khosla, Sean Greenaway, Christopher Self, M. S. Kim, and Johannes Knolle. Simple mitigation of global depolarizing errors in quantum simulations. *Phys. Rev. E*, 104:035309, Sep 2021.

[215] Y. Aoki et al. FLAG Review 2021. *arXiv:2111.09849*, 11 2021.

[216] S. R. Beane, W. Detmold, K. Orginos, and M. J. Savage. Nuclear Physics from Lattice QCD. *Prog. Part. Nucl. Phys.*, 66:1–40, 2011.

[217] Heng-Tong Ding, Frithjof Karsch, and Swagato Mukherjee. Thermodynamics of strong-interaction matter from Lattice QCD. *Int. J. Mod. Phys. E*, 24(10):1530007, 2015.

[218] Raul A. Briceno, Jozef J. Dudek, and Ross D. Young. Scattering processes and resonances from lattice QCD. *Rev. Mod. Phys.*, 90(2):025001, 2018.

[219] Claudia Ratti. Lattice QCD and heavy ion collisions: a review of recent progress. *Rept. Prog. Phys.*, 81(8):084301, 2018.

[220] Zohreh Davoudi, William Detmold, Kostas Orginos, Assumpta Parreño, Martin J. Savage, Phiala Shanahan, and Michael L. Wagman. Nuclear matrix elements from lattice QCD for electroweak and beyond-Standard-Model processes. *Phys. Rept.*, 900:1–74, 2021.

[221] Esteban A. Calzetta and Bei-Lok B. Hu. *Nonequilibrium Quantum Field Theory*. Cambridge Monographs on Mathematical Physics. Cambridge University Press, 9 2008.

[222] Julian Schwinger. On Gauge Invariance and Vacuum Polarization. *Phys. Rev.*, 82(5):664–679, June 1951.

[223] Julian Schwinger. Gauge Invariance and Mass. II. *Phys. Rev.*, 128(5):2425–2429, December 1962.

[224] Julian Schwinger. The Theory of Quantized Fields. II. *Phys. Rev.*, 91:713–728, Aug 1953.

[225] D. Banerjee, M. Dalmonte, M. Müller, E. Rico, P. Stebler, U.-J. Wiese, and P. Zoller. Atomic Quantum Simulation of Dynamical Gauge Fields coupled to Fermionic Matter: From String Breaking to Evolution after a Quench. *Phys. Rev. Lett.*, 109(17):175302, October 2012.

[226] Erez Zohar, J. Ignacio Cirac, and Benni Reznik. Quantum simulations of lattice gauge theories using ultracold atoms in optical lattices. *Rep. Prog. Phys.*, 79(1):014401, December 2015.

[227] Dayou Yang, Gouri Shankar Giri, Michael Johanning, Christof Wunderlich, Peter Zoller, and Philipp Hauke. Analog quantum simulation of $(1+1)$-dimensional lattice QED with trapped ions. *Phys. Rev. A*, 94(5):052321, November 2016.

[228] Zohreh Davoudi, Mohammad Hafezi, Christopher Monroe, Guido Pagano, Alireza Seif, and Andrew Shaw. Towards analog quantum simulations of lattice gauge theories with trapped ions. *Phys. Rev. Research*, 2(2):023015, April 2020.

[229] Federica M. Surace, Paolo P. Mazza, Giuliano Giudici, Alessio Lerose, Andrea Gambassi, and Marcello Dalmonte. Lattice gauge theories and string dynamics in Rydberg atom quantum simulators. *Phys. Rev. X*, 10(2):021041, May 2020.

[230] Di Luo, Jiayu Shen, Michael Highman, Bryan K. Clark, Brian DeMarco, Aida X. El-Khadra, and Bryce Gadway. Framework for simulating gauge theories with dipolar spin systems. *Phys. Rev. A*, 102:032617, Sep 2020.

[231] Bárbara Andrade, Zohreh Davoudi, Tobias Graß, Mohammad Hafezi, Guido Pagano, and Alireza Seif. Engineering an effective three-spin hamiltonian in trapped-ion systems for applications in quantum simulation. *arXiv:2108.01022*, 2021.

[232] Christine Muschik, Markus Heyl, Esteban Martinez, Thomas Monz, Philipp Schindler, Berit Vogell, Marcello Dalmonte, Philipp Hauke, Rainer Blatt, and Peter Zoller. U(1) Wilson lattice gauge theories in digital quantum simulators. *New J. Phys.*, 19(10):103020, October 2017.

[233] N. Klco, E. F. Dumitrescu, A. J. McCaskey, T. D. Morris, R. C. Pooser, M. Sanz, E. Solano, P. Lougovski, and M. J. Savage. Quantum-classical computation of schwinger model dynamics using quantum computers. *Phys. Rev. A*, 98:032331, Sep 2018.

[234] Hsuan-Hao Lu, Natalie Klco, Joseph M. Lukens, Titus D. Morris, Aaina Bansal, Andreas Ekström, Gaute Hagen, Thomas Papenbrock, Andrew M. Weiner, Martin J. Savage, and Pavel Lougovski. Simulations of subatomic many-body physics on a quantum frequency processor. *Phys. Rev. A*, 100:012320, Jul 2019.

[235] Bipasha Chakraborty, Masazumi Honda, Taku Izubuchi, Yuta Kikuchi, and Akio Tomiya. Digital Quantum Simulation of the Schwinger Model with Topological Term via Adiabatic State Preparation. *arXiv:2001.00485*, 1 2020.

[236] Jesse R Stryker. Shearing approach to gauge invariant trotterization. *arXiv:2105.11548*, 2021.

[237] Zohreh Davoudi, Norbert M. Linke, and Guido Pagano. Toward simulating quantum field theories with controlled phonon-ion dynamics: A hybrid analog-digital approach. *Phys. Rev. Research*, 3:043072, Oct 2021.

[238] Giovanni Pederiva, Alexei Bazavov, Brandon Henke, Leon Hostetler, Dean Lee, Huey-Wen Lin, and Andrea Shindler. Quantum State Preparation for the Schwinger Model. In *38th International Symposium on Lattice Field Theory*, 9 2021.

[239] Abhishek Rajput, Alessandro Roggero, and Nathan Wiebe. Hybridized Methods for Quantum Simulation in the Interaction Picture. *arXiv:2109.03308*, 9 2021.

[240] Hannes Bernien, Sylvain Schwartz, Alexander Keesling, Harry Levine, Ahmed Omran, Hannes Pichler, Soonwon Choi, Alexander S. Zibrov, Manuel Endres, Markus Greiner, Vladan Vuletić, and Mikhail D. Lukin. Probing many-body dynamics on a 51-atom quantum simulator. *Nature*, 551(7682):579–584, November 2017.

[241] Alexander Mil, Torsten V. Zache, Apoorva Hegde, Andy Xia, Rohit P. Bhatt, Markus K. Oberthaler, Philipp Hauke, Jürgen Berges, and Fred Jendrzejewski. A scalable realization of local U(1) gauge invariance in cold atomic mixtures. *Science*, 367(6482):1128–1130, March 2020.

[242] Zhao-Yu Zhou, Guo-Xian Su, Jad C Halimeh, Robert Ott, Hui Sun, Philipp Hauke, Bing Yang, Zhen-Sheng Yuan, Jürgen Berges, and Jian-Wei Pan. Thermalization dynamics of a gauge theory on a quantum simulator. *arXiv:2107.13563*, 2021.

[243] Wibe A de Jong, Kyle Lee, James Mulligan, Mateusz Płoskoń, Felix Ringer, and Xiaojun Yao. Quantum simulation of non-equilibrium dynamics and thermalization in the schwinger model. *arXiv:2106.08394*, 2021.

[244] John Kogut and Leonard Susskind. Hamiltonian formulation of Wilson's lattice gauge theories. *Phys. Rev. D*, 11(2):395–408, jan 1975.

[245] C. J. Hamer, Zheng Weihong, and J. Oitmaa. Series expansions for the massive Schwinger model in Hamiltonian lattice theory. *Phys. Rev. D*, 56:55–67, Jul 1997.

[246] Masuo Suzuki. General theory of fractal path integrals with applications to many-body theories and statistical physics. *J. Math. Phys.*, 32(2):400–407, February 1991.

[247] Thomas Monz, Philipp Schindler, Julio T. Barreiro, Michael Chwalla, Daniel Nigg, William A. Coish, Maximilian Harlander, Wolfgang Hänsel, Markus Hennrich, and Rainer Blatt. 14-Qubit Entanglement: Creation and Coherence. *Phys. Rev. Lett.*, 106(13):130506, March 2011.

[248] Yuan Su, Hsin-Yuan Huang, and Earl T. Campbell. Nearly tight trotterization of interacting electrons. *Quantum*, 5:495, Jul 2021.

[249] Dong An, Di Fang, and Lin Lin. Time-dependent unbounded hamiltonian simulation with vector norm scaling. *Quantum*, 5:459, May 2021.

[250] Changhao Yi and Elizabeth Crosson. Spectral analysis of product formulas for quantum simulation. *arXiv:2102.12655*, 2021.

[251] Qi Zhao, You Zhou, Alexander F Shaw, Tongyang Li, and Andrew M Childs. Hamiltonian simulation with random inputs. *arXiv:2111.04773*, 2021.

[252] Burak Şahinoğlu and Rolando D. Somma. Hamiltonian simulation in the low-energy subspace. *npj Quantum Inf.*, 7(1):119, Jul 2021.

[253] Yu Tong, Victor V. Albert, Jarrod R. McClean, John Preskill, and Yuan Su. Provably accurate simulation of gauge theories and bosonic systems. *arXiv:2110.06942*, October 2021.

[254] Natalie Klco, Martin J. Savage, and Jesse R. Stryker. Su(2) non-abelian gauge field theory in one dimension on digital quantum computers. *Phys. Rev. D*, 101:074512, Apr 2020.

[255] Yasar Y. Atas, Jinglei Zhang, Randy Lewis, Amin Jahanpour, Jan F. Haase, and Christine A. Muschik. Su(2) hadrons on a quantum computer via a variational approach. *Nat. Comm.*, 12(1):6499, Nov 2021.

[256] Sarmed A Rahman, Randy Lewis, Emanuele Mendicelli, and Sarah Powell. Su(2) lattice gauge theory on a quantum annealer. *Phys. Rev. D*, 104:034501, Aug 2021.

[257] Jan F Haase, Luca Dellantonio, Alessio Celi, Danny Paulson, Angus Kan, Karl Jansen, and Christine A Muschik. A resource efficient approach for quantum and classical simulations of gauge theories in particle physics. *Quantum*, 5:393, 2021.

[258] Indrakshi Raychowdhury and Jesse R. Stryker. Loop, string, and hadron dynamics in SU(2) Hamiltonian lattice gauge theories. *Phys. Rev. D*, 101(11):114502, 2020.

[259] Zohreh Davoudi, Indrakshi Raychowdhury, and Andrew Shaw. Search for efficient formulations for hamiltonian simulation of non-abelian lattice gauge theories. *Phys. Rev. D*, 104:074505, Oct 2021.

[260] M. Sohaib Alam, Stuart Hadfield, Henry Lamm, and Andy C. Y. Li. Quantum Simulation of Dihedral Gauge Theories. *arXiv:2108.13305*, 8 2021.

[261] Anthony N. Ciavarella and Ivan A. Chernyshev. Preparation of the SU(3) Lattice Yang-Mills Vacuum with Variational Quantum Methods. *arXiv:2112.09083*, 12 2021.

[262] Natalie Klco, Alessandro Roggero, and Martin J. Savage. Standard Model Physics and the Digital Quantum Revolution: Thoughts about the Interface. *arXiv:2107.04769*, 7 2021.

[263] P. Campagne-Ibarcq, A. Eickbusch, S. Touzard, E. Zalys-Geller, N. E. Frattini, V. V. Sivak, P. Reinhold, S. Puri, S. Shankar, R. J. Schoelkopf, L. Frunzio, M. Mirrahimi, and M. H. Devoret. Quantum error correction of a qubit encoded in grid states of an oscillator. *Nature*, 584:368–372, 2020.

[264] Darrick E. Chang, Vladan Vuletić, and Mikhail D. Lukin. Quantum nonlinear optics — photon by photon. *Nature Photonics*, 8:685–694, 2014.

[265] D. Porras and J. I. Cirac. Bose-einstein condensation and strong-correlation behavior of phonons in ion traps. *Phys. Rev. Lett.*, 93:263602, Dec 2004.

[266] S. Debnath, N. M. Linke, S.-T. Wang, C. Figgatt, K. A. Landsman, L.-M. Duan, and C. Monroe. Observation of hopping and blockade of bosons in a trapped ion spin chain. *Phys. Rev. Lett.*, 120:073001, Feb 2018.

[267] Mark Um, Junhua Zhang, Dingshun Lv, Yao Lu, Shuoming An, Jing-Ning Zhang, Hyunchul Nha, M. S. Kim, and Kihwan Kim. Phonon arithmetic in a trapped ion system. *Nature Communications*, 7(1):11410, April 2016. Number: 1 Publisher: Nature Publishing Group.

[268] Or Katz and Christopher Monroe. Programmable quantum simulations of bosonic systems with trapped ions. *Phys. Rev. Lett.*, 131:033604, Jul 2023.

[269] Wentao Chen, Yao Lu, Shuaining Zhang, Kuan Zhang, Guanhao Huang, Mu Qiao, Xiaolu Su, Jialiang Zhang, Jing-Ning Zhang, Leonardo Banchi, M. S. Kim, and Kihwan Kim. Scalable and programmable phononic network with trapped ions. *Nature Physics*, 19:877–883, 2023.

[270] Marion Mallweger, Murilo Henrique de Oliveira, Robin Thomm, Harry Parke, Natalia Kuk, Gerard Higgins, Romain Bachelard, Celso Jorge Villas-Boas, and Markus Hennrich. Single-shot measurements of phonon number states using the autler-townes effect. *Physical Review Letters*, 131(22), November 2023.

[271] C. Flühmann, T. L. Nguyen, M. Marinelli, V. Negnevitsky, K. Mehta, and J. P. Home. Encoding a qubit in a trapped-ion mechanical oscillator. *Nature*, 566:513–517, 2019.

[272] Brennan de Neeve, Thanh-Long Nguyen, Tanja Behrle, and Jonathan P. Home. Error correction of a logical grid state qubit by dissipative pumping. *Nature Physics*, 18:296–300, 2022.

[273] V. G. Matsos, C. H. Valahu, T. Navickas, A. D. Rao, M. J. Millican, M. J. Biercuk, and T. R. Tan. Robust and deterministic preparation of bosonic logical states in a trapped ion, 2023.

[274] Xiang Zhang, Kuan Zhang, Yangchao Shen, Shuaining Zhang, Jing-Ning Zhang, Man-Hong Yung, Jorge Casanova, Julen S. Pedernales, Lucas Lamata, Enrique Solano, and Kihwan Kim. Experimental quantum simulation of fermion-antifermion scattering via boson exchange in a trapped ion. *Nature Communications*, 9(1), January 2018.

[275] J. Casanova, L. Lamata, I. L. Egusquiza, R. Gerritsma, C. F. Roos, J. J. García-Ripoll, and E. Solano. Quantum simulation of quantum field theories in trapped ions. *Phys. Rev. Lett.*, 107:260501, Dec 2011.

[276] Dayou Yang, Gouri Shankar Giri, Michael Johanning, Christof Wunderlich, Peter Zoller, and Philipp Hauke. Analog quantum simulation of $(1+1)$-dimensional lattice qed with trapped ions. *Phys. Rev. A*, 94:052321, Nov 2016.

[277] Hideki Yukawa. On the Interaction of Elementary Particles I. *Proc. Phys. Math. Soc. Jap.*, 17:48–57, 1935.

[278] Philipp Gerhold and Karl Jansen. The phase structure of a chirally invariant lattice higgs-yukawa model for small and for large values of the yukawa coupling constant. *Journal of High Energy Physics*, 2007(09):041–041, sep 2007.

[279] Michael E. Peskin and Daniel V. Schroeder. *An Introduction to quantum field theory.* Addison-Wesley, Reading, USA, 1995.